SAIMM
JOURNAL OF THE SOUTHERN AFRICAN INSTITUTE OF MINING AND METALLURGY
FOUNDED 1894
VOLUME 118 NO. 3 MARCH 2018

MINING WITH

ELBROC
MINING PRODUCTS (PTY) LTD

ELBROC OMNI PROP

Dynamic Support

The Omni sacrificial and re-usable hydraulic prop performs in accordance with COMRO guidelines for rock-burst and rock-fall conditions.

- Safe remote installation
- Resilient in rock-burst conditions
- Superb energy absorption
- Can accommodate numerous seismic events
- Constant support resistance
- Reusable
- Light, easy and quick to install
- Cannot be over extended
- Standard attachments
- Controlled yielding

OMNI 89

- 89mm diameter
- 20 ton support resistance
- Blast on dynamic load bearing
- Covers stoping widths up to 2.0m
- Light weight

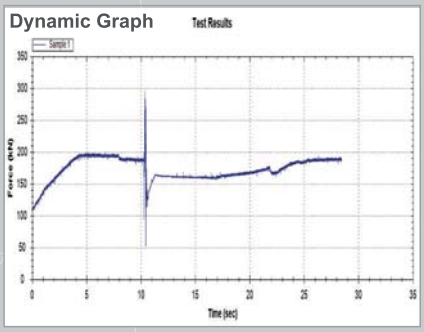

OMNI 127

- 127mm diameter
- 20 ton support resistance
- Blast on dynamic load bearing
- Covers stoping widths up to 4.5m

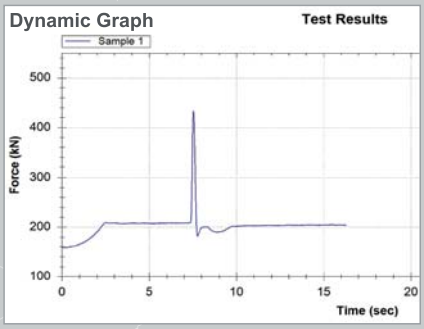

OMNI 150

- 150mm diameter
- 20 & 40 ton support resistance
- Blast on dynamic load bearing
- Covers stoping widths up to 6m
- Longer lengths available

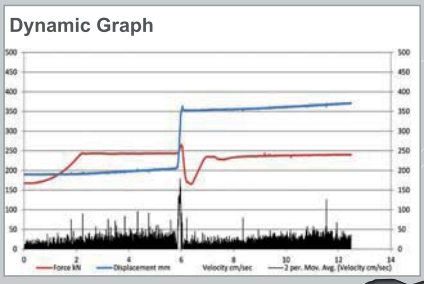

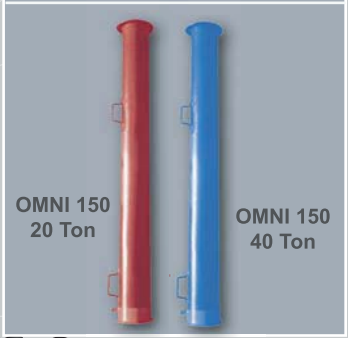

SABS ISO 9001

FOR OUR FULL PRODUCT RANGE PLEASE VISIT OUR WEBPAGE

a member of the rbh royal bafokeng holdings

Tel: 011 974-8013 • sales@elbroc.co.za

www.elbroc.co.za

mogs mining, oil and gas services

The best blast, on time, every time

The future of mining is electronic initiation

DetNet continues to strive towards excellence in electronic initiation. As a world leader in our field, we aim to deliver the latest technology, consistent quality, and improved loading and fragmentation, all to ensure mining becomes more sustainable today and into the future. You can rely on DetNet to provide the best blast, on time, every time.

detnet™

detnet.com

the future of electronic initiation

OFFICE BEARERS AND COUNCIL FOR THE 2017/2018 SESSION

Honorary President
Mxolis Donald Mbuyisa Mgojo
President, Chamber of Mines of South Africa

Honorary Vice-Presidents
Mosebenzi Joseph Zwane
Minister of Mineral Resources, South Africa

Rob Davies
Minister of Trade and Industry, South Africa

Naledi Pandor
Minister of Science and Technology, South Africa

President
S. Ndlovu

President Elect
A.S. Macfarlane

Senior Vice-President
M.I. Mthenjane

Junior Vice-President
Z. Botha

Immediate Past President
C. Musingwini

Honorary Treasurer
J.L. Porter

Ordinary Members on Council

V.G. Duke
I.J. Geldenhuys
M.F. Handley
W.C. Joughin
E. Matinde
M. Motuku
D.D. Munro
G. Njowa
S.M Rupprecht
A.G. Smith
M.H. Solomon
D. Tudor
D.J. van Niekerk
A.T. van Zyl

Past Presidents Serving on Council

N.A. Barcza
R.D. Beck
J.R. Dixon
M. Dworzanowski
H.E. James
R.T. Jones
G.V.R. Landman
R.G.B. Pickering
S.J. Ramokgopa
M.H. Rogers
D.A.J. Ross-Watt
G.L. Smith
W.H. van Niekerk
R.P.H. Willis

G.R. Lane–TPC Mining Chairperson
Z. Botha–TPC Metallurgy Chairperson

A.S. Nhleko–YPC Chairperson
K.M. Letsoalo–YPC Vice-Chairperson

Branch Chairpersons

Botswana	L.E. Dimbungu
DRC	S. Maleba
Johannesburg	J.A. Luckmann
Namibia	N.M. Namate
Northern Cape	W.J. Mans
Pretoria	R.J. Mostert
Western Cape	R.D. Beck
Zambia	D. Muma
Zimbabwe	S. Matutu
Zululand	C.W. Mienie

Corresponding Members of Council

Australia:	I.J. Corrans, R.J. Dippenaar, A. Croll, C. Workman-Davies
Austria:	H. Wagner
Botswana:	S.D. Williams
United Kingdom:	J.J.L. Cilliers, N.A. Barcza
USA:	J-M.M. Rendu, P.C. Pistorius

PAST PRESIDENTS

*Deceased

* W. Bettel (1894–1895)
* A.F. Crosse (1895–1896)
* W.R. Feldtmann (1896–1897)
* C. Butters (1897–1898)
* J. Loevy (1898–1899)
* J.R. Williams (1899–1903)
* S.H. Pearce (1903–1904)
* W.A. Caldecott (1904–1905)
* W. Cullen (1905–1906)
* E.H. Johnson (1906–1907)
* J. Yates (1907–1908)
* R.G. Bevington (1908–1909)
* A. McA. Johnston (1909–1910)
* J. Moir (1910–1911)
* C.B. Saner (1911–1912)
* W.R. Dowling (1912–1913)
* A. Richardson (1913–1914)
* G.H. Stanley (1914–1915)
* J.E. Thomas (1915–1916)
* J.A. Wilkinson (1916–1917)
* G. Hildick-Smith (1917–1918)
* H.S. Meyer (1918–1919)
* J. Gray (1919–1920)
* J. Chilton (1920–1921)
* F. Wartenweiler (1921–1922)
* G.A. Watermeyer (1922–1923)
* F.W. Watson (1923–1924)
* C.J. Gray (1924–1925)
* H.A. White (1925–1926)
* H.R. Adam (1926–1927)
* Sir Robert Kotze (1927–1928)
* J.A. Woodburn (1928–1929)
* H. Pirow (1929–1930)
* J. Henderson (1930–1931)
* A. King (1931–1932)
* V. Nimmo-Dewar (1932–1933)
* P.N. Lategan (1933–1934)
* E.C. Ranson (1934–1935)
* R.A. Flugge-De-Smidt (1935–1936)
* T.K. Prentice (1936–1937)
* R.S.G. Stokes (1937–1938)
* P.E. Hall (1938–1939)
* E.H.A. Joseph (1939–1940)
* J.H. Dobson (1940–1941)
* Theo Meyer (1941–1942)
* John V. Muller (1942–1943)
* C. Biccard Jeppe (1943–1944)
* P.J. Louis Bok (1944–1945)
* J.T. McIntyre (1945–1946)
* M. Falcon (1946–1947)
* A. Clemens (1947–1948)
* F.G. Hill (1948–1949)
* O.A.E. Jackson (1949–1950)
* W.E. Gooday (1950–1951)
* C.J. Irving (1951–1952)
* D.D. Stitt (1952–1953)
* M.C.G. Meyer (1953–1954)
* L.A. Bushell (1954–1955)
* H. Britten (1955–1956)
* Wm. Bleloch (1956–1957)
* H. Simon (1957–1958)
* M. Barcza (1958–1959)
* R.J. Adamson (1959–1960)
* W.S. Findlay (1960–1961)
* D.G. Maxwell (1961–1962)
* J. de V. Lambrechts (1962–1963)
* J.F. Reid (1963–1964)
* D.M. Jamieson (1964–1965)
* H.E. Cross (1965–1966)
* D. Gordon Jones (1966–1967)
* P. Lambooy (1967–1968)
* R.C.J. Goode (1968–1969)
* J.K.E. Douglas (1969–1970)
* V.C. Robinson (1970–1971)
* D.D. Howat (1971–1972)
* J.P. Hugo (1972–1973)
* P.W.J. van Rensburg (1973–1974)
* R.P. Plewman (1974–1975)
* R.E. Robinson (1975–1976)
* M.D.G. Salamon (1976–1977)
* P.A. Von Wielligh (1977–1978)
* M.G. Atmore (1978–1979)
* D.A. Viljoen (1979–1980)
* P.R. Jochens (1980–1981)

G.Y. Nisbet (1981–1982)
A.N. Brown (1982–1983)

* R.P. King (1983–1984)

J.D. Austin (1984–1985)
H.E. James (1985–1986)
H. Wagner (1986–1987)

* B.C. Alberts (1987–1988)

C.E. Fivaz (1988–1989)
O.K.H. Steffen (1989–1990)

* H.G. Mosenthal (1990–1991)

R.D. Beck (1991–1992)

* J.P. Hoffman (1992–1993)
* H. Scott-Russell (1993–1994)

J.A. Cruise (1994–1995)
D.A.J. Ross-Watt (1995–1996)
N.A. Barcza (1996–1997)

* R.P. Mohring (1997–1998)

J.R. Dixon (1998–1999)
M.H. Rogers (1999–2000)
L.A. Cramer (2000–2001)

* A.A.B. Douglas (2001–2002)

S.J. Ramokgopa (2002-2003)
T.R. Stacey (2003–2004)
F.M.G. Egerton (2004–2005)
W.H. van Niekerk (2005–2006)
R.P.H. Willis (2006–2007)
R.G.B. Pickering (2007–2008)
A.M. Garbers-Craig (2008–2009)
J.C. Ngoma (2009–2010)
G.V.R. Landman (2010–2011)
J.N. van der Merwe (2011–2012)
G.L. Smith (2012–2013)
M. Dworzanowski (2013–2014)
J.L. Porter (2014–2015)
R.T. Jones (2015–2016)
C. Musingwini (2016–2017)

Honorary Legal Advisers
Scop Incorporated

Auditors
Genesis Chartered Accountants

Secretaries
The Southern African Institute of Mining and Metallurgy
Fifth Floor, Chamber of Mines Building
5 Hollard Street, Johannesburg 2001 • P.O. Box 61127, Marshalltown 2107
Telephone (011) 834-1273/7 • Fax (011) 838-5923 or (011) 833-8156
E-mail: journal@saimm.co.za

Typeset and Published by
The Southern African Institute of Mining and Metallurgy
P.O. Box 61127
Marshalltown 2107
Telephone (011) 834-1273/7
Fax (011) 838-5923
E-mail: journal@saimm.co.za

Printed by
Camera Press, Johannesburg

Advertising Representative
Barbara Spence
Avenue Advertising
Telephone (011) 463-7940
E-mail: barbara@avenue.co.za

ISSN 2225-6253 (print)
ISSN 2411-9717 (online)

SAIMM
JOURNAL OF THE SOUTHERN AFRICAN INSTITUTE OF MINING AND METALLURGY
VOLUME 118 NO. 3 MARCH 2018

Contents

Journal Comment: AfriRock 2017
by W. Joughin . . . . . v–vi

President's Corner: Shaping the mining sector through inclusive leadership
by S. Ndlovu vii

Wits Mining School jumps to 15 on world ranking
by S. Braham viii

AFRIROCK 2017 INTERNATIONAL SYMPOSIUM

Early assessment of dynamic rupture hazard for rockburst risk management in deep tunnel projects
by M.S. Diederichs 193
A multistep semi-empirical methodology has been developed for early prediction of strain burst or dynamic rupture potential along deep tunnel alignments in variable ground conditions. The burst hazard potential rankings obtained can be used directly to apply corresponding rockburst support recommendations.

Microseismic events for slope stability analysis – a case study at an open pit mine
by X. Luo, M. Salvoni, P. Dight, and J. Duan 205
Both trigger mode and continuous mode were used to record microseismic events at an open pit mine. The preliminary results show that the weak events are equally as important as the strong seismic events for slope stability assessment.

Mining with crush pillars
by M. du Plessis and D.F. Malan 211
A limit equilibrium model implemented in a displacement discontinuity boundary element program is used to demonstrate crush pillar behaviour, and the influence of mining losses (potholes) and the use of sidings are discussed as possible contributors to pillar behaviour. The results are compared to the pillar behaviour at an underground investigation site.

Progress of brittle microfracturing in crystalline rocks under cyclic loading conditions
by E. Ghazvinian and M.S. Diederichs 217
The effect of stress rotation and stress fatigue on crack damage thresholds is systematically investigated using state-of-the-art laboratory testing and monitoring techniques in combination with advanced grain-based numerical modelling.

Reassessing continuous stope closure data using a limit equilibrium displacement discontinuity model
by D.F. Malan and J.A.L. Napier 227
A time-dependent limit equilibrium model is used to simulate historical closure profiles collected in deep, hard-rock mines.

Rockburst prevention *via* destress blasting of competent roof rocks in hard coal longwall mining
by P. Konicek and Schreiber 235
Destress blasting was successfully used to decrease the rockburst risk in hard coal longwall mining under very unfavourable geomechanical conditions.

SAIMM
JOURNAL OF THE SOUTHERN AFRICAN INSTITUTE OF MINING AND METALLURGY
VOLUME 118 NO. 3 MARCH 2018

Contents *(continued)*

AFRIROCK 2017 INTERNATIONAL SYMPOSIUM

Keyblock stability analysis of longhole stopes
by D. Sewnun, W. Joughin, R. Armstrong, and A. Cooper 243
A risk-based approach to the design of longhole stopes is presented, in which a probabilistic keyblock stability analysis was conducted to assess the rockfall potential considering various stope orientations in relation to major structures.

Early access microseismic monitoring using sensors installed in long boreholes
by T. Butler and B. Simser 251
Lessons learned from the installation and operation of seismic systems at Glencore's Nickel Rim South and Fraser Morgan mines are presented, and proposed strategies for establishing new seismic monitoring systems at new mines discussed.

PAPERS OF GENERAL INTEREST

Development of the MOSH Leading Practice Adoption System – a science-based system for managing behaviour change
by J.M. Stewart and S.M. Malatji 259
The substantial improvement in safety performance achieved by the South African mining industry since 2003 is reviewed and various contributing factors identified. The value of adopting a holistic long-term systems approach to address multi-faceted challenges, such as behavioural change and occupational health and safety, is highlighted.

A structured key cost analysis methodology to identify value-contributing activities in mining projects: a case study of the Chuquicamata Underground Project
by E. Córdova, V. Mobarec, E. Pizarro, and A.R. Videla 279
A systematic model for managing the economic risk of the operating costs for an ongoing 'supercave' project is presented. Key cost generators are identified, and their inherent variability is characterized.

Trials of the Garford hybrid dynamic bolt reinforcement system at a deep-level gold mine in South Africa
by F. Sengani. 289
In order to protect workers from the effects of small seismic events on deep-level mines, a yielding support system consisting of weld-mesh and 2.5 m long Garford hybrid bolts has been developed. The effectiveness of the Garford hybrid bolt is discussed.

A review of lashing methods used in shaft sinking
by T.J. Frangakis 297
The main lashing techniques used in modern shaft sinking are reviewed and compared in terms of efficiency and safety. An analysis of lashing duration as a function of shaft diameter and bucket volume is also presented, and opportunities for further developing opposed bucket loaders discussed.

Silicomanganese production at Transalloys in the twenty-tens
by J.D. Steenkamp, P. Maphutha, O. Makwarela, W.K. Banda, I. Thobadi, M. Sitefane, J. Gous, and J.J. Sutherland 309
Transalloys is currently the largest producer of silicomanganese in Africa, with an installed production capacity of 180 kt/a. The company has mature technology and systems in place, which are described in this paper.

Prediction of cuttability from rock cutting resistance
by V. Raghavan and Ch.S.N. Murthy 321
The objective of this investigation was to predict rock cuttability from measurements of rock cutting resistance (RCR) during the cutting process, and to study the influence of mechanical properties on the depth of cut achieved.

AfriRock 2017

This edition of the *Journal* is dedicated to AfriRock 2017, the International Society for Rock Mechanics (ISRM) International Symposium for 2017, which was held at the International Convention Centre in the beautiful city of Cape Town, South Africa from 3 to 5 October 2017. This is the first conference of that name and the first African-hosted ISRM International Symposium since the Tunisian and Zimbabwean national groups joined the African Region of the ISRM. The Symposium was well attended by 264 delgates from 42 countries. Each of the ISRM regions were represented; Africa (135 delegates), Asia (56, including 33 from China), Australasia (10), Europe (36), North America (13), and South America (14). Africa's proud participation was evident through the number of delegates from Botswana, the DRC, Egypt, Ghana, Lesotho, Swaziland, Tunisia, Zambia, and Zimbabwe, with a substantial number from South Africa.

Prior to the Symposium, the ISRM Board meeting was held over 30 September and 1 October, followed by the ISRM Commission and Council meetings on 2 of October. The ISRM Advisory Forum met on the evening of 3 October.

Dr Nick Barton and Professor John Cosgrove presented their informative short course on 2 October, spanning a wide array of technical aspects such as empirical methods, rock mechanics, and structural geological methods useful for excavation in jointed and fractured media.

The Symposium opened on 3 October, commencing with addresses by the Symposium Chairman, Mr William Joughin; the President of SANIRE, Mr Jannie Maritz; the President of the ISRM, Dr Eda F. de Quadros; the President of the SAIMM, Professor Selo Ndlovu and the Secretary General of the ISRM, Dr Luís Lamas. These were followed by the Rocha Medal presentation by Dr Bryan Tatone and the Franklin Lecture by Professor Francois Malan. Four excellent keynote lectures were presented by Professor Dick Stacey, Dr Nick Barton, Dr Luís Lamas, and Professor Sergio Fontoura. Technical papers were presented during plenary sessions as well as during two parallel sessions. The Symposium proceedings contain 94 papers, 50 of which are from Africa (South Africa, Tunisia, Zimbabwe, Zambia, Ghana, and Egypt). Given that mining is a key driver of the economies in several African countries, many of the papers dealt with rock engineering research and case studies for mines. The civil engineering industry was well represented, and some papers from the petroleum industry are also included in the Symposium proceedings. Topics included geotechnical investigations, laboratory testing, new investigation technologies, monitoring, seismic analysis, numerical modelling, support design, slope stability, underground mine design, pillar design, stability of tunnels and caverns, dam foundations, hydraulic fracturing, reservoir engineering, and borehole stability. The Symposium proceedings were provided electronically to delegates and will be made available to the industry at large in the near future on the following websites: www.sanire.co.za, www.saimm.co.za, www.onemine.org and www.onepetro.org.

Induction of ISRM Fellows

The first Early Career Forum (ECF) was held on 4 October, where rock mechanics practitioners in the earlier phases of their career were given the opportunity to present case studies and research. It was a very successful undertaking and demonstrated promising talent and enthusiasm from Africa. The ECF delegates were funded by the ISRM Secreteriat and the ISRM Education Fund Committee.

Early Career Forum, ISRM Board, and SANIRE President

Technical excellence was recognized in the form of awards for 'best papers', which were presented to Dr Dave Roberts and Dr Ehsan Ghazvinian (young author), and Edeshni (Candice) Munsamy was recognized as the best ECF presenter. The Symposium closing address was given by Mr William Joughin.

A technical exhibition was on display adjacent to the main hall throughout the Symposium, creating ideal opportunities for sponsors to showcase their products and engage in lively technical discussions during tea and lunch breaks.

In addition to the technical presentations and discussions, professional networking opportunities were aplenty. A cocktail function was held on the evening of 2 October to welcome delegates. The banquet was hosted on 4 October at the Castle of Good Hope, a bastion fort built by the Dutch East India Company in the 17th century, which made for an unforgettable experience.

The post-symposium technical tours took place on 6 of October. The Chapmans Peak tour provided an excellent opportunity to see the rockfall protection measures installed to protect the incredibly scenic Chapman's Peak drive in Cape Town. The tour also visited various local attractions and the fantastic geology of Cape Town and surrounding areas. Delegates were also given the

Journal Comment *(Continued)*

opportunity to tour one of the deepest gold mines in the world, Kloof No. 4 shaft at Kloof Gold Mine and see the challenges associated with deep-level mining in high-stress, seismically active conditions. The mine is situated near the border of Gauteng and Northwest Provinces approximately 75 km from Johannesburg.

AfriRock 2017 was jointly organized by the Southern African Institute of Mining and Metallurgy (SAIMM) and the South African National institute of Rock Engineering (SANIRE). The Symposium was generously sponsored by IDS GeoRadar, New Concept Mining, Reutech Mining, TRE Altamira, Optron, Aciel Geomatics, Geobrugg, Groundwork, Maccaferri Africa, Minova, Rocbolt Technologies, QualiRock, SRK Consulting, FST Mining Engineering, M&J Mining, and Sandvik.

Technical tour – Chapman's Peak rockfall protection

Technical tour to Kloof No. 4 Shaft

W. Joughin

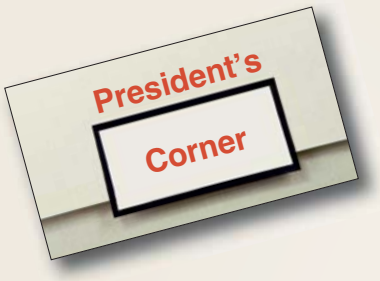

Shaping the mining sector through inclusive leadership

Two weeks ago while having my morning cup of tea, I contemplated, reflected, and marveled at the changes that have occurred in the country and the mining sector in the first six months of my term as the President of the SAIMM. I did not realize then that there was one big change around the corner. They say that a week is a long time in politics, and we have seen how true this statement can be with the recent significant changes that have transpired in Southern Africa; in our beloved neighbor country Zimbabwe as well as our home country South Africa. The mining sector has played, and continues to play, a significant role in the history and development of these two countries. At the same time, leadership and governance play a major part in paving the path for the mining sector.

According to a recently released Chamber of Mines survey, the creation of attractive policies, a regulatory and governance environment through ethical leadership, good governance, and the adoption of stable and predictable policies can result in significant investment in the mining sector. Clearly, leadership is a crucial element in the development of the mining sector. Leadership is instrumental in achieving social change, and is imperative in unlocking growth and transformation in any industry. Good and visionary leadership can shift a country from obscurity into the spotlight. A good and visionary leader can shift a company from a loss- making entity to a profit-making organization that can make a significant and meaningful contribution to national revenue or gross domestic product. There are a few examples in the history of the mining sector that attest to this. Similarly, a good community leader can drive and achieve significant social change leading to community upliftment. Imagine, therefore, what a country stands to gain when leaders from all sectors work together. Imagine if the leadership of the mining stakeholders such as the government, labour, business, and the community played an equal and a more prominently positive role in policy development. The potential for the development of attractive policies that can boost private sector investment, stimulate growth, and improve employment, with benefits that cascade down to and transform local communities, is extremely high.

Recently, the Presidency announced its commitment to resolving the impasse on the Mining Charter and facilitating a process of developing a Charter inclusive of all stakeholders, and in the interests of the industry and the country as a whole. In the words of the new South African President, 'by working together in a genuine partnership underscored by trust and shared vision, I am certain we will be able to resolve the current impasse and agree on a Charter that both accelerates transformation and grows the vital sector of our economy.' Clearly, success in industry, not only in mining but also in other supporting industries such as manufacturing, banking, education, and services, depends on leadership, trust, shared vision, and working together. In order to lay the foundation of true success, we need leaders who are visionary, see potential, remove obstacles, and build confidence. Such leaders can energize and encourage people to do more for personal and organizational growth. We need stakeholders who are not only committed to the vision of the future, but who also work together to establish a stronger, more competitive, more resilient, and prosperous mining industry. It is only through such an approach that we can ensure that our industry is forever a sunrise industry that extends opportunities to as many people as possible. And it is only through such an approach that we can truly say that our country is richly endowed.

S. Ndlovu
President, SAIMM

Wits Mining School jumps to 15 on world ranking

7 March 2018 – Johannesburg

Professor Cuthbert Musingwini, Head of the School of Mining Engineering at the University of the Witwatersrand

The School of Mining Engineering at the University of the Witwatersrand has shot up the world league tables to take 15th place in the 2018 QS World University Rankings (www.qs.com/world-university-rankings-2018).

Up from its position as number 22 in last year's rankings, it is the only mining engineering school in Africa to feature in the top 50 ranking of mining engineering schools worldwide. This accolade also makes it the highest ranked school at Wits.

'It is extremely encouraging to earn this recognition, in the light of our ongoing efforts to keep our school at the leading edge of learning and research,' says Head of School Professor Cuthbert Musingwini.

With approximately 800 undergraduate and postgraduate students – about 15% of them from countries outside South Africa – the school manages the largest mining engineering programme in the English-speaking world.

The QS World University Rankings name the world's top universities in 46 different subject areas and five composite faculty areas. It is the only international ranking recognized by the International Ranking Expert Group.

S. Braham
On behalf of the Wits School of Mining

6–7 June 2018, Focus Rooms, Sunninghill, South Africa

SAIMM
THE SOUTHERN AFRICAN INSTITUTE OF MINING AND METALLURGY

Contact: Conference Co-ordinator, Yolanda Ndimande
Tel: +27 11 834-1273/7 • Fax: +27 11 833-8156 or +27 11 838-5923 • E-mail: yolanda@saimm.co.za
Website: http://www.saimm.co.za

Whatever terminology you wish to use, it is obvious is that the world of work is changing rapidly.

The Mining Industry, along the Mining Value Chain, has to be a part of this in order to remain competitive, and to reach its ambition of Zero Harm.

Mining businesses in Africa need to join this journey, to stay alive, or be left behind. This event is a showcase and learning experience for everyone people associated with the Mining Industry, to learn about Global Best Practices, to network with global leaders in mining and other businesses, and to do so in an exciting and interactive format that we have never used before.

Be prepared to be BLOWN AWAY and to come away excited, informed and modernized!

Conference Announcement

http://dx.doi.org/10.17159/2411-9717/2018/v118n3a1

Early assessment of dynamic rupture hazard for rockburst risk management in deep tunnel projects

by M.S. Diederichs

Synopsis

Managing rockbursting conditions in mine development and operational environments is a complex and difficult challenge. The hazard and the associated risks can be managed based on local experience, monitoring, and informed data-rich analysis. On the other hand, blind development for deep tunnelling is being carried out around the world at depths in excess of 2 km and rockbursting has become a common and serious challenge. The rockburst mechanism is predominantly tunnelling-induced dynamic rupture or strain bursting, distinct from the remote or mine-generated events that impact mining excavations. Considerations of rock petrology, fabric, mechanical parameters, and structure allow an estimate of brittle response. The potential for energy storage and rapid release must be accounted for in order to understand the burst potential early in the basic design stage for deep tunnels. Failure to do so can result in unsafe conditions and years of delay. In this paper a multistep semi-empirical approach for early assessment of strain burst or dynamic rupture potential along deep tunnel alignments in variable ground is presented.

Keywords

tunnelling, high stress, dynamic rupture, rockburst, hazard assessment, risk management.

Introduction

Rockbursts are explosive failures of rock which occur when high stress concentrations are induced around underground openings (Hoek, 2006) in brittle rock or rock masses with brittle structure. The Canadian Rockburst Handbook (Kaiser, McCreath, and Tannant, 1996) defines a rockburst as: 'damage to an excavation that occurs in a sudden or violent manner and is associated with a seismic event'. Codelco (2008) uses the following definition of rockburst: 'Loss of continuity of the production process of the mining operation, caused by the rupture and instant projection of the rock mass, associated with a seismic event.' It is important to note the evolution, through these three definitions, from a term describing a mechanical phenomenon to a general and then a specific form of damage causing defined consequences. From a hazard and risk management perspective it is important to maintain a separation between the physical process of 'dynamic rupture' of the rock around a tunnel (the hazard) and the operational 'rockburst' impact (risk). The assessment of the hazard of dynamic rupture is the subject of this paper.

In mining, there are many different mechanisms that lead to rockbursts. Pillar failure can be very violent if the pillar core reaches capacity and the mine geometry is such that instantaneous deformations (system unloading) are large. Large stress changes associated with large-scale mining can result in fault slip distant from the drift or shaft but capable of inducing sympathetic strain-bursts (due to stress wave propagation) or seismically induced falls of ground involving previously damaged rock.

In tunnelling, however, the most important mechanism, is 'strain bursting' (Kaiser, McCreath, and Tannant, 1996) of walls and the tunnel face, with or without structural control and as a result of the complex stress path within the near-field rock as the tunnel advances (Diederichs, Eberhardt, and Fisher, 2013). In this case the stress changes, energy storage, and release mechanisms are often coincident and local to the tunnel boundary. This mechanism is one of dynamic rupture of a competent rock at high induced stress around the tunnel, as shown in Figure 1.

The extent and dynamic intensity of the failure can be mitigated by (or enhanced by) structural, compositional, and geometrical components within the rock-tunnel system. The dynamic rupture event can be self-triggered (spontaneous failure of rock with rapid release of stored strain energy), or can be triggered by a seismic strain wave from more distant structures or excavation influence zones.

Kaiser, McCreath, and Tannant (1996) classify low-, medium-, and high-level strain bursts (termed here 'dynamic rupture events') as involving depths of rupture less than

* *Department of Geological Sciences and Geological Engineering, Queen's University, Kingston, Canada.*

This paper was first presented at the AfriRock 2017 International Symposium, *30 September–6 October 2017, Cape Town Convention Centre, Cape Town.*

Figure 1—Examples of (left) minor and (right) major dynamic rupture or strain burst

0.25 m, 0.75 m, and 1.5 m, respectively. Depths of rupture greater than 1.5 m represent an extreme event in a tunnelling context (for a tunnel span of 5–10 m). The minimum ejection velocity for a classification of strain burst is 1.5 m/s. Kaiser, McCreath, and Tannant consider velocities greater than 3 m/s to be very high in the context of self-triggered dynamic rupture, although higher velocities can be generated through ejection of rock due to the transfer of energy from shock waves from a distant event. For self-triggered events, kinetic energies greater than 10 kJ per square metre of tunnel surface are considered high, and energies greater than 35 kJ/m2 are considered extreme (with respect to modern support technology). The classification of potential intensity for a dynamic rupture event should be considered in the absence of support. The real intensity of a strain burst is impacted by the effectiveness of reinforcement and support elements (within the rock and on the rock surface).

Dynamic rupture mechanics

Most of the discussions on rockburst damage in mining environments have been based on the primary mechanism of a remote seismic event, triggered by large-scale mine stoping, and the effect on a tunnel within the mine infrastructure. For tunnelling not associated with mining, the primary source of seismicity is the rock mass around the tunnel itself. It is possible for the stress changes and blasting associated with a large isolated tunnel to generate structural seismicity some distance away from the active heading, although for a single-heading tunnel, far more common are strain bursts (dynamic rupture events) at or near the active tunnel face. These events can involve the bulking of fractured rock or can be primarily ejection-based.

In terms of understanding and likelihood assessment, it is important to understand the mechanics of rockbursting in terms of the components:

- Stress concentration (geometry, geology, structural creep)
- Deconfinement (tunnel perimeter/face geometry)
- Energy storage (high strength capacity, structural resistance)
- Failure (brittle intact rock or brittle failure of structural interlock)
- Rapid release (stiff rock or soft surroundings, rapid coalescence through structure)
- Volume (instantaneous yield or release of structural integrated volume).

Stress concentration

Stress concentrations around a tunnel perimeter can be simple or complex, depending on the geology at the tunnel boundary away from the advancing face. According to the classic formula for maximum wall stress, in terms of the principal stresses within the plane of the tunnel section:

$$\sigma_{max} = 3\sigma_1 - \sigma_3 \quad [1]$$

In the case of a vertical principal stress the following equations can be used:

$$\sigma_{roof} = (Ak - 1)\sigma_{vert} \quad , \quad \sigma_{wall} = (B - k)\sigma_{vert} \quad [2]$$

For a circular opening, A=B=3. For a square opening assume A=B≈2, although stresses at the corners of the excavation will be higher than those predicted at the roof or walls. These high corner stresses can create hazards where bedding or persistent jointing is present and sub-parallel to or slightly inclined to the surface of the excavation (including the face). For narrow arched tunnels with height similar to or slightly greater than the span, A≈3.5 while B≈2.5. For typical wider tunnels (span greater than height), A≈2 and B≈4 provide a starting estimate.

For predictive analysis early in a project it is useful to combine these simple equations for maximum induced stress with functions (of location or depth) defining the *in-situ* stress state (in a plane perpendicular to the tunnel for initial 2D assessment). Examples of stress models from the Canadian Shield and from the Andes Mountains (Chile) are shown in Figure 2. These can then be used to predict the potential for rock yield (depth) from empirical tools or more rigorous analysis.

Figure 3 depicts a now classic predictor for the maximum volume of rock around a tunnel available for release in a rockburst, using the maximum tunnel stress calculated in the previous step. Figure 4 shows results from a more rigorous numerical analysis and can be used to estimate the maximum failure depth and the angular extent of failure for a circular tunnel (see functions in caption). These functions are obtained through the brittle yield approach by Diederichs (2007) using a nonlinear finite element code and the peak and residual parameters described in Figure 5.

In order to use the relationships in Figure 4 the following procedure can be used:

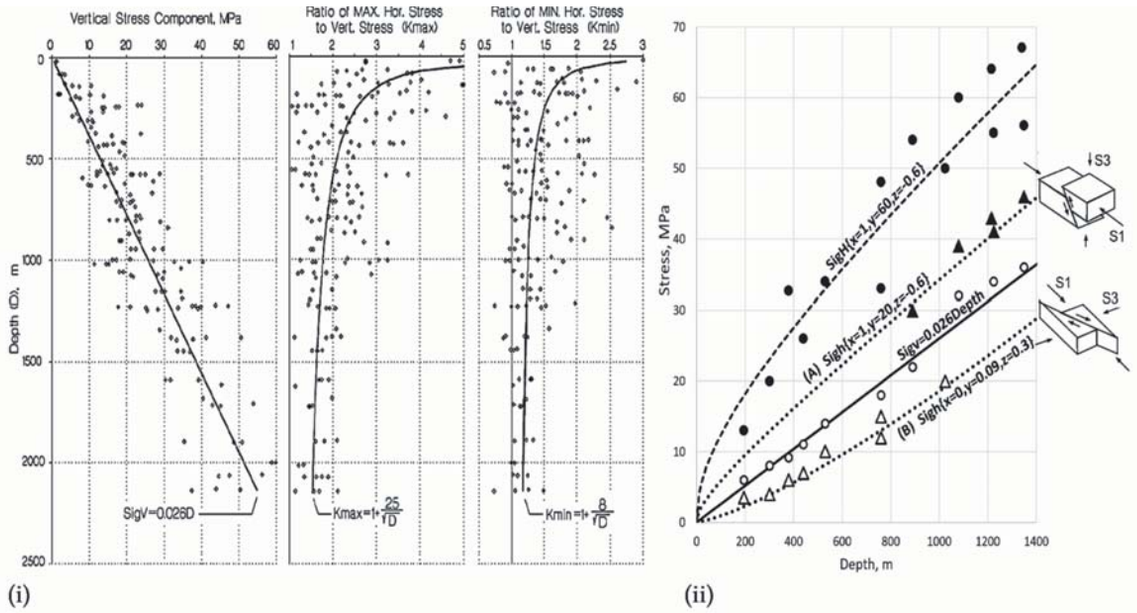

Figure 2—(i) Example of data-driven regional stress model for the Canadian Shield (after Diederichs, 2002. (ii) Contrasting local models (k=x+yD^z) for two neighbouring but tectonically distinct regions in the Andes: (A) thrust regime; (B) strike-slip regime

1. Obtain an estimate of principal stresses σ^1 and σ^3 in a 2D plane perpendicular to the tunnel.
2. Obtain damage threshold CI for rock types along tunnel (Use 0.5 × UCS if no data exists).
3. Calculate the strength ratio:
$$SR = \frac{3\sigma_1 - \sigma_3}{CI} \quad [3]$$
4. Use the in-plane *in-situ* stress ratio
$$K = {}^{\sigma_1}/_{\sigma_3} \quad [4]$$
5. Calculate calibration factors:
$$M = 0.4K^{-0.27} \quad N = 0.65K^{0.14} \quad [5]$$
6. Calculate breakout ratio:
$$BR = 1 + M(SR - 1)^N \quad [6]$$
7. Predicted depth of failure:
$$D_f = BR \times R \quad R = tunnel\ radius\ or\ \frac{1}{2}span \quad [7]$$

Simple 2D analysis of typical tunnel shapes is recommended to confirm estimates of failure depth, D_f, especially for non-circular geometries. Using a brittle-yield criterion (Diederichs 2007) the influence of geometry can be determined as in Figure 6. The sequence or timing of brittle fracture development in the face and tunnel perimeter with respect to advance can be analysed using 3D finite element analysis as in Figure 7.

The 3D nature of *in-situ* stress may be important for the prediction of dynamic rupture. Figure 8 illustrates a tunnel case in Peru (Diederichs, Eberhardt, and Fisher, 2013) where the major stress rotated from perpendicular to axial with respect to the tunnel axis due to the crossing of a tectonic thrust. In the latter case the major bursting moved from the tunnel roof to the face due to a high perimeter stress spike during advance.

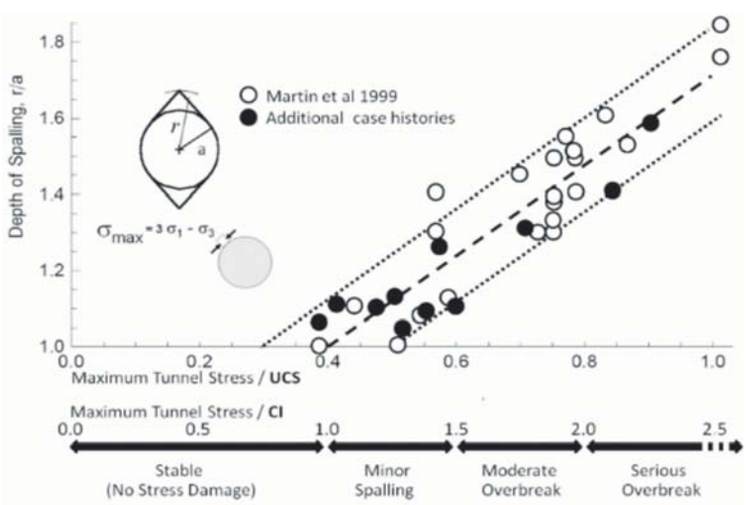

Figure 3—Depth of damage (available for bursting) around a tunnel. Crack initiation stress, CI (Diederichs and Martin 2010), is typically 0.4–0.5 for crystalline rocks

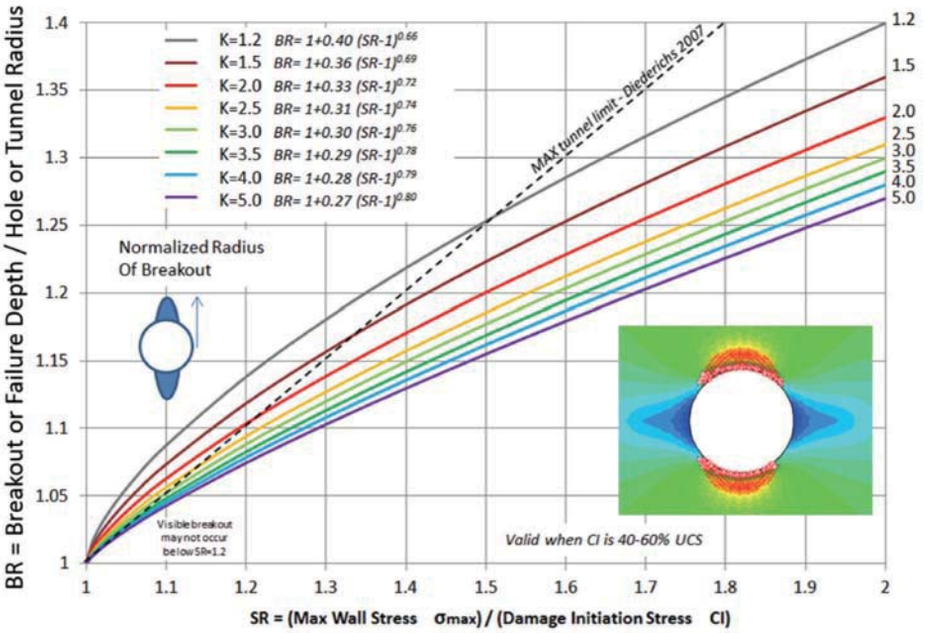

Figure 4—Failure depth predicted as a function of maximum wall stress, CI (typically 40–50% of UCS but measured independently during UCS testing) and *in-situ* stress ratio K. BR can be expressed as BR=1+M(SR–1)N, where M = 0.4K$^{-0.27}$ and N=0.65K$^{0.14}$

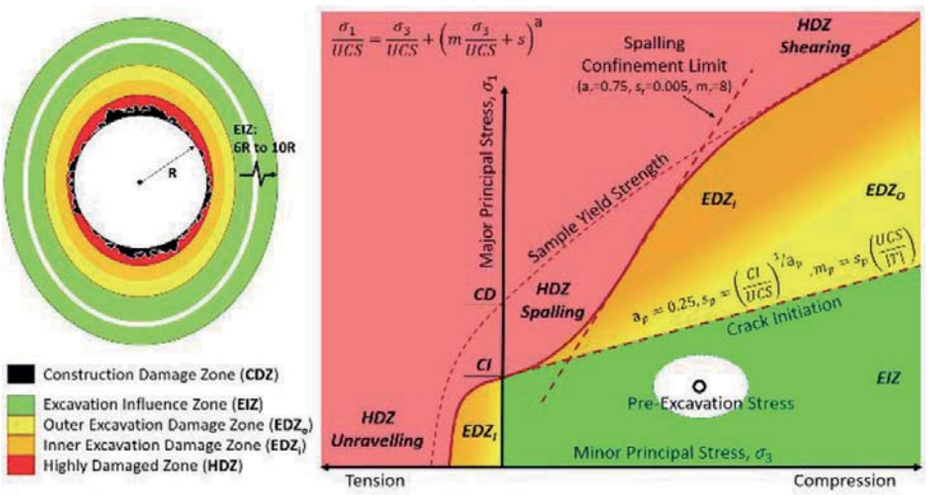

Figure 5—Damage zones corresponding to the DISL brittle modelling approach by Diederichs *et al.,* (2003, 2007, 2013). Equivalent Hoek-Brown parameters for initiation and confinement limit for brittle failure (HDZ) are shown

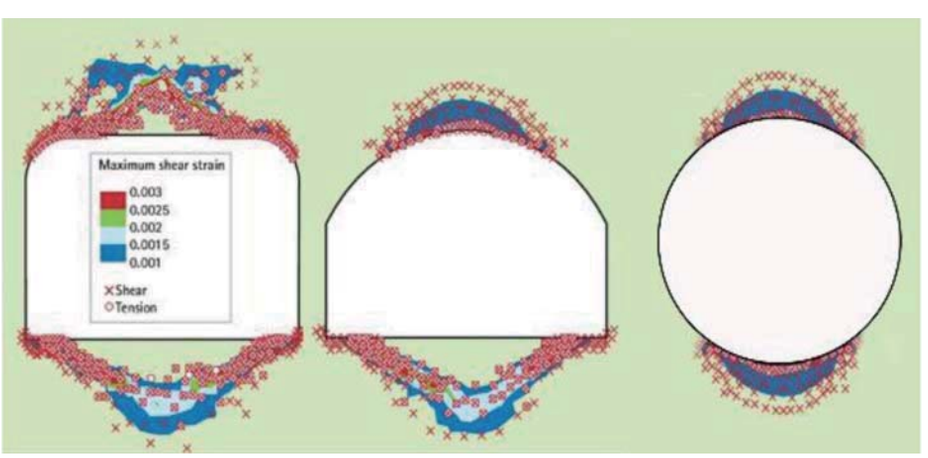

Figure 6—Typical final brittle failure geometries for different tunnel shapes. K=2 for this example detailed in Cain and Diederichs (2017). Note the unyielded mass of rock next to a flat roof or floor surface bounded by brittle fracture. This has been observed by the author in numerous actual cases

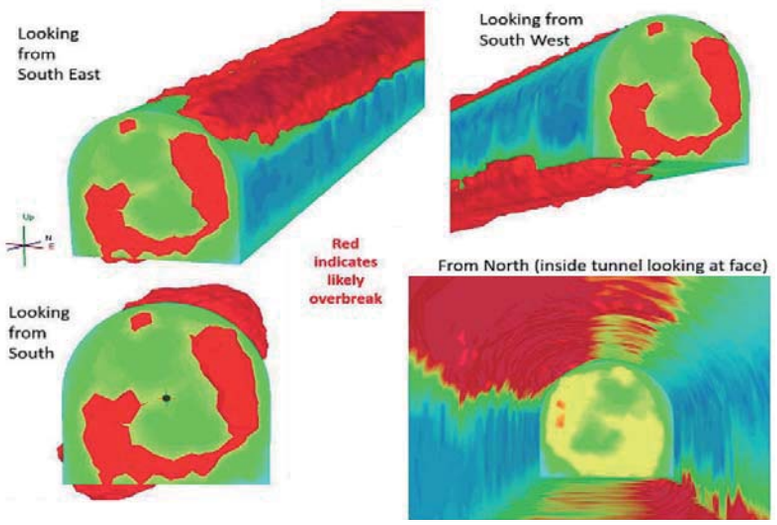

Figure 7—Example of a staged (2 m advance for a 5 m span) 3D nonlinear finite element analysis using the brittle criteria of Diederichs (2007), showing the development of brittle fracture (burst potential) in the face and in the tunnel perimeter (red) as the tunnel advances. This fracture geometry was verified for this case with observed face bursting, moderate roof bursts, and dynamic floor heave

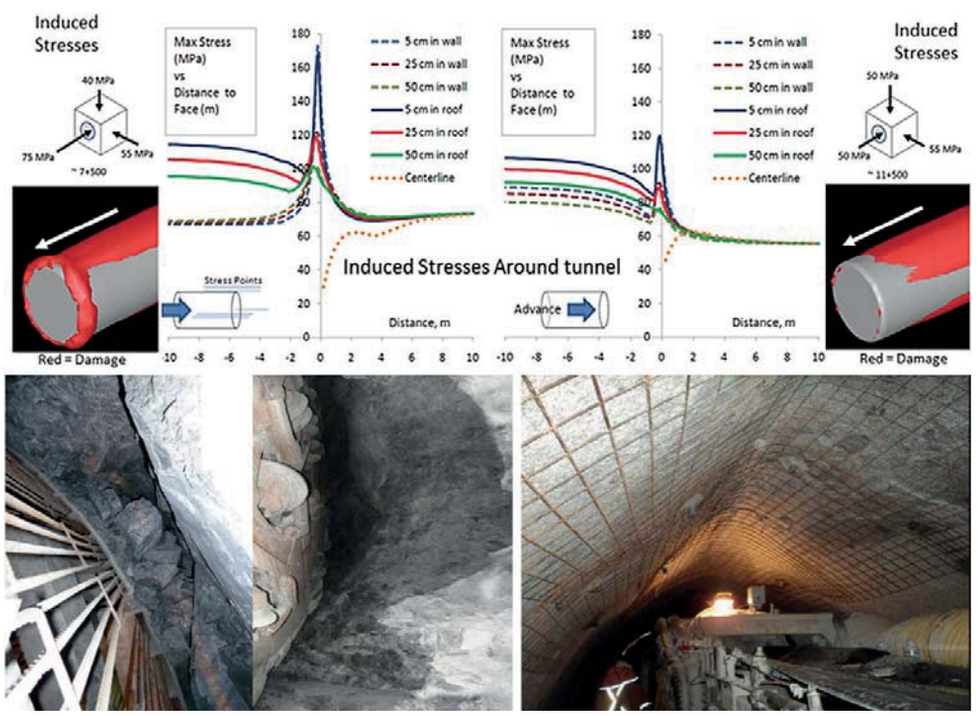

Figure 8—3D elastic stress path analysis of the Olmos Tunnel, Peru, from Diederichs, Eberhardt, and Fisher (2013). Upper left: high stress axial to the tunnel creates near-face stress concentration leading to extreme bursting in the face and around TBM head (bottom left). Top right: tunnel with lower axial stress shown at right – here nonviolent spalling in the roof dominated behaviour (bottom right)

Deconfinement

As shown in Figure 4, brittle fracturing is very sensitive to confinement. The loss of confinement (normal to the tunnel boundary) enhances the brittle failure caused by stress concentrations parallel to the tunnel surface, creating the potential for violent buckling or sudden asperity rupture and shear as rockburst mechanisms. Deconfinement of sub-parallel structure with increased coplanar stress during excavation can lead to sudden failure as the effects of small interlocking asperities are nullified by small amounts of dilation. Flat walls and corners are not ideal in a high-stress environment, as seen in Figure 5. In addition, deconfinement due to overscaling and the loss of a smooth excavation profile can lead to unpredictable and dynamic failure, particularly in ground with jointing (or bedding). Maintaining the excavation profile and providing for some minimum curvature on all surfaces is recommended. The orientation of *in-situ* stress and the tunnel geometry can affect the stress path such that strain energy (see the next section) can be stored and then released suddenly, as in Figure 9.

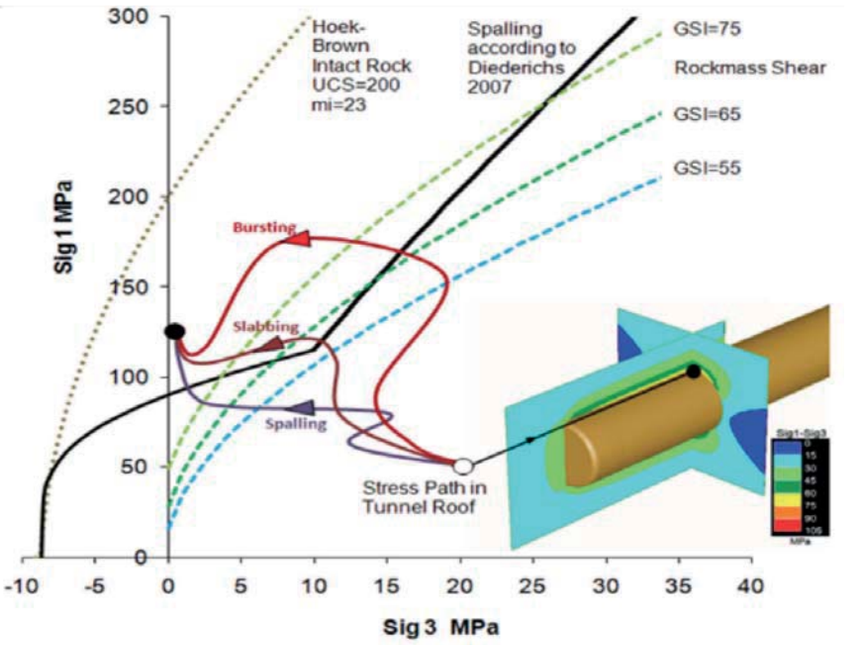

Figure 9—Burst potential based on energy storage and release according to stress path. Stress path curves are from simple elastic 3D models. GSI curves are as per Hoek, Carrenza-Torres, and Corkum (2002). Spalling criterion is based on Diederichs (2007)

Energy storage

An issue related in some ways to the deconfinement factor is that of energy storage. Geometry and stress state can play a large part in the ability of a rock mass or a local structure to store strain energy during the excavation cycle. Figure 9 illustrates the concept of energy storage and release based on *in-situ* stress orientation and magnitude and the deconfinement associated with the stress path. Figure 10 illustrates the variability in induced stress as a tunnel passes through heterogeneous ground with contrasts in stiffness. Energy is stored in the softer units but transferred to the stiffer units as they reach critical stress first. Stiffness contrasts result in face bursting and near-face dynamic rupture as the tunnel advances.

Brittle failure

For massive or moderately jointed rock with a high ratio of compressive to tensile strength, brittle spalling damage initiates (Diederichs, 2003, 2007) at a wall stress of around 40–60% of the intact UCS, following the 'spalling criterion' in Figure 11. Closely spaced fractures with random orientations oblique to the tunnel face and wall result in 'rock mass shear' behaviour (Figure 11). This is reflected in the 'spalling' and 'rock mass shear' envelopes in Figure 9. The first envelope to be intersected by the stress path will govern the mode and extent of failure.

Spalling is a brittle damage and yield process but does not necessarily lead automatically to a violent failure event or dynamic rupture (strain burst). For this to occur at a scale

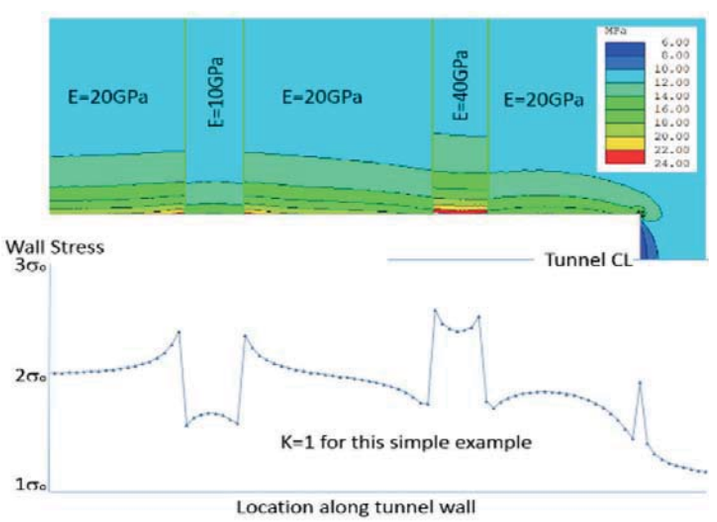

Figure 10—Effect of variable stiffness on induced stress magnitudes during tunnelling

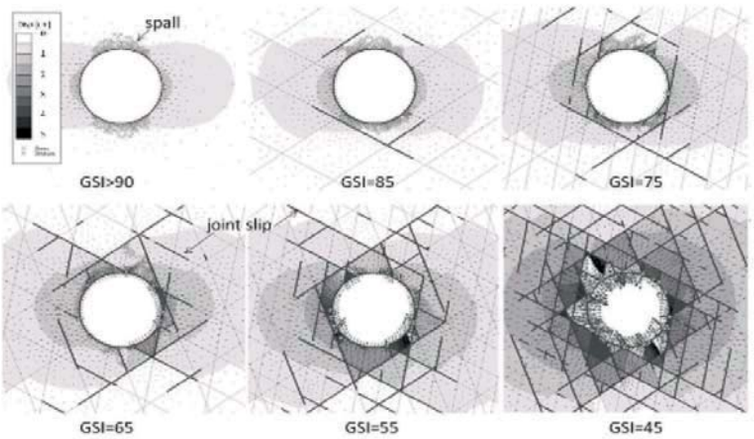

Strength Ratio	GSI < 55	GSI = 55 to 65	GSI = 65 to 80	GSI >80
UCS/T < 8	shear	shear	shear	shear
UCS/T =9 to 15	shear	shear	shear/spall	spall/shear
UCS/T=15 to 20	shear	shear/spall	spall/shear	spall
UCS/T > 20	shear	shear/spall	spall	spall

Figure 11—Transition from brittle spalling to rock mass shear (after Diederichs, 2007)

that poses a design and safety challenge, there must be energy storage and instantaneous release.

Without considering heterogeneity, geometry, and structure for the moment, it is possible to rank rock types with respect to their dynamic rupture potential (DRP) based on their brittle character, represented by the ratio of UCS to *T* (true tensile strength or estimate from Brazilian tensile strength such that *T*=BTS/1.3, after Perras and Diederichs, 2014), and the capacity for energy storage, represented simply by unconfined strength (Figure 12).

Energy release and volume

Brittle failure in massive ground around a circular tunnel with an anisotropic stress field will be self-limiting in size and may also be progressive in its failure mode (many smaller dynamic releases making up a major overbreak). Geometrical variances such as flat walls, loss of profile due to ground fall and overscaling, and excess round length can increase energy release rate and volume. Structure is a major contributor to instantaneous energy release (as well as

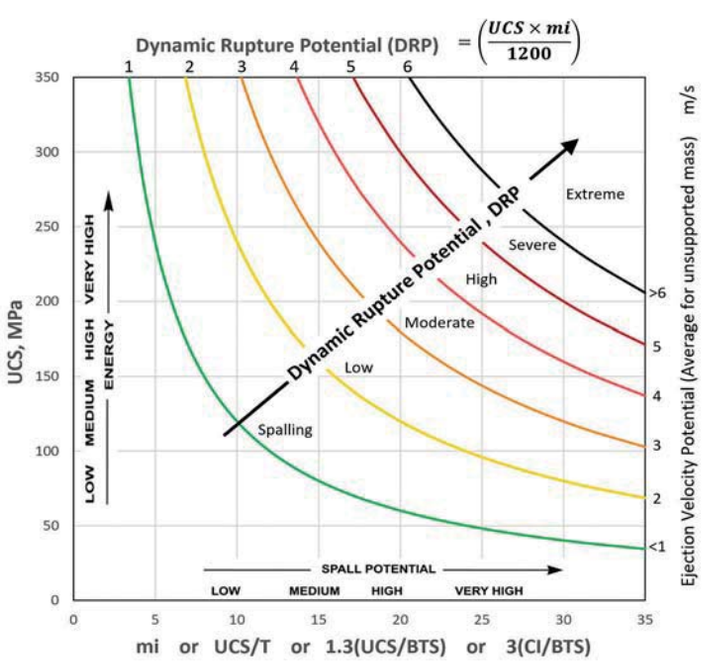

Figure 12—Dynamic rupture potential (DRP) indicator for massive rock (modified from Diederichs, 2007). The horizontal axis proposes several indicators for brittleness. Note that velocities for small surficial pieces may be higher than the 'average' estimated on right axis

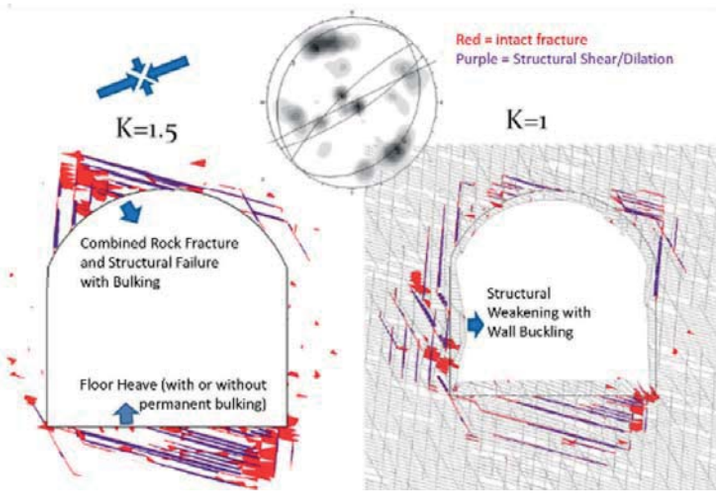

Figure 13—Variations in structurally controlled but stress-induced rupture in a tunnel

storage) and can also drastically increase the volume of rock that can spontaneously fail as the structure interacts with induced rock fracture.

Dynamic rupture hazard assessment

The hazard assessment used in this paper is based on a recommended ranking from 0 to 4+ to describe the level of hazard due to dynamic rupture, as summarized in Table I, based primarily on mining guidelines by Kaiser, McCreath, and Tannant (1996), modified by the author for blind tunnelling (span 5–10 m) and updated to account for modern burst support capabilities. Energy demand is the prime indicator of hazard level in Table 1 – other indicators are non-unique and illustrative only.

The initial step for hazard assessment is to combine the depth of predicted failure, D_f, with the potential for dynamic rupture, DRP. In order to end with a ranking consistent with Table I, the following relationship has been developed and validated by the author through case histories in Chile and Peru:

Damage depth potential:

$$DDP = \alpha \left(D_f\right)^{0.5}$$ where D_f is the estimated depth of failure (m) [8]

Dynamic rupture potential:

$$DRP = \beta \left(\frac{UCS \cdot m_i}{1200}\right)$$ where $m_i \approx UCS/T$ or $1.3UCS/BTS$ or $3CI/BTS$ [9]

Suggested empirical constants to match Table I (can be calibrated for local conditions):

α=4.5; β=1

Burst hazard potential:

$$BHP = (DDP \times DRP)^{0.5}$$ considering intact rock only [10]

Table I

Classes of burst hazard potential (BHP)

Class	Hazard level	Issues
0-0.1	Low stress	No indications
0.1-0.5	Local stress concentration	Minor local and intermittent stress noise
0.5-1	Consistent stress	Consistent stress 'popping' for several hours after blast
1-2	Spalling	Visible slab formation <5 cm thick, with rock noise but minimal kinetic energy (or velocity) developing after blasting and scaling – stops after 1–3 diameters of advance
2-3	Minor dynamic rupture(burst)	Slabbing with significant noise, minor ejection (5–20 cm thick) at or near the face. Less than 2 kJ/m^2 kinetic energy of release (per unit wall area). Less than 5 cm closure potential
3-4	Moderate dynamic rupture (burst)	Constant or strong noise with high frequency of ejection 15–65 cm thick at >3–4 m/s initial surface velocity for hours after blasting, near or away from face. Kinetic energy 2–14 kJ/m^2 or 5–15 cm closure potential
4-5	Major or severe dynamic rupture (burst)	Large volumes of ejection or dynamic heave (floor) with constant and large noise events, occurring after blast, near face or well after blast and back into tunnel away from face or with long delay. 30–85 cm average thickness at >4 m/s surface velocity or 14–35 kJ/m^2 ejection or 15–30 cm closure potential
5+	Extreme bursting	Very large events >85 cm average thickness, >6 m/s velocity, kinetic energy >35 kJ/m^2, >30 cm closure potential. Can occur any time

Adjustment for structural control

Some discrete structures with unfavourable orientations can enhance the energy storage and rapid release potential as well as increasing the volume of failure. Based on experience with tunnels in Chile, Peru (Diederichs, Eberhardt, and Fisher, 2013), Canada, and Switzerland, a scheme has been developed to estimate the added hazard potential, based on the initial BHP for intact rock, due to structure as shown in Figure 14. These observationally validated adjustments, while approximate and empirical, can be summarized by a generalized cubic function as shown. The structural hazard increments, SHI_i, calculated for each dominant class of unfavourable structure are summed and the result added to the initial BHP. If desired, each SHI_i can be multiplied by a factor from 0–1, where zero indicates the absence of structure and unity indicates fully dominant and pervasive structure.

Finally, the impact of ubiquitous, softening structure must be considered. The structures above are normally fresh and unaltered features (possibly infilled with hard minerals). Dense isotropic structure and weathering can be considered through GSI. The impact (as a multiplier) of GSI on bursting can be approximated by the function in Figure 15. Low GSI reduces BHP while increasing squeezing potential.

BHP_s is calculated by summing the individual structural hazard increments (for each major controlling class of structure) and adding the sum to the base BHP (calculated for intact rock) in order to integrate the impact of structural control on the bursting process:

$$BHP_s = BHP + \Sigma_1^n SHI_i \quad [11]$$

The impact of softening structure (through GSI) is then included through a factoring of BHPs to obtain the final ranking BHP_{rm} for the whole rock mass and structural system:

$$BHP_{rm} = BHP_s / \{1 + exp([40 - GSI)/10]\} \quad [12]$$

This process of initial hazard assessment, facilitated by

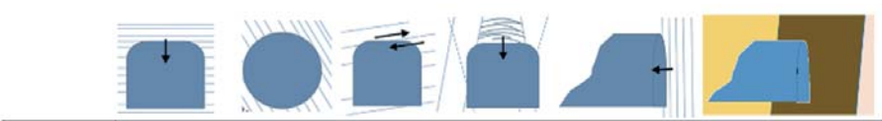

BHP These numbers are based on existing hazard index INITIAL INTACT ROCK RESPONSE	ROCKBURST HAZARD INCREASE DUE TO STRUCTURE (sum all that apply and add to BHP to get BHPs)									
	LAMINATIONS << 20 cm thick			BEDDING (>> 20cm wide) or SPACED PERSISTANT JOINTS			STRUCTURE PARALLEL to FACE spacing:		STIFFNESS CHANGE Aproaching <15m or next to tunnel wall <6m	
	Horizontal	Vertical Parallel to Tunnel	Inclined 20-45 degrees	Horizontal	Dip > 60 Parallel to Tunnel	Inclined Dip 10-45 degrees	<10 cm	> 10 cm	Soft to Stiff	Stiff to Soft
0	0	0	0.1	0.1	0	0	0	0	0	0
0.1	0.2	0	0.2	0.2	0	0	0.1	0	0	0.2
0.5	0.5	0.1	0.5	0.5	0	0.1	0.3	0.1	0.1	0.5
1	0.7	0.2	0.5	0.5	0.2	0.2	0.5	0.2	0.2	0.7
2	0.7	0.5	0.5	0.5	0.5	0.5	0.5	0.5	0.5	0.7
3	0.2	0.5	0.2	0.5	0.5	0.5	0.2	0.5	0.5	0.7
4	0	0	0	0.2	0.2	0.2	0	0.2	0	0.5

Cubic Function Fit Parameters $SHI_i = A(BHP^3) + B(BHP^2) + C(BHP) + D$ Sum for each condition: $BHP_S = BHP + \sum_1^n SHI_i$

A	0.0847	-0.0485	0.0504	0.0219	-0.044	-0.0339	0.046	-0.0339	-0.0485	0.0554
B	-0.6716	0.1693	-0.4085	-0.2301	0.1746	0.1115	-0.396	0.1115	0.1693	-0.4659
C	1.3291	0.0978	0.7962	0.5872	0.053	0.1453	0.8467	0.1453	0.0978	1.107
D	0	0	0.1	0.1	0	0	0	0	0	0

Figure 14—Structural control of stress-induced rupture in a tunnel and adjustment to BHP to obtain BHPs

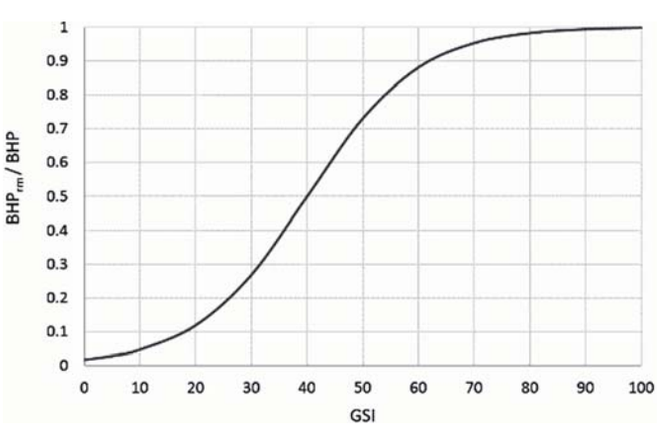

Figure 15—Quantified influence of GSI on brittle failure on final rock mass BHPrm

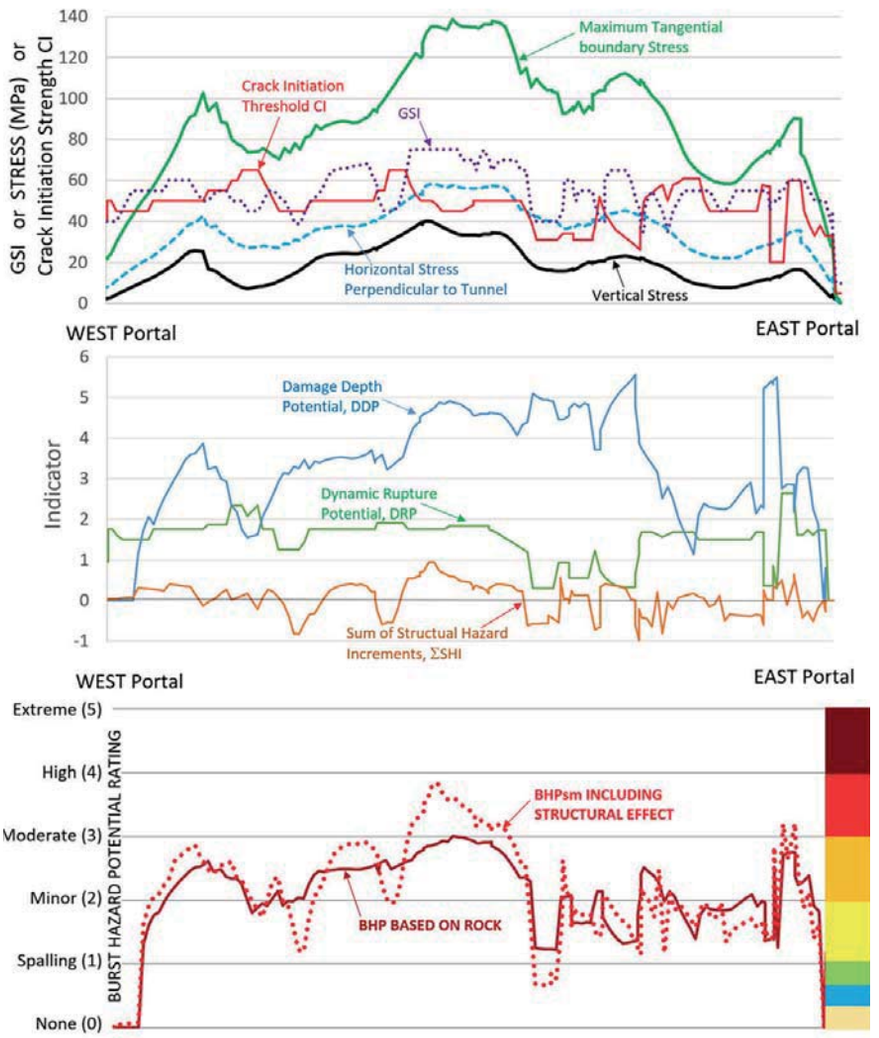

Figure 16—Example application of rock mass dynamic rupture hazard or burst hazard potential, BHP_{rm}

Equations [1] through [12], can be integrated easily into a spreadsheet format where rock and structural information can be input from borehole logs, surface exposures, or refined geological modelling and structural assumptions (to be verified as observational data becomes available). Stress values along the tunnel alignment can be calculated from the tunnel orientation and a functional stress model for the local area and depth. The resulting assessment and hazard prediction for an example project (a deep Andean tunnel in the preconstruction stage) based on available knowledge is shown in Figure 16.

Managing hazard and risk

This is of course a qualitative assessment of hazard and the definitions of the hazard level, summarized for this work in Table I, are open to informed debate, and the indicator thresholds of energy demand, ejection velocity, and failure volume constituting each level will evolve gradually over time as routinely available and economical support technology improves. Using Table I as a basis, the primary indicator of severity for dynamic rupture or strain burst event is the excess energy demand (not including energy consumed by yielding rock and any functioning support present) per unit surface area. This can be back-calculated for verification based on the relationship in Kaiser, McCreath, and Tannant (1996):

$$Excess\ Energy\ Demand = t\rho g d^2 / \left(4\left[h + d\frac{\sin\theta}{\cos\theta}\right]\cos^2\theta\right) \quad [13]$$

where t = average failing thickness
ρ = density of the rock
d = horizontal ejection distance (observed limit of main ejected mass)
h = vertical height limit of main failure volume (pre-event)
θ = angle (negative down from horizontal) of initial ejection trajectory*

*equation is valid only for trajectories from –45 to +89 degrees

This relationship is graphically illustrated in Figure 17.

The reader is referred to Kaiser, McCreath, and Tannant (1996), Potvin and Wesseloo (2013), Cai (2013), and Villaescusa, Player, and Thompson (2014) for more discussion on the design of dynamic support. Kaiser,

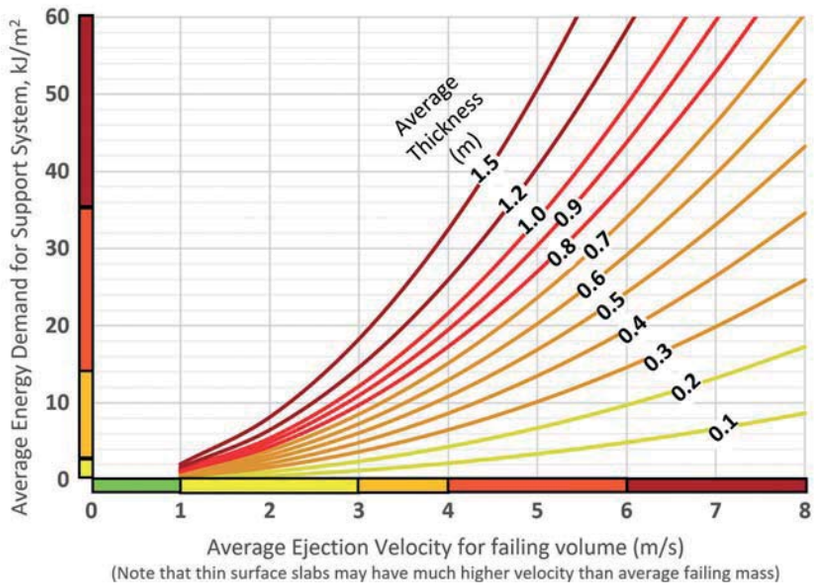

Figure 17—Energy demand (for support) as a function of ejection velocity and failure thickness

McCreath, and Tannant (1996) advocated a multipurpose support system consisting of:

- Stiff reinforcement functionality to maintain rock mass integrity and internal strength
- Dynamic displacement capacity and energy capacity in the event of violent rupture, and
- Integrated surface retention to resist uncontrolled bulking and to ensure energy transfer.

Support design is only one component of a management strategy for dynamic rupture hazard and rockburst risk. It is beyond the scope of this paper to explore all mitigation strategies in depth, but Figure 18 lays out the options. The hazard is assessed based on the triggers as outlined in this paper. The likelihood of dynamic rupture and the magnitude of the rupture events can be controlled to some degree through the 'Control' options listed in Figure 18. Anticipation of hazardous conditions can be informed by probe drilling, and the nature of the hazard can be verified by seismic monitoring and video recording (of the face area) during the construction cycle.

In many conditions, some level of dynamic rupture is inevitable and cannot be engineered away. In this case, the impact must be mitigated through the 'Management' options shown in Figure 18. Some management strategies may result in costs, delays, or other issues that would also be considered 'risks'. The right side of the figure highlights the priority in which risk must be viewed, and in many cases certain risks (damage to robotic support installation equipment, for example) can be viewed as acceptable if they reduce the potential for more critical risk such as project shutdown, injury, or death. Figure 19 illustrates a number of risk management strategies that can be used when the potential for dynamic rupture hazard cannot be avoided.

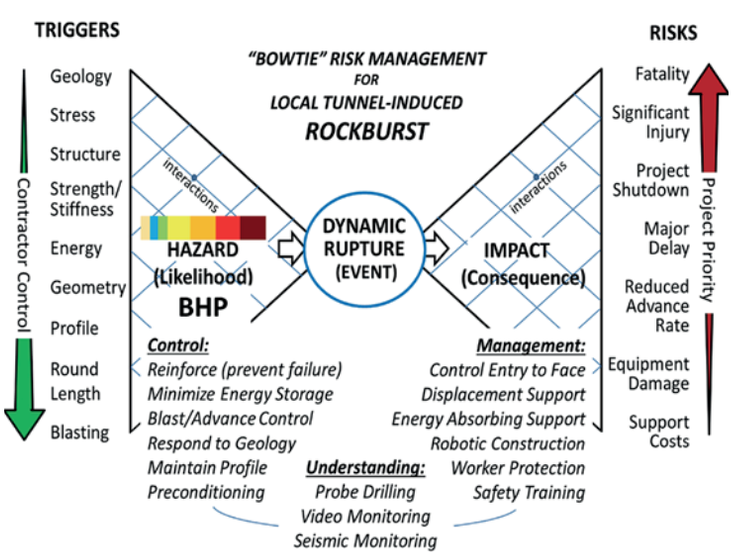

Figure 18—Hazard control for dynamic rupture hazard and risk management for rockbursts in tunnels

Figure 19—Risk management tools for rockbursts in tunnels (clockwise from top left): layered support with redundant energy and retention capacity to maintain safety in the event of dynamic rupture; robotic bolting and mesh installation to reduce worker exposure; a rock retention and worker protection system for TBM drives; and a multi-function cage for work at a tunnel face or under incomplete support

Conclusions

A multi-step methodology has been developed for early prediction of dynamic rupture or strain burst potential along the alignments of deep tunnels in variable ground conditions. Although the approach is empirical, based on past work and on the experience of the author in active tunnelling cases, it is designed to allow for calibration to regional experience with geological environments beyond the scope of the Andean, Alpine, and Cordilleran experience upon which it is based. The approach considers stress concentration, tendency of the intact rock to yield in a brittle manner, and sudden energy release upon failure. In addition, discrete structural configurations likely to increase the probability or magnitude of dynamic energy release are considered through a hazard increment that can be based on drill core, if available, or on a sound geological model with attention to lithological contacts and likely geological structures. The influence of more intense random or isotropic joints and fractures is accounted for by a function of GSI (where a lower GSI reduces the potential for bursting while possibly increasing the potential for other stress instabilities such as squeezing).

The burst hazard potential system developed by the author and presented here results in an index or ranking for potential dynamic rupture that is consistent with those previously published by others for support in bursting ground. The BHP rankings can be used directly to apply corresponding rockburst support recommendations such as those by Kaiser, McCreath, and Tannant (1996), Cai (2013), Potvin and Wesseloo (2013), and others.

References

Cai, M. 2013. Principles of rock support in burst prone ground. *Tunnelling and Underground Space Technology*, vol. 36, no. 6. pp. 46–56.

Cain, S. and Diederichs, M.S. 2017. Shape matters: the impact of geometry on brittle damage for repository engineering. *Tunnels and Tunnelling*, 2017, no. 2. pp. 32–37.

Codelco. 2008. Procedimiento General para Emergencias por Estallido de Roca en la Mina. Informe GMIN-GRL-P-005 con fecha mayo de 2008, Versión 3.

Diederichs, M.S. and Martin, C.D. 2010. Measurement of spalling parameters from laboratory testing. *Proceedings of Eurock 2010*, Lausanne, Switzerland, 15–18 June 2010. Taylor & Francis, London. pp. 323–326.

Diederichs, M.S. 2002. Stress induced damage accumulation and implications for hard rock engineering. *Proceedings of NARMS* 2002, Toronto. Hammah, R., Bawden, W.F., Curran, J., and Telsnicki, M. (eds). University of Toronto Press. pp. 3–14.

Diederichs, M.S. 2007. The 2003 Canadian Geotechnical Colloquium: Mechanistic interpretation and practical application of damage and spalling prediction criteria for deep tunnelling. *Canadian Geotechnical Journal*, vol. 44, no. 9. pp. 1082–116.

Diederichs, M.S., Eberhardt, E., and Fisher, B. 2013. Consideration of stress and structural influence on high stress response in deep tunnelling – the Olmos Tunnel, Peru. *Underground. The Way to the Future. Proceeding of the World Tunnel Congress*, Geneva, Switzerland. Anagnostou, G. and Ehrbar, H. (eds). CRC Press. pp. 1998–2005.

Hoek, E. 2006. The development of rock engineering. https://www.rocscience.com/documents/hoek/corner/02_The_development_of_rock_engineering.pdf

Hoek, E., Carrenza-Torres, C.T., and Corkum, B. 2002. Hoek-Brown failure criterion – 2002 edition. *Proceedings of the ARMS-TAC Joint Conference*, Toronto, Canada. pp. 267–273.

Kaiser, P.K., McCreath, D.R., and Tannant, D.D. 1996. Canadian Rockburst Support Handbook. Canadian Rockburst Research Program, Vol II, Book I (1990-1995). Canadian Mining Industry Research Organization, Sudbury, Ontario. 343 pp.

Martin, C.D., Kaiser, P.K., and McCreath, D.R. 1999. Hoek-Brown parameters for predicting the depth of brittle failure around tunnels. *Canadian Geotechnical Journal*, vol. 36, no. 1. pp. 136–151.

Perras, M.A. and Diederichs, M.S. 2014. A review of the tensile strength of rock: concepts and testing. *Geotechnical and Geological Engineering*, vol. 32, no. 2. pp. 525–546.

Potvin, Y.H. and Wesseloo, J. 2013. Towards an understanding of dynamic demand on ground support. *Journal of the Southern African Institute of Mining and Metallurgy*, vol. 113, no. 12. pp. 913–922.

Villaescusa, E., Player, J.R., and Thompson, A.G. 2014. A reinforcement design methodology for highly stressed rock masses. *Proceedings of the 8th Asian Rock Mechanics Symposium*, Sapporo, Japan, 14-16 October 2014. American Rock Mechanics Association. pp. 87–94. ◆

http://dx.doi.org/10.17159/2411-9717/2018/v118n3a2

Microseismic events for slope stability analysis – a case study at an open pit mine

by X. Luo*, M. Salvoni†, P. Dight†, and J. Duan*

Synopsis

Slope instability is one of the major concerns in open pit mining. A significant collapse of the pit wall can result in injuries or fatalities, damage to mining equipment, interruptions to production, and potential loss of reserves. Properly interpreted microseismic data can be used to augment surface monitoring systems in identifying potential instability and the associated failure mode. A challenge for this microseismic application is that many seismic events associated with slope movements are weak and they hardly trigger a microseismic monitoring system that is set up to record an event in a trigger mode. A research project carried out at an open pit mine in Australia used both trigger mode and continuous mode to record microseismic events. The preliminary results have shown that the weak events are equally important as the strong seismic events for slope stability assessment, and they should not be ignored in microseismic monitoring for open pit mining.

Keywords

open pit, slope stability, microseismics, weak seismic events, prediction.

Introduction

Maintaining slope stability is a major task for open pit mining and civil engineering. Microseismic monitoring techniques have been recognized as an efficient tool to map rock fracture network development for slope stability assessment (Hardy and Kimble, 1994; Lynch and Malovichko, 2006). Properly interpreted microseismic data can be used to augment surface monitoring systems in identifying potential instability and the associated failure mode. This technique has been used for identifying potential failure locations (Trifu, Shumila, and Leslie, 2008), estimating potential damage scales and unstable volume (Wesseloo and Sweby, 2008), and prediction of impending failures and improving understanding of how mining affects the pit stability (Lynch *et al.*, 2005).

Microseismic monitoring techniques measure seismic signals generated from rock breakage or movement inside the open pit. As microseismic sensors can measure rock fracture events remotely, these techniques are capable of mapping the 4D pattern and dynamic development of rock fractures before any deformation on the slope surface can be observed.

A microseismic system used for open pit monitoring normally consists of a geophone network with a number of geophones installed in the ground, spaced at 100–200 m. In order to obtain the 4D pattern of seismicity, the seismic signals must be recorded by four or more geophone stations. The system is commonly operated in a trigger mode, based on a short-time averages (STA) and long-time averages (LTA) algorithm. When at least four stations experience a STA/LTA ratio greater than the set threshold, the system is triggered and the event is recorded. This approach was developed for underground mines, where there has been a focus on larger events leading to hazard identification and re-entry protocols (Mendecki, 1997).

However, near an open pit mine slope, the rock mass can be highly fractured because of blasting, destressing, and weathering. The fractured nature of the rock near surface may cause significant attenuation of the seismic waves. (Willenberg *et al.*, 2002) and a small seismic event may not be strong enough to trigger four geophones.

Due to the weakness of the initiated seismic energy and fracture attenuation, many weak seismic events may only trigger one or two nearby geophones. It is possible for many weak events that are not recorded by the trigger mode to occur near the slope before ground movement can be observed. Weak seismic events are as important as strong seismic events for open pit stability assessment. However, there has been lack of investigations of these weak seismic events in previous microseismic monitoring projects at open pit mines.

* *Geomechanics and Ground Control, CSIRO Energy, Australia.*

† *Australian Centre for Geomechanics, the University of Western Australia, Australia.*

 This paper was first presented at the AfriRock 2017 International Symposium, *30 September –6 October 2017, Cape Town Convention Centre, Cape Town.*

Microseismic events for slope stability analysis – a case study at an open pit mine

An investigation of weak seismic events was carried out using a microseismic data-set that was continuously recorded at an open pit in Australia. The objectives of this project were to investigate the characteristics of the weak events and to explore the feasibility of using these events for the stability assessment of an open pit. In this paper, the preliminary results from this study are presented.

Monitoring site and the microseismic system

The Century mine is an open pit mine owned and operated by Minerals and Metals Group (MMG) Limited. It is located near Lawn Hill in North Queensland. Since mining in the southwest corner commenced, the area has represented an ongoing challenge for engineers on site, due to persistent unravelling on bedding planes and ground deformation. The pit wall is mainly developed in shales and it is characterized by the presence of two main structures, the Pandora's and Page Creek faults (Figure 1). Moreover, a massive block of carbonate breccia (CBX), covering approximately four benches, outcrops along Pandora's Fault. The pit wall has a total height of 300 m and an overall slope angle of 40°. In order to prevent further development of instability in the lower section of the wall during mining, a buttress was left *in situ* (approx. 28° overall angle). More details on the instability history and geological/geotechnical settings of the area are discussed in Hendersonhall *et al.* (2010), Kurukuk and Sweeney (2012), and Salvoni *et al.* (2015).

As direct access to the pit wall was limited for the installation of traditional subsurface monitoring instrumentations (inclinometers, piezometers and/or extensometers), there were no indications on how extensively the rock mass was damaged behind the pit wall. For this reason, in 2013 MMG management decided to implement a microseismic monitoring system. The Australian Centre for Geomechanics (ACG) led the project, with the aim to assess any potential for a deep-seated failure development.

The microseismic monitoring system was provided by the Institute of Mine Seismology (IMS) and comprised 16 geophones, installed in four long (approx. 400 m) inclined and two short (approx. 10 m) vertical boreholes. Due to the limited access to the area and the pit geometry, navi-drilling behind the pit crest was the only option to get the instruments sufficiently close to the instability area. The technical specifications of the geophones and seismic instruments, data acquisition, and transmission equipment are discussed in Salvoni *et al.* (2015). The seismic events were recorded based both on a triggered scheme and in continuous mode. IMS personnel were in charge of manually processing the triggered data and made it available for the engineers on site within 10 minutes of an event. From December 2013 to June 2014, a collaborative project was also established between the ACG and CSIRO in order to conduct further investigations, looking at the data recorded in the continuous mode.

Surface displacement survey and microseismicity

Prior to the installation of the microseismic array, the instability of the southwest wall was monitored through a surface monitoring system. This comprised a geodetic prism network and a ground-based, real aperture radar. A review of the historical data-set from surface monitoring has indicated how surface deformations are related to the wet and dry seasonal cycle typical of this area, with the water acting as a triggering mechanism for movement (Figure 2). Rates of displacement following rainfall events can exceed 10 mm/d, with cumulative displacements of several metres. The CBX block appeared to be involved in an active-passive wedge mechanism, being rotated and pushed out from the wall (Salvoni *et al.*, 2015). During the dry season, movements maintain steady displacements of approximately 1 mm/d. However, Salvoni *et al.*, (2015) stressed that inferring rock mass behaviour at depth from surface deformations may be misleading. In fact, after exposure the shales tend to rapidly break up and deteriorate due to the high clay mineral content (montmorillonite) and the sulphide mineral pyrite (FeS_2). Several authors emphasized how in shales of low durability, mechanisms of slaking, erosion, and surface creep are dominant (Franklin, 1981; Marques, Vargas, and Antunes, 2005; Alonso and Pineda, 2006). This case study provided us with a good opportunity to compare results obtained from the microseismic and surface monitoring systems.

From the middle of February 2014, after several days of rainfall, an extended reactivation of the instability in the upper section of the pit wall and in the CBX block was

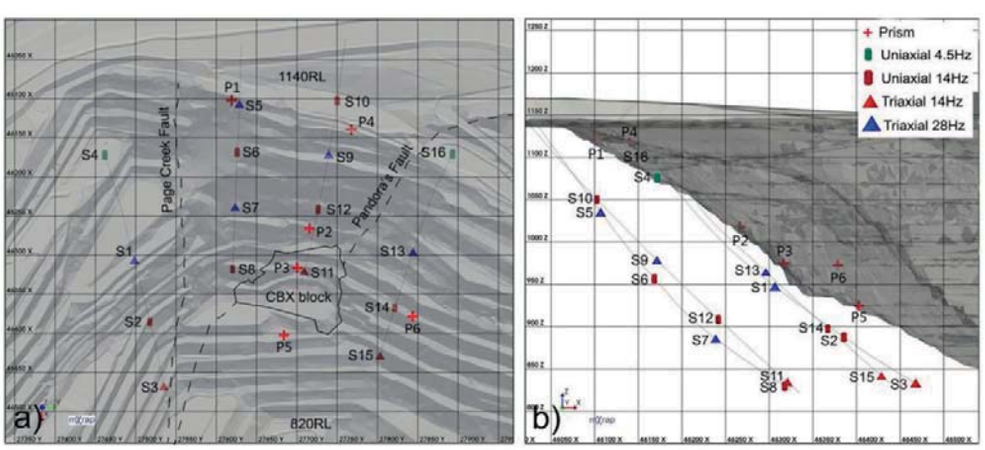

Figure 1—Microseismic array configuration showing location and type of geophones (S1-S16) installed. P1-P5 are the locations of the prism survey points. Plan view (a) and sectional view (b)

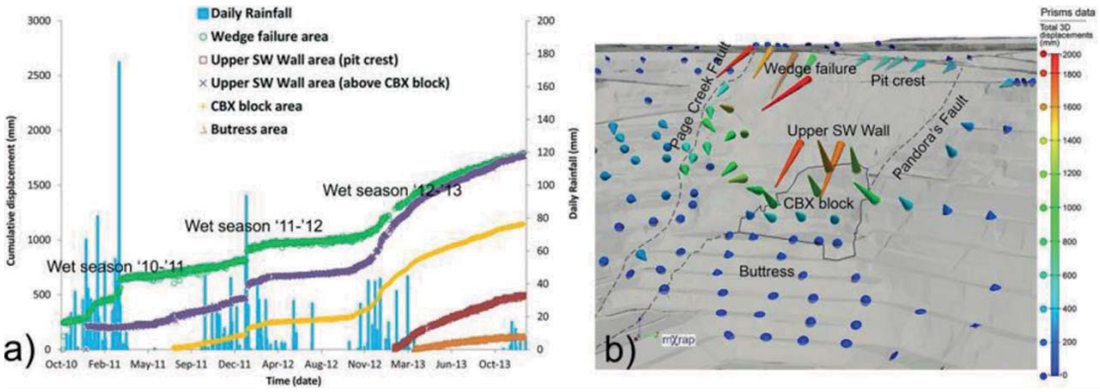

Figure 2—Ground displacements recorded by the prism monitoring and daily rainfall between October 2010 and January 2014 in different areas of the slope. (a) 3D view showing the displacement vectors for the same time period and coloured by total cumulative displacement, (b) the microseismic monitoring project was started in October 2013

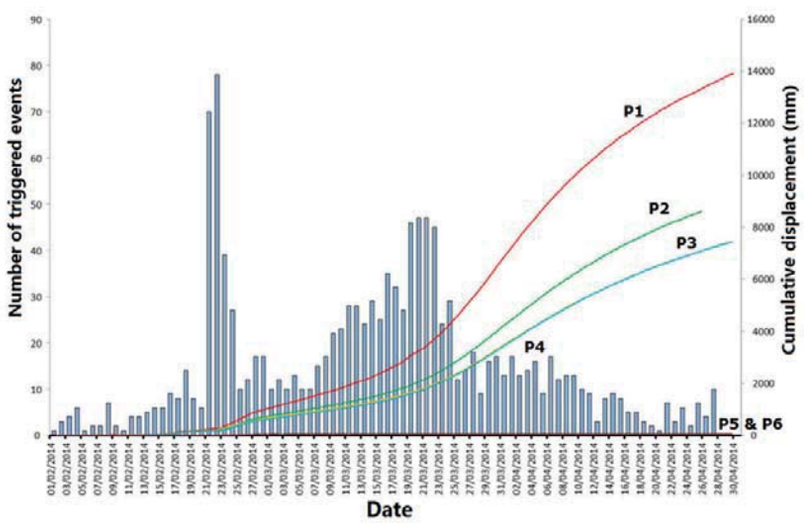

Figure 3—Pit surface displacements observed at the prism points (P1-P6) and the seismicity associated with 1305 triggered events, from 1 February to 30 April 2014

observed, with total cumulative displacements over 10 m in only 3 months. No major deformations were experienced in the lower section of the wall (buttress area). At the same time, seismic activity rates increased sharply, with a total of 1241 events recorded between February and April using the triggered database (Figure 3). In particular, on 23 and 24 February a spike in seismicity rate was observed related to a small failure that occurred in upper section of Page Creek Fault. Following this, a general rise of seismicity was observed behind the pit wall, with activity concentrated mainly in the upper section of the slope and the base of the CBX block (Figure 4).

Analysis of weak events and discussion

In the continuous microseismic data-set, many weak seismic events were found to be recorded by only one geophone station. Figure 5 shows a typical weak event recorded only by geophone S5. This event occurred at 11:47 am on 25 February, when the southwest wall started to move. Figure 6 shows the zoom-in waveforms and signal frequency contents of this event, on the three geophone components of S5. Figures 7 and 8 show another weak event recorded by geophone S9, at 18:40 on the same day.

The data processing for the weak events was conducted manually on the continuous data-set that does not contain the reported triggered events. As the continuous data-set is huge, at the first stage we concentrated our effort on the data for two special days – February 10 when the slope was in a stable condition, and February 25 when obvious surface movement was observed.

The amplitudes of the weak events have been found to be in the range of 10^{-7} m/s, whereas the amplitudes of strong signals are above 10^{-6} m/s. The dominant frequency of the weak signals is in the range from 110-150 Hz, much higher than that of the strong events showing 30-60 Hz. The smaller amplitude and higher frequency may imply that a weak event is associated with a brittle rock fracturing event or a sudden movement of a structure at a small scale near the slope and close to the geophone location.

The identification of the weak events was carried out on the events that were recorded by only one geophone station (Figures 5 and 7, for example). On these two days, geophone

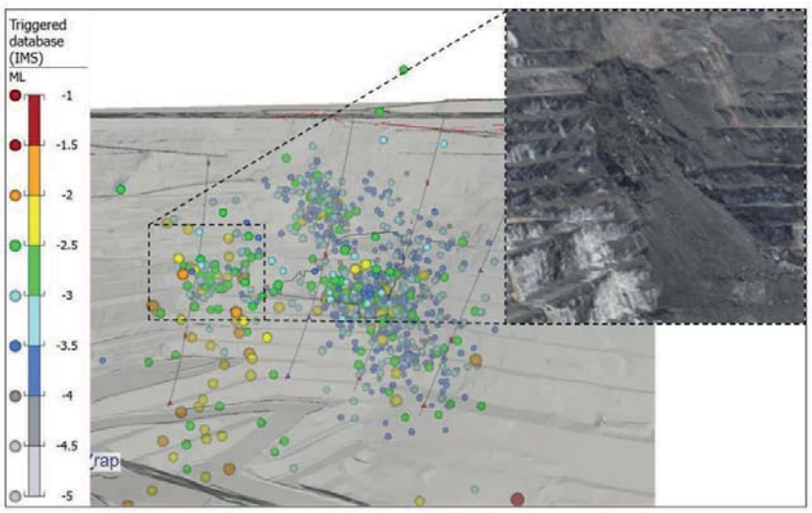

Figure 4—Seismic events located by IMS from 11 February to 31 April 2014; events are coloured and sized based on local magnitude (ML)

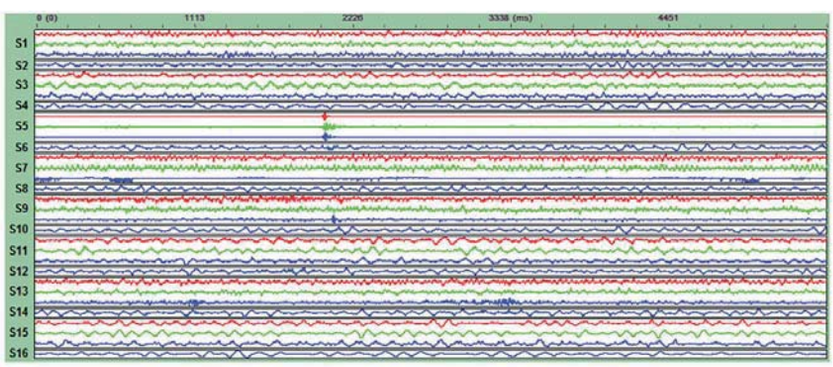

Figure 5—A typical weak event recorded by the 3-component geophone, S5. For a 3-component geophone, the red, green, and blue traces are the north, east, and vertical components, respectively. The waveform of a single-component geophone is shown in blue. Each of the seismic waveforms is normalized to its own maximum amplitude

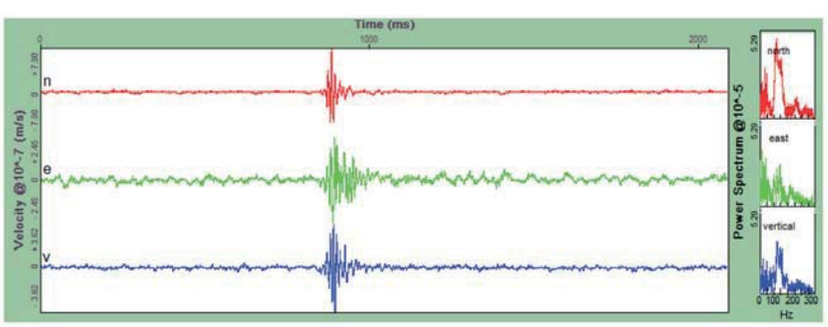

Figure 6—A zoom-in on the seismic waveforms of the event recorded by S5 and shown in Figure 3. The frequency contents associated with the seismic signals are displayed on the right

S16 did not work properly and it was excluded from the data processing. The rest of the geophones (S1-S15) were in good working condition.

The number of the weak events identified on the two days is summarized in Table I. It is evident that there is a big difference in seismicity on these two days. On February 10 when the ground was stable, only seven events were observed. However, on the day that the slope started to move, 1768 events occurred. As a seismic event is associated with a rock fracturing or a defect weakening event inside the pit wall, this increase in seismicity may have indicated a significant deterioration of the ground in the vicinity of the geophones that recorded high seismic activity rates. Compared to the weak events, there were no triggered events

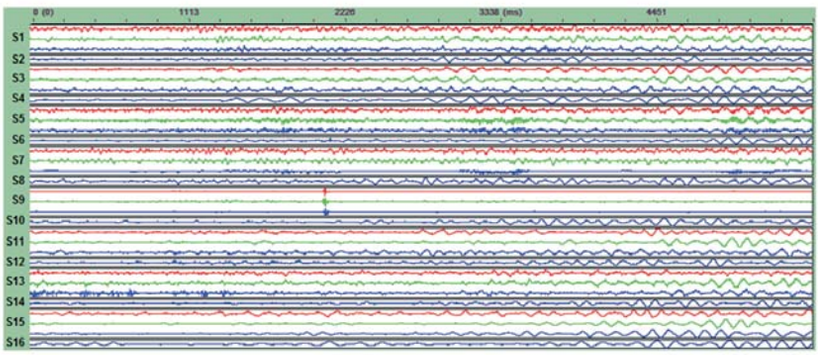

Figure 7—A weak event recorded by the 3-component geophone S9

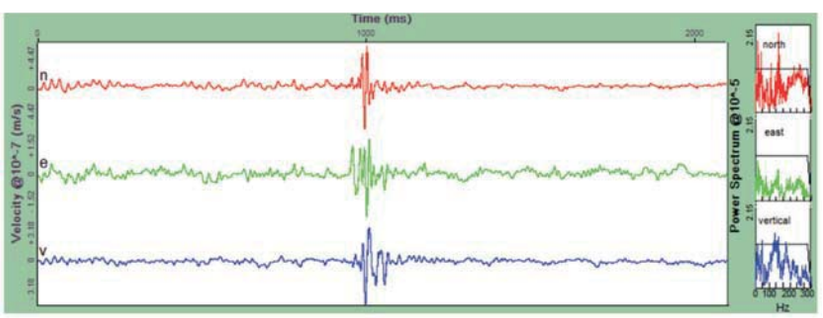

Figure 8—A zoom-in on the seismic waveforms of the event recorded by S9 and shown in Figure 5. The frequency contents associated with the seismic signals are displayed on the right

within 20 m of the sensors. This means that close to the sensors we have only weak events.

An interesting fact shown in Table I is that seismic sensors S5, S9, and S10 recorded more events than the others. These geophones are located close to the prism points P1, P2, and P4, where noticeable ground movement was measured (see Figure 3). Sensor S13 also recorded a large number of events, but no prism point was installed close by to enable comparison of the results. However, significant surface movements were visually observed after 25 February near S13.

The different seismic activity rates at different geophone stations provided good information for estimating ground weakening locations. Figure 9 shows the locations of the weak seismicity recorded by individual geophones and strong events recorded by the trigger mode on 10 and 25 February. On these two days, the strong events are sparsely distributed and it is difficult to use these locations to infer the location of potential ground movement. However, the different seismic activity rates at different geophone locations indicate different scales of ground failures near the geophone stations, from which the location of potential ground movement can be inferred.

Table I

The number of the weak seismic events recorded on the day of no ground movement and the day when the ground started moving

Geophone station	Number of weak seismic events	
	Stable ground (10 February 2014)	Moving ground (25 February 2014)
S1	1	14
S2	0	2
S3	0	0
S4	0	0
S5	3	139
S6	0	14
S7	0	2
S8	0	0
S9	0	44
S10	0	884
S11	0	1
S12	1	7
S13	1	638
S14	0	18
S15	1	5
S16	Not in working condition	
Total	7	1768

Conclusions

This study has shown the value of continuous data in order to detect weak events and have a better comprehension of the rock mass damage close to the sensor locations. It is suggested that weak seismic events can be as important as strong seismic events for slope stability assessment and they should not be ignored in a microseismic monitoring project.

The design of a microseismic network for slope stability monitoring should consider capturing both the strong and weak events, using both triggered and continuous recording modes.

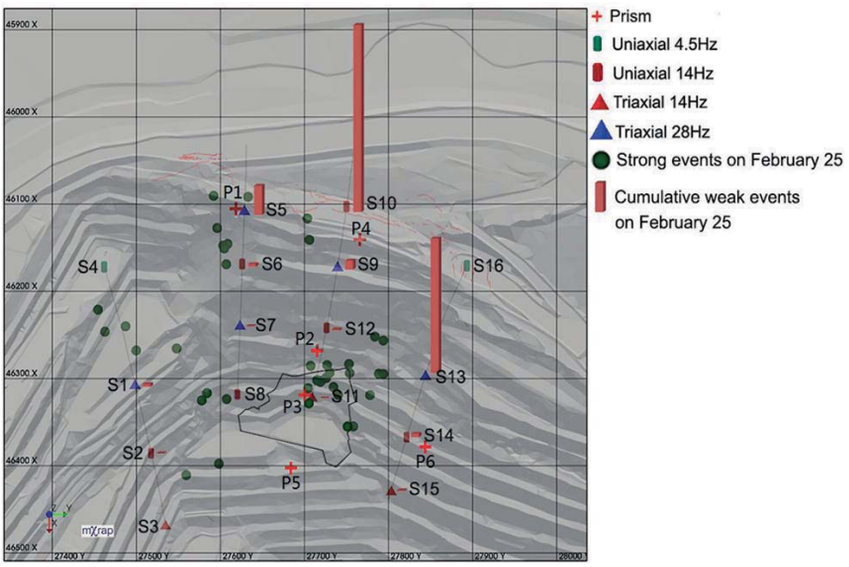

Figure 9—Locations of weak seismicity (red bars) and triggered strong events (colour circles) that were recorded on 10 and 25 February 2014. The seismicity on 10 February is very minor and the red bars actually show seismicity on 25 February

Only results from the analysis of the weak seismic events for two particular days were presented. Analysis of the data recorded on other days is still in progress, in order to obtain the whole picture about the characteristics of the weak events against the surface dislocations. Several issues will be addressed in our following research:

- The characteristics of seismic signals of the weak events associated with different stages of ground movement
- The relationship between the weak and triggered events
- Interpretation of the source mechanisms of the weak events and evaluation of event location methods using a single station, for estimating the weak events locations
- Automatic and reliable identification and selection of the weak events.

Acknowledgements

The authors are deeply grateful to MMG Limited for funding the project and allowing access and providing logistic support to the study area. We thank Gerrit Olivier and Stephen Myer of IMS for providing the SEGY continuous data-set for processing and for their patience in explanation of their methods for seismic source location and energy estimation. This project is mainly supported by ACG. CSIRO provided in-kind support to this study.

References

Alonso, E.E. and Pineda, J.A. 2006. Weathering and degradation of shales: experimental observations and models of degradation. *Proceedings of the VI South American Congress of Rock Mechanics*, Cartagena de Indias, Colômbia, 8–13 October 2006. International Society for Rock Mechanics, Lisbon, Portugal.

Franklin, J.A. 1981. A shale rating system and tentative applications to shale performance. *Transportation Research Record*, vol. 790. pp. 2–12.

Hardy, H.R. and Kimble, E.J. 1991. Application of high-frequency AE/MS techniques to rock slope monitoring. *Proceedings of the Fifth Conference on Acoustic Emission/Microseismic Activity in Geologic Structures and Materials*, Pennsylvania State University, 11–13. June 1991. Hardy, H.R. (ed.). Trans Tech, Clausthal-Zellerfeld, Germany. pp. 457–477.

Hendersonhall, B.D., Lucas, D., Kerr, N., and Pennisi, C. 2010. Practical management of progressive large failures at Minerals and Metals Group Century Mine. *Proceedings of the Seventh Large Open Pit Mining Conference*, Perth, Australia. Australasian Institute of Mining and Metallurgy, Melbourne.

Kurukuk, N. and Sweeney, E. 2012. Slope stability assessment Century. *Proceedings of the 9th Australia - New Zealand Young Geotechnical Professionals Conference*, Melbourne, Australia, 11–14 July 2012. Australian Geomechanics Society.

Lynch, R.A., Wuite, R., Smith, B.S., and Cichowicz, A. 2005. Microseismic monitoring of open pit slopes. *Proceedings of the 6th International Symposium on Rockburst and Seismicity in Mines*, 9–11 March 2005. Potvin, Y. and Hudyma M. (eds.). Australian Centre for Geomechanics, Perth. pp. 581–592.

Lynch, R.A. and Malovichko, D.A. 2006. Seismology and slope stability in open pit mines. *Proceedings of the International Symposium on Stability of Rock Slopes in Open Pit Mining and Civil Engineering*, Cape Town. Southern Africa Institute of Mining and Metallurgy, Johannesburg. pp. 375–390.

Marques, E.A.G., Vargas Jr, E.D.A., and Antunes, F.S. 2005. A study of the durability of some shales, mudrocks and siltstones from Brazil. *Geotechnical and Geological Engineering*, vol. 23. pp. 321–348.

Mendecki, A. J. 1997. Seismic Monitoring in Mines. Chapman and Hall.

Salvoni, M. and Dight, P. 2016. Rock damage assessment in a large unstable slope from microseismic monitoring-MMG Century mine (Queensland, Australia) case study. Engineering Geology, 2016.

Trifu, C-I., Shumila, V., and Leslie, I. 2008. Application of joint seismic event location techniques at Chuquicamata open pit mine, Chile. *Massmin 2008: Proceedings of the 5th International Conference and Exhibition on Mass Mining*, Luleå, Sweden, 9–11 June, 2008. Schunnesson, H. and Nordlund, E. (eds). Luleå University of Technology. pp. 943–952.

Willenberg, H., Spillmann, T., Eberhardt, E., Evans, K., Loew, S., and Maurer, H.R. 2002. Multidisciplinary monitoring of progressive failure processes in brittle rock slopes – concepts and system desig. *Proceedings of the 1st European Conference on Landslides*, Prague, Czech Republic, 24–26 June, 2002. Rybar, J., Stemberk, J., and Wagner, P. (eds.). CRC Press. pp. 477–483. ◆

http://dx.doi.org/10.17159/2411-9717/2018/v118n3a3

Mining with crush pillars

by M. du Plessis* and D.F. Malan†

Synopsis

Crush pillars have been extensively applied on the Merensky Reef horizon since the late 1970s. Once in a crushed state, the residual strength of the pillar provides a local support function and must support the hangingwall to the height of the highest known parting. The design of crush pillars is mainly limited to specifying a width to height ratio (w:h) of approximately 2:1. It is also required that a pillar crushes close to the face, while the pillar is being formed. On many mines the crush pillar system is problematic owing to the difficulty of controlling pillar sizes. This is mainly caused by poor drilling and blasting practices. As a result, pillar crushing is not always achieved. Crush pillars are implemented at relatively shallow depth, the pillar dimensions have remained essentially unchanged over many years, and the impact of regional pillars and geological losses contributing to the regional behaviour of the rock mass are overlooked. In many cases the pillar system is the source of seismicity. In this paper, the influence of mining losses (potholes) and the use of sidings are discussed as possible contributors impacting on crush pillar behaviour. A limit equilibrium model implemented in a displacement discontinuity boundary element program is used to demonstrate crush pillar behaviour. The results are compared to the pillar behaviour at an underground investigation site, which supports the preliminary findings.

Keywords

crush pillar behaviour, limit equilibrium model, regional pillars, geological losses.

Introduction

Crush pillars have been extensively used in Merensky Reef stopes. The key function of the pillar system is to prevent the occurrence of back-breaks (large-scale collapses in the back area of a stope) occurring as a result of hangingwall separation along parting planes or fractures. One such problematic parting is the Bastard Merensky Reef, situated between 5–45 m above the Merensky Reef. The pillar dimensions are selected such that the pillars should be fractured while being formed at the mining face. This is typically achieved when a pillar is cut at a width to height (w:h) ratio of approximately 2:1 (Ryder and Jager, 2002). Once crushed, the residual strength of the pillar provides the required support function.

Factors influencing pillar stress (*i.e.* mining depth, pillar width, mining height, percentage extraction) will impact on crush pillar behaviour. Du Plessis and Malan (2015) demonstrated how oversized pillars could potentially result in unpredictable pillar behaviour. The execution of a mining layout can impact on the size of the pillar cut at the mining face. This is demonstrated by the examples and case study presented in this paper. Similarly, the presence of potholes or blocks of unmined ground will influence pillar crushing. While these are common occurrences on most mines using crush pillars, these factors have historically not been associated with poor pillar crushing or pillar seismicity.

Numerical analyses

A limit equilibrium model (Napier and Malan, 2014) implemented in the TEXAN displacement discontinuity boundary element code was used to simulate the impact of both geological losses and sidings on crush pillar behaviour. The model used was representative of the behaviour of crush pillars in a typical layout. This provided insights into when pillars will crush, where they will crush relative to the mining face, and why some pillars can potentially burst.

Mining and geological losses

The effect of unmined blocks of ground or geological losses on crush pillar behaviour has not previously been considered as a factor affecting pillar crushing or pillar seismicity. For this reason, it was investigated in this study. In the platinum mines, intact blocks of ground are left *in situ* where poor ground conditions are encountered, or where geological features such as potholes are intersected. A pothole can be described as a random, approximately circular area where the reef slumps and pinches to such an extent that regular mining cannot be conducted. In the

* *Lonmin Platinum, Marikana, South Africa.*

† *Department of Mining Engineering, University of Pretoria, South Africa.*

 This paper was first presented at the AfriRock 2017 International Symposium, *30 September –6 October 2017, Cape Town Convention Centre, Cape Town.*

Bushveld Complex (BC), potholes make up the largest component of 'mining and geological' losses. Potholes can contribute to an extraction loss of between 5–25%. Figure 1 shows the pothole distribution at a site along the western limb of the BC. The potholes vary in size from 5–420 m in diameter. Most of the pothole diameters range between 20–100 m and the spans between adjacent potholes are typically less than 100 m.

To quantify the effect of a pothole adjacent to a line of crush pillars, an idealized crush pillar layout (Figure 2) was simulated. The layout consists of a 30 m × 70 m stope panel with a second panel being mined in a sequential fashion adjacent to this first panel. The layout was simulated as eight mining steps with seven crush pillars being formed during this process. The unmined block was simulated as a square block, the dimensions of which [(x m) × (y m)] were selected to simulate the percentage reef locked up in the area defining mining step 1 [*e.g.* pothole area (10 m × 10 m)/(30 m × 70 m) ≈ 5%]. For the second panel, the size of each mining step was 10 m and the sizes of the crush pillars were 4 m × 6 m. A 2 m mining height was used (w:h = 2:1). The element sizes were 0.5 m.

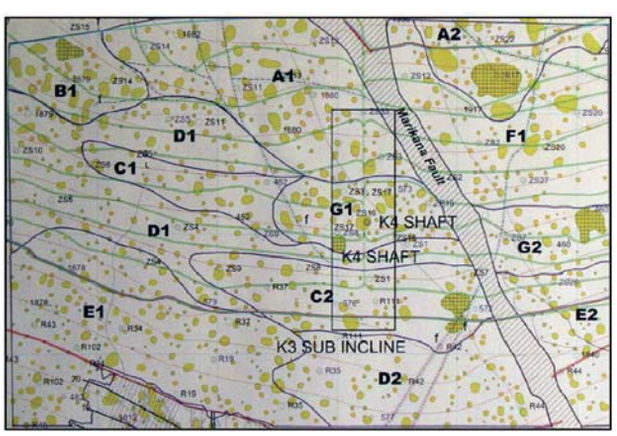

Figure 1—Seismic survey indicating the density of potholes at a site along the western limb of the BC (area approx. 6 km × 6 km). The potholes are indicated by the yellow areas

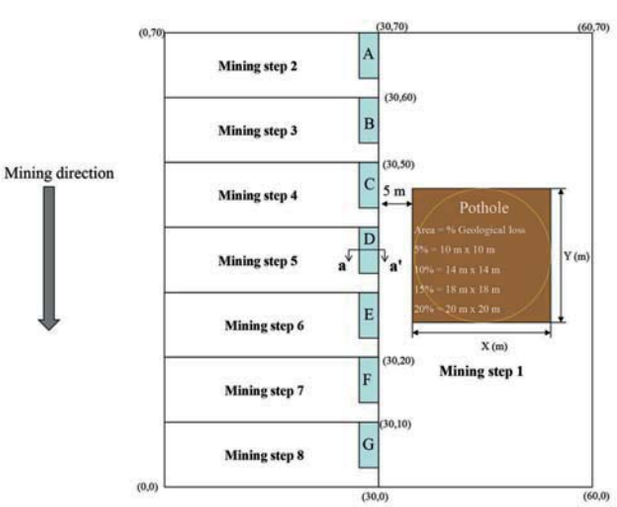

Figure 2—Idealized crush pillar layout used to simulate the effect of unmined ground adjacent to a pillar on pillar crushing

The parameters used for the simulations were as follows: Young's modulus 70 GPa, Poisson's ratio 0.25, contact friction angle 35°, intact and residual material strength 5 MPa, mining depth 600 metres below surface (mbs), and reef dip 0°. These values were chosen arbitrarily. The intent was to establish trends regarding the pillar behaviour, even though the parameters selected may not fully represent the underground environment. A sensitivity analyses was conducted to determine the effect of each input parameter on the behaviour of the model and simulated pillars in the layout. The results indicated that the choice of parameters produced qualitative agreement with observed crush pillar behaviour and historical underground measurements.

The results highlighted the importance of taking the geological environment into consideration when implementing a crush pillar system. The pillar stress is affected by the additional stability provided by unmined blocks of ground. This causes a reduction in the pillar stress and prevents effective pillar crushing. To overcome this would require the cutting of smaller pillars, which could be impractical.

The preliminary modelling results indicated that:

- Crush pillars implemented at a depth of 600 mbs with a w:h = 2:1 will not crush if a 10% mining loss is present adjacent to the pillar line. Pillars with a reduced width will be required in the area to ensure that pillar crushing is achieved (*e.g.* w:h = 1.5 is required at 600 mbs).
- Pillars located as far as 20 m behind or ahead of an unmined block will also be affected, resulting in either partially crushed (core still solid) or intact pillars.
- Crush pillars implemented at depths of more than 800 m below surface are impacted to a lesser extent when in close proximity to a pothole. Large mining losses (>10%) and potholes situated closer than 10 m from the pillar line can nevertheless prevent pillar crushing.

The case study presented in the second half of the paper indicated that a crush pillar situated in close proximity to a pothole at a depth of 1300 mbs was not in a crushed state.

The impact of sidings

A siding is a 1–2.5 m wide ledge or heading carried on the one side of an on-reef development end, adjacent to the panel being mined (Figures 3 and 4). These sidings are typically carried at between 3 and 6 m behind the panel face (depending on the standard applied by the particular mining company). The main function of the siding is to either modify the fracture patterns resulting from high face stress or to move the crush pillars away from the travelling way, to prevent failed rock from falling on people. The sidings, being approximately 2 m wide, are difficult to clean (hand-lashed) and support. For this reason, mining of the siding is frequently behind schedule.

In some cases, sidings lag the face by 20–30 m and are then developed as a single mining face. A lagging siding will impact the width of the pillar being formed at the mining face (Figure 4). Until now, the impact of a lagging siding on the pillar width has not been identified as a contributor to undesired pillar behaviour, or a source of pillar seismicity.

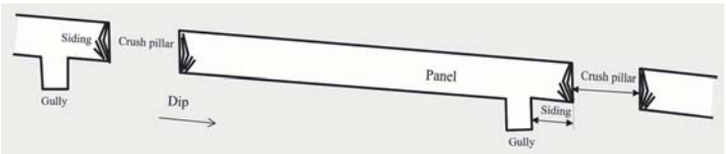

Figure 3—Section view of a typical intermediate depth mining geometry with a crush pillar layout

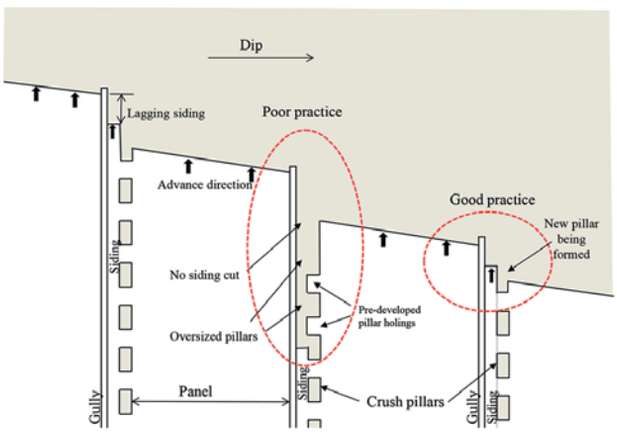

Figure 4—The impact of a large lagging siding on crush pillar formation (plan view). If pillar holings are not pre-developed the problem will be exacerbated

Once the siding of an advancing panel lags behind the adjacent lagging panel face, oversized pillars are created. The pillars will be reduced in size to the required dimension only when the siding is blasted. At this point the pillar might not be able to crush sufficiently, as it is already in the back area of the stope.

To investigate the impact of a lagging siding on crush pillar behaviour, the simulated mining sequence of the layout in Figure 2 was adjusted. The mining loss indicated in step 1 was excluded. A 2 m wide siding was added to the layout by initially simulating the pillars as being 6 m wide (w:h = 3). The siding was then mined by simulating the additional 2 m portion of pillar as being mined. The length of the oversized pillar resulting from a lagging siding was controlled by the delayed mining of the pillar holings. Initially a 6 m wide by 20 m long pillar was formed. The siding was mined, reducing the pillar width (at the pillar position) to 4 m (w:h = 2:1). The final pillar (2 m × 4 m) was created only when the pillar holing was developed. This took place when the pillar was 20 m in the back area.

The layout was simulated at various depths as shown in Figure 5. All the results presented are for pillar D. Mining depth does not appear to have any impact on the overall behaviour of the pillar (although the pillar is subjected to a higher stress level). These findings illustrate how important it is to achieve pillar crushing while the pillar is close to, or is being formed at, the mining face. The results in Figure 5 can be compared to results presented by du Plessis and Malan (2014), where pillar crushing causes load shedding if the pillars are cut to the correct width.

The results indicate that a lagging siding could impact on pillar crushing. These pillars could therefore become sources of seismicity when located in the back area of a stope.

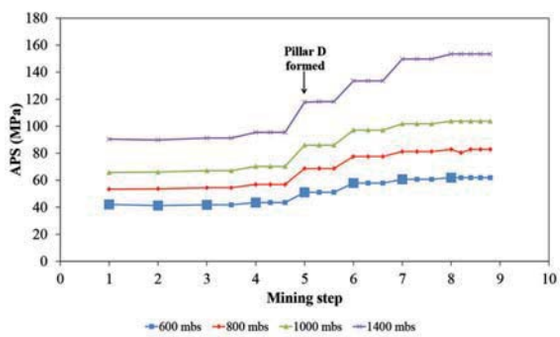

Figure 5—The effect of a lagging siding on crush pillar behaviour (pillar D, Figure 2) at various depths (w:h = 2). Note that the pillar does not crush and shed load. Crushing and load shedding of a correctly mined crush pillar is shown in du Plessis and Malan (2014)

Case study supporting the simulated pillar behaviour

An investigation was conducted at a mine applying crush pillars on the Merensky Reef at a depth of approximately 1300 mbs. The objective was to verify some of the numerical modelling results and to investigate the failure mechanism of the pillars.

The mining layout requires 2.5 m wide × 4 m long crush pillars, separated by a 2 m wide pillar holing. The stoping width is approximately 1.2 m high and the reef dips approximately 10° towards the north. Conventional breast mining is applied with long panels (approximately 35 m inter-pillar spans) being mined adjacent to a gully. A 2 m wide siding is cut adjacent to the pillar line. The mine standard requires that the siding does not lag the mining face by more than 4 m.

As can be seen in Figure 6, actual pillar dimensions varied greatly as a result of poor mining practice. Pillar 19 is approximately the correct dimension (2.5 m × 3.8 m). Of the pillars cut, 63% had a width to height ratio greater than 2 and only four of the pillar holings were less than 2 m wide. The practice underground is to mine the pillar holings in an updip direction. The panel siding lag was kept at the 4 m standard. Accurate mining of the lagging panel was required to ensure that the pillars were cut to the correct dimension (pillar width). This was not done. The holings were also not always mined as required, impacting on the pillar length. This resulted in several significantly oversized pillars. Pillars 13 and 16 are examples of this. Pillars 17 and 18 were only split when the pillars were located some distance from the face. Pillars 13 and 16 are further examples of this bad practice. As a result, pillar 16 experienced a magnitude ML 1.9 seismic event. At the time of the event, the pillar holing indicated by the black square (step 2) and the holing between pillars 16 and 17 were being mined. Pillar 16, at this point was approximately 25–30 m in the back area.

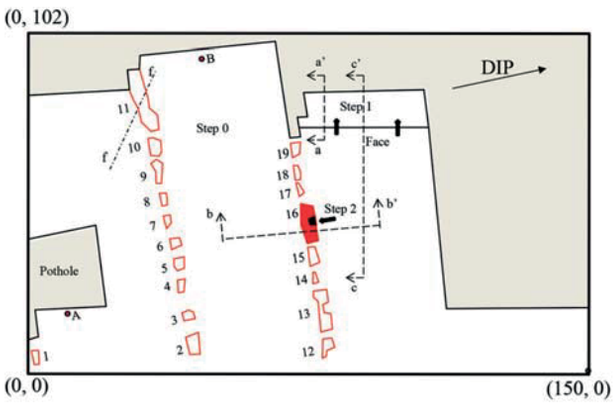

Figure 6—Plan view indicating the simplified pillar layout and mining configuration of the area where the site visit was conducted

The underground investigation revealed the following.

- Pillar 1, although adequately sized to ensure crushing (2 m × 4 m), was in an uncrushed state as a result of its proximity to the pothole (Figure 7).
- The edge of the pothole was severely fractured due to the abutment stress (point A in Figure 6).
- Similarly, the face abutment at point B was also severely fractured. This face was left unblasted for approximately 5 months to rectify the lead-lag sequence.
- Pillar 11 was left oversized to clamp a fault. The pillar was in an unfractured state (similar to the condition of pillar 1). There were signs of footwall punching along the downdip side of the pillar.
- Pillar 19, a newly cut pillar, was in a fractured state (Figure 8). The pillar displayed the same fracture profile as described by du Plessis and Malan (2016). As can be seen from the figure, the majority of the fractures propagated towards the side of the pillar which was exposed first. The side of the pillar exposed by the lagging face displayed little to no fracturing. Once the pillar is completely formed and the face advances, the fractures continue to dilate. Where fractures intersect at approximately the centre of the pillar, a wedge-like structure is formed.
- Pillar 16 was, at the time of the investigation, in a completely fractured state. This was most likely a result of the seismic event. The updip side of the pillar bulged as the fractured material was pushed out (Figure 9). The downdip side of the pillar showed signs of ejected material scattered into the panel below. The footwall experienced heave and the timber support in the panel below the pillar was damaged as a result of the event (Figure 10).

Back-analysis

The underground observations supported some of the modelling results described in the previous section. It was nevertheless important to understand the failure mechanism contributing to pillar instability (*i.e.* pillar 16). The limit equilibrium model was also used to simulate the behaviour of the crush pillars for this particular underground layout. Du Plessis and Malan (2016) demonstrated that by applying this method, they successfully simulated the observed and

Figure 7—Condition of pillar 1. The pillar was situated adjacent to a pothole, which prevented the pillar from crushing

Figure 8—Fracture pattern along the width of failed crush pillar 19

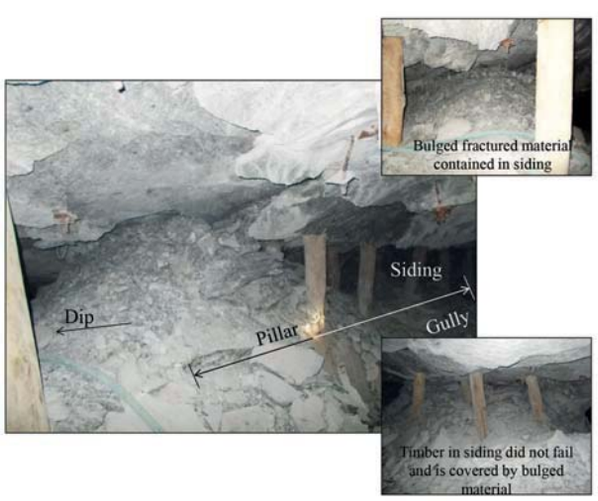

Figure 9—Photograph of the updip side of pillar 16. Note that the elongates did not fail and they are partially covered by the fractured pillar material

measured behaviour of crush pillars for a large-scale underground trial site.

The layout for the underground investigation site (Figure 6) was approximated using straight line polygons to enable the area to be easily discretised using triangular elements. The mining steps considered were:

Figure 10—Photograph of the panel along the down-dip side of pillar 16. The elongates were damaged during the seismic event. There were also signs of footwall heave

- Step 0: The layout with the face positions prior to the seismic event.
- Step 1: Panel advance to determine the effect on the pillar stress.
- Step 2: Mining of a 2 m × 2 m slot into pillar 16 at the holing position to determine the impact on the pillar stress.

The element sizes selected for the mining steps were 1 m, and for the pillars 0.5 m. Following several successive cycles of parameter testing, the selected modelling parameters provided results which closely resembled the observed underground pillar behaviour. A dip of zero degrees was used in the model to simplify the analysis. The vertical stress at this depth was 38.5 MPa. The horizontal stress was assumed to be the same in both directions (k-ratio = 1.8). The intact and residual strengths of the limit equilibrium material were set to 1225 MPa and 20 MPa respectively. The high value for the intact strength is associated with the onset of pillar failure and was required to ensure that the model could replicate the observed underground pillar behaviour. A friction angle of 50° was used.

The numerical model was useful to establish trends and comparisons. The general results indicated that:

- The pothole adjacent to pillar 1 prevented the pillar from crushing.
- High stresses were present along the solid abutments (Figure 11). This explains the significant scaling observed along the pothole edge and stopped panel face.
- The average convergence across the entire mining region was approximately 36 mm. It increased by approximately 1.5 mm during the extraction of mining step 1 and by another 1.5 mm during step 2. The additional convergence experienced during step 2 (mining of the slot along the pillar holing) was a result of pillar 16 crushing. It is insightful to note the impact which late pillar crushing in the back area has on the overall rock mass behaviour. This finding should be explored in more detail.
- The oversized pillars (11, 13, 16) were intact (*e.g.* Figure 12). Pillar 16 only fails in step 2 when the pillar is partially mined by the slot defining the pillar holing.
- Pillar 19 was completely crushed and in a residual state.

The vertical stress across pillar 16 (section b-b' in Figure 6) indicated that the pillar had high stress levels on the edge and an intact core. Mining of step 1 caused some additional damage to the pillar edge, as can be seen in Figure 12. The outer 0.5 m of specifically the updip side of the pillar (initially exposed side) assumes a residual state. As the outer edges of the pillar fail, the high edge stresses are transferred towards the core of the pillar. Once the slot along the planned pillar holing is mined (step 2), the pillar fails completely and enters a residual state.

A convergence profile across section b-b' is shown in Figure 13. A significant change in convergence is experienced across the pillar when the pillar fails (approx. 40 mm). Another convergence profile was constructed along section c-c', extending from the face position (including step 1) to 50 m in the back area of the mined-out panel, to also include the effect of pillar 16. The results show that the intact pillar has a significant impact on the convergence experienced in the panel in proximity to the pillar 16 position. Once the pillar fails, the convergence increases (step 2). However, there were other oversized intact pillars in the back area (*i.e.* pillar 13). As a result, a certain amount of convergence is prevented by the intact pillar. The system (pillar and rock mass) is therefore not at a state of equilibrium, and this can potentially result in violent pillar behaviour.

Du Plessis and Malan (2014) demonstrated the effect of oversized crush pillars in the back area of a stope. The findings indicated that if an oversized pillar did not crush at

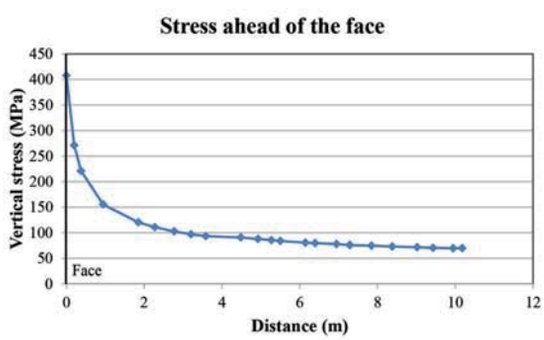

Figure 11—High abutment stress ahead of the mining face. Refer to section a–a' in Figure 6

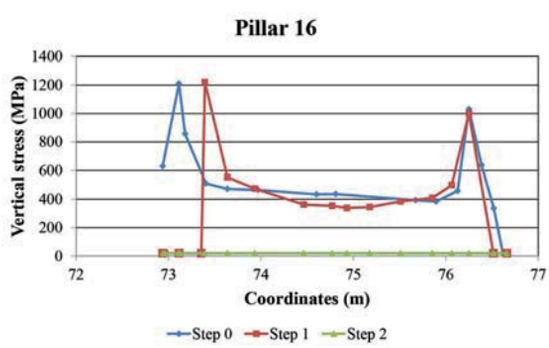

Figure 12—Vertical stress profile through pillar 16. Refer to section b–b' in Figure 6

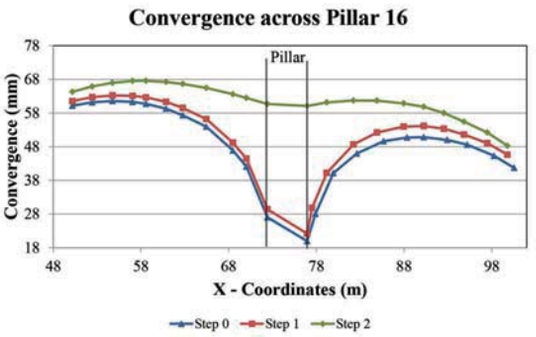

Figure 13—Convergence simulated across pillar 16. Refer to section b–b' in Figure 6

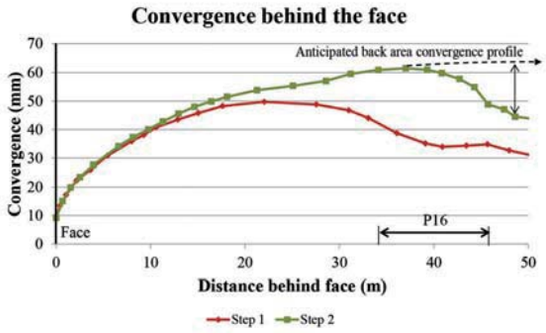

Figure 14—Convergence profile along the mined panel down-dip of pillar 16 (section c-c' in Figure 6). Notice the impact of the oversized intact pillars (13 and 16) in the back area

the face while being cut, as these pillars move into the back area as the mining face advances, they experience a higher stress level. The change in stress caused by a mining increment is lower than when the pillar is formed at the face. The pillar may therefore either not crush (especially when oversized) or fail violently. The stresses on these pillars in the back area are much higher and the loading environment has become much softer, as the pillar is no longer close to the face abutment. The results in Figure 14 provide an illustration of the increase in convergence as a result of possible violent crush pillar behaviour.

Du Plessis and Malan (2016) determined that the amount of convergence experienced in a crush pillar site could be directly related to pillar deformation (pillar fracturing or dilation along fracture planes). If the convergence (deformation) is restricted as a result of an intact pillar, it will impact on the amount of energy potentially available to cause violent pillar failure.

Salamon (1970) showed that the equilibrium between a pillar being loaded and the post-peak behaviour is stable irrespective of the convergence experienced by the pillar if:

$$(k + \lambda) > 0 \quad [1]$$

where

k = Stiffness of loading strata (rock mass)
λ = Post-peak pillar stiffness.

Various stiffness criteria to ensure 'stable' pillar behaviour for rigid and yielding pillar systems were presented by Ozbay (1989), Ozbay and Roberts (1988), and Ryder and Ozbay (1990). Unfortunately, the literature and methodologies described do not fully support the behaviour of crush pillars and this needs to be further investigated. The preliminary analysis was therefore not included in the paper.

Conclusion

This paper illustrates the importance for crush pillars to enter a residual stress state while being formed at the mining face. Factors such as geological (*i.e.* potholes) or mining losses, in close proximity to the pillar, will impact on the behaviour of a crush pillar. Furthermore, a lagging siding or delayed pillar holings will impact on the size of the pillar formed at the mining face. Early pillar crushing is therefore not achieved and this can result in unpredictable pillar behaviour.

The underground case study verified the preliminary modelling results. The model was able to replicate the behaviour of the pillars observed underground. It was insightful to note the impact of late pillar crushing in the back area on the convergence behaviour in the mined region. The study indicated that a reduced amount of convergence, as a result of an intact pillar, may be indicative of potential violent pillar failure. This finding should be further explored.

Acknowledgements

Part of the work described in this paper formed part of Dr Michael du Plessis' PhD studies at the University of Pretoria. The contribution of Professor John Napier with regard to the development of the limit equilibrium model as well as the TEXAN code is acknowledged.

References

Du Plessis, M. and Malan, D.F. 2014. Evaluation of pillar width on crush pillar behaviour using a limit equilibrium solution. *Proceedings of the 2014 ISRM European Rock Mechanics Symposium (Eurock 2014)*, Vigo, Spain, 27-29 May. CRC Press, Leiden, The Netherlands.

Du Plessis, M. and Malan, D.F. 2015. Designing controlled pillar failure – crush pillar support. *Journal of the Southern African Institute of Mining and Metallurgy*, vol. 115. pp. 481–488.

Du Plessis, M. and Malan, D.F. 2016. The behaviour of Merensky crush pillars as measured at a trial mining site. *Proceedings of EuRock 2016*, Cappadocia, Turkey. International Society for Rock Mechanics.

Napier, J.A.L. and Malan, D.F. 2014. A simplified model of local fracture processes to investigate the structural stability and design of large-scale tabular mine layouts. *Proceedings of the 48th US Rock Mechanics / Geomechanics Symposium*, Minneapolis, USA. American Rock Mechanics Association, Alexandria, VA.

Ozbay, M.U. 1989. The stability and design of yield pillars located at shallow and moderate depths. *Journal of the South African Institute of Mining and Metallurgy*, vol. 898, no. 3. pp. 73–79.

Ozbay, M.U. and Roberts, M.K.C. 1988. Yield pillars in stope support. *Proceedings of the SANGORM Symposium in Africa*, Swaziland. South African National Institute for Rock Mechanics. pp. 317–326.

Ryder, J.A. and Ozbay, M.U. 1990. A methodology for designing pillar layouts for shallow mining. *Proceedings of the International Symposium on Static and Dynamic Considerations in Rock Engineering*, Swaziland. International Society for Rock Mechanics. pp. 273–286.

Ryder, J.A. and Jager, A.J. 2002. A Textbook on Rock Mechanics for Tabular Hard Rock Mines. Safety in Mines Research Advisory Committee, Johannesburg.

Salamon, M.D.G. 1970. Stability, instability and design of pillar workings. *International Journal of Rock Mechanics and Mining Sciences*, vol. 7. pp. 613–631. ◆

http://dx.doi.org/10.17159/2411-9717/2018/v118n3a4

Progress of brittle microfracturing in crystalline rocks under cyclic loading conditions

by E. Ghazvinian* and M.S. Diederichs†

Synopsis

The stress at onset of yielding for the walls of deep underground excavations in hard rock is significantly less than the laboratory strength of intact rock samples. The wall stability is rather controlled by the microfracturing strength of the rock (*i.e.* crack propagation (CD) and initiation (CI) thresholds). Factors such as loading and unloading effect of excavation, glaciation, stress rotation in front of a tunnel face, *etc.* can contribute to the progressive damage of the rock, influencing the CI and CD thresholds and therefore contributing to the damage intensity around underground openings. The effect of stress rotation and stress fatigue on crack damage thresholds is systematically investigated in this paper through state-of-the-art laboratory testing and monitoring techniques in combination with advanced grain-based numerical modelling.

Keywords
brittle microfracturing, cyclic loading, crack initiation, crack propagation.

Introduction

The long-term stress path for the near-field rock surrounding deep underground excavations is typically more complex than simple monotonically increasing deviatoric stress conditions. The state of stress for a point in the wall of an underground opening can go through multiple loading and unloading cycles as the excavation advances and moves past the point. For underground structures such as deep geological repositories (DGRs) with ultra-long design life (*e.g.* a million years), the stress oscillation can continue after the excavation is completed due to glacial loading/unloading cycles. Microfracturing behaviour of intact rocks can change significantly when they undergo mechanical loading/unloading cycles, in comparison to the crack damage parameters that are measured from the initial state of the rock.

Strength degradation through accumulation of crack damage for brittle rocks was examined in detail by Martin (1993), Eberhardt (1998), and Diederichs (2000) through cyclic testing of the Lac du Bonnet granite. Martin (1993) captured the cohesion loss and mobilization of friction that resulted from accumulation of crack damage within intact brittle rocks through a series of damage-controlled cyclic tests in which the maximum applied stress was increased in each consecutive load cycle. This was mainly accomplished by the investigation of the critical damage (CD) locus that was defined from the collected strain gauge data. Eberhardt (1998) further advanced the knowledge of the 'fatigue' strength of brittle rocks by using the acoustic emission (AE) technique in addition to the measured strain data collected from damage-controlled cyclic tests whereby samples were loaded beyond CD, below the CD threshold, or loaded incrementally to reach failure.

The effect of stress fatigue on the crack initiation (CI) and crack propagation (CD) thresholds is further investigated in this paper. The strength degradation and damage accumulation for the pink Lac du Bonnet granite is studied through damage-controlled tests. Monitoring of the loading/unloading cycles with novel techniques such as lateral P-wave velocity (V_p) measurement and the associated discrete element method-based grain-based models (GBMs) provided a useful insight into the mechanics of crack damage accumulation in brittle intact rocks.

UCS testing of the Lac du Bonnet granite

The pink Lac du Bonnet granite was chosen for investigation in this paper. The previous research and existing literature on this rock type provide a good platform for comparison of the new findings and previous conclusions. Samples of the granite were obtained from the Cold Spring Quarry site in Manitoba, which is a surface exposure of the massive granite found at depth within the AECL's Underground Research Laboratory (URL). The

* *Itasca Consulting Group, Minneapolis, MN, USA.*
† *Queen's University, Kingston, ON, Canada.*
 ISSN 2225-6253. This paper was first presented at the AfriRock 2017 International Symposium, *30 September – 6 October 2017, Cape Town Convention Centre, Cape Town.*

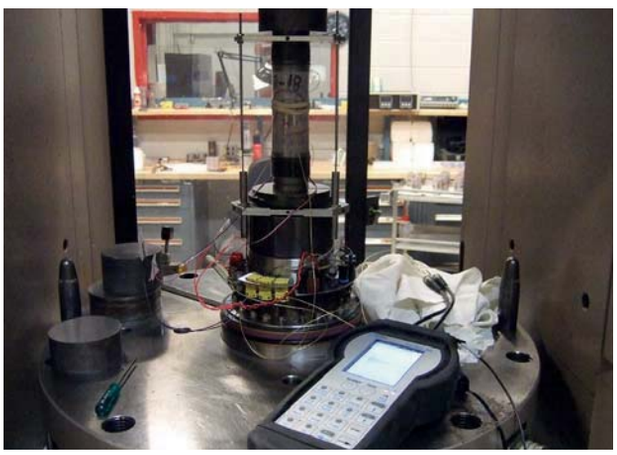

Figure 1—Test set-up for the UCS and cyclic damage-controlled testing of the Lac du Bonnet granite

samples from the quarry contain minimal pre-existing damage in comparison to the grey Lac du Bonnet granite from the 420 m level or the pink granite from the 240 m level of the URL (Martin, 1993; Eberhardt, 1998).

In the current work, mechanical properties of the intact pink Lac du Bonnet granite were measured from two UCS tests (on specimens LdB-1 and LdB-2) to establish the base properties for comparison with the damage-controlled experiments. The testing set-up for the Lac du Bonnet granite is shown in Figure 1.

The lower- (CI_L) and upper-bound crack initiation threshold (CI_U) are estimated from the AE data (Ghazvinian, Diederichs, and Martin, 2012). The CD threshold was not evident in the AE data collected for the specimens, therefore the reversal point of volumetric strain was approximated as the crack propagation threshold for the tested samples. The intact mechanical properties of the investigated Lac du Bonnet granite are presented in Table I, and the properties measured in this work are compared with those from the literature. The literature values are taken from Diederichs (2000), where the data available for the pink Lac du Bonnet granite was summarized from documents by Martin (1993), Martin and Stimpson (1994), Martin and Chandler (1994), Eberhardt (1998), Hommand-Etienne, Hoxha, and Shao (1998), Gorski and Yu (1991), Wilkins (1980), Kelly, Peck, and James (1993), and Lajtai (1988).

The difference between the measured CD and UCS in this study and the values from the literature can be attributed to the level of pre-existing damage in the specimens. Other researchers mostly reported the mechanical properties of the Lac du Bonnet granite from the 130 m level of URL for undamaged rock, while the samples tested for this study were taken from the Cold Spring Quarry.

Damage-controlled testing of the Lac du Bonnet granite

Two damage-controlled cyclic tests were performed on the Lac du Bonnet granite specimens (LdB-DC1 and LdB-DC2). The specimens were loaded in uniaxial compression up to an axial stress above the CD threshold for the rock. The specimens were then unloaded, completing one cycle, and then loaded again to an identical axial stress as in the first cycle and then unloaded again. The same routine was repeated until the specimens were loaded up to failure during the last cycle. The loading histories for the two specimens are shown in Figure 2 and the loading conditions are listed in Table II. Interestingly, the load cycling had no significant effect on the peak strength of the Lac du Bonnet granite specimens (listed in Table II and shown in Figure 3) when compared to the values obtained from the UCS tests in this study and those reported in the literature. A similar observation was reported by Martin (1993).

Table I

Mechanical properties of the undamaged Lac du Bonnet granite

Mechanical parameters	Measured properties			Literature values (Cold Spring Quarry to URL 130 m level)
	LdB-1	LdB-2	Average	
E (GPa)	71.6	71.4	71.5	65-70
v	0.21	0.22	0.22	0.22-0.26
UCS (MPa)	257.6	265.9	261.8	200-230
CI_L (MPa)	63.7	68.8	66.3	72 (AE) – (Hommand *et al.*, 1995) 71 – (Duevel and Haimson, 1997) 75 – (Read, 1994) 80 – (Diederichs, 2000) 81 (AE) – (Eberhardt, 1998)
CI_U (MPa)	93.4	98.2	95.8	95 – (Duevel and Haimson, 1997) 100 – (Read, 1994) 93 – (Diederichs, 2000) 104 (AE) – (Eberhardt, 1998)
CD (MPa)	207.9	215.4	211.7	156 – (Eberhardt, 1998)

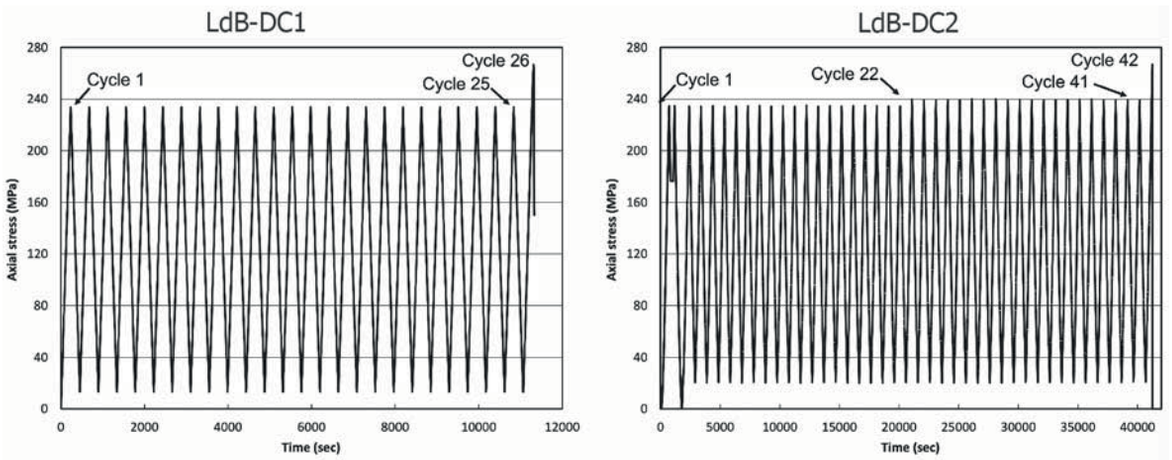

Figure 2—Axial stress *versus* time for the cyclic damage-controlled tests performed on the LdB-DC1 and LdB-DC2 specimens

Table II

Mechanical properties and cyclic loading conditions for the Lac du Bonnet granite specimens

Mechanical parameters	LdB-DC1	LdB-DC2
Peak strength at the final cycle (MPa)	266.6	267.3
E – first cycle (GPa)	68.8	67.8
v – first cycle	0.21	0.19
Number of cycles	25	41
Loading stress (MPa)	Approx. 234	235 (cycles 1-21) 240 (cycles 22-41)
Unloading stress (MPa)	Approx. 13	20

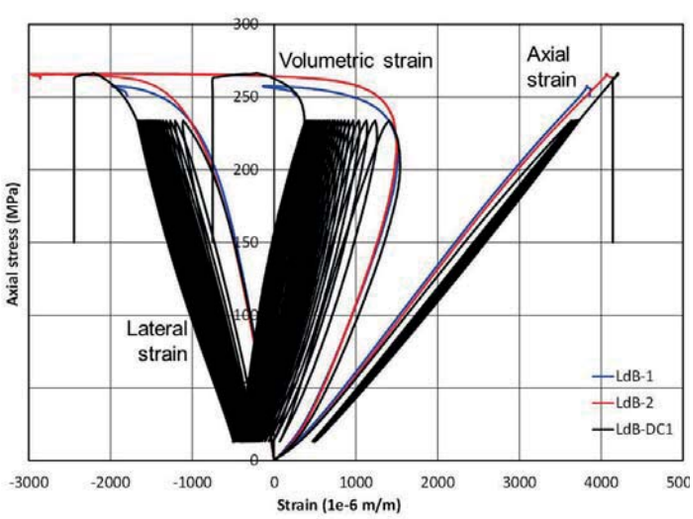

Figure 3—Comparison of the mechanical behaviour of the Lac du Bonnet granite samples tested in monotonically increasing compressional load and in cyclic damage-controlled loading conditions

For accurate estimation of crack volumetric strain, the elastic constants for each loading and unloading increment of each cycle were calculated independently over a range between 30 and 80 MPa to minimize the effect of crack closure and formation of new fractures on the calculated elastic parameters. The calculated elastic constants for sample LdB-DC1 are shown in Figure 4. The Young's modulus suddenly increases from cycle 1 to cycle 2; this could be the result of crack closure in cycle 1, which was not repeated in the following cycles since the minimum unloading stress (13 MPa) did not allow for the fractures to open as a result of relaxation. According to Eberhardt (1998), collapse of

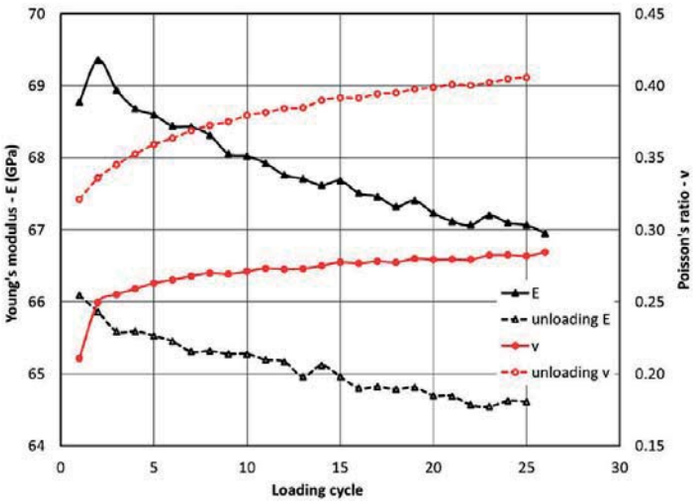

Figure 4—The elastic constants calculated for the loading and unloading increments of each loading cycle for LdB-DC1

bridging material between cracks could be a stiffening mechanism for the intact rock and another reason for the sudden increase in the Young's modulus. The major collapse of bridging material occurs in the first cycle after surpassing the CD threshold, therefore this effect cannot be observed in the unloading Young's modulus and the Young's moduli of following cycles. An abrupt increase in the Poisson's ratio is also observed between cycles 1 and 2, while the changes after cycle 2 are gradual. This sudden increase is attributed to the formation of a large population of extensile fractures in the first cycle after the axial stress in the rock passes the CI threshold. In general, a gradual reduction in the moduli of the rock as a function of accumulation of damage concurrent with gradual increase in the Poisson's ratio is observed for the Lac du Bonnet sample with increasing loading cycles.

The CI threshold, axial stress associated with the maximum crack volumetric strain, according to Martin (1993), for each cycle for the LdB-DC1 specimens is marked in Figure 5 with red circles and the CI locus is shown with the red line. It can be seen in this figure that if the crack volumetric strain is accepted as an indicator of the CI threshold, then the CI locus remains constant with each loading-unloading cycle. The same behaviour is reported by Martin (1993), who concluded that the CI threshold is independent of damage accumulated in the sample.

Investigation of the AE data collected from the damage-controlled testing of LdB-DC1 (Figure 6a) shows that the AE events at the CI threshold and between the CI and CD thresholds occur only during the first loading cycle and the AE activity of the sample at the CI threshold diminishes after the first cycle. From cycle 2 onward, the sample is acoustically active only at the CD threshold and stresses above this threshold. This is also in agreement with the findings of Eberhardt (1998), in which the so-called CI threshold estimated from the AE method in damage-controlled test for cycles 2 onward is within a very close

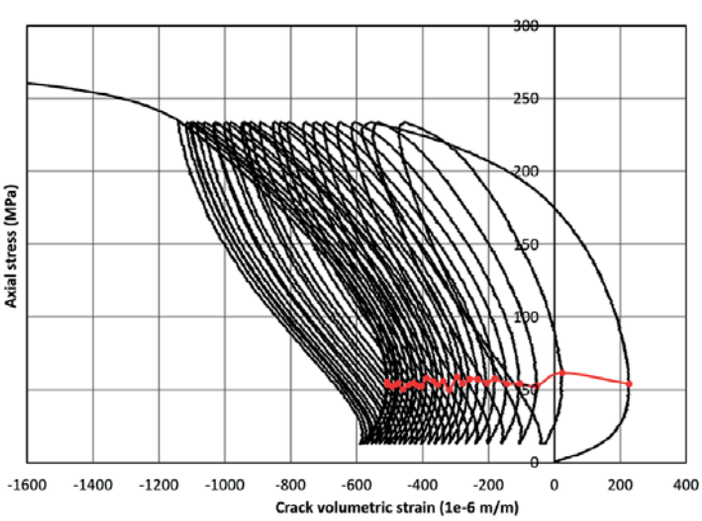

Figure 5—Crack volumetric strain for the specimen LdB-DC1; the maximum crack volumetric strains from the loading part of each cycle are connected with the red line

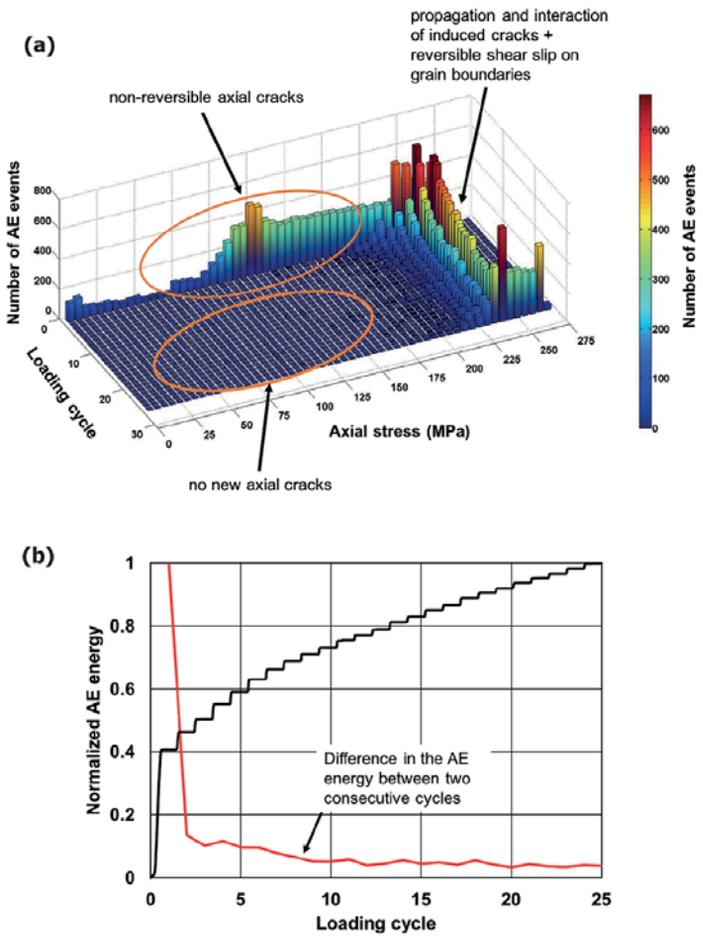

Figure 6 —AE results for LdB-DC1. (a) Histogram of AE events that occurred during each cycle, and (b) normalized cumulative AE energy that has been dissipated by the rock in each cycle of the damage-controlled test

range to the CD stress level. A look at the energy associated with the AE events for LdB-DC1 (Figure 6b), calculated according to Pollock (2012), shows that most of the energy dissipated by microfracturing during the test occurs in the first cycle. Considering that all of the AE events after cycle 1 occur at the CD threshold and higher stresses, they are mainly associated with the coalescence of the local fractures and development of existing fractures. The amount of energy that is released by the specimen after cycle 1 gradually decreases with increasing number of loading cycles. This decrease in release of energy is also observed in the form of a decline in the number of AE events as a function of loading cycles. This demonstrates that the formation and/or the extension of a microcrack network within the intact rock requires more energy (higher axial stress) for further extension and interaction of the existing microcracks.

The AE data contradicts the notion that the CI threshold, as estimated from the reversal of crack volumetric strain, is independent of the damage accumulated in the sample as suggested by Martin (1993). It can be realized from the AE data (release of the majority of the AE energy at the CI threshold in the first cycle), and also the sudden increase of the Poisson's ratio between cycles 1 and 2, that the CI threshold and the notion of crack initiation, in a given orientation, occurs only once for a rock specimen.

A study of the accumulation of shear and tensile microcracks during the first six loading cycles of specimen LdB-DC2 (Figure 7a) and the entire duration of the test (Figure 7b) reveals that the majority of the tensile events occur in the first cycle. However, the accumulation of shear-dominated events that mostly occur around the CD threshold after cycle 1 continues to evolve until complete failure. This can be attributed to the fact that the fractures forming the CI threshold are mostly tensile, while the CD threshold in rocks is controlled by the shear fractures that allow coalescence and formation of transgranular bridges. Interaction and coalescence of microfractures play a significant role in controlling the short-term strength of brittle rocks.

Numerical replication of progressive damage in the Lac du Bonnet granite

A suite of laboratory test data for the pink Lac du Bonnet granite was evaluated and discussed in the previous section. In order to further examine the conclusions based on the laboratory test data, a 3D Voronoi grain-based model (GBM) was set up to replicate the mechanical behaviour of the Lac du Bonnet granite numerically. The findings in the previous section can be summarized in two major points:

- Formation of the majority of the microcracks at the crack initiation threshold occurs the first time this limit

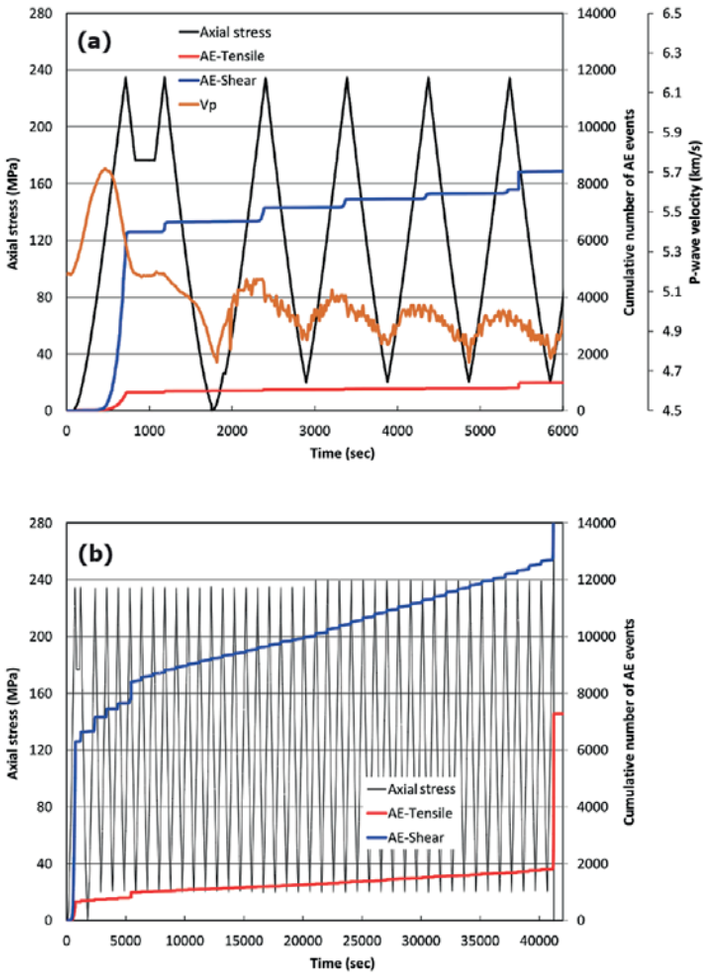

Figure 7 – (a) Accumulation of acoustically captured shear- and tensile-dominated fractures and the associated lateral P-wave velocity during the first six loading cycles for LdB-DC2, and (b) accumulation of acoustically captured shear and tensile fractures during the damage-controlled testing of LdB-DC2

is surpassed and further crossing of this limit, for instance through stress cycling, is not critical to the crack density within the rock (in other words the CI threshold for a rock only occurs once in a given orientation).

- Initiation of the dominant microcracks at the CI threshold is mostly extensile while the propagation, bridging, and coalescence of the fractures at the CD limit occur mainly in shear.

The Lac du Bonnet granite 3D GBM provides a controlled test environment that the assumptions about the mechanical behaviour of the rock can be tested against, within the limits of the model.

Specimen generation, numerical set-up, and calibrated properties

A cylindrical specimen was generated in Neper (Quey, Dawson, and Barbe, 2011; Ghazvinian, Diederichs, and Quey, 2014) with radius of 50 mm and length of 125 mm (Figure 8a). The cylindrical vessel was filled with 5000 Voronoi grains, each zoned with tetrahedral elements with an average edge length of 1 mm. The grain size was chosen to be consistent with the representative volume element (Ghazvinian, Diederichs, and Quey, 2014) to minimize its effect on the model response. The model micro-parameters were calibrated in an iterative process following the method described in Ghazvinian, Diederichs, and Quey (2014). Elastic behaviour was assumed for the grains, and failure within the model was allowed only along the grain contacts. The elastic properties of the grains were taken from Lama and Vutukuri (1978) to approximately represent the minerals composing the Lac du Bonnet granite. To have a better control on the damage thresholds, a distribution of one standard deviation was introduced for the cohesion and tensile strength at the contacts; this also required calibration according to CI and CD thresholds. This distribution was applied to the contacts randomly using a normal distribution. The calibrated micro-parameters and the corresponding model macro-response are listed in Table III. The stress-strain behaviour of the calibrated UCS model for the Lac du Bonnet granite is shown in Figure 8b.

UCS model

In the grain-based model developed for the Lac du Bonnet granite, the orientation of normal vectors to the surface of the

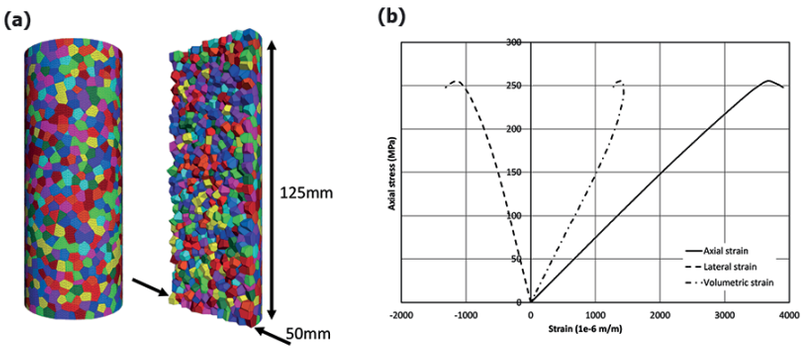

Figure 8 – (a) 3D GBM specimen, including 5000 grains, (b) stress-strain curves for the UCS model calibrated to the Lac du Bonnet granite properties

Table III

Calibrated micro-parameters for Lac du Bonnet granite and the resulting model macro-response

Model micro-parameters		Model macro-properties	
Contact normal stiffness k_n (GPa/m)	68 000	UCS (MPa)	255.5
Contact normal to shear stiffness ratio k_n/k_s	5	CI (MPa)	64
Contact peak cohesion c_p (MPa)	120 (±10)*	CD (MPa)	235
Contact residual cohesion c_r (MPa)	0	E (GPa)	74.8
Contact peak tensile strength T_p (MPa)	90 (±5)*	ν	0.25
Contact residual tensile strength T_r (MPa)	0		
Contact peak friction angle ϕ_p (°)	0		
Contact residual friction angle ϕ_r (°)	20		
Grain Young's modulus E (GPa)	150		
Grain Poisson's ratio ν	0.28		

*Values in parentheses are the one standard deviation for the contact strength components that were assigned to contacts with a uniform distribution.

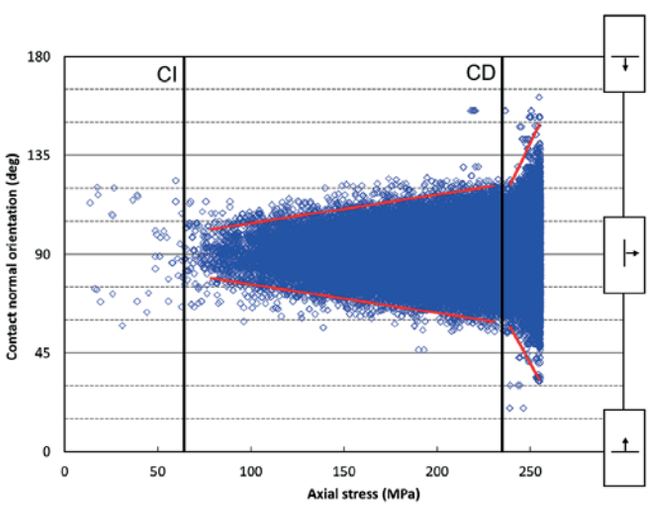

Figure 9—Orientation of normal vectors for sub-contacts failed in tension for the LdB granite UCS model

sub-contacts which failed in tension was recorded with respect to the orientation of the loading axis. Sub-contacts with surface-normal angles equal to 90° are perfectly aligned with the direction of applied load. With the change of a sub-contact normal angle from 90°, the sub-contact surface first becomes sub-parallel to the loading direction and with further changes, at extreme limits (normals equal to 0° or 180°) it becomes perpendicular to the direction of loading.

The progress of damage and the orientation of normal vectors for sub-contacts which failed in tension for the Lac du Bonnet UCS model are shown in Figure 9. The CI and CD thresholds are also overlain on this figure. It is interesting to note in this figure that the most critical cracks in the model are aligned parallel to sub-parallel to the direction of loading. The sub-contacts with normals within a range of 75° to 105° are those that fail first. The range for the normal of the less

critical sub-contacts grows to 60°–120° immediately before the onset of CD threshold. As soon as the CD threshold is crossed, the sub-contacts with normals within the range of 30°–150° become unstable and fail.

Damage-controlled models

Damage-controlled numerical simulations were performed on the Lac du Bonnet granite grain-based model through load cycling, similar to the cyclic tests performed in the laboratory. Three tests were simulated with different limits for maximum applied stress in each cycle. Model DC-140 was loaded up to 140 MPa (above CI and below CD), model DC-200 was loaded up to 200 MPa (slightly below CD), and model DC-240 was loaded up to 240 MPa (above CD) in each cycle (Figure 10).

The unloading stress limit for all the models was set to 15 MPa. Due to the existing hysteresis in the models (time-stepping is needed to notice the effect of change in applied stress in the middle of the specimen), usually a 10 MPa overshooting was observed in loading and approximately 2 MPa overshooting when switching between unloading to loading. The axial stress cycling for the models *versus* time-steps and the corresponding stress-strain behaviour are shown in Figure 10. Models DC-140 and DC-200 were cycled six times and then were loaded up to failure in cycle 7. Model DC-240 was cycled four times, and upon completion of cycle 4 (unloading) it had failed and could not be loaded up again.

Similar to the laboratory testing results, the stress cycling for models DC-140 and DC-200 had no influence on the peak strength of the models. These models failed at approximately 255 MPa in cycle 7, at a stress similar to the UCS model in the previous section. The DC-240 model that was cycled to a stress (just under 250 MPa) close to the UCS for this model (255.5 MPa) experienced a drop in the peak strength. The study of the stress-strain curves for the damage-controlled models shows that as the cycling stress limit is increased, the permanent damage that is represented in the deformational behaviour of the models (softening) is more distinct.

To further investigate the dominance of tensile fractures at the CI threshold, the progressive damage in the damage-controlled models is shown in Figure 11, presenting the orientation of normal vectors to the sub-contacts failed in tension. The ranges for normal vector orientation for the most critical sub-contacts from the UCS model (Figure 9) are shown in Figure 11 with dashed red lines. The major accumulation of failure of critical sub-contacts (normal vectors between 75° and 105°) occurs in the first cycle for all of the cyclic models. In DC-140 and DC-200, where the CD is not surpassed during stress cycling, the steeper sub-contacts (less critical) with normal vectors mainly ranging between

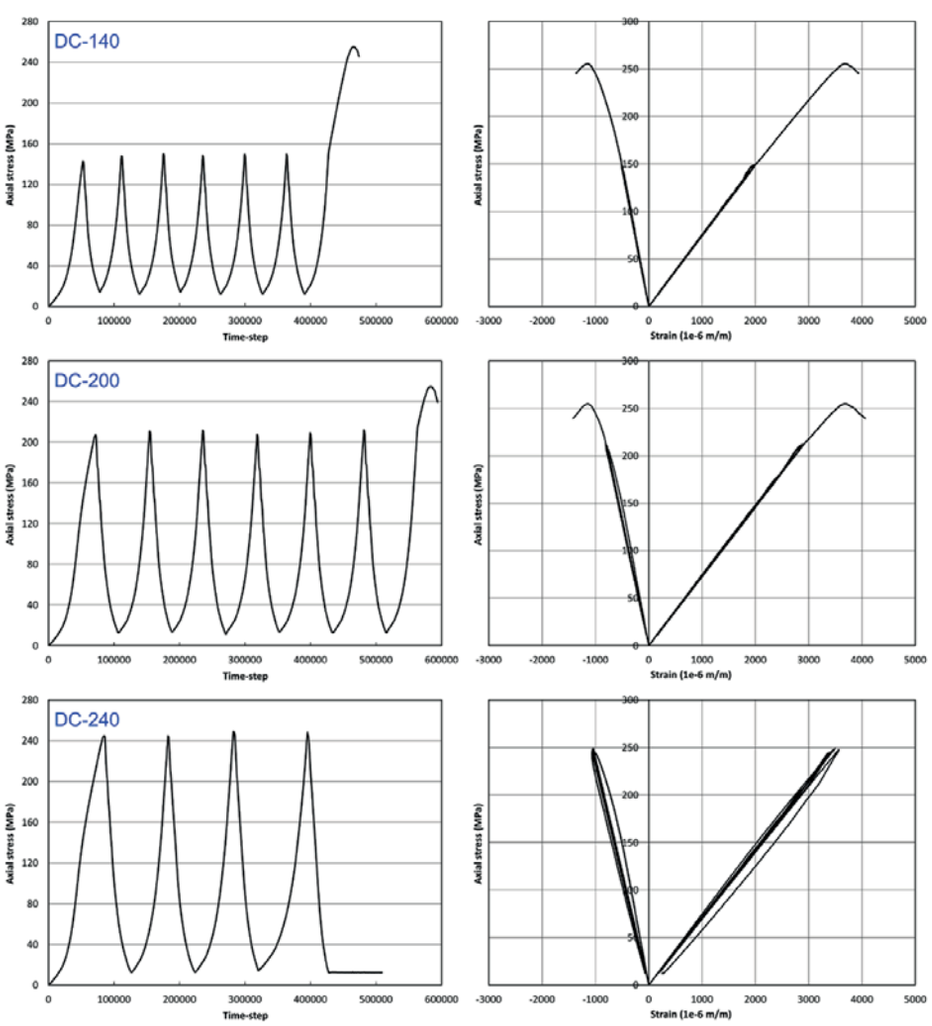

Figure 10—Axial stress *versus* time-step and the associated stress-strain behaviour for damage-controlled models DC-140, DC-200, and DC-240

15° and 165° start to fail after crossing the CD threshold limit in the last loading increment where the models are taken to complete failure. In the DC-240 model, for which the measured stress in the model goes beyond the CD threshold in the first cycle, the range for sub-contact normals that fail in each cycle grows larger with each consecutive cycle, and in the final cycle (cycle 4) sub-contacts with normal vectors as steep as approximately 0° or 180° are observed to fail. It appears from the comparison of the plots and the range of contact-normal orientations in Figure 11 that the extent of damage and the maximum stress threshold that a rock has experienced in the past play a key role in exciting isolated microcracks, or the least-critical grain boundaries, to mobilize.

Unloading damage in the form of sub-contact failure is observed to happen at the unloading increment of cycle 1 only for models DC-140 and DC-200. For DC-240, the unloading damage is observed to occur at all cycles and it becomes more severe with each loading cycle. In Figure 11, the unloading damage for DC-140 and DC-200 in cycle 1 appears to be mostly due to the failure of sub-vertical critical sub-contacts (normal vectors between 75° and 105°). However, the arched shape of each loading cycle for DC-240 in Figure 10 indicates that the unloading damage is due to failure of sub-contacts with steep normal vectors. Based on previous discussions, this could represent bridging and coalescing shear microcracks in a laboratory sample.

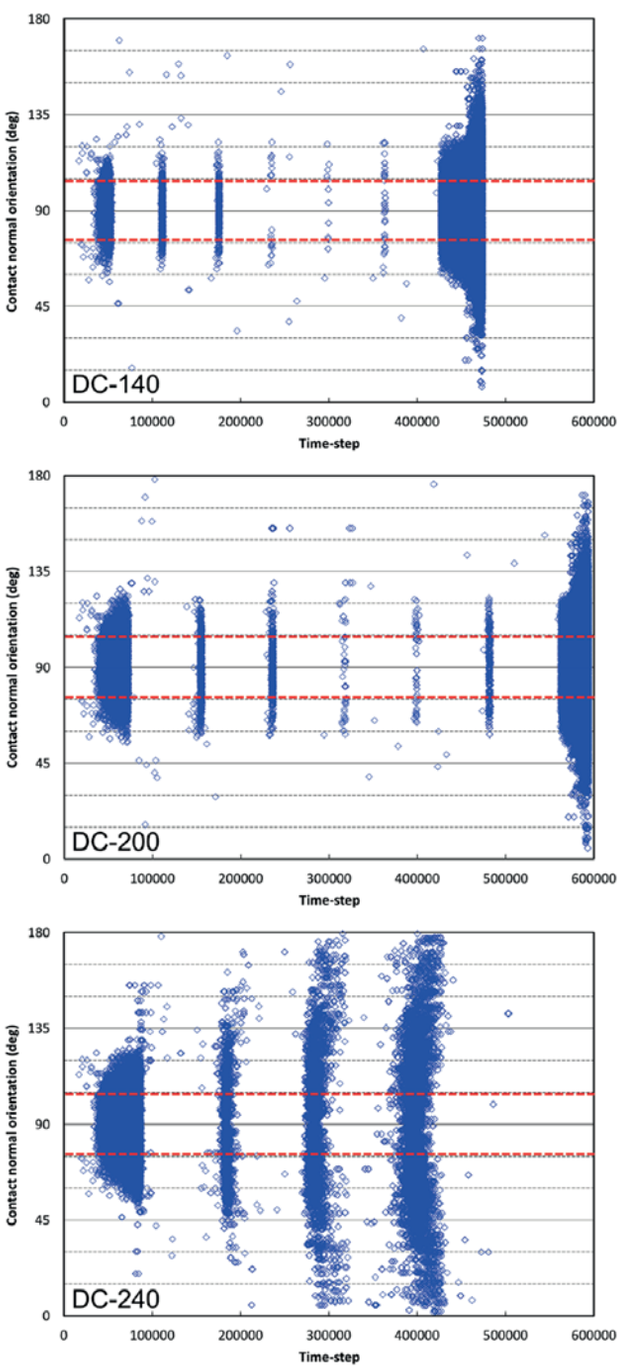

Figure 11—Orientation of normal vectors for sub-contacts failed in tension for models DC-140, DC-200, and DC-240

Conclusions

The concept of stress fatigue and its effect on crack initiation and crack propagation thresholds for brittle rocks was investigated. Accumulation of damage and subsequent degradation of strength was studied for the pink Lac du Bonnet granite from the Cold Spring Quarry in Manitoba, Canada through laboratory damage-controlled cyclic tests. The associated discontinuum simulations by means of 3D Voronoi grain-based models proved to be significantly helpful in developing a better understanding of the mechanisms of damage at CI and CD thresholds.

The peak strength of the Lac du Bonnet granite appeared to be unaffected by the stress fatigue (loaded beyond the CD threshold) within the number of cycles (maximum of 41) the samples were tested in this study. However, according to one of the damage-controlled grain-based models, if the maximum stress in each cycle is close to the UCS value, a drop in the peak strength may be observed. It should be noted that damage-controlled testing is a lengthy process, and therefore a fast loading rate is usually employed. It can be speculated that with decreasing loading rates, the mobilized microfractures will have the chance to propagate and possibly degrade the strength of the rock with increasing loading cycles.

The crack propagation threshold (CD) for the Lac du Bonnet granite appeared to gradually increase with each loading cycle when the sample is loaded beyond the CD threshold in each cycle. This behaviour was observed in both the strain (stress associated with the reversal of volumetric strain) and the AE data. The decay in the number of AE events and reduction in the dissipated AE energy with increasing loading cycles suggests a slowing in the rate of propagation of mobilized fractures and the need for higher energy in the form of increased axial stress for further propagation. This explains the increase in CD threshold with each loading cycle. The study by Eberhardt (1998), however, showed that if the cycling continues after the gradual increase in CD threshold, it would start to decline eventually.

Interesting results from the AE monitoring, which had the capability to distinguish between the shear and tensile events for a damage-controlled test on the Lac du Bonnet granite, and the numerical models proved that the crack initiation threshold (CI) for a rock occurs only once, the first time this threshold is crossed. While this can also be detected by a sudden jump in Poisson's ratio from the first cycle to the second, crack volumetric strain appeared not to be sensitive enough and accordingly estimated a similar CI for all the loading cycles of a damage-controlled test.

The AE results from the laboratory tests and damage-controlled grain-based numerical simulations indicate that the majority of the critical links within an intact brittle rock, which are commonly either perfectly aligned or are sub-parallel to the direction of major principal stress, dilate in an extensile mode when the CI threshold is reached. Therefore no other critical extensile weak links are left undilated within the intact rock to mobilize the next time this threshold is crossed within a loading-unloading condition. Conversely, the propagation, coalescence, and bridging of existing fractures that define the CD threshold and commonly have a shear mechanism, continue to grow and involve microfracture paths with steeper orientations with respect to the orientation of major principal stress with each cycle.

Acknowledgements

The authors would like to acknowledge the Nuclear Waste Management Organization of Canada (NWMO) and the National Science and Engineering Research Council of Canada (NSERC) for supporting this research. Special thanks to Denis Labrie from CanmetMINING, Natural Resources Canada, as well as Tobias Backers and Tobias Meier of geomecon GmbH for providing access to high-quality laboratory testing and insightful discussions.

References

Diederichs, M.S. 2000. Instability of hard rock masses: the role of tensile damage and relaxation. PhD thesis, University of Waterloo, Waterloo, Ontario.

Duevel, B. and Haimson, B. 1997. Mechanical characterization of pink Lac du Bonnet Granite: Evidence of nonlinearity and anisotropy. *International Journal of Rock Mechanics and Mining Sciences and Geomechanics Abstracts*, vol. 34, no. 3-4. Paper no. 117.

Eberhardt, E. 1998. Brittle rock fracture and progressive damage in uniaxial compression. PhD thesis, Department of Geological Sciences, University of Saskatchewan, Saskatoon. 334 pp.

Ghazvinian, E. Diederichs, M.S., and Martin, C.D. 2012. Identification of crack damage thresholds in crystalline rock. *Proceedings of Eurock 2012*, Stockholm, Sweden. International Society for Rock Mechanics, Lisbon, Portugal.

Ghazvinian, E. Diederichs, M.S., and Quey, R. 2014. 3D random Voronoi grain-based models for simulation of brittle rock damage and fabric-guided micro-fracturing. *Journal of Rock Mechanics and Geotechnical Engineering*, vol. 6, no. 6. pp. 506–521.

Gorski, B. and Yu, Y.S. 1991. Tensile strength tests on URL rock samples from Borehole 401-009-HF1. *CANMET report* MRL 91-080(TR). Natural Resources Canada.

Hommand-Etienne, F. Hoxha, D. and Shao, J.F. 1998. A continuum damage constitutive law for brittle rocks. *Computers and Geotechnics,* vol. 22, no. 2. pp. 135–151.

Hommand, F. Hoxha, D. Shao, J.F. Sibai, M., and Duveau, G. 1995. Endommagement de granites et de marnes: Essais mechaniques, identification des parameters d'un modele d'endommagement et simulation. *Final Report* B RP O.ENG/O.LML 95.015. ENGS Laboratoire de Géomécanique, Nancy, France.

Kelly, D. Peck, D.C., and James, R.S. 1993. Petrography of granitic samples form the 420m Level of the Underground Research Laboratory, Pinawa, Manitoba. Contractor's report to AECL Research. Laurentian University, Sudbury, Ontario.

Lajtai, E.Z. 1988. The deformation, fracture and strength of Lac du Bonnet granite. *Research Report* 19. Geological Engineering Deptartment, University of Manitoba, Winnipeg, MB.

Martin, C.D. 1993. The strength of massive Lac du Bonnet granite around underground openings. PhD thesis, Department of Civil and Geological Engineering, University of Manitoba, Winnipeg, MB.

Martin, C.D. and Chandler, N.A. 1994. The progressive fracture of Lac du Bonnet granite. *International Journal of Rock Mechanics and Mining Sciences and Geomechanics Abstracts*, vol. 31, no. 6. pp. 643–659.

Martin, C.D. and Stimpson, B. 1994. The effect of sample disturbance on laboratory properties of Lac du Bonnet granite. *Canadian Geotechnical Journal,* vol. 31, no. 5. pp. 692–702.

Pollock, A.A. 2012. AE signal features: energy, signal strength, absolute energy and RMS. acoustic emission tech notes. *Technical report* TN-103-22-9/11. Mistras Group Inc., Princeton Junction, NJ

Quey, R. Dawson, P.R., and Barbe, F. 2011. Large-scale 3D random polycrystals for the finite element method: generation, meshing and remeshing. *Computer Methods in Applied Mechanics and Engineering*, vol. 200, no. 17. pp. 1729–1745.

Read, R.S. 1994. Interpreting excavation induced displacements around a tunnel in highly stressed granite. PhD thesis, University of Manitoba, Winnipeg, MB.

Wilkins, B.J.S. 1980. Slow crack growth and delayed failure of granite. *International Journal of Rock Mechanics and Mining Sciences and Geomechanics Abstracts*, vol. 17. pp. 365–369. ◆

http://dx.doi.org/10.17159/2411-9717/2018/v118n3a5

Reassessing continuous stope closure data using a limit equilibrium displacement discontinuity model

by D.F. Malan and J.A.L. Napier

Synopsis

Time-dependent closure data in deep hard-rock mines appears to be a useful diagnostic measure of rock behaviour. Understanding this behaviour may lead to enhanced design criteria and modelling tools. This paper investigates the use of a time-dependent limit equilibrium model to simulate historical closure profiles collected in the South African mining industry. Earlier work indicated that a viscoelastic model is not suitable for replicating the spatial behaviour of the closure recorded underground. The time-dependent limit equilibrium model available in the TEXAN code appears to be a useful alternative as it can explicitly simulate the on-reef time-dependent failure of the reef. A key finding in this paper is that the model gives a much better qualitative agreement with the underground measurements. For both the model and actual data, the rate of time-dependent closure decreases into the back area. Calibration of the constitutive model nevertheless led to some unexpected difficulties, and element size plays a significant role. It was also noted that the simulated closure is complex as it reflects the combined result of a number of elements failing at different times. The closure rate does not decay according to a simple exponential model. Explicit simulation of the fracture zone in the face appears to be a better approach to simulating the time-dependent behaviour in deep hard-rock stopes. The calibration of the limit equilibrium model is very difficult, however, and further work is required.

Keywords

stope closure, time-dependent deformation, limit equilibrium model, TEXAN code.

Introduction

Several research studies have been conducted to investigate the use of continuous stope closure as a diagnostic measure of rock mass behaviour in deep gold mines of South Africa (*e.g.* Malan, 1995; Napier and Malan, 1997). The rock mass undergoes significant time-dependent deformation in some geotechnical areas and the closure data is useful for identifying different geotechnical areas and areas prone to face-bursting (Malan *et al.* 2007). The value of continuous closure measurements was also demonstrated for the platinum industry. An example is shown in Figure 1 to illustrate the significant 'creep' component recorded in some of the areas. For the gold mines, it was proposed that the data may be useful to identify remnants that can be safely extracted. A difficulty faced in these early studies was that no numerical tool could simulate the time-dependent rock mass behaviour on a stope-wide scale. It was hypothesised that the time-dependent behaviour in the hard-rock gold mines is caused by time-dependent fracturing and other inelastic processes, such as gradual slip on parting planes. In the platinum mines, the face fracturing is less intense and the behaviour is most likely dominated by the time-dependent failure of the crush pillars. The commonly used elastic modelling programs cannot simulate this behaviour and the simulated convergence is simply a function of the mine geometry, depth, and elastic constants. The analytical viscoelastic models that were derived for the previous studies could not be used for complex geometries and the elasto-viscoplastic finite difference models were limited to 2D and to a small number of mining steps (Malan, 1999). Recent studies have indicated that a limit equilibrium displacement discontinuity model with a time-dependent failure criterion may be useful for simulating on-reef time-dependent failure processes on a mine-wide scale (Napier and Malan, 2012, 2014). This paper explores the use of this model in the TEXAN code to simulate the historical time-dependent closure measurements.

Case study of measurements in a deep Venterdorp Contact Reef (VCR) stope

In 1997, the authors were involved with measurements conducted in the W3 updip panel in the 87/49 longwall at a mine in the Carletonville area. These particular measurements were valuable as they indicated that care should be exercised when using a

* *Department of Mining Engineering, Faculty of Engineering, Built Environment & IT, University of Pretoria, South Africa.*

 This paper was first presented at the AfriRock 2017 International Symposium, *30 September –6 October 2017, Cape Town Convention Centre, Cape Town.*

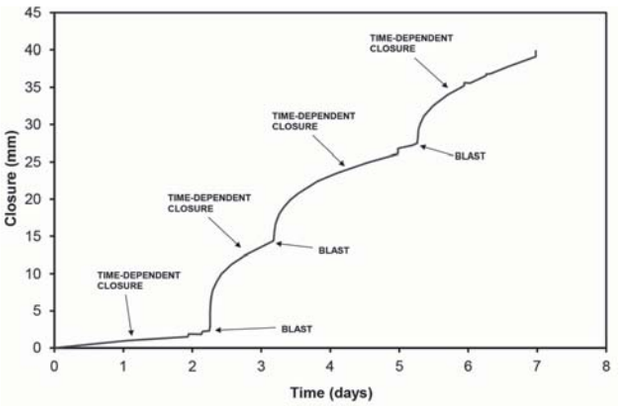

Figure 1—Typical closure data recorded in deep gold mines and some of the deeper platinum mines. This particular data-set was recorded in a Merensky Reef stope (after Malan *et al.*, 2007). Similar examples for the gold mines can be found in the references cited above

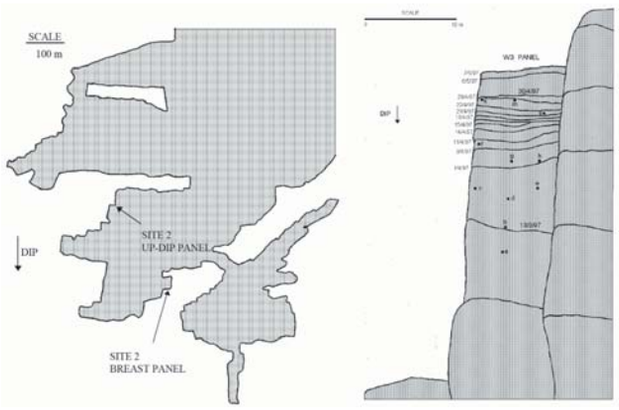

Figure 2—Layout of the VCR stope (left) where the closure data was collected. An enlarged view of the updip panel is given on the right (after Malan, 1999)

viscoelastic model when simulating the time-dependent closure. The layout of the area is shown in Figure 2. Five closure instruments were installed simultaneously in different positions to investigate the effect of measurement position on the rate of time-dependent closure.

Figure 3 illustrates the increase in closure after a blast on a specific day. All three measurements in the graph apply to the same blast, so the differences are only a function of the measurement position. This data illustrates the decrease in rate of time-dependent closure as the distance to the face increases.

A further important characteristic of the data is that the rate of time-dependent closure appears to be constant in the short term, but it gradually decreases when there is no blasting or seismic activity. This is illustrated in Figure 4. This particular data-set was obtained for the site in Figure 2 during a period when there was no mining activity for several days. The time-dependent closure can be approximated by an exponential decay function of the form:

$$\Delta S_{SS} = a(1 - e^{-bt}) \qquad [1]$$

where a and b are parameters and t is time. The time-dependent closure for station no. 2 in Figure 4 after the seismic event was plotted in Figure 5 together with the model given in Equation [1]. The parameters used to obtain this fit were a = 3.85 mm and b = 0.015 h^{-1}.

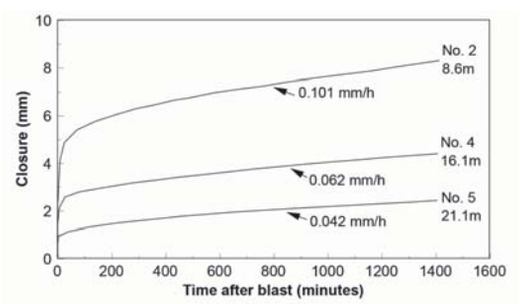

Figure 3—Closure as a function of time after blasting for different distances to the face. The distance below each instrument number is the distance to the face before the blast (after Malan, 1999)

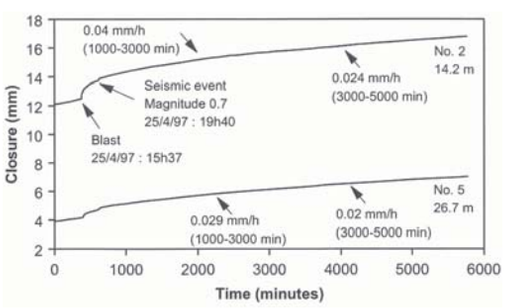

Figure 4—Closure recorded in a VCR (hard lava) panel when there was no mining activity for four days. The time periods in brackets indicate the intervals used to calculate the time-dependent closure rates. Two closure instruments at different distances to the face were used to collect the data (after Malan, 2003)

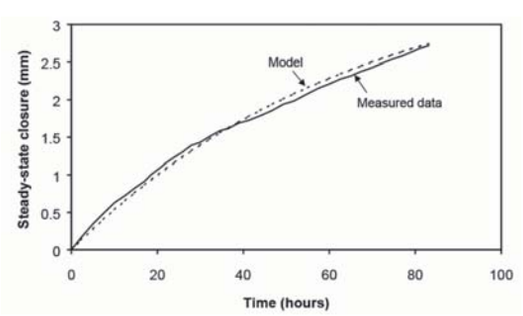

Figure 5—Measured and simulated values of time-dependent closure for the data in Figure 4 (after Malan, 2003)

The problem with viscoelastic theory

To simulate the time-dependent deformations recorded in tabular excavations, a viscoelastic approach was investigated (Malan, 1999). A two-dimensional closure solution for a parallel-sided tabular excavation in a viscoelastic medium was derived for this study. In linear viscoelastic theory, complex strain-time behaviour can be described by various combinations of two principal states of deformation: elastic behaviour and viscous behaviour. The historical use of different viscoelastic models to simulate the creep of rocks is given in many papers (*e.g.* Ryder and Jager, 2002). Malan (1999) assumed a Burgers model to describe the time-dependent behaviour shown in Figure 1. This model is shown in Figure 6. The complete viscoelastic closure solution when assuming this model is given in Malan *et al.* (2007).

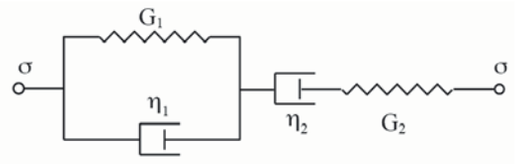

Figure 6—Representation of the Burgers viscoelastic model with the viscosity coefficients η_1 and η_2 and shear moduli G_1 and G_2

Using this approach, a good fit with data over a short period of time (*e.g.* 1 day) could be obtained. Problems were nevertheless encountered when attempting to calibrate the model at various distances from the mining face (*e.g.* Figure 3). These problems arise as the viscoelastic model predicts that the rate of time-dependent convergence increases towards the centre of the stope. This can be shown by taking the time derivative of the viscoelastic closure solution. For time $t\rightarrow\infty$, the rate of convergence is given by (see Malan, 1999):

$$\left.\frac{dS_z}{dt}\right|_{t\rightarrow\infty} = \frac{-2W_z\sqrt{\ell^2 - x^2}\left(1+\frac{dx}{2}\right)}{\eta_2} \quad [2]$$

where

$$W_z = \frac{-\rho g h}{2}[(1+k)+(1-k)\cos 2\alpha] \quad [3]$$

$$d = \frac{\sin\alpha\cos\beta}{h} \quad [4]$$

and S_z is the stope closure, 2ℓ is the span of the stope, ρ is the density of the rock, x is the position in the stope relative to the centre, g is the gravitational acceleration, h is the depth below surface, k is the ratio of horizontal to vertical stress, α is the dip of the reef, β is the angle between the x-axis and the dip, and t is time. The Burgers viscosity coefficient η_2 is defined in Figure 6. As $t\rightarrow\infty$, the rate of convergence is therefore only a function of geometric parameters, stress magnitude, and the viscoelastic parameter η_2. This is intuitively expected from Figure 6.

The rate of time-dependent convergence (Equation [2]) is plotted as a function of the position x in Figure 7. The rate of convergence is highest in the centre of the stope, and reduces to a value of zero at the stope face. This can be compared to the data collected in the mining stope (Figure 3), illustrating the opposite trend, where the rate of time-dependent closure decreases with increasing distance from the stope face. Additional data from the experimental site is given in Figure 8.

A further problem with the Burgers model is that it predicts that the rate of time-dependent closure remains constant. For $t\rightarrow\infty$, Equation [2] does not tend to zero, but indicates a constant rate of convergence. In contrast, Equation [1] can be differentiated to give the rate of time-dependent convergence for the actual data as:

$$\frac{dS_{SS}}{dt} = (ab)e^{-bt} \quad [5]$$

Equation [5] indicates that the rate of time-dependent closure tends to zero as $t\rightarrow\infty$.

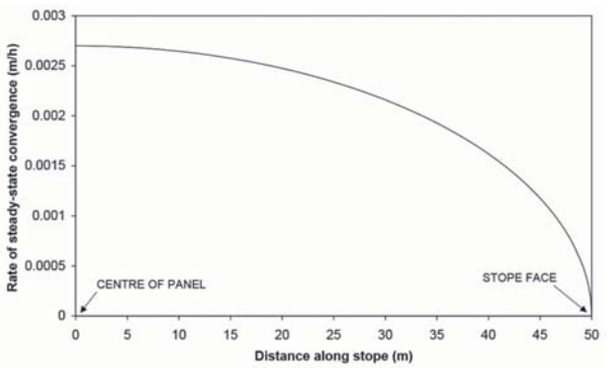

Figure 7—The rate of time-dependent convergence along a panel of 100 m span at $t\rightarrow\infty$. Values used in this simulation are $\eta_2 = 2\times10^{12}$ Pa.h, H = 2000 m, α = 0°, k = 0.5, g = 9.81 m/s², and ρ = 2700 kg/m³

Figure 8—Additional closure data from the stope in Figure 2 (after Malan, 2003). In contrast to Figure 7, the rate of time-dependent closure decreases as the distance to the face increases. Note that the stope face is to the left in Figure 8 and to the right in Figure 7

A proposed time-dependent limit equilibrium model

As an alternative to the viscoelastic model, a time-dependent limit equilibrium model built into the displacement discontinuity code TEXAN was used to investigate the closure behaviour described above. A description of the TEXAN code and the limit equilibrium model is given by Napier and Malan (2012, 2014). Following this approach, the fracture zone surrounding the excavations is simplified as the model restricts failure to the on-reef plane. A key feature of the model is that the intact rock strength is differentiated from the residual strength according to specified intact and residual failure strength envelopes. The strength of the intact seam or reef material ahead of the stope face is assumed to be defined by a linear relationship of the form

$$\sigma_n = \sigma_c^i + m_i\sigma_s, \quad [6]$$

where σ_c^i and m_i are the intercept and slope parameters respectively, σ_s is the average seam-parallel confining stress, and σ_n is the seam-normal stress component. Once a point in the seam fails, the strength parameters are postulated to decrease immediately to values σ_c^0 and m_0, which define an initial limit stress state in which there is a fixed limit equilibrium relationship between σ_n and σ_s of the form

$$\sigma_n = \sigma_c^0 + m_0\sigma_s \quad [7]$$

The limit strength parameters are then assumed to decay towards residual values σ_c^f and m_f. The strength values $\sigma_c(t)$ and $m(t)$ at an elapsed time t after failure, are defined according to the relationships:

$$\sigma_c(t) = \left(\frac{1}{2}\right)^{\frac{t}{\lambda}} \left[\sigma_c^0 - \sigma_c^f\right] + \sigma_c^f \quad [8]$$

$$m(t) = \left(\frac{1}{2}\right)^{\frac{t}{\lambda}} \left[m_0 - m_f\right] + m_f \quad [9]$$

where λ is a half-life parameter. The limit stress components σ_n and σ_s at a given seam or reef position and time t are then given by an appropriate equation of similar form to Equation [6]:

$$\sigma_n = \sigma_c(t) + m(t)\sigma_s \quad [10]$$

The reef-parallel (or seam-parallel) stress is determined by setting up an averaged force balance at each point in the fracture zone, which depends on the effective fracture zone height H and on the contact friction coefficient μ_L between the broken material and the intact rock enclosing the fracture zone (Napier, 2016). It is apparent that the distribution of the limit stress values will in general depend on the distribution of failure times at all points in the fractured material, and consequently depends in a complex evolutionary manner on the planned mining sequence and extraction rate. A given mining problem must therefore be solved in a series of time-steps which include mining increments that are scheduled at appropriate time-step intervals. The problem time-scale will be determined essentially by the chosen half-life parameter, λ. A novel solution algorithm has been developed to calculate the distribution of stress components σ_n and σ_s, as well as the overall extent of the fracture zone arising in each simulated time step. A detailed description of this procedure is given by Napier (2016).

Simulation of time-dependent closure

The simplified geometry shown in Figure 9 is used to illustrate the characteristics of the time-dependent limit equilibrium model. This is a stope of size 100 m × 50 m situated at a depth of 2000 m. The stope is surrounded by a region of elements which assume the constitutive behaviour described by Equation [8] to [10] once failure is initiated. Closure profiles were recorded at points A, B, and C. These measurement positions varied slightly depending on the element sizes used, but for 1 m elements, the distances to the excavation face were A = 0.5 m, B = 4.5 m, and C = 24.5 m. The model parameters are given in Table I. These parameter values are assumed and need to be calibrated in future.

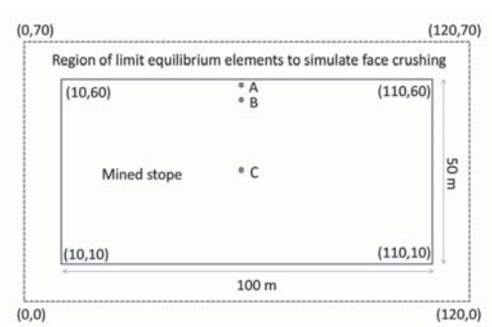

Figure 9—Geometry simulated

The first simulation attempted to replicate the underground closure behaviour shown in Figure 3. The simulated results are shown in Figure 10 and the time-dependent nature of the closure is clearly visible. Note that the rate of time-dependent closure decreases into the back area of the stope, similar to the underground observations. This model is therefore clearly an improvement on a simple viscoelastic approach, which could not replicate this behaviour. Figure 11 illustrates the failed limit equilibrium elements (red) and the intact elements (green).

Table I

Parameters used for the initial simulations

Parameter	Value
Depth	2000 m
Mining height	3 m
Young's modulus	70 GPa
Poisson's ratio	0.2
Intact seam strength	40 MPa
Intact seam slope parameter	7
Initial crush strength	40 MPa
Initial crush slope parameter	4
Residual strength	1
Residual slope parameter	2
Interface friction angle	20°
Seam stiffness modulus	80000 MPa/m
Half-life	20 h

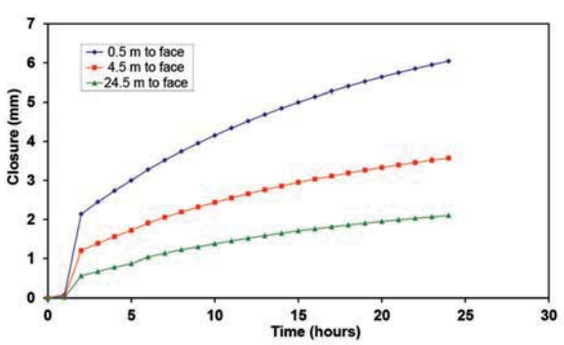

Figure 10—Simulated time-dependent closure at various distances to face. This shows only the time-dependent closure and not the initial elastic convergence. The jump in closure at t = 1 hour is discussed in the section below

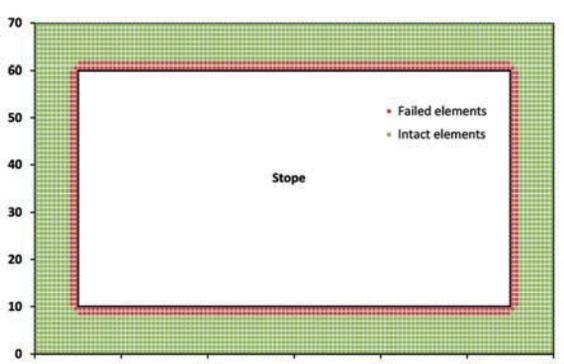

Figure 11—Failed elements (red) at the edge of the stope for the simulation in Figure 10 at t = 24 hours. The intact elements are shown in green

Effect of grid size

Although the results in Figure 10 look encouraging, it was noted during further simulations that the grid size and sequential failure of the elements affect the simulated closure profiles. An example is illustrated in Figure 12. The parameters for these simulations were identical to those in Table I, except for the red closure profile where it was specified that the initial crush slope parameter was 7 (similar to the intact slope parameter). Note the jumps in closure. The mining geometry remains constant during these jumps, which are caused by the sequential failure of the next row of limit equilibrium elements. As the grid consists of square elements and the geometry is regular, the failure of the elements occurs row by row in an organized pattern. A particular row is activated and a jump in closure occurs as the stress is transferred to the solid ground according to the model in Equations [8] and [9]. The next row eventually fails and the process repeats. Figure 13 illustrates the extent of the failed zone after 168 hours. The number of rows of elements activated corresponds to the number of jumps in closure visible in Figure 12. The first part of Figure 12 is enlarged in Figure 10, and this explains the anomaly at the beginning of the curve in Figure 10. A possible solution would be to reduce the element size as shown in Figure 14. For smaller elements, the jumps in closure are more frequent, but smaller in magnitude. This improves further if the intact strength and initial crush strength are identical (not shown here).

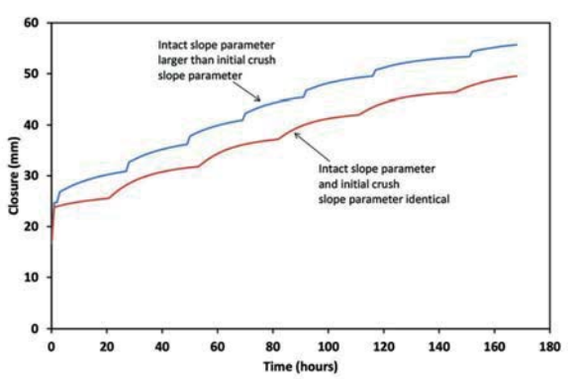

Figure 12—Incremental activation of the elements leads to the closure profiles shown in the figure. No change in mining geometry occurred during these simulations. This was recorded at position A, which is 0.5 m from the face (Figure 9)

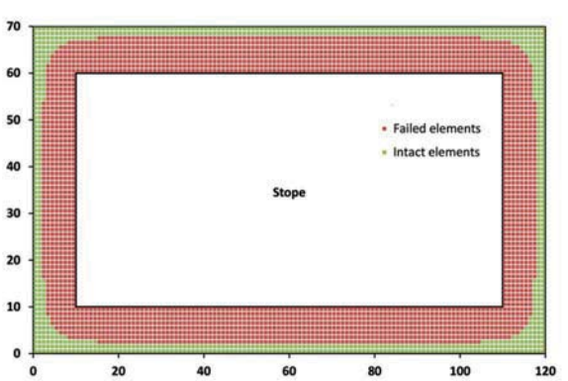

Figure 13—Failed elements at the edge of the stope for the simulation in Figure 12 at t = 168 hours. This can be compared to Figure 11 to illustrate the time-dependent growth in the fracture zone

Partial element fracturing

Figure 15 depicts a conceptual view of the stress profile transition between the edge of the fractured rock at position L and the adjacent intact material. (Figure 15 may be considered to represent a local section profile that is aligned in the normal direction to the fracture zone edge.) The basic solution algorithm (Napier 2016) that has been developed to infer the transition from an intact state to a failed state is accurate only to the resolution of the element grid size, g. A revised scheme has been developed more recently to predict the intermediate position L of the fracture front between successive collocation points, as shown in Figure 15. Once the front position L has been estimated, a fractional sub-element with an appropriate shape, centre position, and self-effect coefficient is constructed within the partially fractured element to determine the effective displacement discontinuity strain and reef-normal stress in the element. A current restriction on the new algorithm is that the controlling rock strength parameter ratios must be such that

$$\sigma_c^i/m_i = \sigma_c^0/m_0 = \sigma_c^f/m_f$$

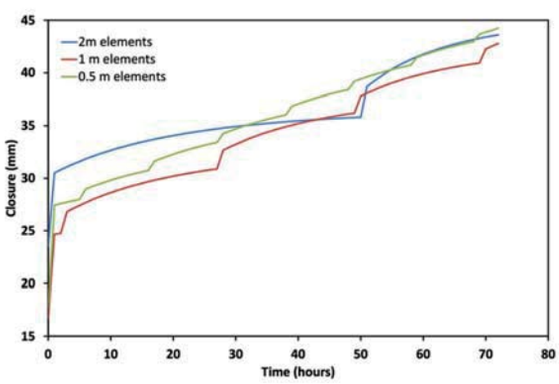

Figure 14—Effect of element size on closure profiles. No changes in geometry occurred during these simulations. The parameters for all three simulations were identical to those in Table I. It should be noted that these profiles were recorded at slightly different positions with respect to face owing to the different element sizes. These were 0.5 m elements - 0.75 m to the face, 1 m elements - 0.5 m to the face, and 2 m elements - 1 m to the face

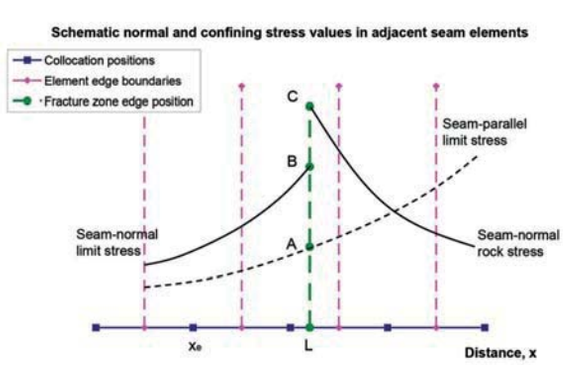

Figure 15—Schematic stress profiles adjacent to the edge of the fracture zone. The seam-parallel limit stress is reset at all crush element collocation points at the start of each time-step

Figure 16 shows a comparison between the proposed partial element fracturing scheme and the existing algorithm for the rectangular excavation layout shown in Figure 9. The incremental closure profiles are measured at point A in Figure 9. It is apparent that the partial fracturing algorithm allows the fracture zone to extend in more continuous steps than in the base case, where an abrupt failure transition occurs after time step 42 (see the bottom curve in Figure 16). It is also observed that the fracture zone extent increases over a greater distance in the case where partial element fracturing is included.

The upper curve in Figure 16 shows the incremental closure profile that would arise in the case of a plane strain parallel-sided excavation with a nominal span of 50.0 m and with a very fine element mesh size g of approximately 0.0909 m. This case was evaluated to determine approximately the asymptotic effect of reducing the element grid size. It should be noted that the effective layout depth in the plane strain case was reduced from 2000 m to 1760 m (a factor of approximately 0.88) to compensate for the infinite lateral span of the parallel-sided panel, compared to the 100.0 m lateral span in the rectangular excavation (see Figure 9). Figure 16 shows that the fine grid behaviour is approximately replicated by the partial element fracturing algorithm, but that the underlying fracture front transitions are still somewhat dependent on the element mesh size.

Figure 17 shows the incremental closure profiles that are obtained for the rectangular excavation shown in Figure 9 following a mining step of 1.0 m at the upper face after time-step 72. The profiles are monitored at points A, B, and C shown in Figure 9. Figure 17 illustrates the progressive decrease in the incremental rate of closure as the distance from the mining face is increased. The strength parameters used in the partial element fracturing results in Figure 16 and Figure 17 are as follows:

$$\sigma_c^i = 70\text{MPa}; m_i = 7.0; \sigma_c^0 = 40\text{MPa}; m_0 = 4.0;$$
$$\sigma_c^f = 10\text{MPa}; m_f = 1.0; \lambda = 20.0$$

The remaining parameters are as summarized in Table I.

Calibration of the half-life parameter

The rate of change for the underground closure data shown in Figure 4 is approximated by the exponential decay model in Equation [5]. For the numerical model, the decay of the strength of the failed limit equilibrium elements gives rise to the stress transfer and the simulated time-dependent closure. It is therefore postulated that the actual underground closure data can be used to calibrate the half-life parameter of the numerical model. If Equation [8] is differentiated, the rate of strength decrease for a failed limit equilibrium element is:

$$\frac{d\sigma_c(t)}{dt} = k\left(\frac{1}{2}\right)^{\frac{t}{\lambda}} \quad [10]$$

where

$$k = -\frac{[\sigma_c^0 - \sigma_c^f]\ln(2)}{\lambda} \quad [11]$$

It is known that $\left(\frac{1}{2}\right)^{\frac{t}{\lambda}}$ and e^{-bt} (see Equation [5]) are equivalent formulae to describe exponential decay, and it can be shown that:

$$\lambda = \frac{\ln(2)}{b} \quad [12]$$

For Figure 5, it was found that b = 0.015 h^{-1} gives a good fit to the data, and from Equation [12] it follows that λ = 46.2 hours. Time-dependent closure data from the platinum mines fitted with the model described in Equation [1] is also given in Roberts *et al.* (2006). Table II illustrates the data currently available for which the b parameter was calculated and the corresponding value of λ is given.

Care should be exercised for the two sites in Table II with calibrated λ values greater than a hundred. The hangingwall at these two sites was unravelling. This caused the large ongoing time-dependent closure. In contrast, the failure processes and stress transfer ahead of the face or in pillars dominated at the other two sites. As the current implementation of the model in TEXAN makes provision for both the seam strength and seam slope parameter to undergo exponential decay, care should be exercised when calibrating the model using the λ values in Table II. To illustrate this, a model similar to Figure 9 with element sizes of 2 m and just one row of limit equilibrium models at the edge of the stope

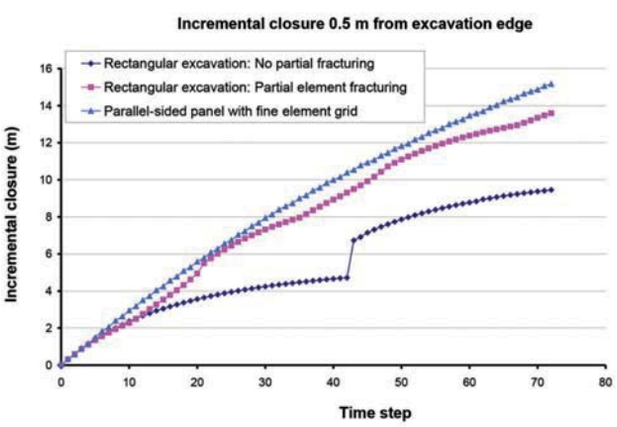

Figure 16—Comparison of incremental closure profiles measured 0.5 m from the stope face at point A in Figure 9, illustrating the behaviour of the partial element fracturing algorithm. These are compared to the results obtained in plane strain for a parallel-sided panel

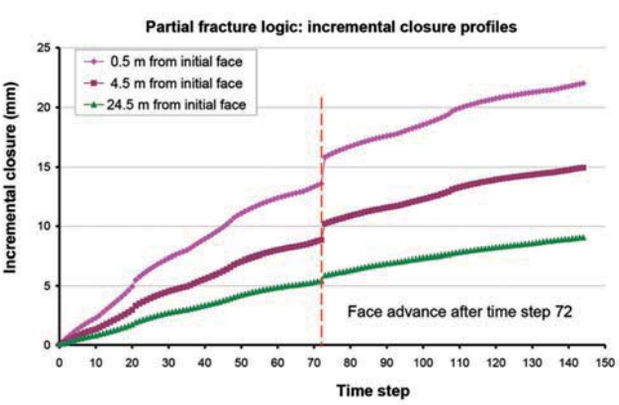

Figure 17—Comparison of incremental closure profiles at points A, B, and C in Figure 9 for the partial element fracturing algorithm. The upper face of the excavation shown in Figure 9 is advance by one metre after time-step 72

Table II

Calibrated values of *b* and *λ* for different mining areas. The platinum mine data was obtained from the SIMRAC SIM040207 report (Roberts *et al.*, 2006)

Site	*b*	*λ*	Qualitative description of conditions
Frank II 30 East Panel 42	0.012	57.8	Stable hangingwall. Good conditions in panel
Impala 10 Shaft Panel 1874a-5N	0.006	115.5	Large collapses in adjacent panels. Open joints in hangingwall. Panel stopped.
Union Spud Shaft 26/27 Panel 2N	0.0036	192.5	Blocky hangingwall conditions with the possible risk of large collapses. Panel stopped.
VCR gold mine 87/49 W3 (Figure 2)	0.015	46.2	Stable hangingwall. Hangingwall discontinuties tightly clamped due to dilation ahead of face.

was used. The resulting time-dependent closure curve is shown in Figure 18. The parameters were similar to those in Table I, with minor changes as indicated in the figure caption. Note that a single row of elements that fail simultaneously where only the seam parameter (and not the slope parameter) is allowed to decay, also results in a simple exponential decay for the closure. In contrast, if both parameters are allowed to decay using the same half-life value, more complex behaviour is the result and the fit of the simulated closure with Equation [1] is not good.

To complicate matters, the sequential activation of a larger number of limit equilibrium elements at different times leads to a simulated closure profile that differs from the simple exponential decay model. To illustrate this, the model in Figure 9 was simulated with 0.5 m element sizes. The parameter values in Table I were assumed, except that all three slope parameters were assigned a value of 4. The time-dependent closure between t = 1 h and t = 168 h is plotted in Figure 19. The numerical model assumed a half-life of 20 h. The exponential decay model with the equivalent b-value gives a very poor fit. It appears that the sequential activation of the elements (Figure 20) results in a closure profile that cannot be simulated with a simple exponential model.

Conclusions

Time-dependent closure data in deep hard-rock mines appears to be a useful diagnostic measure of rock behaviour.

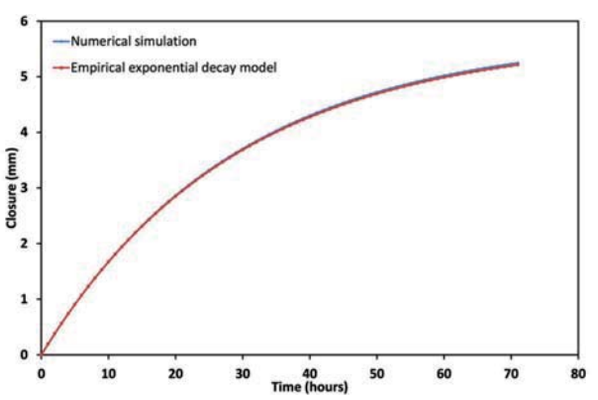

Figure 18—A good comparison between the numerical simulation and the closure exponential decay model can be obtained if only the seam strength parameter is allowed to decay (and not the slope parameter). The model parameters are identical to those in Table I, except that all three slope parameters were assigned a value of 4. The *b*-value (0.0347) for the exponential model was calculated using Equation [12]. For this simulation, only a single row of limit equilibrium elements was allowed to fail at the edge of the stope

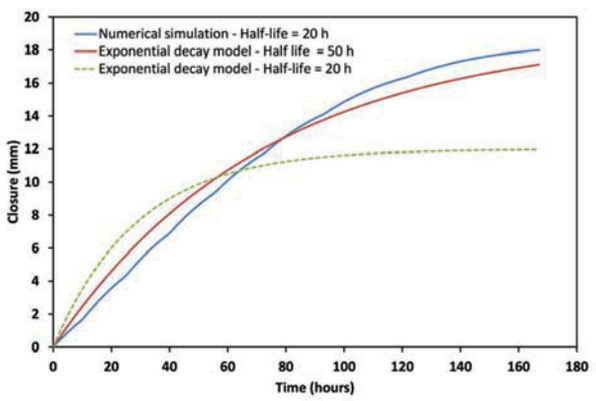

Figure 19—Comparison between the numerical simulation and the exponential decay model with two different values of half-life

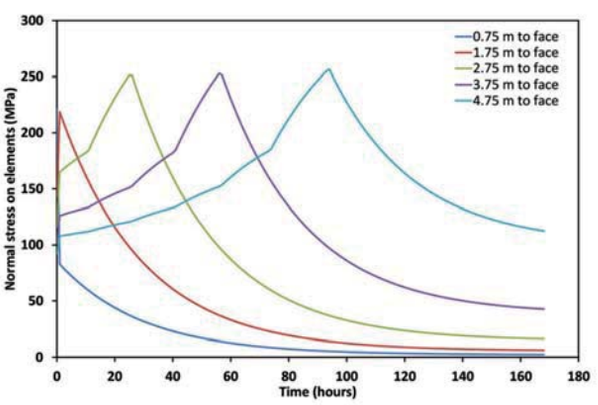

Figure 20—Sequential loading and failure of limit equilibrium models ahead of the face with time. Note the exponential decay in stress for each element after failure

Understanding this behaviour may lead to enhanced design criteria and modelling tools. This paper investigates the use of a time-dependent limit equilibrium model to simulate historical closure profiles collected in the South African mining industry. Earlier work indicated that a viscoelastic model is not suitable for replicating the spatial behaviour of the closure recorded underground. The time-dependent limit equilibrium model available in the TEXAN code appears to be a useful alternative, as it can explicitly simulate the on-reef time-dependent failure of the reef seam. A key finding in this paper is that the model gives a much better qualitative agreement with the underground measurements. For both the model and actual data, the rate of time-dependent closure

decreases into the back area. Calibration of the constitutive model nevertheless led to some unexpected difficulties, and element size plays a significant role. It appears that this problem can be addressed to some extent by introducing a sub-element construction algorithm that allows the moving edge of the fracture zone to be simulated in partially fractured elements. Further work on this procedure is required.

It was noted also that the simulated closure profile is complex as it reflects the combined result of a number of elements failing at different times. The closure rate does not decay according to a simple exponential model. In conclusion, explicit simulation of the fracture zone in the face appears to offer a better approach to describe the observed time-dependent behaviour in deep hard-rock stopes. The calibration of the limit equilibrium model half-life decay parameter requires additional field measurements in different geotechnical areas.

References

Malan, D.F. 1995. A viscoelastic approach to the modelling of transient closure behaviour of tabular excavations after blasting. *Journal of the South African Institute of Mining and Metallurgy*, vol. 95. pp. 211–220.

Malan, D.F. 1999. Time-dependent behaviour of deep level tabular excavations in hard rock. *Rock Mechanics and Rock Engineering*, vol. 32, no. 2. pp. 123–155.

Malan, D.F. 2003. Guidelines for measuring and analysing continuous stope closure behaviour in deep tabular excavations. Safety in Mines Research Advisory Committee (.SIMRAC), Johannesburg. August 2003.

Napier, J.A.L. 2016. Application of a fast marching method to model the development of the fracture zone at the edges of tabular mine excavations. *Proceedings of the 50th US Rock Mechanics/Geomechanics Symposium*, Houston, Texas, 26-29 June, 2016. American Rock Mechanics Association.

Napier, J.A.L. and Malan, D.F. 1997. A viscoplastic discontinuum model of time-dependent fracture and seismicity effects in brittle rock. *International Journal of Rock Mechanics and Mining Sciences & Geomechanics Abstracts*, vol. 34. pp. 1075–1089.

Napier, J.A.L. and Malan, D.F. 2012. Simulation of time-dependent crush pillar behaviour in tabular platinum mines. *Journal of the Southern African Institute of Mining and Metallurgy*, vol. 112. pp. 711–719.

Napier, J.A.L. and Malan, D.F. 2014. A simplified model of local fracture processes to investigate the structural stability and design of large-scale tabular mine layouts. *Proceedings of the 48th US Rock Mechanics/Geomechanics Symposium*, Minneapolis, MN, 1-4 June, 2014. American Rock Mechanics Association.

Roberts, D.P., Malan, D.F., Janse van Rensburg, A.L., Grodner, M., and Handley, R. 2006. Closure profiles of the UG2 and Merensky reef horizons at various depths, using different pillar types, in the Bushveld Complex. *Final report* SIM040207. Safety in Mines Research Advisory Committee (SIMRAC), Johannesburg.

Ryder, J.A. and Jager, A.J. 2002. A Textbook on Rock Mechanics for Tabular Hard Rock Mines. Safety in Mines Research Advisory Committee (SIMRAC), Johannesburg. ◆

http://dx.doi.org/10.17159/2411-9717/2018/v118n3a6

Rockburst prevention *via* destress blasting of competent roof rocks in hard coal longwall mining

by P. Konicek* and Schreiber†

Synopsis

Although the application of destress blasting as an active rockburst mitigation measure is not yet commonplace in hard coal longwall mining, the method is assuming heightened importance due to increases in mining depth and high horizontal stresses in the rock mass. The main goals of destress blasting are the softening of competent rock layers, the reduction of strain energy storage, and rock mass stress release, which together contribute to minimizing rockburst occurrence and risk. One such region in which destress blasting in competent rock is applied is the Upper Silesian Coal Basin, mainly in its Czech part.

Here a case study of destress blasting is presented and evaluated in terms of rockburst prevention, focusing on a thick coal seam (about 5 m) subject to longwall mining under very unfavourable geomechanical conditions (great depth – 1200 m, competent rigid rocks between coal seams, unfavourable stress field due to long-term mining). Destress blasting stages were carried out in groups of between four and eight boreholes 95 mm in diameter, with the total explosive charge ranging from 2100 kg to 3750 kg, detonated regularly at distances of 43 m to 114 m ahead of the advancing longwall face. Evaluation of destress blasting based on seismic monitoring revealed that the longwall blasts were very successful in terms of rock mass stress release and decreasing the rockburst risk, with only one rockburst occurring on a roadway 210 m from the longwall face. The following longwall section was mined safely without rockburst occurrence.

Keywords
rockburst, destress blasting, longwall mining.

Introduction

In the hard coal reserve of the Upper Silesian Coal Basin (USCB), which is shared by the Czech Republic and Poland, longwall mining is the dominant underground mining method. The Czech part of the USCB, known as the Ostrava–Karvina Coalfield (OKR), lies in the northeastern part of the country (Figure 1). The exhaustion of the upper seams due to the continuation of coal mining for around 200 years has shifted activity to a greater depth (> 800 m). Under existing mining and geological conditions in the Karvina sub-basin of the USCB, underground extraction of coal is typically accompanied by rockbursts, the first of which occurred in 1912 (Pelnar, 1938). A number of attempts have been made to address rockburst activity in both the Czech (Straube *et al.*, 1972; Holecko *et al.*, 1999; Takla *et al.*, 2005; Holub, Rušajová, and Holecko, 2011) and Polish parts of the USCB (Dubinski and Konopko, 2000; Drzewiecki and Kabiesz, 2008).

There are various rock mechanics challenges associated with the underground mining of deep-seated coal seams (Singh *et al.*, 2011; Yang *et al.* 2011; Konicek *et al.*, 2013). Analysis of geotechnical data from different mines (Chase, Mark, and Heasley, 2002; Konicek, Saharan, and Mitri, 2011; Konicek *et al.*, 2013) has revealed that the nature of the overlying strata plays a significant role in the success of such mining, with rockbursts considered the major problem encountered during the underground mining of deep coal seams under strong roof strata (Figure 2). Furthermore, the presence of rigid overlying rock strata typically results in dynamic loading during their caving, which also increases the chance of rockburst occurrence.

Both active and passive approaches have been adopted in order to control the increasing frequency of rockbursts in the working horizon. In certain mines the consequences of rockbursts can be reduced using passive approaches such as improvements in mining and support systems, the restriction of miner presence in underground openings, and blocking access to selected roadways. However, for a difficult site such as coal seam no. 3, an active approach (destress blasting in competent roof rocks) is needed in order to reduce rockburst frequency. Destress blasting, which is predominantly employed under conditions of high rockburst risk in underground ore mining, has been used in the Czech part of the USCB since the 1980s to

* *The Czech Academy of Sciences, Institute of Geonics, Ostrava, Czech Republic.*

† *GreenGas, Inc., Paskov, Czech Republic.*

 This paper was first presented at the AfriRock 2017 International Symposium, *30 September –6 October 2017, Cape Town Convention Centre, Cape Town.*

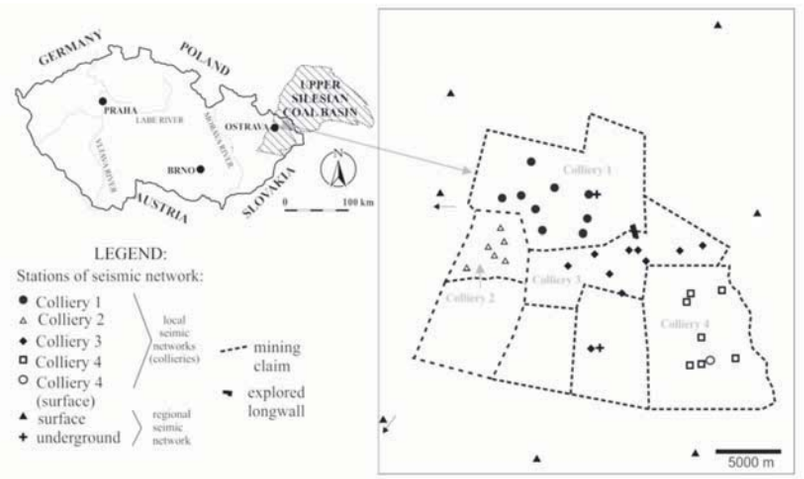

Figure 1—USCB location and map of seismic networks

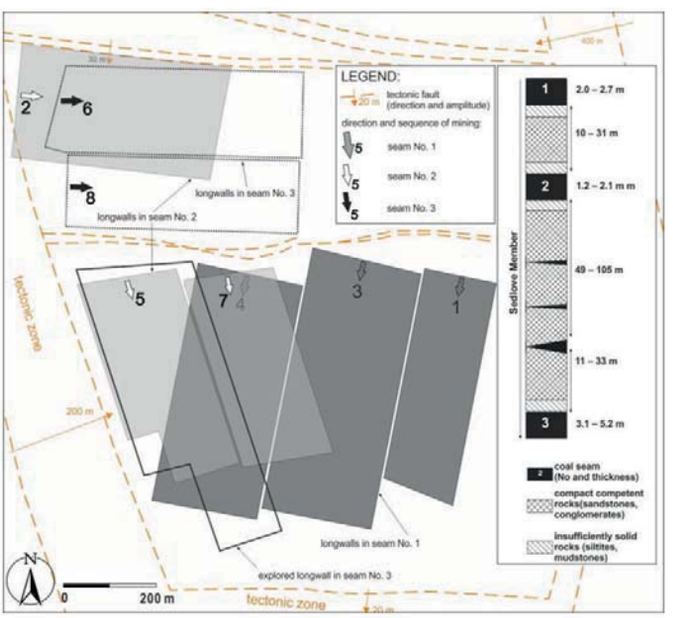

Figure 2—Sequence of mining in the described mining block and the lithological profile of the rock mass

prevent rockbursts (Dvorsky *et al.*, 2003; Przeczek, Dvorsky, and Konicek, 2004; Dvorsky and Konicek, 2005; Konicek and Przczek, 2008; Konicek, Saharan, and Mitri, 2011; Konicek *et al.*, 2013), with more than 2600 such blasts carried out in the region between 1990 and 2014 (Konicek, 2016).

Site details

The borders of the mining block in which the longwall is situated are formed by tectonic faults or fault zones with amplitudes ranging from 20 to 400 m (see Figure 2). Mining in this area covers three thick coal seams (nos. 1, 2, and 3) that were mined in the past at distances up to 200 m above the explored longwall panel (coal seam no. 3) in the bottom coal seam of the Sedlove Member (seam no. 3 in Figure 2) and which were subject to the evaluation of the rock mass according to official rockburst prevention guidelines (OKD, DPB, Inc. 2005). Further seams mined in higher overburden were not considered in the evaluation of rockburst risk level and thus are not described in this paper. The sequence and direction of mining are illustrated in Figure 2.

Seam no. 1 (Figure 2) was mined by three longwalls running from east to west (direction of mining north to south for every longwall) with thicknesses ranging from 2.0 to 2.7 m. The unmined part of the seam was left in the forefield of the terminated longwall no. 1 in Figure 2 as a consequence of a split in the coal seam and an increase in the thickness of the siltstone parting in the coal seam, while the northern part of the mining block was not mined due to the low thickness of the coal seam. Mined areas of coal seam no. 1 are situated around 75 to 169 m above coal seam no. 3.

Seam no. 2 (Figure 2) was mined in two isolated areas due to the local tectonic structure and the development of coal seam thickness. One longwall panel was mined in the northern area of the mining block from west to east, and two longwalls were mined in the southern part of the mining block from north to south (Figure 2). The thickness of the coal seam ranged from 2.1 to 2.6 m. Unmined pillars were left in the southern part of the mining block in the forefield of the longwall panels as a consequence of coal seam splitting and an increase in the thickness of the siltstone parting. Mined areas in coal seam no. 2 are located 60 to 138 m above coal seam no. 3.

Seam no. 3 (Figure 2) has been mined until the present day in the northern part of the mining block. Two longwall panels (nos. 6 and 8 in Figure. 2) were mined from west to east, with mining thickness ranging from 3.9 to 5.4 m. The selected longwall panel was mined from north to south in the southern part of the mining block, but was interrupted (after about 3 months) due to spontaneous combustion. After this incident the longwall face was shortened in length (106 m) up to the termination line.

Geology

The selected longwall is situated in coal seam no. 3, which is part of the Sedlove Member in the Karvina Formation of the USCB (Carboniferous age, Namur and Westphal). The ground border of the Karvina Formation in the Sedlove Member is aligned with the bottom of coal seam no. 3. Within the study area the development of the Sedlove Member is characterized by the alternation of fine- and coarse-grained sandstones with the siltstone and coal seams. The thickness of sandstone varies from 15.2 m between seams no. 1 and 2 up to a maximum of 63.6 m between seams no. 2 and 3. In between there exist siltstone layers up to 3 m thick, which also include coal strips accompanied by layers of root siltstones with thicknesses ranging from 1 to 2.4 m. The coal seams within the surrounding layers vary in thickness, with seam no. 1 ranging from 1.1 m to 2.7 m, seam no. 2 at around 2.6 m, and seam no. 3 from 3.9 to 5.4 m. The proportion of competent rocks between seams is estimated to be about 95%, based on cores drilled in the area (see Figure 2). The layers of the Sedlove Member are sub-horizontally deposited from southwest to northeast, with a total thickness of 274 m in the studied profile, which dips in the same direction at an approximately 12° angle. The studied longwall was excavated at depths ranging from 1115 m to 1160 m below surface level.

The area's tectonic structure is very complex due to the Variscian and Alpine orogenic stages that involved the initial sedimentation and subsequent alteration of the USCB (Grygar and Waclawik, 2011). The studied longwall is situated alongside a large southwest-northeast trending tectonic fault zone to the west with an amplitude of 200 m and angle of 70°, as well as a significantly smaller fault to the north with an amplitude of 4 m and angle of 75° running in a south-north direction.

Mining

The colliery responsible for the studied mine in the USCB adopted longwall mining to extract underground coal from the explored panel of the bottom coal seam of the Sedlove Member. The length of the coalface panel was 520 m and the width varied from 106 m to 190 m (Figure 2). Mining of the panel began in November 2015 and was completed in January 2017. The entire thickness of the panel coal seam, which ranged from 4.0 to 5.4 m, was extracted via a fully mechanized longwall face with caving.

The selected panel was the third longwall worked in the mining block of seam no. 3 (Figure 2). Mining of this panel took place near the tectonic zone and in an area impacted by the edges of previously extracted longwall panels in seams no. 1 and 2 (Figure 2) via overburden. As mentioned above, the goafs of the two overlying coal seams, with average heights of 84 m and 122 m, respectively, also likely influenced the development and concentration of stress during longwall mining of coal seam no. 3. Importantly, the positions and orientations of the extracted panels in both of the overlying coal seams were not superimposed in the same direction, mainly due to irregularity of coal seam thickness. Average daily longwall advance varied from 0.4 to 4.4 m according to site conditions during different longwall phases (see Figure. 4). Seismic activity response to longwall advance is described later in the section entitled 'Seismic monitoring'.

Rockburst risk

In the Czech part of the USCB, potentially hazardous mining locations are subject to an official rockburst prediction system and prevention methods in order to provide the safest possible environment for both workers and equipment. The prediction system is designed to determine if the rock mass presents a rockburst hazard, based on studies of the geomechanical properties of the coal and surrounding rocks. A system of preventive methods, both active (*e.g.* water injection into coal seams, destress blasting, *etc.*) and passive (*e.g.* mining strategy or improvement in mining and support system, restriction of access by miners, *etc.*), was prepared, aimed at reacting appropriately to hazardous conditions in the mine.

According to the rockburst classification system, the Sedlove Member is described as potentially rockburst-hazardous, and as such a three-level classification scheme (Takla *et al.*, 2005) was applied for coal seam no. 3 and the selected longwall. Based on the depth (up to 1160 m below the surface) at which coal was excavated and due to the presence of the edges of previously excavated coal seams (nos. 1 and 2), which put additional stress on roof rocks, the longwall was classified as belonging to the third level of rockburst risk, representing the most hazardous.

In order to set rules for continuous rockburst prognosis based on possible longwall conditions, individual observations and test drilling were carried out. A drilling-yield test was conducted daily on the face via boreholes 13 m in length (19 m in areas of overstressed pillars) and 42 mm in diameter. The typical spacing between these holes was kept at 28 m. Tests were also conducted at least twice a week both at the gateroads in the mining-induced stress zone and at the longwall coalface. The dimensions and spacing of the boreholes at the gateroads were similar to those along the coalface (weekly cycles at distances of 20, 50, 80, and 114 m ahead of the advancing longwall). All other activities that could potentially influence the stability of the rock mass were prohibited during the drilling-yield tests; continuous seismic monitoring was also carried out and is described in a separate section below.

As the main passive measure of rockburst prevention, a rockburst danger area was established (comprising the longwall face, longwall gates at a distance of 114 m ahead of the longwall face, and all gates ahead of the longwall face during the period of longwall termination) within which miner movement and numbers were restricted, mainly during periods of active mining at the longwall face.

As an active preventive method, destress blasting in roof rocks was considered to be the most effective, based on the area's mining history and conditions (see next paragraph). Coal wetting was also implemented as a basic active rockburst mitigation measure in the coal seam, covering the entire area of the longwall panel using infusion boreholes drilled from the gates (diameter 75 mm, length 90 to 96 m, spacing 10 m, pumped volume of water 530 l per metre of borehole).

Destress blasting

The main goal of destress blasting was to weaken the strength/massiveness of the overlying competent rock strata prior to the commencement of underground mining. After the horizon of the competent overlying strata was identified based on the previously procured core samples, different sets of predefined, long boreholes were drilled from the gateroads, targeting both these competent strata and existing mining activity in and around the panel. Design of the destress blasting programme was informed by an earlier destress blasting project (Kratky and Vlcek 2015).

Very similar problems of the softening of competent rocks are described by authors from South African mines. For instance Lightfoot *et al.* (1996) described work aimed at softening the rock on the excavation plane, as opposed to the roof rock as described in this paper, but the fundamental mechanisms are the same as in the case study from the USCB. Latilla *et al.* (2007) described softening of a problematic dolerite sill in the overburden at Matla Colliery, South Africa.

A schematic diagram (of both the section and the plan) of the adopted design of long borehole drilling carried out for destress blasting in the panel is shown in Figure 3. All of these boreholes were drilled upwards at angles of between 13° and 25° from both of the longwall gateroads (part of the starting area of longwall mining near the crosscut and in the area of the longwall termination) and from the main gate (the central part of the longwall panel). Perpendicular boreholes from the gates were suitably complemented by oblique boreholes drilled into the area of the tectonic zone west towards the longwall and in the area of perpendicular borehole stemming. Borehole length varied from 47 m to 90 m. In view of the calculated amount of explosive required for destress blasting, the diameter of these boreholes was set at 95 mm and the spacing at 10 m. Due to the suitable length and angle combinations of these boreholes, the bottoms (ends) of all boreholes were situated in a similar horizon inside the roof, nearly 28 m above coal seam no. 3.

All of the upward-drilled boreholes were charged pneumatically using the plastic gelatine explosive Perunit E (heat of explosion 4100 kJ.kg^{-1}), with sand employed for the stemming. The length and amount of explosive in each borehole varied according to the surrounding geo-mining conditions, with the length of charge ranging from 27 m to 65 m, length of sand stemming from 15 m to 25 m, and the percentage loaded length from 55% to 72%. Individual groups of loaded boreholes, typically ranging from four to eight in number, were fired in advance according to the predefined firing order. All of the charged boreholes in each group were fired simultaneously, without any delay, with the weight of explosive charge in the different holes varying according to the borehole diameter and length, from 225 kg to 550 kg. The total amount of explosive (for the four to eight boreholes in each group) blasted at any one time in the panel varied from 2100 kg to 3750 kg (Table I).

According to the site conditions, boreholes no. 92–101 and 1–11 (Figure 3) were employed to create a network of fissures in the competent strata overlying the commencement area of the longwall panel. Boreholes no. 1–47, 59–70, 74–87, 104–116, and 120–130 were used to dilute the influence of the edges between the mined and unmined parts of the seams in the overburden, as well as to dilute the influence of the nearby tectonic zone to the west towards the longwall. Boreholes no. 59–70, 102, 103, and 117–119 covered the area of the stemmings of the perpendicular boreholes. The competent strata over the remaining pillars situated between the main gate and the tectonic zone were managed via boreholes no. 74–87. Blasting in boreholes no. 40–47, 104–116, and 120–130 was carried out to decrease additional stress ahead of the advancing longwall face in the area of the longwall panel termination. The competent overlying rock strata, which were continuously fractured due to these blasts, were also observed to be caving-friendly. The decision to blast different individual groups of boreholes at different stages was made according to not only the surrounding

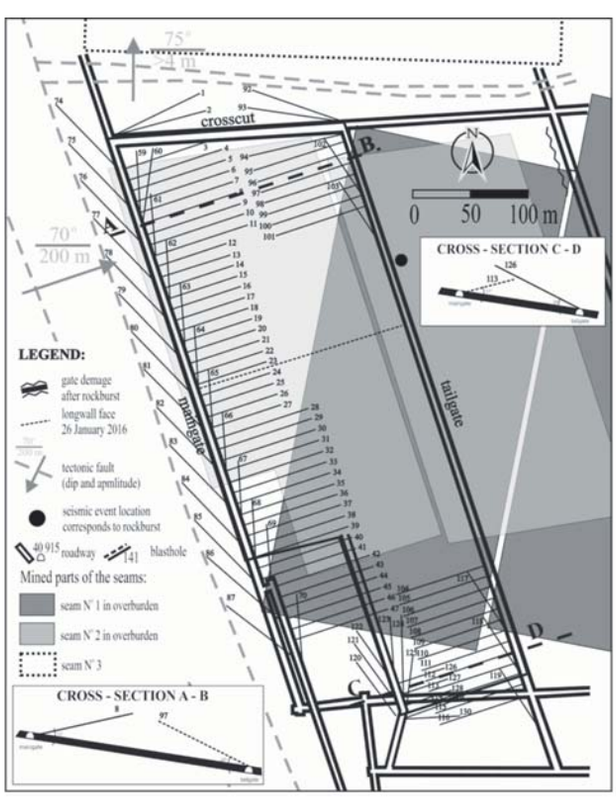

Figure 3—Design of destress blasting in overlying rocks

Table I

Parameters of destress blasting

Stage no.	Borehole nos.	Date and time	Explosive charge (kg)	Registered seismic energy (J)	Seismic effect	Percentage shear/total volume change (maximal) in the focal area (%)
1	1–5, 74, 75	3.11.2015, 16:37	2775	6.30E+04	12.2	43.9
2	6–8, 59, 60, 76	6.11.2015, 15:19	2725	9.70E+04	19.1	29.3
3	92–98, 102	8.11.2015, 15:42	3750	8.70E+04	12.5	79.3
4	99–101, 103	17.11.2015, 14:01	3725	2.04E+05	29.4	35.2
5	11–15, 62, 78	22.11.2015, 14:43	2700	8.10E+04	16.1	28.6
6	16–19, 63, 79	6.12.2015, 16:11	2100	5.20E+04	13.3	32.1
7	20–22, 64, 80,81	20.12.2015, 14:53	2150	8.00E+04	20.0	34.6
8	23–26, 65, 82	3.1.2016, 15:07	2275	9.60E+04	22.7	18.8
9	27–30, 66, 83	17.1.2016, 15:22	2850	9.70E+04	18.3	31.9
10	31–34,67, 84	31.1.2016, 15:24	2975	2.20E+05	39.8	41.4
11	35–38, 68, 85	7.2.2016, 16:19	2925	2.00E+05	36.8	42.1
12	39–42, 69, 86	28.2.2016, 15:12	2675	1.50E+05	30.1	41.2
13	43–47, 70, 87	24.4.2016, 15:23	2900	9.70E+04	18.0	35.1
14	104–109, 117	8.5.2016, 14:21	3225	1.70E+05	28.3	43.3
15	110–111, 118, 121-124	2.10.2016, 18:02	2750	4.70E+04	9.2	33.6
16	112–114, 120, 125-126	16.10.2016, 15:21	2200	6.40E+04	15.6	30.8
17	115–116, 119, 127-130	22.11.2016, 15:49	2275	2.30E+04	5.4	33.3

workings and strata, but also the development of seismic activity during mining and the advance of the longwall face. Based on expert knowledge of the area and valid legislation (OKD, DPB, Inc. 2005), the distance the boreholes were fired ahead of the longwall face was in the range of 43 to 114 m. The amount of charge fired was dependent on the boreholes selected for firing, which itself was based on mining conditions, natural conditions, and the development of registered seismic activity as per the above legislation.

The effectiveness of destress blasting is connected to, among other factors, stress release in the rock mass. This stress release was here evaluated using the seismic effect (SE) index, a methodology first established in the Czech part of the USCB and subsequently verified by Konicek *et al.* (2013) and Konicek (2016). The seismic effect (SE) is defined as the ratio of seismic energy released in the rock mass when blasting, to the energy of the particular detonated charge (Konicek *et al.*, 2013). It can be calculated according to the following formula:

$$SE = \frac{E_{ICM}}{K_{ICM} Q} \quad [1]$$

where:

E_{ICM} is the seismic energy calculated by the seismic network in the investigated coal mine (J)

Q is the mass of the explosive charge (kg)

K_{ICM} is the coefficient characterizing the conditions in the assigned mine (J.kg^{-1}).

The employed method of coefficient determination is described in detail in Konicek *et al.* (2013). According to the latest verification of this coefficient by Konicek (2016), the results of which were implemented in the OKR rockburst prevention rules, K_{ICM} = 1.86 for the seismic effect calculation presented in Table I. The classification index developed to evaluate SE values (based on Konicek *et al.* (2013) and verified by Konicek (2016)) using the criteria obtained from the distribution of SE probabilities and according to Equation [1], is presented in Table II.

Examination of Table I reveals that all the calculated seismic effect values were high; most can be classified as excellent in terms of stress release (only one was evaluated as very good and four as extremely good). This means that the stress release strategy carried out in coal seam no. 3 was successful in all stages of destress blasting, especially stages 2, 4, 5, 7-14, and 16.

Seismic monitoring

As one of the methods developed to ensure miner safety, seismic monitoring was employed to analyse the geomechanical activity of the rock mass. Such nondestructive methods are very popular because of the large amount of information that can be gathered regarding seismic activity taking place during mining, such as the number and energy levels of tremors in the area.

For the studied longwall, three systems were employed in order to gather the maximum amount of relevant information. Firstly, data from the regional seismic monitoring network (SP) was used (see Figure 1). This network consists of ten triaxial short-period WDS seismometers (f = 0–2.0 Hz), six of which are located in boreholes (depth 30 m), three installed underground in active mines, and one situated in a short gallery at the Ostrava-Krasne Pole seismic station. The frequency range of the network is f = 2–32 Hz and the dynamics of the recorded

Table II

Seismic effect evaluation

Seismic effect	Evaluation of seismic effect (success of stress release)
SE < 2.5	Insignificant
2.5 ≤ SE< 4.1	Good
4.1 ≤ SE< 7.0	Very good
7.0 ≤ SE< 13.6	Extremely good
SE ≥ 13.6	Excellent

seismic signals around 120 dB, with sampling frequency 125 Hz. Secondly, data from the local seismological network (see Figure 1) of active mines was used. The stations comprising this network are situated in the local mine and are equipped with monoaxial, low-frequency and low-periodical vertical SM-3 seismometers. The basic parameters of these seismometers are as follows: input sensitivity 16–5 mV, amplification maximum 74 dB, frequency range 1.5–20 Hz, and sampling frequency 100 Hz. Finally, a seismo-acoustic monitoring system was used (not discussed in the present paper). According to local legislation, such a system must be employed in longwalls (such as that analysed here) that are classified as subject to the third level of possible rockburst occurrence.

In order to evaluate the collected seismological activity data, graphs of daily registered seismic energy sum and the weekly slope of registered seismic energy were constructed (Figure 4). From these graphs, four phases (A, B, C, and D in Figure 4) can be identified that are characterized by the most significant weekly energy variations.

The first stage (A) is distinguished by a rapid increase in seismic activity, in this case clearly connected with the initialization phase of the longwall run based on the similar shape of the two curves (daily and weekly seismic activity). During this initial stage of excavation the longwall in question was situated in a location where additional stress was generated from earlier longwalls in seams no. 1 and 2.

During phase B, when the longwall advanced into a partly protected area made by the previously excavated longwalls in the upper coal seams, seismic activity began to decrease. Also during this phase, weekly variations in seismic activity mirrored the longwall's daily advance, although with a lower order of energy.

In the third phase (C), seismic activity was generally at a minimum because of the break in mining progress caused by the spontaneous combustion of coal. Even during the second half of phase C, activity remained low due to the presence of an existing protected area from seams no. 1 and 2.

In the final phase (D), seismic activity increased significantly. This is likely connected to the fact that the longwall reached a position similar to that of phase A, with no protected area and subjected to additional stresses derived from the mining edges of earlier excavated longwalls and other mining works (roadways *etc.*) ahead of the longwall. After the re-initiation of longwall mining, seismic activity rose, decreasing only some time after the termination of mining works.

Figures 4 and 5 illustrate the clustering of seismic event locations over the study period. During phase A, a number of both high- and low-energy events were localized north of and adjacent to the longwall; this seismic activity was likely caused by existing additional stress from the mining edges of seams no. 1 and 2. During phase B, the distribution of seismic events was uniform across the entire excavated area, while the total number of events decreased. However, most high-energy events were localized in the eastern part of the longwall during its advance, probably due to additional stress from the mining edges and the absence of a protected zone, unlike on the western side. During phase C, the decrease in the number of events was significantly greater and event distribution was correlated mostly with the longwall's position, with events also recorded in the goaf, related to the stabilization of the rock mass. A few high-energy events occurring during this phase were localized to the south due to the resumption of mining in this area. In the final phase D, the localization of events closely corresponded with the advance of the longwall to the south, during which time the longwall moved out of the protected zone and was subject to additional stress from mining edges. Event distribution was homogenous, with most events taking place around the position of the longwall, in addition to random occurrences in the goaf.

An analysis was also carried out regarding the focal areas of each round of destress blasting and every high-energy seismic event (with energy greater than 10^4 J). In this evaluation, the directions of shear plane poles were studied by construction of polar diagrams, with volume changes in the focal areas also calculated (Figure 6), indicating the main directions of the shear planes and the total sum of radiated energy and energy used by the shear mechanism, respectively. The proportion of shear/total volume change (maximal) in focal areas (see Table I) was determined in

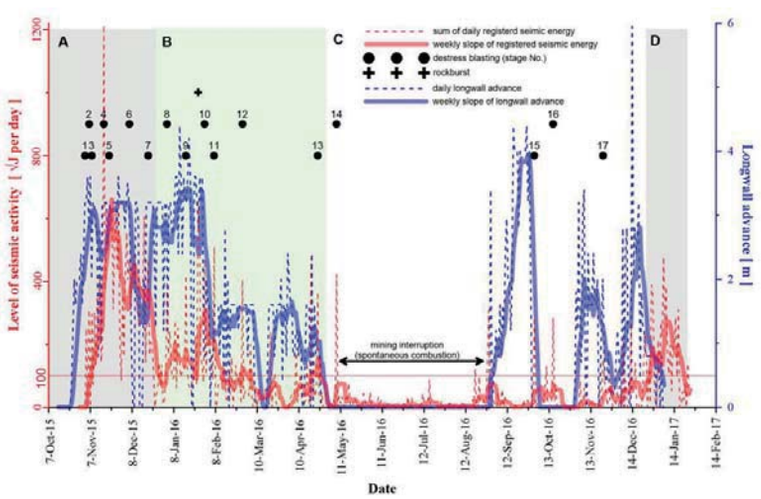

Figure 4—Registered seismic activity and longwall advance

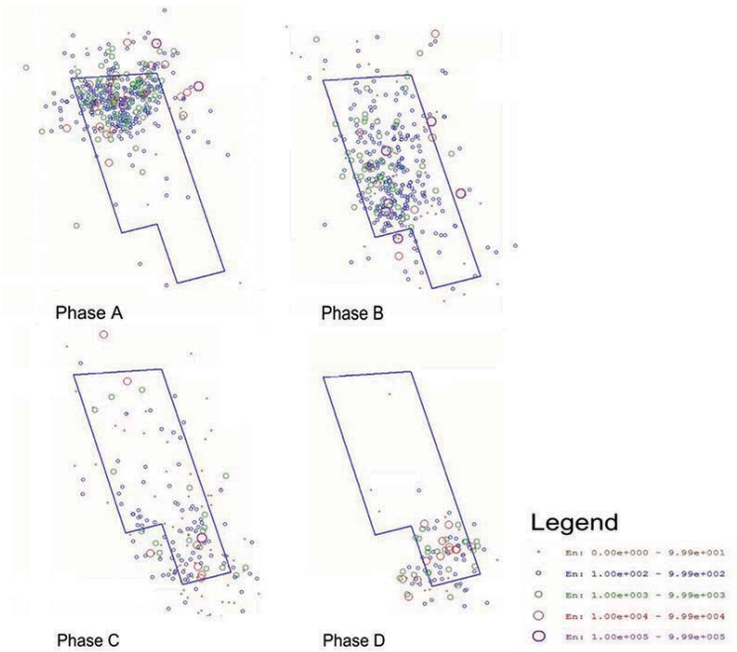

Figure 5—Location map of seismic events registered during different longwall phases (see Figure 4)

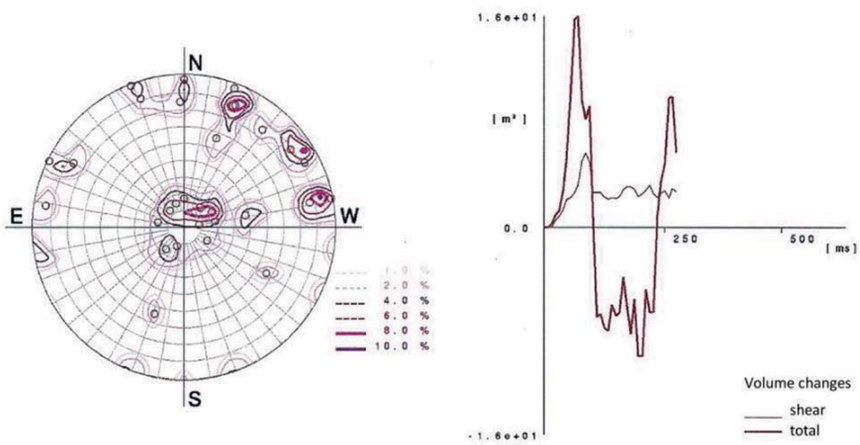

Figure 6—Example evaluation of the focal area of the registered seismic event corresponding to destress blasting stage no. 4. Right—volume changes, left—contour diagram of poles of shear planes; equal angle projection, lower hemisphere, N = 113

order to confirm stress release, with high levels of shear volume changes corresponding to shear failure considered as important stress release evidence by a number of authors (*e.g.* Stec and Drzewiecki, 2012; Wojtecki *et al.*, 2016). A comparison of SE values and the proportion of shear/total volume changes in the focal areas (Table I) of seismic events corresponding to destress blasting reveals that in many cases both parameters are indicative of stress release in the rock mass. Based on an evaluation of specific seismic events with radiated energy greater than 10^4 J registered during the excavation period, it can be stated that most of these events had a positive impact on stress conditions in the rock mass, promoting the release of accumulated stress according to the energy required for shear failure. Examination of Figure 6 reveals the reverse pattern of the phases, with the explosion represented in the first part of diagram, followed by implosion and a final increase. The total amount of radiated energy in these cases was higher than the energy required for shear failure, which leads to the conclusion that the blasts were effective in achieving stress release.

Despite all the above efforts, in January 2016 a strong-motion seismic event (registered energy 3.13 E+05 J, magnitude 1.66) classified as a rockburst occurred close to the longwall face but mainly manifested (roadway deformation, one fatality, and several minor injuries) approximately 210 m east of the longwall (see Figure 3) in an area of additional stress due to edges of previous mining in overburden – see Figure 2. The event was located 104 m above the mined coal seam (in approximately the stratigraphic position of seam no. 2 in the overburden – see

Figure 3). Rock mass damage was recorded relatively far from the epicentre of the event but not in the vicinity of the longwall. This could be due to softening of competent rocks in the overburden due to destress blasting, as well as a decrease in the stress level in the protected as a result of previous mining of seam no. 2 in the overburden of the longwall. On the other hand, we also have to take into consideration the accuracy of the seismic event location (around 100 m).

Conclusions

Systematic planning and design of a destress blasting programme carried out in roof rocks enabled safe longwall mining in a rockburst-prone area. The amount of explosive used at different stages during the destress blasting process varied from 2100 kg up to a maximum of 3750 kg. The proposed classification of destress blasting based on the value of the seismic effect was also validated through seismic observations. Out of the total of 17 stages comprising the destress blasting of the longwall panel, one stage was categorized as achieving very good stress release (SE 5.4), four stages as extremely good (SE varied from 9.2 to 13.3), and the remaining 12 as excellent (SE varied from 15.6 to 39.8). The success of stress release based on SE evaluation is also supported in most cases by the evaluation of shear percentage/total volume changes in the focal area of seismic events corresponding to destress blasting. Despite the adverse conditions only a single rockburst event occurred. Many more rockbursts would have been expected if the competent rock has not been softened by destress blasting stages. The success of the energy release strategy is demonstrated by the SE values and the fact that only one burst was recorded. Although mining was undertaken in very unfavourable geomechanical conditions, the longwall panel was mined safely even after initial rockburst problems, with no further issues encountered.

Acknowledgements

This article was written in connection with the Project Institute of Clean Technologies for Mining and Utilisation of Raw Materials for Energy Use – Sustainability. reg. no. MSMT LO1406, which is supported by the Research and Development for Innovations Operational Programme financed by the Structural Funds of the European Union and the Czech Republic.

References

Chase, F.C., Mark, C., and Heasley, K.A. 2002. Deep cover pillar extraction in the U.S. coalfields. *Proceedings of the 21st International Conference Ground Control in Mining*, Morgantown, WV. University of West Virginia. pp. 68–80.

Drzewiecki, J. and Kabiesz, J. 2008. Dynamic events in roof strata – occurrence and prevention. *Coal Science & Technology Magazine*. pp. 55–57.

Dubinski, J. and Konopko, W. 2000. Rockbursts – assessment, prediction and control – working rules. Central Mining Institute, Katowice. [in Polish].

Dvorsky, P. and Konicek, P. 2005. Systems of rock blasting as a rockburst measure in the Czech part of Upper Silesian coal basin. *Proceedings of the 6th International Symposium on Rockbursts and Seismicity in Mines*, Perth. Potvin, Y. and Hudyma, M. (eds). Australian Centre for Geomechanics, Perth. pp. 493–496.

Dvorsky, P., Konicek, P., Morkovska, E., and Palla, L. 2003. Rock blasting as a rockburst control measures in the safety pillar of SW crosscuts at Lazy Colliery in Orlova. *Proceedings of the 10th International Scientific-Technical Conference - Rockbursts 2003*, Ustron, Poland. Central Mining Institute, Katowice. pp. 37–45.

Grygar, R. and Waclawik, P. 2011. Structural-tectonic conditions of Karviná Subbasin with regard to its position in the apical zone of Variscan accretion wedge. *Acta Montanistica Slovaca*, vol. 16, no. 2. pp. 159–175.

Holecko, J., Ptacek, J., Takla, G., and Konecny, P. 1999. Rockbursts in the Czech part of the Upper Silesian Coal Basin – Features, theoretical models and conclusions for practice. *Proceedings of the 9th International Congress on Rock Mechanics*, Paris. Taylor & Francis. pp. 1101–1104.

Holub, K., Rušajová, J., and Holecko, J. 2011. Particle velocity generated by rockburst during exploitation of the longwall and its impact on the workings. *International Journal of Rock Mechanics and Mining Sciences*, vol. 48. pp. 942–949.

Konicek, P. 2016. Destress blasting mechanism around the borehole and its impact on the stress field. Habilitation thesis, VŠB-Technical University, Ostrava, Czech Republic. [in Czech].

Konicek, P. and Przeczek, A. 2008. Study of selected cases of local stress reduction due to rock blasting. *Proceedings of the 15th International Scientific-Technical Conference GZN 2008*, Targanice, Poland. Główny Instytut Górnictwa, Katowice. pp. 143-161.

Konicek, P., Saharan, M.R., and Mitri, H. 2011. Destress blasting in coal mining – state-of-the-art review. *Proceedings of the First International Symposium on Mine Safety Science and Engineering*, Beijing. Elsevier. pp. 158–173.

Konicek, P., Soucek, K., Stas, L., and Singh, R. 2013. Long-hole destress blasting for rockburst control during deep underground coal mining, *International Journal of Rock Mechanics and Mining Sciences*, vol. 61. pp. 141–153.

Kratky, D. and Vlcek, S. 2015. Project of rockburst prevention, OKD, Inc. [in Czech].

Latilla, J., van Wijk, J.J., Booysen, H., Silver, C., and Fourie, P. 2007. Pre-split surface blasting to modify goaf behavior above shortwall panels. *Proceedings of the 11th ISRM Congress*, Lisbon, Portugal, 9–13 July 2007. International Society for Rock Mechanics, Lisbon.

Lightfoot, N., Kullman, D.H., Toper, A.T., Stewart, R.D., Grodner, M., Janse van Rensburg, A.L., and Longmore, P. 1996. Preconditioning to reduce the incidence of face bursts of highly stressed faces. *GAP303 Final Report*, Safety in Mines Research Advisory Committee, Johannesburg. http://hdl.handle.net/10204/1640

OKD, DPB, Inc. 2005. Working rules of rockburst control in OKR OKD, DPB, Inc. [in Czech].

Pelnar, A. 1938. Rockbursts in Ostrava-Karvina Coalfield. *Mining Bulletin*, vol. XX. pp. 25–58. [in Czech].

Przeczek, A., Dvorsky, P., and Konicek, P. 2004. System of rock blasting in boreholes diameter more than 100 mm as a rockburst measure. *Proceedings of the 12th International Scientific-Technical Conference - Rockbursts 2004*, Ustron, Poland. Central Mining Institute, Katowice. pp. 253–269.

Singh, A.K., Singh, R., Maiti, J., Kumar, R., and Mandal, P.K. 2011. Assessment of mining induced stress development over coal pillars during depillaring. *International Journal of Rock Mechanics and Mining Sciences*, vol. 48. pp. 794–804.

Stec, K. and Drzewiecki, J. 2012. Mine tremor focal mechanism: an essential element for recognising the process of mine working destruction. *Acta Geophysica*, vol. 60, no. 2. pp. 449–471.

Straube, R., Brothánek, J., Harášek. V., Košťál. Z., Kovács, Z., Mikeska, J., Paděra, Z., Rozehnal, V., and Vavro, M. 1972. Rockbursts in Carboniferous Rock Mass. SNTL, Prague. [in Czech].

Takla, G., Ptacek, J., Holecko, J., and Konicek, P. 2005. Stress state determination and prediction in rock mass with rockburst risk in Ostrava-Karvina coal basin. *EUROCK 2005*, *Proceedings of the International Symposium of the International Society for Rock Mechanics*, Brno, Czech Republic. CRC Press. pp. 625–628.

Yang, W., Lin, B.Q., Qu, Y.A., Li, Z.W., Zhai, C., Jia, L.L, and Zhao, W.Q. 2011. Stress evolution with time and space during mining of a coal seam. *International Journal of Rock Mechanics and Mining Sciences*, vol. 48. pp. 1145–1152.

Wojtecki, L., Mendecki, M., Zuberek, W., and Knopik, M. 2016. An attempt to determine the seismic moment tensor of tremors induced by destress blasting in a coal seam. *International Journal of Rock Mechanics and Mining Sciences*, vol. 83. pp. 162–169. ◆

http://dx.doi.org/10.17159/2411-9717/2018/v118n3a7

Keyblock stability analysis of longhole stopes

by D. Sewnun*, W. Joughin*, R. Armstrong*, and A. Cooper†

Synopsis

The orientations of discontinuity sets and major geological structures greatly influence the stability of an excavation. Excavations should therefore, where possible, be orientated such that major discontinuity sets and structures are considered, allowing the likelihood of rockfalls in a longhole stope to be kept to a minimum. The longhole stopes are non-entry excavations, which are remote cleaned to avoid exposure of personnel. However, excessive rockfalls can significantly influence productivity and cause damage to mining machinery. This paper presents a risk-based approach to design, where the failure potential of mining stopes for the Platreef mine was determined considering the influence of major structures. The probabilistic keyblock analysis software JBlock was used in this capacity. In this study, the failure potential of keyblocks was determined in JBlock for the longhole stopes of various proposed orientations, considering structural domains and a major geological fault which was identified across the project area. Results of the analysis indicated that stopes orientated sub-parallel to Platreef's major fault (Tshukudu Fault) resulted in the largest rockfalls. Overall, JBlock was used successfully as a design tool to assess the stability of the longhole stopes. Outcomes of the study have provided Platreef mine with valuable information that will assist in the decision-making process when finalizing stope orientations. This study therefore attempts to serve as a reference point for solutions to similar situations, with the objective that risk-based designs are called upon more frequently in the future.

Keywords

longhole stope, stope stability, keyblock, probabilistic analysis, JBlock.

Introduction

Ivanplats (Pty) Ltd, a subsidiary of Ivanhoe Mines Ltd, has undertaken an investigation to assess the feasibility of developing a new 4 Mt/a underground platinum mine (the Platreef mine) accessed via a vertical shaft system. Platreef mine is located on the northern limb of the Bushveld Complex in South Africa, near the town of Mokopane, approximately 280 km northeast of Johannesburg.

It is planned to extract the wide, shallow-dipping orebody using longhole stopes (15 m wide, 25 m high, and between 40 m and 200 m long), which are post-filled. The stopes will be mined in a primary-secondary sequence using mining machinery and will be non-entry once blasted. In areas which are flat dipping (<10°), the stopes can be orientated in any direction, but where the dip is greater than 10°, they can either be oriented longitudinally (parallel to strike) or transversely.

The orientation of the proposed stopes must be optimized to minimize rockfalls and the consequences of production disruptions and damage to machinery. A risk assessment of the failure potential of geological discontinuities in the stope back and walls was therefore carried out. A structural analysis was conducted utilizing logged and wireline discontinuity data from across the project area. Structural domains were then defined based on identified discontinuity sets and major geological structures interpreted in the area. The discontinuity sets for each structural domain were then evaluated for the proposed transverse and longitudinal mining stopes using the keyblock analysis software JBlock (Esterhuizen, 2003). This approach has been applied by several authors for the analysis of stability of tunnels and subhorizontal, narrow tabular stopes (Esterhuizen and Streuders, 1998; Dunn and Stacey, 2008; Dunn, Earl, and Watson, 2008; Dunn, 2010; Joughin *et al.*, 2012).

Major structural geology

Through the collection and analysis of drill-hole data, the Tshukudu major fault was identified by Ivanplats geologists (Ivanhoe Mines, 2015). The Tshukudu Fault strikes approximately from north to south and traverses the entire project area (Figure 1). The true thickness of the fault varies from 5 m to 57 m, typically ranging from 10 m to 25 m (Ivanhoe Mines, 2016). This fault represents a significant geotechnical hazard and comprises a wide fracture zone of influence with intensely altered and brecciated fault gouge (Ivanhoe Mines, 2016). The fault is generally

* *SRK Consulting (Pty) Ltd, South Africa.*

† *Ivanplats (Pty) Ltd, South Africa.*

 This paper was first presented at the AfriRock 2017 International Symposium, *30 September –6 October 2017, Cape Town Convention Centre, Cape Town.*

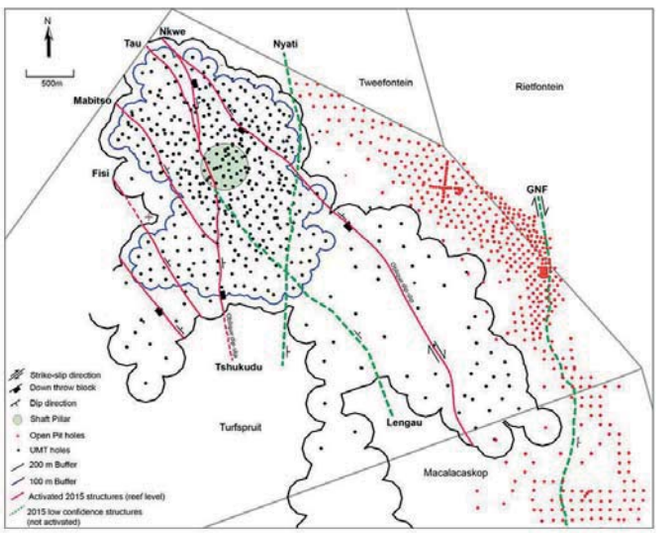

Figure 1—Platreef major structures – plan (Brits and Nielson, 2015)

steeply inclined (50° to 70° dip) with an east-northeast dip direction and oblique normal sense of movement (Ivanhoe Mines, 2015). The combination of weak infill, a high degree of fracturing, the width, the zone of disturbance, and the steep dip results in a high likelihood of uncontrolled unravelling (running).

Other major structures have been identified across the project area (Figure 1). These were not considered to pose significant geotechnical risk, but were used in the compilation of the geotechnical model.

Local structural geology

Rock mass instabilities adjacent to excavations can often be attributed to naturally occurring discontinuities or induced fractures (Windsor and Thompson, 1992). It is thus essential to have an insight on the orientation and the nature of discontinuity sets present across the mining area.

Based on discontinuity sets that were identified in the context of the large-scale structural model, structural domains were delineated for the proposed mining area. Wireline and structural logs from 34 drill-holes were used to identify five structural domains (north, west, central, south east, and east) and six discontinuity sets (Figure 2 to Figure 7 and Table I).

The local structural geology may be summarized as follows:

- Discontinuity set 1 (DS1) is a dominant set present across the project area and strikes parallel to the Nkwe Fault system (approximately 55°, dipping to the northeast), however is generally flatter dipping (Figure 2 and Table I.).
- Discontinuity set 2 (DS2) is a dominant easterly to southeasterly dipping set present in the north, west, and central domains. This set is parallel to the Kibaran-age structures, which form part of a system of closely spaced extensional faults that are developed across the central and western part of the project area. The Tshukudu and Nyati faults are included in this group.

Table I

Summary of discontinuity sets identified in each structural domain

	Domain	North	West	Central	Southeast	East
DS1	Mean dip Mean dip direction No. of discontinuities	36 048 146	38 060 283	42 062 499	42 064 236	47 054 90
DS2	Mean dip Mean dip direction No. of discontinuities	69 104 134	62 100 153	61 097 275	- - -	- - -
DS3	Mean dip Mean dip direction No. of discontinuities	- - -	18 194 173	16 072 264	11 169 60	18 142 27
DS4	Mean dip Mean dip direction No. of discontinuities	60 262 98	- - -	- - -	- - -	43 274 65
DS5	Mean dip Mean dip direction No. of discontinuities	- - -	- - -	- - -	62 169 147	- - -
DS6	Mean dip Mean dip direction No. of discontinuities	- - -	- - -	- - -	88 300 67	- - -

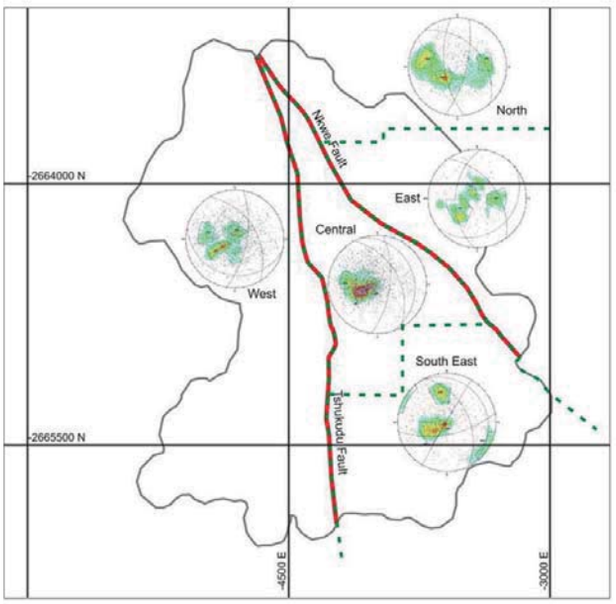

Figure 2—Platreef structural domains

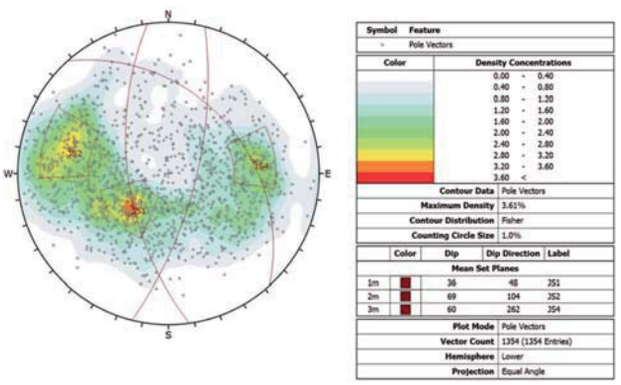

Figure 3—Stereographic projection – north domain

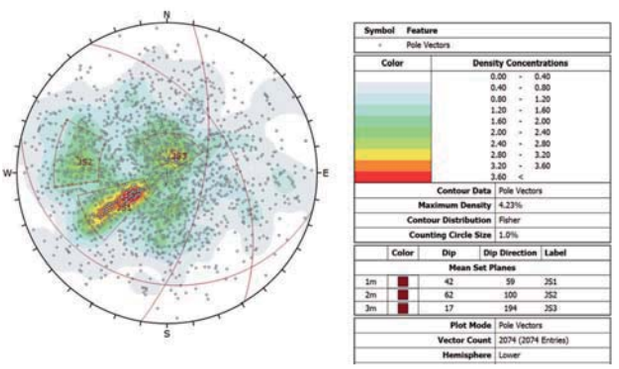

Figure 4—Stereographic projection – west domain

- Discontinuity set 3 (DS3) consists of flat-dipping discontinuities, which are present across the majority of the project area.
- Discontinuity set 4 (DS4) is a westerly moderately dipping set present in the north and the east domains.
- Discontinuity set 5 (DS5) is a south-southeast dipping set present in the southeast domain.
- Discontinuity set 6 (DS6) is a minor discontinuity set based on data from two drill-holes and consists of steep dipping discontinuities present in the southeast domain, which may lead to slabbing in the sidewalls, depending on the direction of mining.
- The majority of discontinuities (69%) are roughly planar across the project area. Where discontinuities have infill, the infill is generally soft with fine sheared material.
- The majority of the boreholes used in the analysis have been drilled at a dip of approximately 85°, at various dip directions. This was ideal for the identification of DS1 and DS3, which are shallow dipping and are thus orientated almost normal to the borehole orientations (Table I).

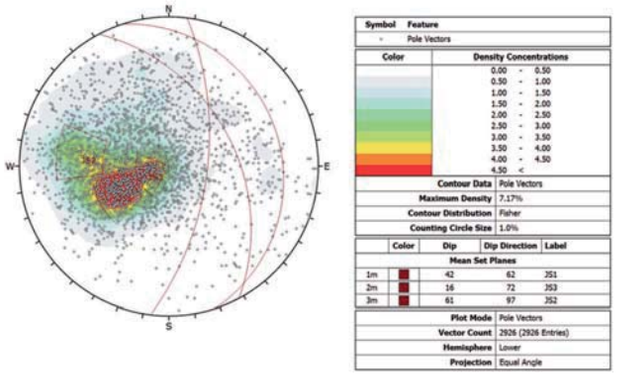

Figure 5—Stereographic projection – central domain

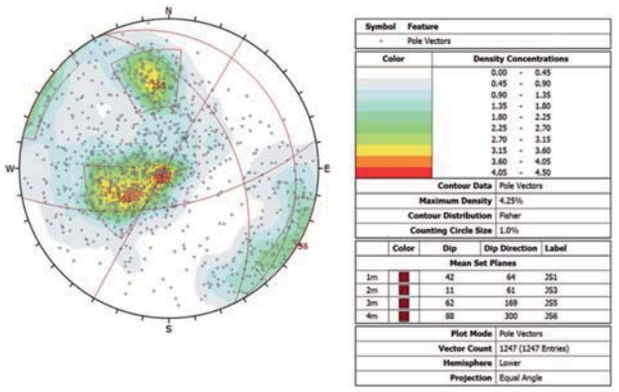

Figure 6—Stereographic projection – southeast domain

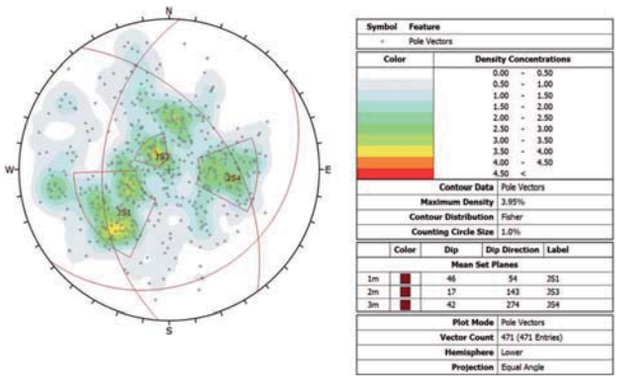

Figure 7—Stereographic projection – east domain

- As DS2, DS4, DS5, and DS6 are more steeply dipping and are therefore orientated sub-parallel to the boreholes, note that these sets may be more prominent than is indicated (currently affected by directional bias).

Discontinuity set characteristics

Discontinuity shear strength parameters were selected using Barton's (2002) equation, where the friction angle is based on the joint surface roughness and infill and discontinuities are considered to be cohesionless, as presented in Equation [1]:

$$\emptyset = \arctan(Jr/Ja) \quad [1]$$

where: Φ is the friction angle, Jr is the joint roughness and Ja is the joint alteration, according to Barton's 1974 Norwegian Q system (Barton, Lien, and Lunde, 1974). Friction angles determined for each discontinuity set are presented in Table II.

Discontinuity spacing was determined by calculating the apparent spacing between consecutive discontinuities for each set in their respective drill-holes. True discontinuity spacing was then calculated for each discontinuity set by adjusting the apparent spacing according to the orientation of the drill-holes. As data could only be collected from boreholes, note that a directional bias exists. This can be reduced by undertaking scanline mapping in various directions once mining commences.

The mean true discontinuity spacing determined for discontinuity sets across the project area is presented in Figure 8.

Structural data was obtained solely from drill-holes and therefore joint length data was not available. Joint lengths were assumed based on observations from adjacent projects in the area and are presented in Table III.

Keyblock stability analysis

A probabilistic keyblock stability analysis was conducted using JBlock (Esterhuizen, 2003) to assess the likelihood of rockfalls occurring considering proposed stope orientations and the defined structural domains. JBlock was developed to evaluate the potential for gravity-driven rockfalls using probabilistic methods to determine the dimensions of potential unstable blocks (known as keyblocks) and their interaction with support. JBlock creates and analyses a large number of keyblocks based on joint set characteristics, from which it derives a statistical failure distribution. The influence of various support types and patterns on the failure distribution can also be simulated. This approach thus allows for the relative hazard associated with various support designs or excavation orientations to be obtained (Esterhuizen and Streuders, 1998).

A keyblock analysis was conducted on proposed transverse and longitudinal stope orientation zones (SOZs) provided by the mine planning team. Transverse stopes are generally orientated at a high angle relative to the strike of the Tshukudu Fault, while longitudinal stope orientations are sub-parallel to the fault. Additional analyses were carried out on stopes orientated in a northerly direction.

Stope orientations and structural domains that were analysed are indicated in Figure 9. Stopes orientations are schematically represented within the appropriate stereographic projections in Figures 10 and 11. A summary of the stope orientations analysed is presented in Table IV.

Keyblock generation

The first step in the analysis is the generation of keyblocks, based on the following information for each structural domain:

Table II

Friction angle results

Discontinuity set	DS1	DS2	DS3	DS4	DS5	DS6
Min.	21	21	21	21	21	21
Mean	37	37	36	36	33	32
Max.	72	72	72	72	72	56
St. dev.	17	18	18	17	16	21

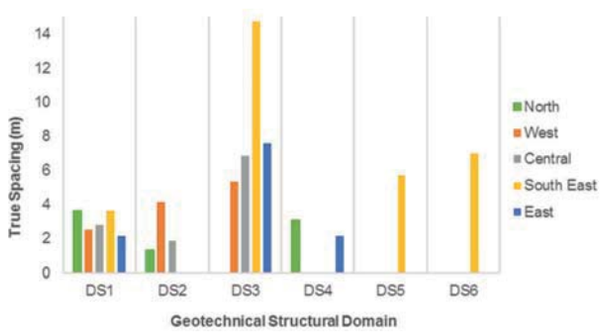

Figure 8—True discontinuity spacing for identified discontinuity sets in each structural domain

Table III

Discontinuity length assumptions

	Discontinuity length (m)
Minimum	2
Mean	10
Maximum	40

Table IV

Stope orientations analysed for each structural domain

Stopes	SOZ	Orientation	Structural domain
Transverse	SOZ1a	065	West
	SOZ1b	115	West
	SOZ2	085	North
	SOZ3	010	East
	SOZ4	035	Central
	SOZ4	035	Southeast
	SOZ5	090	West
Longitudinal	SOZ1b	030	West
	SOZ2	150	North
	SOZ2	000	North
	SOZ5	155	West
	SOZ5	000	North

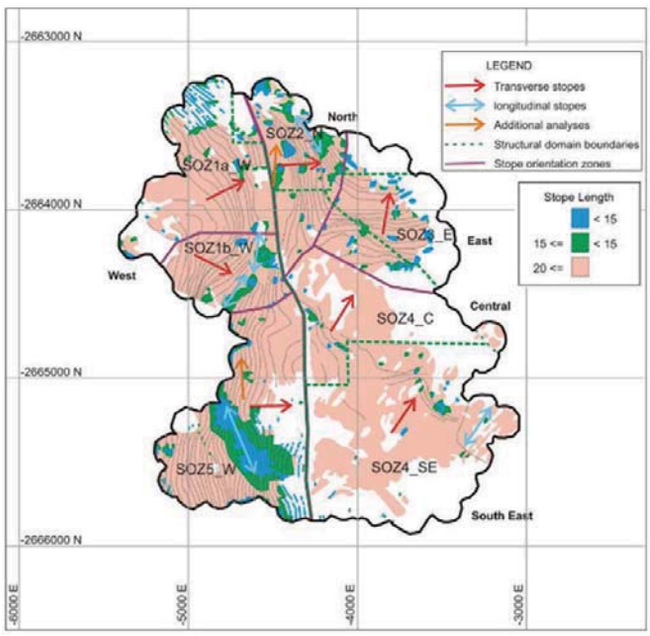

Figure 9—Stope orientations zones in each structural domain

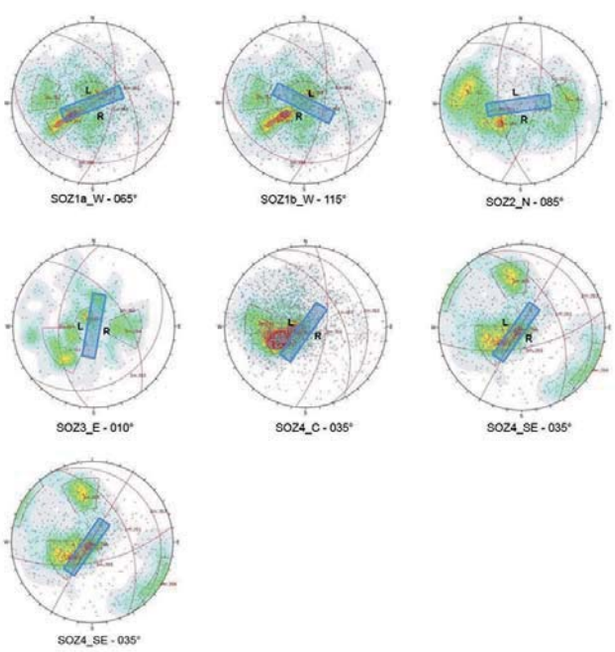

Figure 10—Stereographic projections with transverse stope orientations overlaid for each structural domain

Table V

Stope dimensions

Length (m)	60
Width (m)	15
Height (m)	25
Dip of excavation (°)	0

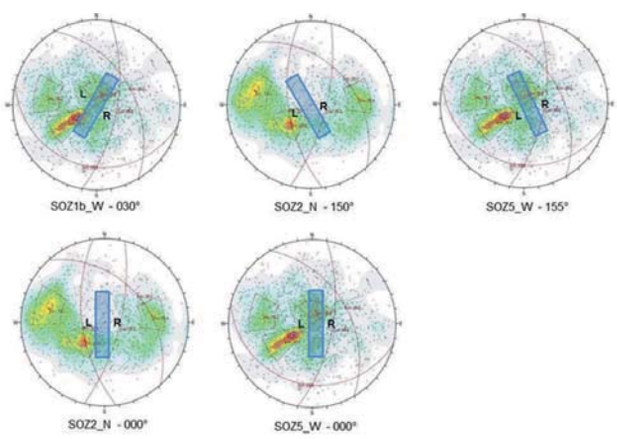

Figure 11—Stereographic projections with longitudinal stope orientations overlaid for each structural domain

- Dip and dip direction of each discontinuity set (Table I.)
- Friction angles for each discontinuity set (Table II). Note that JBlock uses a truncated normal distribution to represent the discontinuities' friction angles. A minimum and maximum cut off of 15° and 75° were thus chosen based on the results from the friction angle calculations
- Discontinuity spacing for each set (Figure 8)
- Discontinuity trace lengths (Table III)
- Stope dimensions (Table V).

JBlock is limited in that it can analyse only one surface at a time (Dunn, Earl, and Watson, 2008). Keyblocks were therefore generated and analysed for three excavation surfaces independently and the results combined. While this provides a useful analysis, it should be noted that the blocks in corners of the stope are not taken into account. The excavation surfaces analysed are as follows:

- Left stope wall (without support)
- Right stope wall (without support)
- Back (with mesh and resin rebar support).

An example of the creation of keyblocks is illustrated in Figure 12a. A typical keyblock size distribution based on keyblock generation is presented in Figure 12b.

Rockfall simulation

Support patterns were applied to the backs with generated keyblocks in each SOZ. The support consisted of 3 m long, 150 kN bolts spaced at 1.5 x 1.8 m, with 750 kN/m grout and 15 kN/m^2 mesh (support represents a 6 m wide arched profile drift above a 15 m wide stope). Jblock uses a very simple method to account for mesh and the mesh strength was set to ensure that the bulk of the smaller blocks are held in place.

Rockfalls from the keyblocks, and the support pattern in the case of the stope back, were simulated for each SOZ. During a rockfall simulation a limit equilibrium analysis is performed on each of the keyblocks, which are placed in random positions within the walls or back of the stope to determine whether failure occurs or not. It then tests for support failure, failure between support, and rotational failure (Esterhuizen, 2003). Should failure occur, the exposed surface area from the rockfall is recorded, which allows the number of simulated rockfalls to be normalized.

Additional input parameters required for the rockfall simulations are presented in Table VI. A rockfall simulation in progress is presented in Figure 13.

Results

The results of the keyblock analyses are summarized in Tables VII and VIII, which indicate the combined results for the stope back and stope walls. Using these results, expected linear overbreak was calculated by dividing the fallout volume by the total area exposed for each SOZ. This is based on the ELOS (equivalent linear overbreak/slough) approach (Clark and Pakalnis, 1997).

The resultant rockfalls normalized to a 60 m advance for a range of block sizes are presented in Figures 14 and 15 for the transverse and the longitudinal stopes. Note that these results combine the sidewalls and the back of the excavation. The simulated number of rockfalls was determined for block sizes from 0.1 m^3 to 1 000 m^3. Note that the results were normalized to rockfalls per 60 m advance using the fallout volume and the relevant stope dimensions.

Discussion

The following should be noted from the analysis.

Transverse stopes

- Large rockfalls are more likely to occur in SOZ2_N and SOZ4_SE compared with the rest of the stope orientation zones (more than one 10 m^3 rockfall per 60 m advance).
- This is due to the discontinuity set orientations in the north and southeast domains which are ideally suited

Table VI

Rockfall simulation parameters

General		Hazard analysis	
Density	3000 kg/m^3	Min. no. of mining step simulations	1
External load	10 kPa	Min. no. of times to test each block	3
Aspect ratio	1		

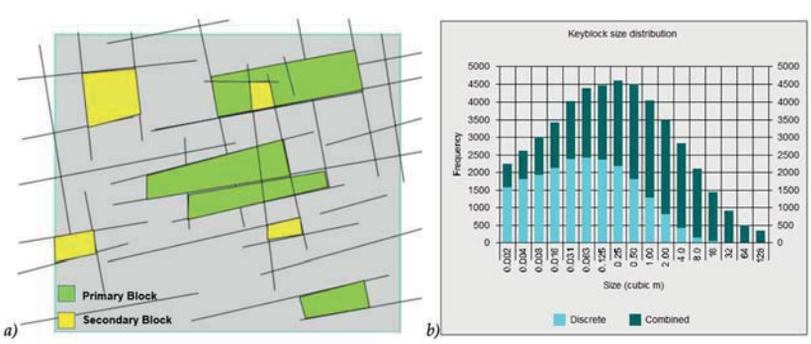

Figure 12—(a) Keyblock generation on an excavation surface, (b) keyblock size distribution from keyblock generation

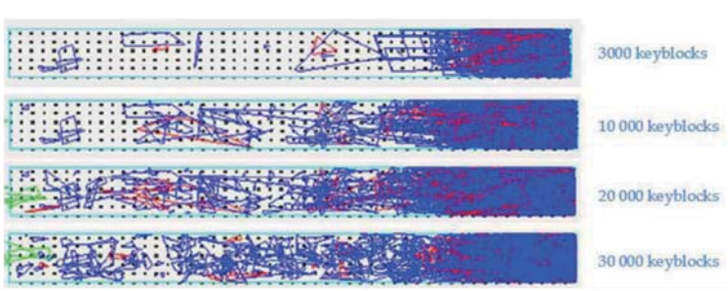

Figure 13—Rockfall simulation as it progresses for a stope back, where blue blocks are stable, green blocks are formed outside the excavation, and red blocks indicate failure of the block

Table VII

Keyblock analysis results for transverse stopes

Likelihood of rockfall	Total no. of keyblocks	No. of failed blocks (%)	Failed area (%)	Failed block overbreak (m)	Expected linear overbreak (m³)	Max. volume (m²)	Max. area	Max. height (m)
SOZ1a_W	751 515	1 754	0.23	0.53	0.004	344	90	8
SOZ1b_W	772 951	5 477	0.71	1.45	0.013	552	143	11
SOZ2_N	440 328	7 712	1.75	4.63	0.046	681	166	11
SOZ3_E	612 899	9 454	1.54	1.92	0.014	388	115	9
SOZ4_SE	663 308	13 129	1.98	4.57	0.034	644	178	9
SOZ4_SE no J6	978 307	7 884	0.81	2.86	0.017	1041	237	11
SOZ4_C	804 185	6 207	0.77	0.64	0.004	120	76	5
SOZ5_W	763 734	2 798	0.37	1.05	0.008	379	129	9

Table VIII

Keyblock analysis results for longitudinal stopes

Likelihood of rockfall	Total no. of keyblocks	No. of failed blocks (%)	Failed blocks (%)	Failed block area (%)	Expected linear overbreak (m)	Max. volume (m³)	Max. area (m²)	Max. height (m)
SOZ1b_W	761 415	34 018	4.47	4.52	0.021	255	179	8
SOZ2_N_150	465 636	26 157	5.62	7.74	0.056	625	193	9
SOZ2_N_000	512 056	42 259	8.25	7.63	0.048	463	198	9
SOZ5_W_155	759 584	46 778	6.16	6.41	0.038	438	139	10
SOZ5_W_000	512 465	18 506	3.61	3.16	0.024	369	122	7

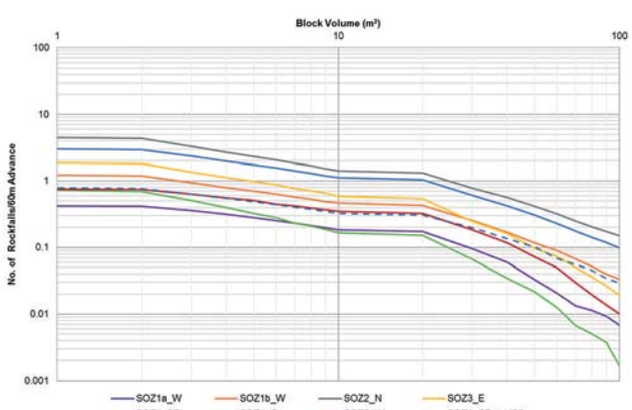

Figure 14—Keyblock analysis results for transverse stopes

to form wedges with the orientation of the stope walls (Figure 10).

- Note that the southeast structural domain was also simulated with and without discontinuity set 6. This set was identified from data from two drill-holes, and is likely to be localized and consequently may have had too much of an influence on the overall result for SOZ4_SE.
- When simulated without DS6, the failed block area for SOZ4_SE reduced from 5% to 3%.
- Overall, the expected linear overbreak from geological structures for these stopes is low and unplanned dilution will not be a major concern.
- The risk of damaging incidents due to large rockfalls is more significant, especially in the walls, for SOZ2_N and SOZ4_SE, but this is considered manageable.

Longitudinal stopes

- Generally, one or more large (> 10 m³) rockfalls are expected per 60 m advance.
- Overall SOZ2_N poses the highest risk of all longitudinal orientations analysed.
- The expected linear overbreak is higher in the longitudinal stopes compared with the transverse stopes. This is expected due to the increased hazard associated with mining parallel to sub-parallel to the orientation of the Tshukudu Fault and associated discontinuity sets.
- The longitudinal stopes are less stable than the transverse stopes.

Figure 15—Keyblock analysis results for longitudinal stopes

Conclusions

Based on the study the following may be concluded:

- There will be less hazard in excavating the transverse stopes in the orientations proposed compared with the longitudinal stopes.
- It would be unfavourable to mine in the longitudinal orientations due to the increased hazard associated with mining parallel to sub-parallel to the orientation of the Tshukudu Fault and associated discontinuity sets.
- Where stope orientations cannot be designed taking into consideration the orientation of major structures, keyblock analyses will also allow the testing of various support scenarios, which will assist in hazard reduction and allow for optimal support design.
- Once the mine is in operation, these analyses should be re-run with mapped data and calibrated with observations from mined stopes in each of the orientations. This will allow for a reduction in the uncertainties related to drill-hole data, such as discontinuity length and directional bias. This will also allow for the identification of localized joint sets and potential wedges/instabilities that may be present.

Keyblock analysis was used successfully as a design tool to assess the stability of the mining stopes at Platreef mine considering the dominant discontinuity sets and the structural domains identified across the project area. Outcomes of the study have provided Platreef mine with valuable information that will assist in the decision-making process when finalizing stope orientations and support requirements.

The risk of production delays and damage to machinery can be mitigated by optimizing the mining direction. This study also brings to light the importance of undertaking thorough structural analyses, which in this case greatly assisted in determining the results produced.

Acknowledgements

The management of Ivanhoe Mines and Ivanplats are thanked for funding the work and for permission to publish the results.

References

Barton, N., Lien, R., and Lunde, J. 1974. Engineering classification of rock masses for the design of tunnel support. *Rock Mechanics*, vol. 6. pp. 189–236.

Barton, N. 2002. Some new Q-value correlations to assist in site characterisation and tunnel design. *International Journal of Rock Mechanics and Mining Sciences*, vol. 39. pp. 185–216.

Brits, J.A.N. and Nielsen, S.A. 2015. Report on the structural interpretation of the farms Turfspruit and Macalacaskop. Ivanplats. 97 pp.

Clark, L. and Pakalnis, R. 1997. An empirical design approach for estimating unplanned dilution from open stope hangingingwalls and footwalls. *Proceedings of the 99th Annual AGM-CIM conference*, Vancouver, BC. CIM, Montreal. pp. 1–34.

Dunn, M.J., Earl, P., and Watson, J. 2008. Support design using probabilistic keyblock methods. *Proceedings of the 6th International Symposium on Ground Support in Mining and Civil Engineering Applications*, Cape Town. Stacey, T.R. and Malan, D.F. (eds.). Southern African Institute of Mining and Metallurgy. Johannesburg. pp. 623–636.

Dunn, M.J. and Stacey, T.R. 2008. Design of stable spans at Tau Lekoa Mine. *Proceedings of the 1st Southern Hemisphere International Rock Mechanics Symposium*. Potvin, Y., Carter, J., Dyskin, A.D., and Jeffrey, R. (eds.). Australian Centre for Geomechanics, Perth. pp. 179–192.

Dunn, M.J. 2010. The application of probabilistic keyblock methods for support design in blocky rock masses. *Proceedings of the 2nd Australasian Ground Control in Mining Conference 2010*, Sydney. Australia. Hagan, P. and Saydam, S. (eds.). Australasian Institute of Mining and Metallurgy, Melbourne. pp. 106–112.

Esterhuizen, G.S. 2003. JBlock User's Manual. Department of Mining Engineering, University of Pretoria.

Esterhuizen, G.S. and Streuders, S.B. 1998. Rockfall hazard evaluation using probabilistic keyblock analysis. *Journal of the South African Institute of Mining and Metallurgy*, vol. 98, no. 2. pp. 59–63.

Hattingh, E. and Hudson, T. 2016. Characterisation and description of the Tshukudu Fault influence zone. Ivanhoe Mines, Mokapane, South Africa. 17 pp.

Ivanhoe Mines. 2015. Report on the structural interpretation of the farms Turfspuit and Macalacaskop – Zone 1 and Zone 3, Platreef Project. Mokapane, South Africa. 86 pp.

Joughin, W.C., Jager, A., Nezomba, E., and Rwodzi, L. 2012. A risk evaluation model for support design in Bushveld Complex underground mines: Part I - Description of the model. *Journal of the Southern African Institute of Mining and Metallurgy*, vol. 112, no. 1. pp. 1-12.

SRK Consulting. 2016. Platreef 4Mtpa Feasibility Study. Section 5 - Underground Mining Geotechnical Investigation and Design. *DRA Report Number* 1051-EV-00-29. Johannesburg, South Africa. 95 pp.

Windsor, C.R. and Thompson, A.G. 1992. Reinforcement design for jointed rock masses. *Proceedings of the 33rd US Symposium on Rock Mechanics*, Sante Fe. American Rock Mechanics Association, Alexandria, VA. pp. 521–530. ◆

http://dx.doi.org/10.17159/2411-9717/2018/v118n3a8

Early access microseismic monitoring using sensors installed in long boreholes

by T. Butler* and B. Simser†

Synopsis

For deep mines where a microseismic monitoring programme will be implemented, one of the obstacles during the early stages of mine development is how to obtain adequate three-dimensional microseismic monitoring coverage with minimal access to the rock volume. The ability to utilize existing or planned exploration or geological boreholes for seismic sensor placement is offered as a cost-effective solution to this problem. For existing mines planning to mine new, deeper ore zones, the ability to install seismic sensors in long boreholes is especially important where long ramps are being developed in high-stress/burst-prone ground where rockbursting could be expected and microseismic monitoring is required as part of a comprehensive ground control safety programme. Lessons learned from the installation and operation of seismic systems at Glencore's Nickel Rim South and Fraser Morgan mines are presented and suggested strategies for establishing new seismic monitoring systems at new mines are discussed. A case study is presented from Glencore's Nickel Rim Deep Project in Sudbury, Ontario, Canada showing how seismic sensors installed in subhorizontal geological 'scout-holes' drilled ahead of the ramp development end are being used for monitoring ramp and infrastructure development of a new mining zone in deep high-stress ground.

Keywords
microseismicity, three-dimensional monitoring, longhole sensors.

Introduction

Establishing microseismic monitoring for mines early in the mine development cycle is important from a worker safety perspective, but early seismic monitoring can also provide valuable information about the nature of the rock mass response to mining when little other rock mass data exists. Seismic information can help identify the seismic nature of different geological units in the rock mass, and may also help determine the location and nature of existing geological discontinuities. The recording of microseismicity early in the mine's life is often the first type of 'deformation feedback' from the rock mass available to the ground control engineer, and the seismic information collected in early stages of mine development can enhance the accuracy of numerical models (Beck and Brady, 2001).

One of the major obstacles to the early deployment of a seismic monitoring system is the perceived lack of access for sensor (geophone or accelerometer) installation. For seismic systems to provide accurate source locations and source parameters, good three-dimensional (3D) spatial positioning of the sensors is usually required, preferably with sensors located around and within the volume of rock mass being monitored. In general, most seismic sensors in new mining areas are installed only after development levels have been established and drill rigs can be positioned to drill short sensor holes, usually just deep enough to ensure good contact beyond the fracture zone. The lack of an adequate number of sensors and/or adequate spatial positioning in the early days of mining will result in inferior seismic monitoring coverage until much later in the mine development cycle when more access is available and additional sensors can be installed.

A basic history of seismic system network deployment for Glencore's Nickel Rim South (NRS) mine and the Fraser Morgan mine is presented, highlighting some lessons learned. This experience, coupled with advances in sensor installation techniques, has resulted in a new strategy of installing sensors in long boreholes to provide early seismic monitoring coverage, initially for safety purposes. This strategy was employed successfully to monitor the first deep-level ramp development for the Nickel Rim Deep (NRD) project from May 2014 to November 2016. Details of this project are presented. The same technique, with some improvements based on knowledge gained from the NRD monitoring project, is being used to provide seismic monitoring coverage for ramp development at Glencore's new

* *Engineering Seismology Group (ESG) Canada Inc., Canada.*

† *Sudbury Integrated Nickel Operations, A Glencore Company, Canada.*

 This paper was first presented at the AfriRock 2017 International Symposium, *30 September –6 October 2017, Cape Town Convention Centre, Cape Town.*

Onaping Depth project (ODP), which started in February 2017. For both projects, the ramp sensors will be used as the starting point for new seismic monitoring arrays to cover additional mine infrastructure development, shaft sinking, and initial mining operations.

Seismic monitoring at Glencore's Sudbury Integrated Nickel Operations

Nickel Rim South Mine

The NRS mine is a nickel/copper operation located in the Sudbury Basin in Ontario, Canada. Stoping operations began in May 2009. Details of the ESG seismic monitoring system installed at NRS and some practical applications can be found in Simser *et al.* (2015) and Simser and Butler (2016). The seismic monitoring programme started in January 2009 with the initial sensors deployed in early development drives. Figure 1 shows the seismic array, with sensor locations as of 2013. The sensors include a mixture of uniaxial accelerometers (50 Hz to 2.5 kHz) and 15 Hz triaxial geophones. The 15 Hz geophones were incrementally added starting in 2010 to provide improved dynamic range. As mining progressed, the NRS seismic array benefitted from both hangingwall and footwall access that provided reasonable 3D coverage of the mining zones. In late 2016 the seismic array consisted of 57 working sensors (21 triaxial 15 Hz geophones and 36 uniaxial accelerometers) with an average sensor spacing of 150 m. This combination of sensors results in good seismic coverage within the moment magnitude range of -2 to +2 (Simser and Butler, 2016). In addition, 4.5 Hz geophones placed in the far field are used for large event magnitude estimates as well as for correlation to the Sudbury Regional Seismic Network (Hudyma and Beneteau, 2010). Array sensor density is highest in the west flank of the orebody, where sensors were installed in first access development from 2007 to 2009.

Fraser Morgan Mine

The Fraser Morgan mine is a blast-hole nickel operation offset a few kilometres from the narrow-vein Fraser copper mine in the Sudbury basin in Ontario, Canada, and is located about 70 km west of NRS. Both Fraser mines are accessed via the same shaft system and each mine has its own seismic monitoring system. The Fraser Morgan mine seismic system currently monitors seismic activity from two distinct mining zones between 1000 and 1500 m below surface. The array started recording seismic events in May 2013, and has been incrementally expanded as mine development has progressed.

Figure 2a shows a plan view of the Fraser Morgan mine 39-2 level development horizon at 1200 m depth, with the seismic sensors plotted as they existed in 2014. The seismic system consisted of seven triaxial 15 Hz geophones and three uniaxial 15 Hz geophones that were installed in development that was available at the time. Unfortunately, development access was only available from the geological footwall side of the orebody, resulting in a seismic array that was largely planar in nature, with most active mining being outside the array. Figure 2b shows the exploration boreholes that had been drilled at Fraser Morgan mine. Figure 2c shows a comparison of seismic event and orepass noise locations at Fraser Morgan 11 zone from 2014 and 2016. In 2016, the seismic system had expanded to nine triaxial 15 Hz geophones, nine uniaxial 15 Hz geophones, five uniaxial accelerometers (50 Hz to 2.5 kHz), and two 4.5 Hz strong ground motion geophones. The reduction in event location scatter in 2016 is clearly evident and is due largely to the enhanced seismic array that provided better 3D coverage and improved event location accuracy. This example illustrates the importance of installing a sufficient number of sensors in a new mining area and having good 3D distribution of these sensors so that accurate seismic event locations are possible.

In hindsight, it would have been possible to install sensors in the long exploration/orebody delineation boreholes drilled from early development drives or in boreholes drilled specifically for the sensors prior to the start of mining in May 2013. Once a drill rig is in place, it is not a large cost to drill a second hole if required. Fraser Morgan mine is in the process of installing several additional sensors in long boreholes to help improve the 3D coverage of the seismic monitoring array.

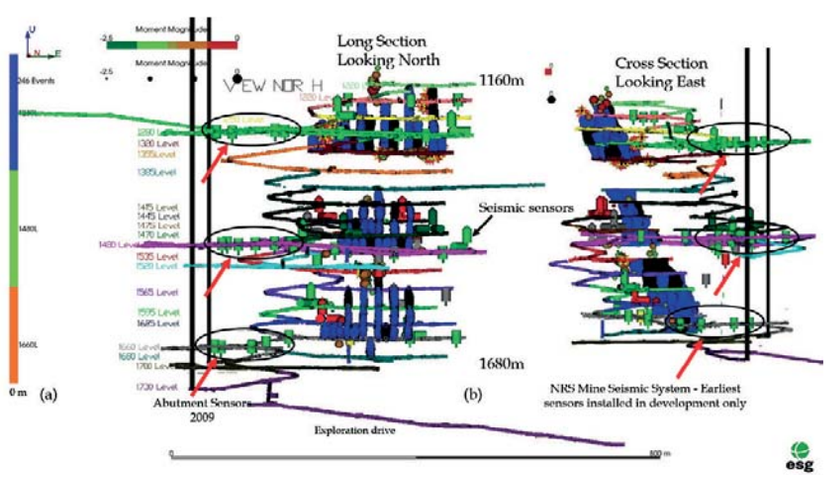

Figure 1—Long section (a) and cross-section (b) of Glencore's Nickel Rim South mine showing mined stopes as of 2013. 5.3 m (H) × 5.0 m (W) mine development is shown in multi-colours. Seismic sensors are shown with exaggerated symbols in green. Red arrows/black circles indicate the initial sensor locations in early development tunnels in 2009

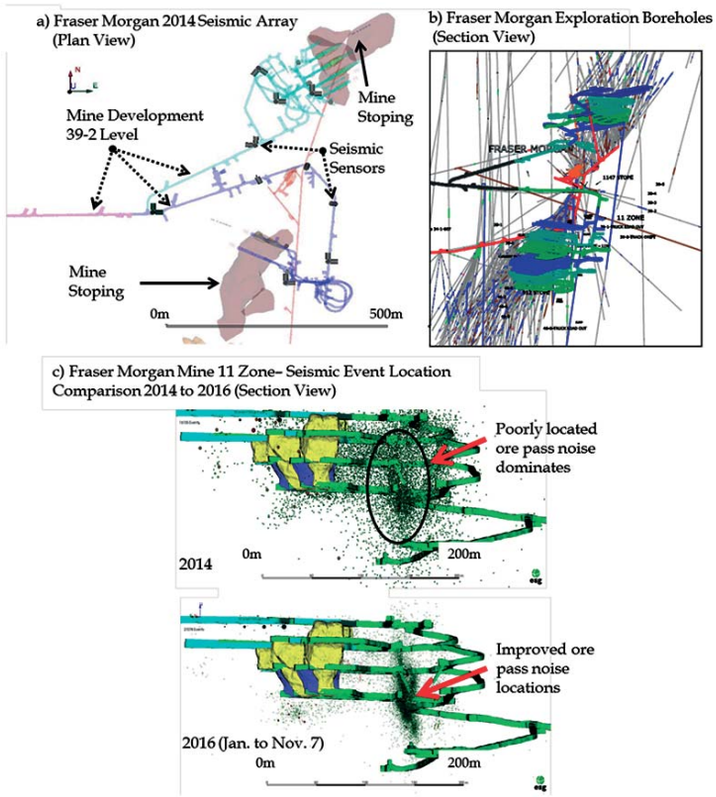

Figure 2—(a) Fraser Morgan seismic array and mining layout at the 39-2 level (1200 m below surface) in 2014, with mining located mostly outside the seismic array. (b) Available exploration boreholes (grey lines) at Fraser Morgan mine that could have been used for sensor installation. (c) Seismic data recorded in Fraser Morgan mine 11 zone during 2014 when the seismic array was planar in nature, compared to data recorded from January 1 to November 7, 2016 with the improved array

The above examples from NRS and Fraser Morgan show the typical life-cycle of deploying a seismic system for new mines. Sensors are installed in short boreholes, only from early development drives, simply because this is generally considered to be the first opportunity to access the rock mass. This approach greatly limits the seismic monitoring array to sensor positions that will rarely be ideal for good, or even adequate, seismic coverage during the early stages of mining. In reality, first access to the rock mass is usually provided by exploration boreholes. These boreholes can often provide a complete 3D opportunity for seismic sensor placement around the orebody and future mining zones.

New approach to establishing early seismic monitoring

Experience gained from establishing the seismic monitoring networks in the Sudbury area suggests that long borehole sensors could be used to monitor seismicity for development and for early establishment of mine-wide seismic monitoring arrays for new mining areas. The future for Glencore mining in the Sudbury area includes two new deep-level projects being accessed from existing Glencore mining infrastructure. These include the NRD project that is being accessed from the NRS mine and the ODP project to be accessed from existing Craig mine infrastructure. Details of the NRD project are presented. Lessons learned from the NRD project are being applied to seismic monitoring for the ODP ramp development, which is very similar in nature to the NRD ramp.

Nickel Rim Deep Project – overview

The conceptual layout for the NRD ramp and early mining infrastructure required to access two copper orebodies located between approximately 2500 m and 2900 m below surface is shown schematically in Figure 3. A 5 m wide × 5.3 m high exploration ramp/drift was driven 2.3 km from east to west, starting at the 1660 level (1660 m below surface) at NRS, from May 2014 to November 2016. The ramp was planned at a 15% grade to reach a maximum depth of 1965 m at the western end of the development drift. The end of the ramp will be the starting point for infrastructure to support mining the deeper deposit via an internal shaft. Face advance was planned at 4 m per day. A twin of the decline ramp started in January 2017 and is located 30 m south of the initial ramp.

Historically, Sudbury operations have encountered significant rockbursting in development far from mining. Post-incident investigations found that these bursts were usually associated with high and/or abnormal stress conditions caused by locally complex geology and/or geological structures. It was known that the NRD ramp would intersect several different rock types and several geological structures, including the Victor Shear striking south-southeast with 300 m apparent left-lateral movement. As a

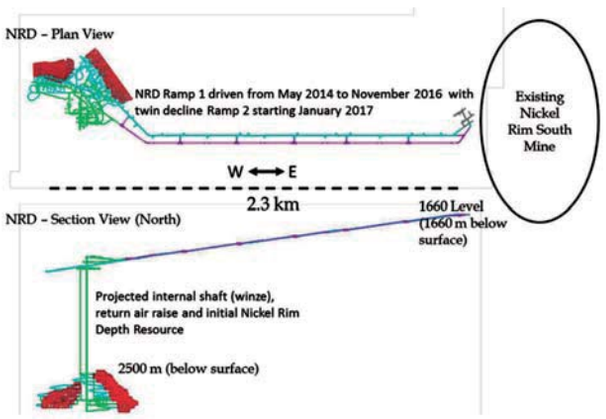

Figure 3—The NRD deposit will be accessed via twinned ramps driven from the existing NRS mine at the 1660 level. The plan is to access the ore zone at 2500 m below surface via an internal shaft (winze)

result, Glencore decided to develop a standardized process to evaluate the potential conditions of new mining areas prior to development. The geological part of this process involved drilling approximately 600 m long subhorizontal (–9° to –14° dip) 'scout-holes' (NQ/76 mm outside diameter) from the ramp out ahead of the face. The scout-holes were collared every 300 m along the drift and were drilled from truck turnaround cut-outs in the ramp. Drill core was obtained and logged for geological and geotechnical properties. Acoustic and optical televiewer instrumentation was pulled along the length of each uncased borehole to image the hole and obtain detailed fracture locations and orientations. The probes were attached to a 1/4 inch Kevlar rope threaded through a pulley that was anchored with a brush assembly installed at the bottom of the hole. It took approximately one hour to pull the probe to the end of the hole. Each scan involved pulling the probe uphole at a rate of 1.5 m/min by electric winch, with the entire scanning process taking six to seven hours per borehole.

At the same time the geological investigation was being planned, NRS ground control engineers were developing seismic monitoring plans for the NRD ramp and infrastructure. Communication between Geology, Ground Control, and ESG prior to ramp development resulted in a plan to use the pulley system to install sensors in the subhorizontal boreholes once the geological probe investigations were complete. Ground Control was confident that reasonable seismic coverage would be available from the main NRS array for the first few hundred metres of ramp development, but if successful, the longhole sensors would provide seismic monitoring coverage for the ramp and would become the backbone for the start of the NRD mining complex array. As a result, each of the nine scout-holes drilled ahead of the ramp face was instrumented with a two-inch diameter dual-element/high-sensitivity 15 Hz geophone. The sensors were installed at distances along the holes ranging from 400 to 450 m, using the same pulley system that was used for the probes. Once in position, the sensor pods were grouted in place to ensure good coupling with the rock mass. The earliest scout-hole sensors were supplemented with shared sensors from the main NRS array that were gradually removed from the NRD network as new scout-hole sensors were installed and increasing source-to-sensor distance eventually made them less effective.

The ramp development sensors will be important for seismic coverage for infrastructure development, shaft sinking, and early stage mining of the NRD orebody. These sensors will be supplemented with additional sensors installed in long vertical boreholes prior to shaft sinking to provide good 3D seismic monitoring coverage during the early stages of mining. The first of these vertical sensors has been installed and will be connected to the network once heavy equipment is finished with work in the hole collar area and the chance of sensor cable damage is minimized. Currently, the array is being used to monitor the twinned ramp and ongoing infrastructure development at NRD.

Nickel Rim Deep Project – seismic monitoring results

The main reason for ensuring adequate seismic monitoring coverage for the ramp development was to obtain information about the rock mass response to mining that could possibly provide early warning for development of a rockburst, such as an increase in seismic event rate. The seismic system at NRS is also used to determine when the rock mass has returned to more normal conditions after a large rockburst. It was expected that the NRD system would be used in the same manner for the ramp if a large seismic event was experienced. Secondary functions were to determine if specific geological structures were more seismically active than others, and whether differences in seismic nature could be observed between the geological units through which the ramp would be driven. The results had the potential to affect the ultimate location of the first ramp and the twinned secondary access ramp if problems related to seismicity were encountered and proved to be severe.

Ramp development started in May 2014, but it was determined that the first 200 m of drifting was close enough to the main NRS array for this system to be used to monitor the initial portion of the ramp. Once the first two scout-hole sensors were installed, a separate NRD network was created on the ESG system, consisting of the two 15 Hz dual-element triaxial geophones, supplemented with 15 uniaxial accelerometers, five triaxial 15 Hz geophones, and three uniaxial 15 Hz geophones shared with the main NRS array. Junction boxes for the scout-hole sensors contain one Paladin IV© data acquisition unit (six channels), allowing data collection from two of the triaxial sensors. Data transmission to surface is via fibre optic cable. The first seismic event recorded with the separate NRD array was on 9 October 2014. As the ramp moved further west from the NRS main array, more 15 Hz dual-element geophones were incrementally added as described above, and main array sensors were incrementally dropped from the NRD array when it was determined they were no longer contributing to the seismic event location solutions.

Figure 4 shows plan and sectional views of all blasting events recorded by the NRD seismic monitoring system from 9 October 2014 to 31 October 2016. Figure 5 shows plan and sectional views for all seismic events recorded and located during the same time period. Scout-hole and sensor positions are indicated in both figures. Fortunately, most of the seismic

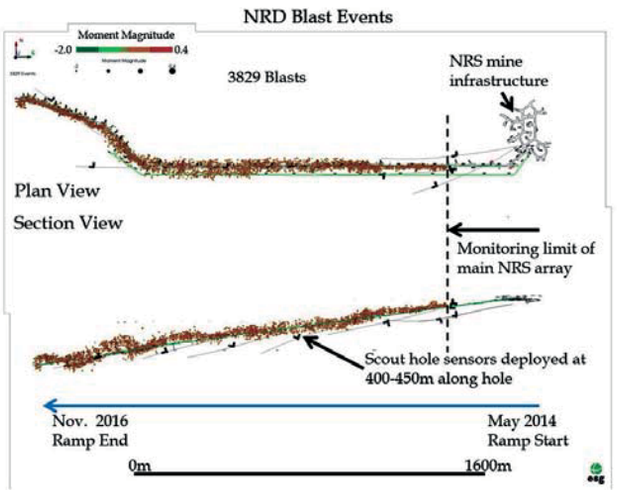

Figure 4—Plan and sectional views of blast events recorded by the NRD seismic monitoring system from 9 October 2014 to 31 October 2016

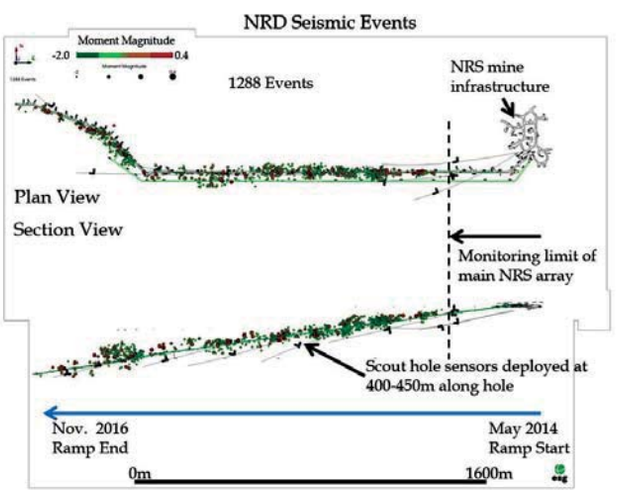

Figure 5—Plan and sectional views of seismic events recorded by the NRD seismic monitoring system from 9 October 2014 to 31 October 2016

events recorded by the NRD array were below moment magnitude 0.0 and no seismic events caused any significant damage during ramp development. There were no instances when workers were required to be removed from the heading.

In general, blasting and seismic events track the ramp development end well, with some scatter observed in the vertical during the latter stages of development as NRS main array sensors became less useful and were dropped from the NRD array. An unintended benefit was the use of the system by production managers for day-to-day ramp development planning. The ramp development was not tied to centralized blasting with the NRS mine due to the long distance between the NRD ramp and NRS main mining areas. A quick check of the seismic system allowed 'next shift' production managers to see at a glance if the previous shift had blasted. This saved time in underground planning for the next shift.

Table I shows the sensor status of the NRD seismic array at various dates throughout the project, and Figure 6 shows the number of uniaxial sensors used in the seismic event solution *versus* the event easting location. Uniaxial accelerometers from the main array were located at mine easting coordinates between E10000 and E10100. Figure 6 shows clearly that as ramp development progressed from an easting coordinate of E9700 to E7700 (2 km distance), the value of the uniaxial accelerometers in the array declined as fewer accelerometers were used in the seismic event solution. This was expected, as signal attenuation increases with sensor distance from the seismic event source. On 3 November 2015, with the ramp heading more than 1.4 km away, the last of the NRS main array sensors were removed

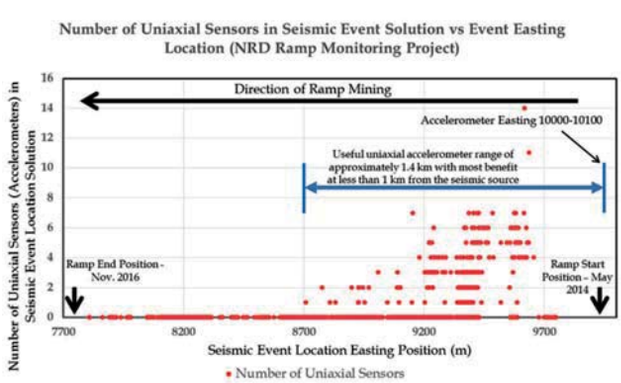

Figure 6—The number of uniaxial sensors included in the seismic event solution compared to the seismic event mine easting coordinate location. The data shows that uniaxial accelerometers are of most value when located less than 1 km from the seismic source

Table I

Sensor type distribution at various dates for the NRD seismic monitoring array

Date	NRD array sensors		NRS main array – supplemental sensors			
	NRD Tri. 15 Hz geo.dual-E	NRD Tri. 15 Hz geo. std	NRS Tri. 15 Hz geo. std	NRS Uni. 15 Hz geo.	NRS Uni. accel.	Total sensors
Oct-14	2	0	5	3	15	25
Mar-15	4	1	4	1	5	15
Apr-15	5	1	2	0	3	11
Jul-15	6	1	2	0	3	12
Aug-15	6	1	2	0	3	12
Oct-15	7	1	2	0	3	13
Nov-15	7	1	0	0	0	8
Mar-16	9	1	0	0	0	10
Oct -16	9	1	0	0	0	10
Dec-16	9	1	0	0	0	10

from the NRD array. This information is important for future monitoring requirements at NRD and for other projects in similar rock types such as ODP, as it indicates that the maximum benefit of the accelerometers is obtained at seismic source to sensor distances of less than 1 km. Beyond 1 km distance between source and sensor, the signal to noise ratio becomes too low for the accelerometers to provide much useful information for small seismic events.

Although there was no overall change in the total number of sensors in the NRD array from March 2016 to December 2016, there were changes in the individual sensors used during this period. A single dual-element 15 Hz geophone sensor was installed in a 700 m long vertical borehole to provide some vertical offset from the linear nature of the array and improve seismic event locations in the vertical direction. This sensor operated briefly and was disconnected when it was found that the junction box was mounted in a place where further development for the twin ramp was required. This sensor will be reactivated once production operations are finished in the area. One of the earlier scout-hole sensors was transferred to the NRS main array to help improve seismic locations of events recorded in the west side of NRS. Other factors influencing the sensitivity of the system and the nature of the data recorded included a triaxial sensor orientation calibration that was performed in December 2015. This calibration allowed the use of sensor orientations in the location algorithms and all previous data was reprocessed using this new algorithm.

The prime purpose of the seismic system was to help ensure the safety of workers at the ramp development face. All changes to the system were made with the intent of providing the best possible timely seismic information to mine personnel. Unfortunately, the changing system sensitivity over time makes seismic event data analysis somewhat more difficult, because it is not always clear if observations from the data are real or are influenced by changes in the seismic monitoring array. All observations discussed below consider the nature of the seismic array in assessing the data, and any conclusions are supported with underground observations from ground control engineers and workers at the face.

Figure 7 shows a plot of the cumulative event rate for all 1288 seismic events recorded by the NRD system and the event easting locations relative to time. The event easting locations generally track the ramp development heading with time, and show a change in slope from October 2015, when the ramp heading advance rate decreased when NRS production requirements took precedence over ramp face advance for NRS working crews.

The cumulative seismic events plotted in Figure 7 are not normalized for system sensitivity, but the large increase in event rate indicated coincides with the change in rock type intersected by the ramp. The ramp moved from the blocky, jointed hangingwall norite, with an unconfined compressive strength (UCS) of 200 MPa, into the stiffer footwall breccias (UCS 250 MPa) at E9570, and re-entered the norite at E8960. From past experience at NRS, a higher seismic event rate was expected in the breccia. Underground observations from workers indicated that the ground was 'working more' with more frequent audible 'pops' when the ramp was in the footwall breccia compared to the norite

Figure 8 shows the moment magnitude of seismic events plotted *versus* the easting position of the event. The general reduction in the number of low-magnitude events recorded with easting position is mostly a function of the loss of accelerometers with distance, as shown in Figure 6. The larger number of events recorded down to moment magnitude –1.4 between E8400 and E8200 coincides with the period when the ramp development intersected a more heavily faulted rock mass. These faults, dipping both east and west between 23° and 65°, are shown on the included mine plan. The increase in event rate during this period is also indicated in Figure 7.

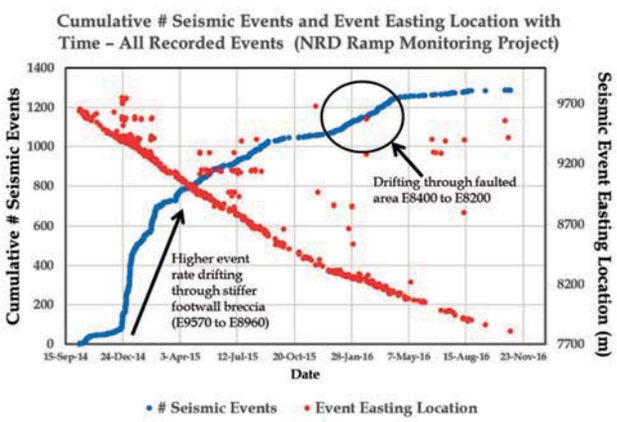

Figure 7—Cumulative number of seismic events and seismic event easting locations plotted with time for NRD ramp monitoring projec

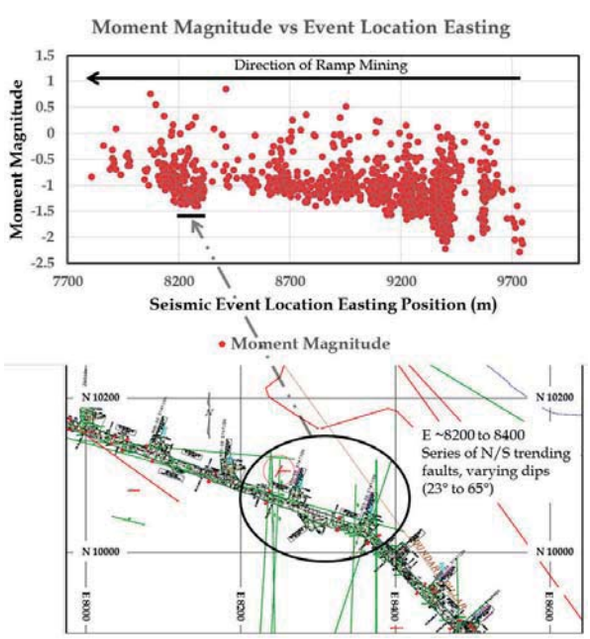

Figure 8—Moment magnitude of seismic events plotted as a function of event easting location. The event rate increased in the highlighted area due to a larger number of smaller seismic events recorded during the period the ramp intersected a series of faults between E8400 and E8200

Discussion and conclusions

The first access to new mining areas is almost always via geological exploration/orebody delineation boreholes. These boreholes can be expensive to drill and it makes sense to make the best use of these holes for the benefit of the entire mining operation. For mines that expect to establish a seismic monitoring programme, once core has been obtained and geological investigations are completed, it is proposed that some of these holes be used for the placement of seismic sensors. With proper planning, these boreholes can be used to help establish a good 3D seismic monitoring array during, or even before, the first stages of mine infrastructure development.

The NRD ramp seismic monitoring project utilized existing geological boreholes to place seismic sensors ahead of the ramp development face. This system helped ensure that any abnormal seismic activity would be recorded and acted upon by mine management, thereby enhancing the safety of workers at the face. The existing NRD ramp monitoring system will be the starting point for ongoing seismic monitoring for infrastructure development for the NRD mine, including shaft sinking operations. Further longhole sensors will be added in new geological exploration boreholes to help provide good 3D coverage of the initial mine development and to provide rock mass deformation information to the ground control department very early in the mine's life. The same techniques are being implemented for Glencore's ODP project, with the first ODP ramp monitoring system being commissioned in February 2017.

Some results were presented from data recorded from the seismic monitoring of the NRD ramp development. Different seismic activity rates were detected as the ramp traversed different geological units with different rock mass strengths and jointing patterns. It was noted that ground control personnel and mine seismologists should consider the impact of changes to the seismic system when interpreting the seismic data.

The strategies and techniques for microseismic monitoring discussed in this paper should be considered for mines that are accessing the orebody from either the hangingwall or footwall alone, as at the Fraser Morgan mine. Quite often the seismic arrays monitoring these types of mines are planar in nature and/or only monitor one side of the mining due to lack of development access. Sensors could be installed in long boreholes to reach the opposite side of the orebody to improve 3D seismic coverage and provide more accurate seismic information.

The strategies discussed should also be considered for new mines developing from surface. The cost savings could be substantial if a seismic monitoring programme could take advantage of the long exploration boreholes drilled from surface for seismic sensor emplacement. There can be hundreds of long boreholes available during the exploration stage, often providing complete 3D access to the entire planned mining volume. Before grouting the holes closed, seismic sensors could be located in positions that will never be accessed again during the life of the mine. Currently, these are simply lost opportunities to create a seismic monitoring array with exceptional 3D coverage. The added advantage of early deployment of seismic monitoring for new mining projects is that background seismicity levels can be established for mines located in naturally seismically active areas.

Early seismic sensor placement at various elevations in exploration boreholes could also be highly beneficial to block caving mines and to mines with flat-lying deposits that suffer from limited access due to the planar nature of the mining. The ability to have sensors located above and below the mining horizon greatly improves the quality of the seismic data recorded.

Using surface boreholes for deep seismic sensor installation could also significantly reduce the quantity of seismic sensors required to be installed from within the mine. This could potentially eliminate the costs of a significant amount of seismic and communication hardware and cable, as well as the associated logistical costs to install and maintain this equipment underground.

Acknowledgements

The authors would like to thank Steve Falconer, Chris Goulet, Chris O'Connor and Ed Deneka from Sudbury Integrated Nickel Operations for their contributions to the NRD monitoring project. Ali Jalbout, formerly of Sudbury Integrated Nickel Operations, was instrumental in organizing the first implementation of the scout-hole sensor deployments and spearheading the start of the NRD monitoring project. Dave Collins and the ESG Advanced Analysis Group performed the triaxial sensor orientation and calibration.

The authors would also like to thank Glencore and ESG management for their support in implementing innovative solutions using new technologies.

References

Beck, D.A. and Brady, B.H.G. 2001. Evaluation and application of controlling parameters for seismic events in hard-rock mines. *International Journal of Rock Mechanics and Mining Sciences*, vol. 39, no. 5. pp. 633-642. doi: 10.1016/S1365-1609(02)00061-8

Hudyma, M. and Beneteau, D. 2010. Sudbury regional seismic network. *Proceedings of the CIM Maintenance Engineering and Mine Operators Conference*, Sudbury, Ontario. CIM, Montreal.

Simser, B. and Butler, T. 2016. Ground support practice at Glencore's nickel rim south mine – with a link to seismic monitoring data. *Proceedings of the Eighth International Symposium on Ground Support in Mining and Underground Construction*, Luleå University of Technology, Luleå, Sweden. Nordlund, E., Jones T.H., and Eitzenberger, A. (eds.). Luleå University of Technology.

Simser, B., Deredin, R., Jalbout, A., and Butler, T. 2015. Use of microseismic monitoring data as an aid to rock mechanics decision making and mine design verification. *Proceedings of the 49th US Rock Mechanics/Geomechanics Symposium*, San Francisco, CA, 28 June–1 July. American Rock Mechanics Association, Alexandria, VA. Paper 15-374.

Sweby, G., Trifu, C., Goodchild, D., and Morris, L. 2006. High resolution seismic monitoring at Mt. Keith open pit mine. *Proceedings of the 41st US Rock Mechanics Symposium*, Golden, CO. American Rock Mechanics Association, Alexandria, VA. Paper 06-1159.

Trifu, C-I., Shumila, V., and Leslie, I. 2008. Application of joint seismic event location techniques at Chuquicamata open pit mine, Chile. *MassMin 2008 – Proceedings of the 5th International Conference and Exhibition on Mass Mining*, Lulea, Sweden, 9-11 June 2008. Schunnesson, H. and Nordlund, E. (eds.). Lulea University of Technology. pp. 943–952. ◆

SAIMM: Diamonds — Source to Use 2018 Conference

'Thriving in Changing Times'

11 June 2018 — Workshop: SAMREC/SAMVAL Reporting – Diamond Projects
12–13 June 2018 — Conference • 14 June 2018 — Technical Visits
Birchwood Conference Centre (Jet Park, Johannesburg)

BACKGROUND

Being the seventh conference in the series, the ***Diamonds – Source to Use*** conferences target the full spectrum of the diamond pipeline from exploration through to sales and marketing. The last conference in this series (***Diamonds – Still Sparkling***) was held in Botswana in 2016 and it is now returning to Johannesburg, where it was last held in 2013

Keynote Speakers

The State of the Diamond Market
E. Blom, *Blom Diamonds (Pty) Ltd*

Financing Diamond Projects
J. Campbell, *Botswana Diamonds PLC*

OBJECTIVE

The objective of the conference is to provide a forum for the dissemination of information relating to the latest tools and techniques applicable to all stages of the diamond industry; from exploration, through mine design, processing, to cutting, marketing and sales.

WHO SHOULD ATTEND

- Geologists
- Mineral (Diamond) Resource Managers
- Mining Engineers
- Process Engineers
- Consultants
- Suppliers
- Sales/marketing
- Diamantaires
- Mine Managers
- Mining Companies
- Students.

TOPICS

- Geology and exploration
- Mine expansion projects
- Mining, metallurgy and processing technology
- Rough diamond sales and marketing
- Cutting, polishing and retail
- Financial services and industry analysis
- Industry governance, beneficiation and legislation
- Mine-specific case-studies
- Value optimization.

Sponsors

De Beers Group of Companies
DEBTECH
DMS POWDERS
GEO-EXPLORE STORE (PTY) LTD
Imexsar DMS Ferrosilicon
MSA THE MSA GROUP
VIBRAMECH

SAIMM
THE SOUTHERN AFRICAN INSTITUTE OF MINING AND METALLURGY

For further information contact:
Camielah Jardine • Head of Conferencing · SAIMM • P O Box 61127 • Marshalltown 2107
Tel: (011) 834-1273/7• Fax: (011) 833-8156 or (011) 838-5923
E-mail: camielah@saimm.co.za • Website: http://www.saimm.co.za

Conference Announcement

http://dx.doi.org/10.17159/2411-9717/2018/v118n3a9

Development of the MOSH Leading Practice Adoption System – a science-based system for managing behaviour change

by J.M. Stewart* and S.M. Malatji†

Synopsis

Poor occupational health and safety performance in the mining sector during the 1980s led to establishment of the Leon Commission of Inquiry and ultimately to the Mine Health and Safety Act of 1996. In striving to achieve the tripartite OHS milestones established in 2003, the major mining companies agreed to pilot a system focused on facilitating the identification and widespread adoption of leading practice. The system included the use of behavioural communication techniques to address resistance-to-change effects. Piloting of the system served, however, to initiate a lengthy process of learning and system development, as many of the fundamental concepts and techniques of behavioural communication were found to be inadequately understood.

Achieving a practically useful understanding of these key concepts and processes took as long as three years, from 2008 to 2011. Evolution of this understanding is outlined in detail and key aspects of the resulting system and its processes are presented in summary form. The emergence of resistance at some mines to use of the MOSH adoption process is recognized and a constructive approach to addressing this issue is outlined.

The substantial improvement in safety performance achieved by industry since 2003 is described and various contributing factors are identified, with the adoption system being one of these. In addition to facilitating the adoption of various leading practices, particularly in the area of falls of ground, an important contribution of the adoption system is considered to be the focus on OHS issues that it has engendered in a large number of key people across the industry. The need for a much greater focus on occupational health issues in future years is highlighted and the new OHS milestones agreed to in 2014 are presented. In conclusion, the value of adopting a holistic long-term systems approach to address multi-facetted challenges, such as behavioural change and occupational health and safety, is highlighted.

Keywords

occupational health and safety, leading practice, technology transfer, innovation, decision science, behaviour change, mental models, risk communication, leadership behaviour, resistance to change.

Introduction

Development of the Mine Occupational Safety and Health (MOSH) Leading Practice Adoption System was initiated by the Chamber of Mines of South Africa on behalf of its members in April 2007. Its development formed part of a concerted effort by South Africa's major mining companies to achieve the 2013 Occupational Health and Safety (OHS) milestones that were agreed to by the tripartite partners in 2003 (MHSC, 2003). In many respects, the establishment of these milestones marked a turning point in addressing the long-standing OHS challenges in the mining industry.

It is in the context of this progress that development of the MOSH Leading Practice Adoption System is relevant. Although features of the Adoption System have been described in a few publications (van Zyl, 2010; Malatji and Stewart, 2013; Stewart and Butte, 2017, Hermanus, Coulson, and Pillay, 2014), no published paper has outlined its lengthy development process or clarified its science base. A similar comment applies to the many unpublished conference presentations, which have focused on the adoption of particular practices at mines. Much about the system and its development is thus not known or correctly understood.

Accordingly, this paper sets out a comprehensive account of the development process, including:

- Historical background to the development of the system
- Exploratory investigations prior to initial development of the system
- An outline of the originally envisaged system
- The extensive development that occurred after piloting of the originally envisaged system
- A summary of the developed system and its science base
- An assessment of the multifacetted impact of the system to date.

Background

Long-standing nature of the OHS challenge

The severity of the mining industry's long-standing OHS challenge is illustrated in Figure 1.

* *JM Stewart Consulting, South Africa.*

† *Chamber of Mines, South Africa.*

 ISSN 2225-6253. Paper received Dec. 2016; revised paper received Jul. 2017.

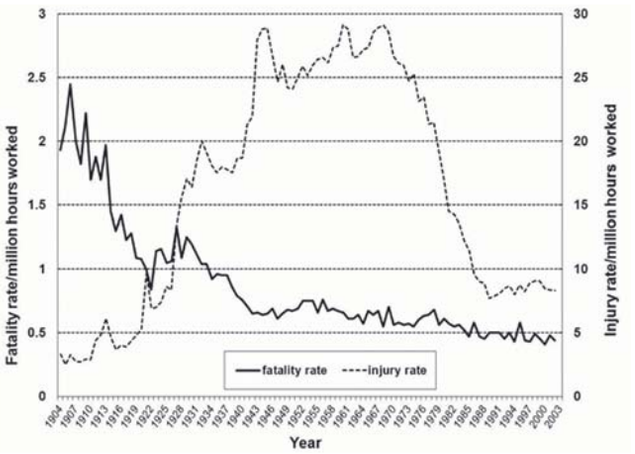

Figure 1—Fatality and injury rates in South African gold mines 1904–2002 (Gouws, 2004)

It should be noted that a fatality rate of 0.5 per million hours worked equates to an annual fatality rate of 1.3 deaths per thousand workers, and that in 1988 the gold mining industry employed as many as 480 000 workers (Harrington, McGlashan, and Chelkowska, 2004). Figure 1 shows that despite an initial period of rapid improvement, high fatality rates in South African Gold mines persisted through to 2002. The changing nature of the safety challenge over the years contributed to this. In the early years, as the extent and depth of mining increased, death from heatstroke due to extremely hot working conditions became a major problem. By 1930 the number of deaths per year from heatstroke had reached a level of about 1 per thousand (Wyndham, 1974). Significantly, as described elsewhere (Stewart 1982), this problem was largely eliminated through the development and application of effective heat tolerance testing and acclimatisation procedures. However, continual change in the scope and nature of mining inevitably gave rise to new challenges. This is illustrated by Figure 2, which, for the period 1984–001 shows the number of accidents per year across the industry that resulted in four or more deaths. Some of these major accidents were disasters, such as explosions and fires, which involved many more than four deaths, but many were caused by falls of ground. In the 1970s and 1980s, much attention was thus focused on the rock pressure problem and the elimination of rockbursts and fall-of-ground accidents. Notwithstanding these efforts, the rate of reduction in the industry's high fatality rate remained disappointingly low (Stewart, 1995).

Emerging dynamics to address safety and health at mines

Towards the end of the 1980s, the high fatality rate and its marginal rate of improvement, together with deteriorating financial circumstances and labour unrest, gave rise to a number of important dynamics in the mining industry. Significantly, given the looming cutbacks in the industry's cooperatively funded research programme, and in order to ensure continued focus on health and safety research, the then Government Mining Engineer established a levy-funded programme of research into occupational health and safety (Stewart, 2004). This programme later became the responsibility of the tripartite Safety in Mines Research Advisory Committee (SIMRAC), established under the Mine Health and Safety Act of 1996. However, and much more importantly, the emerging dynamics led to growing calls for the establishment of a Commission of Inquiry into occupational health and safety at mines.

The Leon Commission of Inquiry into Safety and Health in the South African Mining Industry was established in 1994 and its work was undertaken in the same year. Almost in parallel, and with much input from South African delegates, the International Labour Organization developed its Convention 176 on Mine Safety and Health. The convention was finalized in 1995. Both of these processes had the important effect of involving and focusing the attention of top-level management in each of the South African tripartite partners on how best to address the challenge of health and safety in mines. Significantly, the recommendations of the Leon Commission, together with the provisions of the ILO Convention, served to guide development of the Mine Health and Safety Act of 1996, and thus the tripartite structures and regulatory systems for addressing health and safety in South African mines that were established under the Act.

Establishment of tripartite-agreed OHS milestones

It is against this background that the Occupational Health and Safety milestones agreed to in 2003 by the tripartite partners of the Mine Health and Safety Council must be seen. In particular, it brings out the fact that the 2013 milestones agreed to in 2003 represent the articulation of a growing consensus across industry to both establish, and collectively address, the ultimate goal of achieving conditions of *zero harm* to persons at work. Progress in this direction was significantly accelerated in 2005 when the CEOs of major mining companies publicly committed their companies to achieving both the milestones and the ultimate goal of zero harm. This commitment led to the mobilization of needed resources. In particular, it led to establishment of a high-level task force charged with identifying how best to improve health and safety at mines. One of the areas identified for investigation was that of achieving successful technology transfer, and it was the work commissioned through the

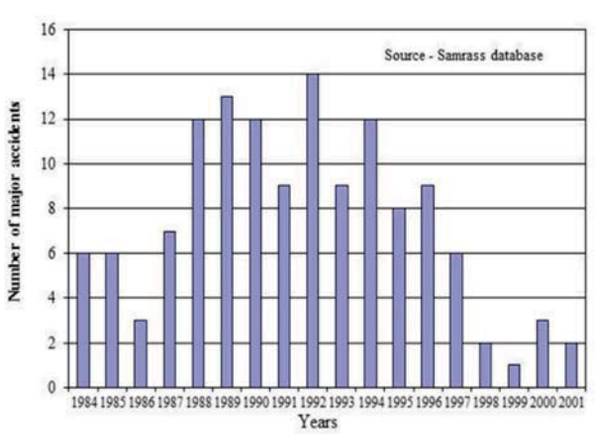

Figure 2—Number of major accidents per year, 1984–2001

Chamber of Mines to investigate this issue that ultimately evolved into the development of the MOSH Leading Practice Adoption System.

Exploratory investigations

The high-level task force recognized that a fresh approach would be needed to achieve the OHS improvements required by the 2013 milestones. In particular, it recognized that the limited time-scale for the required improvements made the adoption of a systematic R&D approach unrealistic. Accelerated use of available technology and best practice was thus identified as an important means of bringing about the improvements sought by 2013, and this became the focus of the work commissioned by the Chamber in 2007 on behalf of the task force. Accordingly, the first step in undertaking this work involved exploratory investigations to review both past and emerging industry experience with the adoption of new technology or practice.

At the time of commissioning the work it was also recognized that a fundamental understanding of the barriers and aids to both sharing and adopting new technology and practice should be established. The importance of achieving such an understanding had emerged in the approach taken by the Mining Association of Canada in their initiative on sustainable mining, (MAC, 2003). A parallel collaborative investigation by Decision Partners, specialists in decision-making and behaviour, was thus also commissioned by the Chamber to acquire this understanding (Stewart, 2007a, 2014).

Available industry experience

During the 1980s, effective technology transfer had become an increasingly important consideration within the Chamber of Mines Research Organization (COMRO), and various workshops and review studies were thus conducted during the period 1980–93. The findings of these investigations, which were summarized in various internal documents, were thus reviewed to distil the key concepts and insights of relevance to the challenge being addressed. In addition, the multifaceted work undertaken by the National Advisory Council on Innovation on the utilization of research findings (NACI, 2003) was similarly reviewed.

Given the ongoing accumulation of experience in operating companies in both technology transfer and the adoption of new practice, the latest experience of a wide range of organizations was also investigated. This included not only the major mining companies committed to achieving the 2013 OHS milestones, but also others. These investigations led to the development of a number of noteworthy insights. The various organizations investigated and the mechanisms identified are presented in Table I, and examples of the many key concepts and insights derived from the review process are given in Table II (Stewart, 2007b).

The findings and insights from this work provided a sound basis for selecting the mechanisms and processes included in the system that was developed and submitted in 2007 to the Chamber for consideration (Stewart, 2007a, 2014).

During the course of the investigations, the instructive value of considering these mechanisms and processes within the broad concept of innovation emerged. Importantly, the concept deals with the full spectrum of innovative activity, from creation to successful application. The requirement for successful application was particularly noteworthy, as it is an essential requirement in meeting the 2013 milestones. The scope of the concept is illustrated by the following definition:

> **Innovation** *involves the creation, exchange, evolution and application of knowledge, in whatever form, for the*

Table I

Organizations investigated and identified technology transfer mechanisms

Organizations investigated		
Impala Platinum	Sandvik	University of the Witwatersrand – School of Mining and Centre for Sustainability in Mining and Industry
Eskom	Sasol Chemicals	Chamber of Mines – Coaltech 2020
World Association of Nuclear Operators	Sasol Mining	International Council on Mining and Metals
Anglo American plc	Anglo American Platinum	Engen
Reunert Systems	BHP Billiton	Gold Fields
Australian Minerals Industry Safety and Health Centre	SIMRAC	Western Mining
Mechanisms identified		
Standalone organization	Communities of practice	Charter-based holistic health and safety management system
Benchmarking database	Project-based steering committees	A central facility for demonstration projects
Steering committees involving key stakeholders	Global peer group review mechanism	Electronic information systems
Specialist focus groups	Local peer group review mechanism	Incident-driven identification of technology and best practice
Mandatory company standards	Partnerships with suppliers	Centrally coordinated technology management system
Manager-level presentations and visits to share best practice	Focused high-level task force	Round-table forum to facilitate development of improved equipment

Table II

Concepts and insights derived from past work on technology transfer

No.	Examples of identified concepts/insights
1	Technology transfer comprises two distinct phases. The first phase involves providing sufficient understanding of the technology and its performance to enable potential recipients to decide whether to adopt the new technology/practice. The second phase is transfer of the knowledge and skills necessary to implement the technology.
2	The potential recipient of a technology/leading practice needs to have a real business incentive to embark upon the acquisition and adoption of the new technology/leading practice.
3	Recipients of the new technology need to be assisted, and to have access to expert assistance at an early stage of the transfer process.
4	The recipient organization needs to have a person at an appropriate level to facilitate and champion the technology transfer process.
5	The technology champion needs to be adequately supported by both his/her superiors and the technical experts of the technology/leading practice.
6	Champions need to be innovative and have credibility and integrity, placing successful implementation above personal ambition.
7	When the risk of implementing a new technology or practice is too great for the first adopter to bear alone, some form of underwriting or risk sharing may be necessary to facilitate successful transfer and implementation.
8	People at all levels must see the benefits to themselves of adopting the technology/practice.
9	Peer communication of applications and benefits of new technology/practice should be facilitated as it enables and generally assists the process of transfer and adoption.
10	The first recipient organizations to adopt a new technology/leading practice should be those that have the greatest need for and potential to benefit from successful adoption.

success of an organisation, the vitality of a nation's economy, and the advancement of society as a whole. Innovation cannot be claimed in the absence of successful application.

Expert model of innovation

While the NACI study referred to earlier had brought out the instructive value of an expert model of innovation, the more detailed expert model of innovation available from Decision Partners (Butte, 2007) was found to be even more useful. Accordingly, this model was then used to guide the overall system design aspects of the present work. A schematic of the model is presented in Figure 3.

A particularly important point brought out by this model is that the innovation process *starts with the establishment of a management orientation that supports and enables the innovation process*. This is a very important first step. In this context, it is important to point out that the various dynamics and developments described earlier had, unknowingly, already indirectly contributed towards the establishment of such a management orientation over the period 1990 to 2005.

Mental models research

In the collaborative work undertaken by Decision Partners, a programme of mental models research was conducted to identify barriers and aids in the South African mining industry to both sharing and operationally adopting new technology and practice. Their approach was based on extensive research, summarized by Morgan *et al.* (2002), that showed that peoples' judgement about complex issues is guided by their mental models, which are *the tacit webs of belief that they draw on to interpret and make inferences about issues that come to their attention*. Accordingly, a mental model may be defined as follows:

*A **mental model** is the sum total of all experience, in the form of knowledge and beliefs, which may be correct, in error, or incomplete, that a person has acquired about a particular topic or situation. It is the basis upon which individuals decide and respond to issues that arise.*

It follows from this that incomplete or incorrect beliefs and information can lead to compromised judgements and inappropriate behaviour.

Mental models cannot be determined without empirical research. The mental models research process undertaken by Decision Partners was briefly as follows. The important first step involved developing an expert understanding of the key factors and dynamics at play in the process of sharing and operationally adopting new technology and practice. This was derived from a meta-analysis of OHS conference presentations, and also discussions with selected industry experts, and was expressed in the form of an expert model. The methodology for deriving such expert models is considered in more detail later. The derived expert model was then taken as an accurate statement of all factors that materially influence OHS performance, including the process of sharing and operationally adopting new technology or

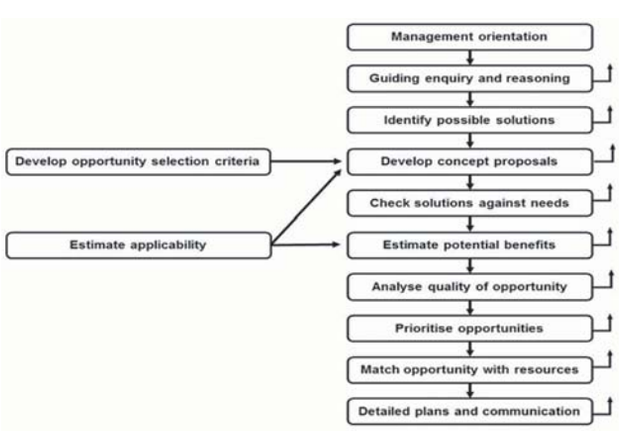

Figure 3—Schematic representation of expert model of innovation (Butte, 2007)

practice. One-on-one semi-structured interviews were then designed and conducted with a selection of individuals and their responses analysed to determine their beliefs and views in various areas. Together, these beliefs and views represent their prevailing mental models. Key findings from the study are presented in Table III. The summary report prepared by Decision Partners on their methodology and findings was included in the report setting out the adoption system that was proposed (Stewart, 2007a, 2014). An important aspect of this table is that in addition to identifying key barriers that need to be addressed, it identifies many avenues that can be positively built upon in adopting any new technology or practice.

Key success factors

In developing the proposal presented to the Chamber in 2007 (Stewart, 2007a, 2014), the following key success factors were identified and taken into account.

1. The key elements of the proposed system must be simple and clear so that industry executives are readily able to consider and adopt them as a basis for enabling implementation of the system.
2. The adoption mechanisms, and also the system, must engender a sense of Industry ownership, particularly for any aspects that might be centrally sponsored or located.
3. The adoption mechanisms must be able to accommodate the different approaches that may be required for the adoption of different technology and\or best practice.
4. The system must facilitate focused attention on the few top-level priorities identified by industry.
5. The time spent by industry persons in working with the system must be minimized and free of undue complexity.

Originally proposed system

Against the above background, the proposed system was designed (Stewart, 2007a, 2014) to facilitate the identification, sharing, and widespread *adoption of*:

- Worthwhile *best practice*
- Worthwhile *technology*, such as that emerging out of the SIMRAC research programme
- A *combination of practices and technologies* specially identified to address a *priority area* of occupational health and safety concern.

In developing the system it was recognized that no single mechanism could be used to achieve widespread operational adoption of technologies or practices in all situations. This important finding emerged during the review investigations. Although various mechanisms and processes individually delivered good results in particular circumstances, no single mechanism was successful in all circumstances. This explained the diversity of reported views and advice on how to achieve the adoption of technology or best practice. Accordingly, a system that used different mechanisms and processes to achieve both the identification and adoption of needed technology or practice for each of the above three situations was developed. However, the essential logic for the three situations remained constant and relatively simple, as follows:

- Assess risks and identify potential risk reduction solutions (operational improvements)
- Identify and document the most promising risk-reduction solution (technology or practice)
- Develop a plan for securing widespread adoption of the selected option

Table III

Key findings from mental models research into prevailing OHS factors across industry (%: Percentage of interviewees who identified the indicated factor)

Aids to implementation (adoption)	%	Barriers to adoption	%
Communicating with management and workforce	70	Resistance to change	55
Demonstrating personal commitment	68	Cost	55
Actively supporting implementation	52	Workforce not seeing benefit	43
Ensuring appropriate technology	29	Technological challenges	33
Providing training	29	Lack of management buy-in	28
Engaging workforce / management for buy-in	27	Training capacity	23
Reinforcing OHS culture	13	Production pressures	20
Monitoring results	13	Lack of workforce buy-in	20
		Lack of skills and education	20
		Organizational culture	19
		Social barriers	17
		Lack of time	15
		Inappropriate incentives	13
		Generation gap	12
		Other	21
Leading OHS activities at mines	**%**	**Most effective communications**	**%**
Implementing technology and best practice	47	Personal interaction	92
Conducting technology R&D	43	Meetings and workshops	55
Monitoring OHS performance	40	Underground site visits	27
Managing operations for OHS	34	Presentations	18
Coaching, training, and communications	25	Campaigns	8
Reinforcing safety culture	17	Visual communications	8
Accident assessment and response	8	On-the-job training	8
Seeking technology or best practice	4	Combination of methods	37
		Other	19

- Demonstrate and document the adoption process and the effectiveness of the selected option
- Communicate adoption details and potential benefits to industry (potential adopters)
- Facilitate a process to achieve widespread adoption.

Key features of the proposed system

In line with the above, the key features of the originally proposed system, which are considered essential, are shown schematically in Figure 4 and explained briefly below.

- *Enabling leadership and management*—In keeping with the expert model presented in Figure 3, the proposal outlined the need for leadership and management to create an environment that is enabling and reinforcing of adoption activity, and personally rewarding to those engaged in the adoption process. In particular, it included the establishment of recognition and reward arrangements for individuals who significantly facilitate the adoption process.
- *Direct industry involvement*—The importance of industry ownership and buy-in emerged as one of the most strongly and consistently expressed views in the exploratory work. Accordingly, the proposal required that the adoption teams, which lead and facilitate the adoption process, should be staffed by persons seconded from industry. Appropriate use of industry experts was also established as a core operational principle of the Adoption System.
- *Specialist secretariat support*—A key finding of the exploratory work was the difficulty that industry persons experience in devoting time to projects that are additional to their normal operational responsibilities. Accordingly, the system included a specialist secretariat to both enable and support the adoption teams, and also to ensure operational continuity and effective institutional memory.
- *Peer group reviews*—Conducting peer group reviews was identified in the exploratory investigations as an effective mechanism to identify and spread the adoption of good practice. The proposed system thus included the use of peer review teams to conduct detailed reviews of operations at participating mines to identify existing best practice, as well as areas in need of improvement. These reviews would be done at the request of mines, or at the request of industry but with approval by the mine in question. Best practices identified during the review would be documented, and then, with the permission of the source mine, openly communicated to other participating mines. The experience of the review team, along with best practice identified in previous reviews, would be considered in advising on any weaknesses identified at the mine being reviewed. Findings from the review would be presented to the mine in a confidential report. As explained later, this aspect of the originally proposed system was held back for later consideration.
- *Demonstration projects*—This element involved demonstrating adoption of an identified leading practice at an operating mine. Such projects would enable the leading practice or technology in question, as well as the adoption process, to be confirmed and refined, to the benefit of future adoption mines. Importantly, through site visits and informal peer-to-peer interaction, key information would be communicated to potential future adopters. In this way, the demonstration process would help spread and build the credibility of both the leading practice and the adoption process.
- *Communities of practice*—For each leading practice, this involved establishing a group of persons directly concerned with, or interested in adopting, the practice to voluntarily interact and exchange useful information in a relatively informal way. This is in line with the literature on communities of practice (Wenger, 1998; Smith, 2006; The Distance Consulting Company, 2000). Such groups serve not only to assist the widespread adoption of the practice, but also in its improvement. However, as outlined later, a much more structured approach was preferred.
- *Champions*—The positive role of 'technology champions' in facilitating the adoption of new technology was a key finding in the review investigation. Accordingly, it was established as a role that the head of each adoption team is expected to play. The key attributes of such a champion were then identified as major considerations in the selection of persons to not only lead the adoption teams, but also to energize and spearhead the process of achieving widespread adoption of the technology or best practice.
- *Facilitating structures and processes*—The establishment of simple but effective facilitating structures and processes was clearly fundamental to success of the system. Noting that different processes apply to each of the three adoption situations presented earlier, the essence of the structure that was originally proposed is presented in Figure 5, but without the Tripartite Advisory Body, which came later.
- *Quality communication*—All parties who play a role in the adoption process are communicating in one way or another all the time. Indeed, it was recognized that even the absence of action, and/or the presence of silence, is in practice a real form of communication; usually negative, and sometimes very powerfully so. This was a very important realization. Accordingly, the

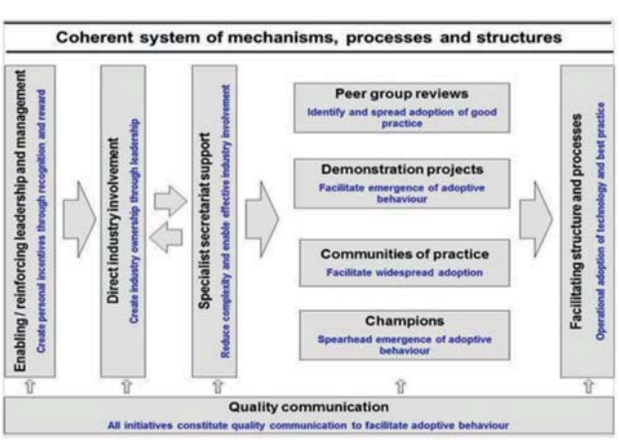

Figure 4—Key elements of originally proposed system for adoption of new technology and practice

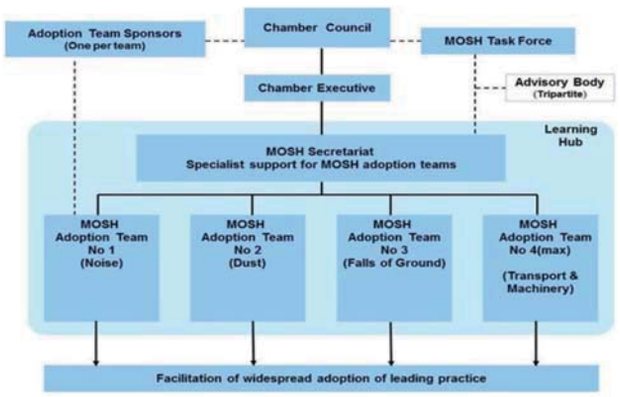

Figure 5—Structural arrangement of the proposed Adoption System

proposed system recognized that successful adoption depends on the full range of communications coming from persons having a stake in the adoption process. In effect, the right thing needed to be communicated to the right persons at the right time and in the right way. Quality communication was thus identified as fundamental to the collective effectiveness of all elements of the proposed Adoption System.

Decision to pilot the system

At the time of presenting the proposed system to CEOs of the major mining companies, it was recognized that pockets of excellence existed across the industry and that some mines were already achieving OHS performance levels in line with that required by the 2013 OHS milestones. This led industry to decide that initial application of the proposed system should be confined to identifying existing pockets of OHS excellence, and then facilitating the widespread adoption of such practices by other mines across industry. Significantly, it was agreed at the highest level that intellectual property in the area of OHS should be freely shared across industry. This is an important aspect of the environment created by leadership to enable innovation. Towards the end of 2007 it was agreed that the proposed system should be piloted, starting in 2008, but with its scope confined to *facilitating the identification and widespread adoption of existing leading practice*. Although the peer review process described above was thus excluded for later consideration, a form of peer review was used to identify existing leading practice, defined as follows:

> A *Leading Practice is a practice that is particularly effective at eliminating or reducing a particular occupational health and safety risk situation, and has potential for beneficial application in similar situations at other mines. It is selected by a MOSH Adoption Team following a rigorous selection procedure.*

Piloting of the system

Piloting of the down-scoped system, which became known as the MOSH Leading Practice Adoption System, formally commenced with a planning workshop in March 2008. A number of important enabling steps were, however, taken before this workshop. Firstly, towards the end of 2007 the MOSH task force identified that *falls of ground, silica dust, noise, and leadership* should be the four areas of OHS risk on which attention should be focused. Secondly, and in line with this, arrangements were made for suitable persons from industry to be seconded to the Chamber to serve as Adoption Team Managers in these areas. They were thus available and able to assist in preparing for the workshop, by providing input into the workbook that was collaboratively developed to guide activities during the workshop (Decision Partners 2008). Lastly, the process of identifying and appointing the high-level Adoption Team Sponsors depicted in Figure 5 was initiated. Appointment of these persons took time, but the important linking and guidance role played by these sponsors has proved to be an important aspect of the Adoption System.

Planning workshop

Participants in the planning workshop included the Adoption Team Managers as well as discipline specialists from the major mining companies. The specialists were selected on the understanding that they would later become advisory members of the adoption teams, but with execution of the agreed programme of work being undertaken by the full-time members of the team. At the planning workshop, the essence of the adoption system and process being piloted was presented as follows:

MOSH Task Force takes overall responsibility for enabling achievement of the 2013 OHS milestones

↓

Task Force identifies up to five top-level industry priorities to be addressed in parallel

↓

Industry leadership provides the necessary resources, in line with their decision to pilot the system

↓

Task Force facilitates establishment of adoption teams to plan and undertake the necessary work

↓

Adoption teams identify best opportunities (leading practices) for OHS improvement

↓

Adoption teams implement action plans to achieve widespread adoption of identified practices

↓

Task Force monitors and assesses outcomes and decides future activity.

During the course of a five-day workshop, each of the four adoption teams assessed the risks in their respective areas and identified the leading practices considered to have potential to improve OHS performance in their area. They then conducted a systematic review to select the practice with the greatest potential, and developed an initial draft plan outlining their future activities. Following the workshop, the teams then set about finalizing and implementing their plans. As outlined in the points that follow, this proved to be problematical and led to a significant learning experience. In retrospect, it marked the beginning of a process that led to clarification and development of many important aspects of the Adoption System, and in particular, the behavioural aspects of the system. Significantly, it is the behavioural aspects of the system that most differentiate it from other processes of innovation.

Process uncertainty

Soon after the planning workshop, it became apparent that the adoption teams differed significantly on how to implement the adoption process. Progress was thus both variable and limited. This issue was addressed by developing and providing a generic schedule to guide adoption team activity. While this provided clarity at one level, it did not provide sufficient guidance at the detail level on a number of the scheduled activities. In particular, it emerged that there was inadequate understanding by the teams of how to develop the behavioural communication plans required to facilitate widespread voluntary adoption of their selected leading practices. With the benefit of hindsight, it is now clear that this inadequate understanding was at a fundamental level. It took as long as three years to evolve a full understanding of the behavioural communication concept, and how it formed part of the broader mental models concept explained earlier in relatively simple terms. Failure to pass on this understanding right up front was a major weakness of the workshop. Unfortunately, it continues to be a challenge in introducing the system to new users. It is now recognized that achievement of the required understanding and buy-in involves a time-based process that cannot, in effect, be reduced to an event. An explanation of this important realisation is provided later.

Guidance notes – an emerging handbook

The uncertainty and variation between the teams in their approach to addressing certain of the scheduled activities led to the preparation of guidance notes to assist the teams to identify and collectively agree on how these aspects should be addressed. The initial guidance notes dealt with issues such as:

- A generic plan to guide the scheduling of adoption activity
- Identification of potential adoption mines and the key persons at those mines
- Documenting of the selected leading practice at its source mine
- Issues to be agreed with a mine prior to it hosting a demonstration project
- Establishing a Community of Practice for Adoption (COPA).

The value of such guidance notes was soon realized, and it became clear that it would be best if all guidance material were coherently consolidated into a single expandable handbook. Accordingly, the issues to be covered in such a handbook were collectively agreed, and a systematic approach to preparing the required guidance material commenced. Over the years, as new understanding and requirements emerged, the Handbook was updated and provided to the MOSH Adoption Teams for their use. The current version of the Handbook, which serves as a resource and guidance document to members of the Chamber's Learning Hub, including the adoption teams, is at revision 4.1 (Stewart, 2014). The Handbook was not, and is not, intended for general use at mines.

It will be evident from what follows that piloting of the system effectively became a process of ongoing system development as experience and understanding evolved.

Development of MOSH behavioural processes

Development of a proper understanding of the MOSH behavioural processes within the Learning Hub was both iterative and at times confusing as new concepts were disentangled from deeply embedded past experience. This stepwise learning and understanding of the science-based mental models concepts (Morgan *et al.*, 2002), which is described below, emerged in collaboration with Decision Partners. It emerged over the period 2008–2011, approximately in the following order:

Step 1: Recognition of the special nature of behavioural communication
Step 2: Appreciation of the need for one-on-one open-ended direct enquiries to identify the issues to be addressed through behavioural communication
Step 3: Recognition of the need for a systematic approach to analysing direct enquiry data
Step 4: Recognition of the need for the risk assessment to serve as a fully detailed expert model
Step 5: Appreciation of the logic and process in developing behavioural communication plans
Step 6: Recognition of leadership behaviour as an integral aspect of the behavioural process
Step 7: Recognition of the need to customize behavioural plans
Step 8: Recognition of the integrated systems nature of the behavioural processes.

The concept of behavioural communication

For many, it was difficult to understand why, and in what way, 'behavioural communication' was different from other forms of communication directed at achieving behavioural change. Some found it difficult to appreciate that the key difference lay in the way in which the content of the communication was derived. In particular, it needed to be derived from a careful process of enquiry in order to empirically determine the knowledge gaps, misperceptions, myths, and other aspects of the prevailing mental models that were influencing the behaviour in the intended recipients. Behavioural communication was thus the set of messages specifically designed to address these and other mental processes that influence behaviour.

It was eventually appreciated that such communication provides persons with information and understanding that enables them to make better decisions. Such communication is thus empowering. Importantly, it results in more appropriate behaviour in response to circumstances as they arise. It therefore has the power to induce a change in behaviour in an entirely respectful way.

Behavioural communication is thus in principle quite different from similar-sounding communication delivered with the purpose of telling or instructing people how they should behave in various circumstances. Unfortunately, the latter is typical of much of the communication traditionally used in the mining industry and thus deeply imbedded in many experienced mining personnel. Adoption of the new paradigm, and the various processes described below for its implementation, proved to be a challenge to such people.

Development of an expert model in assessing risk

While the need to conduct a detailed risk assessment to assist

with the identification and selection of the most beneficial leading practice resonated with the adoption teams, the need for it to also serve as an expert model of the situation was clearly not adequately emphasized during the planning workshop. It was not initially appreciated by all that the risk assessment, expressed in the form of a causal chain, was indeed a form of expert model. The required rigour of the process in developing a fully detailed expert model had thus also not been adequately outlined.

Accordingly, and in keeping with their experience, the adoption teams had focused on the need to identify the key risks and then on how best to address the risk situation. The need for a fully detailed and accurate expert model as a basis for identifying the knowledge gaps, misperceptions, myths, and other mental processes that would be needed later was thus not properly appreciated. This only emerged much later, during the process of developing behavioural communication plans, when the need for such information became clear.

In regard to an expert model, it was important to emphasize that the model must not simply become the adoption team or management's detailed view of the situation. Development of an expert model must involve a process that enlists and considers input from expert sources at all levels. Clearly, the finally agreed outcome of such a process may differ considerably from the view initially held by either the adoption team or operational management.

As a more complete understanding emerged of the crucial need for a high-quality expert model in deriving a sound behavioural communication plan, the value of also developing and expressing the expert model in the form of an influence diagram was recognized. Accordingly, detailed guidance for developing both forms of expert model were developed and made available to the adoption teams. The essential elements of these two forms of expert model are outlined below.

- *Causal chain risk assessment*—A causal chain risk assessment covers the following three primary elements in assessing and describing the risk situation, in both qualitative and quantitative terms:
  - The nature of the hazard
  - Exposure to the hazard
  - Outcomes from exposure to the hazard.

The guidance developed to assist in producing such a risk assessment pointed out that, depending on the situation, each of these elements may warrant being subdivided into sub-elements. Particular aspects of each of the elements then need to be identified and fully described, with data gaps in need of investigation also being identified, along with weaknesses in control and mitigation strategies, and also ways in which the risk can be reduced for those most at risk. The guidance included the template shown in Table IV for presenting the risk assessment.

- *Influence diagram*—An influence diagram similarly identifies the key factors involved in the risk situation, as well as their causal links, but in a way that more clearly depicts the way in which each factor influences other factors. As shown in Figure 6, each factor serves as a node in the influence diagram, with various shapes being used to depict different types of node. The influences are then represented by arrows connecting each node to other nodes that the factor influences. Descriptions of the various factors and each of the influences are then recorded to complete the expert model.

Direct enquiries to identify prevailing mental models

Although the adoption teams readily accepted that the prevailing mental models of a group of persons needed to be determined empirically, the procedure for doing this was initially unclear. Once again the high-level conceptual guidance provided during the initial planning workshop needed to be operationalized into a set of practical guidelines and procedures for planning and conducting a programme of direct enquiries.

Guidance was thus developed for the preparation of a protocol, including a questionnaire, for use in confidential interviews with an appropriate selection of persons. The selected persons needed to be drawn from the complete set of potential adoption mines, and to be representative of persons who would be directly involved in adoption of the leading

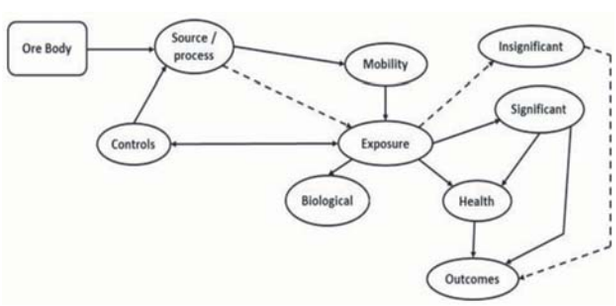

Figure 6—Expert model for dust risk in an early stage of development

Table IV

Tabular format and content requirements of a causal chain risk assessment

Part A: Causal Chain		
Nature of the hazard	Exposure to the hazard	Outcomes of exposure
Data gaps	Data gaps	Data gaps
Part B: Current risk controls and strategies		
Risk controls / strategies	Risk controls / strategies	Risk controls / strategies
Weaknesses	Weaknesses	Weaknesses
Part C: Possible improvements in risk mitigation controls and strategies		
Improvements	Improvements	Improvements
Possible new practices	Possible new practices	Possible new practices

practice. This qualitative research process required that about 25 to 30 people be selected and interviewed. Although larger numbers could be used, previous experience had shown that little additional information emerged after analysis of about 25 to 30 interview records.

The questionnaire needed to be comprised of open-ended probing questions that allow and enable the interviewee to share deeply held thoughts and beliefs about the key aspects of the situation identified in the expert model. This included consideration of:

- What people know about the risks and practice that is correct and essential to making an informed decision
- What people may misunderstand that is consequential
- What they do not know that is consequential
- What they want to know that is important to them
- What they know about the envisaged new practice
- What management's role is in addressing the risks
- What criteria they use to judge the trustworthiness and competence of people, organizations, and communications.

The guidance recognized that the aspect of confidentiality would be of crucial importance, as would be the requirement that all interviewees participate voluntarily in the interview process. These aspects were dealt with in the procedural guidance on setting up and conducting the enquiries.

Analysis of the interview responses in relation to an expert understanding of the risk situation then enables determination of relevant knowledge gaps, misperceptions and misbeliefs, and any other misunderstandings relevant to adoption of the selected leading practice in addressing the risk situation. Together, these elements become a statement of the prevailing mental model. Arriving at this statement does, however, involve a careful process of coding and collating the responses from all interviewees, and guidance was thus developed to assist the adoption teams in undertaking this work. Table V provides an indication of the format and content of a mental model empirically derived from such a process.

A secondary, but significant benefit associated with the direct enquiry process is that it meaningfully engages a number of persons directly involved in adoption of the leading practice. Realization of this benefit does, however, require the provision of meaningful feedback to those involved in the adoption process. Significantly, this requirement is effectively addressed through implementation of the behavioural communication and leadership behaviour plans considered below.

Preparation of generic behavioural plans

Once again, the process of preparing a behavioural communication plan proved to be a learning experience. Indeed, the first behavioural communication plans were prepared under the direct supervision of the collaborating consultants, Decision Partners. Based on their input, guidance to assist the adoption teams in the process for preparing behavioural communication plans was developed and included in the Handbook.

Having determined the prevailing mental models, the process involves the following three relatively simple steps:

- First, logically group the misperceptions, misunderstanding, knowledge gaps, and any other beliefs or considerations that would either facilitate or inhibit successful adoption of the leading practice
- Then, determine the implications of each of these beliefs as well as the information that needs to be successfully communicated to build on or address the identified implications
- Finally, develop a detailed behavioural communication plan that sets out who is to communicate what, and how, to ensure that the identified information reaches the intended recipients.

While the development of a generically applicable behavioural communication plan is undertaken by the relevant MOSH adoption team, the selection of persons to deliver the identified messages at the mine clearly needs to be a mine responsibility. This is an important responsibility, since selection of credible persons to deliver the identified messages is crucially important. The template provided in the Handbook for capturing a detailed behavioural communication plan is shown in Table VI.

Preparation of leadership behaviour plans

Although the enabling role of leadership was brought out in the original design of the system, the key role of leadership

Table V

Format and example content of an empirically derived mental model report

Major theme	Sub-theme	Description of theme	Summary of findings
Cause of falls of ground	Procedures	Procedures are not followed. This could be due to many barriers, such as worker skills or experience, cutting corners, supervision	This was the most significantly mentioned cause mentioned by about 75% of interviewees, representing all mine positions. Interviewees identified 'lack of barring' 'incorrect support', 'poor examination' *etc.*….
	Unforeseen		
	Technical		
Barriers or challenges to address	Skill	Worker skills / experience / expertise / qualifications / not adequate	This was the most commonly mentioned barrier linked to the cause of FOG. Skill was often linked to a lack of understanding of 'why' rather than 'what' or 'how'. For example: 'The people know how to bar but not why – they rush straight to the face and begin face preparation'. *Etc.*……
	Buy-in		
	Etc.		
The report goes on to cover a number other major themes, with each major theme having many sub-themes			

Table VI

Template showing details required in a behavioural communication plan

No.	Belief /issue being addressed	Recipient	Message / communication content	Mode (Meetings training briefings *etc.*)	Tools / means (Scripts presentations) theatre- *etc.*)	When	Responsibility for delivery	Who to ensure	Evaluation/ control measure
1									
2									
Etc.									

Table VII

Template showing details required in a leadership behaviour plan

Leadership levels Details of all relevant level of operation and leadership	Antecedents Things that are required to enable, prompt or precede delivery of identified key behaviours	Behaviour Key behaviours that are essential for successful adoption and operation of the practice	Consequences Actions to be taken to reinforce or discourage observed behaviour
Operator / technician			
First line supervisor			
Second level supervisor			
Third level supervisor			
Others, *etc.*			
Highest level manager			

behaviour, explicitly in the form of the well-known A-B-C concept (antecedent-behaviour-consequences), only emerged during the process of developing the behavioural communication plans.

In simple terms, the elements of the A-B-C concept are as follows:

- ***Antecedents*** are the things that prompt and enable behaviour, such as training, proper tools, briefings, *etc.*
- ***Behaviour*** is anything a person does or says, or fails to do or say, good or bad
- ***Consequences*** are actions or events, that follow exhibited behaviour, and that serve to reinforce or discourage the behaviour in question.

The concept, originally developed by Skinner (1952), has been adapted and used in various ways in industry (Scott Geller, 2005; National Mining Association 2016). Unfortunately, this has sometimes had counterproductive effects, particularly when used in the South African mining industry to identify unsafe behaviour by individuals, and thus to inadvertently apportion blame (Smith, 1999).

Consideration of the A-B-C concept by Decision Partners in the development of behavioural communication plans was thus unexpected, but was in retrospect entirely logical. The logical link between behavioural communication and the A-B-C concept lies in their similarity of purpose. Behavioural communication seeks to inform people to enable better decision-making, and thus more appropriate consequential behaviour in adopting a leading practice to address a prevailing risk situation. Similarly, the A-B-C concept seeks to equip people with the understanding and skills needed to undertake key tasks in operating and overseeing the leading practice being introduced. Significantly, the A-B-C concept also seeks to entrench those behaviours responsible for successful execution of the key operational and oversight tasks associated with ongoing successful operation of the practice. In essence, both therefore seek to equip people to voluntarily behave in appropriate ways in adopting a particular leading practice to reduce risk. Importantly, together, they serve as a means for securing eager, voluntary and sustainable adoption of an identified leading practice.

Based on the above understanding, guidance to assist adoption teams in the preparation of leadership behaviour plans was prepared. This included use of the direct enquiry and mental models process to assist in identifying content for inclusion in the leadership behaviour plans. Guidance was also provided on identification of the key technical and behavioural aspects of successfully operating the leading practice that needed to be addressed in the plan. The template developed for capturing a detailed leadership behaviour plan is shown in Table VII.

Particularly noteworthy aspects of such leadership behaviour plans include the following:

- Details are specified for all levels of operation and leadership that are crucial to successful adoption
- Securing provision of the required antecedents is a key behaviour of higher levels of leadership.
- The identified actions as a consequence of exhibited behaviour are key behaviours of higher leadership levels
- Consistently applied actions as a consequence of observed behaviour are crucial to achieving sustainable adoption
- The plan systematically specifies and integrates the actions of all persons needed to secure successful and sustainable adoption of the leading practice.

Customization of behavioural plans

As understanding of the principles and practicalities of behavioural communication grew, so too did concern about how best to take account of differences between mines. It was recognized that mines could differ quite significantly in both operational and management approach and culture, and that a generally applicable behavioural communication plan would therefore need to be adjusted to address significant mine-specific issues. A simplified direct enquiry and analysis process was thus developed to identify such issues, thus forming a basis for customizing the generic behavioural communication plans developed by the MOSH adoption teams.

An important consideration in developing the customization process was to keep it as simple and practical as possible for application at mines. A relatively simple direct enquiry process based on ten standard questions was thus designed. Although simpler, it still required 25 to 30 persons to be interviewed at the mine. Analysis of the interview responses was then similarly simplified to focus on identifying only those mine-specific issues not already covered by the generic behavioural communication plans. Appropriately, detailed guidance was prepared to assist mines in customizing the generic plans provided by the MOSH adoption teams.

The MOSH behavioural processes as a science-based system

As the above described understanding grew, it became increasingly clear that the various behavioural processes needed to be seen as parts of a coherent behaviour management system. It also became clear that together they gave practical effect to extensive scientific work on both mental models and human behaviour. Based on the above, and as depicted in Figure 7, the essential logic of the integrated system may be summarised briefly as follows:

- ***System logic***—*In any given situation a person's behaviour is guided by their mental model of that situation (for example, the adoption of a new practice to address an OHS risk). This mental model is determined by analysis of responses gained in a one-on-one semi-structured interview. Formulation of the open-ended questions used in the interview is guided by an expert understanding of the situation. This expert understanding, in the form of an expert model, is developed through a prior engagement process involving technical and operational experts. Key issues (knowledge gaps and misbeliefs) in the person's empirically determined mental model are identified by comparison with the expert model. Communication is then developed and used to address the identified mental model issues. In addition, behaviour essential to successfully address the given situation is identified from the expert understanding of the situation. Leadership behaviour needed to enable and sustainably achieve these essential behaviours is then identified and implemented.*

The science base of the integrated system is summarized briefly as follows:

- ***Science base***—*Since 1932, when the concept of a mental model was first defined, many scientific studies have been published (Wood et al., 2017). As described in detail by Morgan et al. (2002), such work provides the basis of the mental models elements of the system. Similarly, since Skinner published his basic work on human behaviour (Skinner, 1952), his concepts have been widely accepted and applied by others (Scott Geller, 2005; National Mining Association, 2016). This work provides the basis of the behaviour management elements of the system. Together, the elements on mental models and behaviour management constitute an integrated science-based system.*

The science-based behavioural processes described above can then be presented as an operational system, as shown in Figure 8.

Importantly, Figure 8 depicts the various behavioural processes as an integrated system designed to facilitate eager, voluntary, and sustainable adoption of a leading practice. This science-based integrated system of practical processes is an aspect of the leading practice adoption system that differentiates it from other processes of technological innovation.

Explanation and detailed guidance on practical implementation of all of the above behavioural concepts and processes is provided in the Handbook (Stewart, 2014).

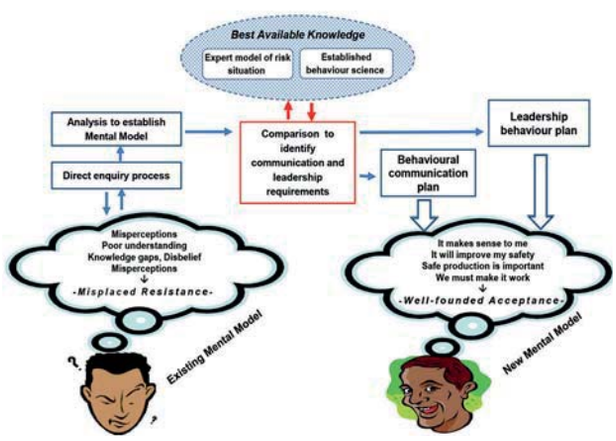

Figure 7—Schematic of factors involved in behaviour management

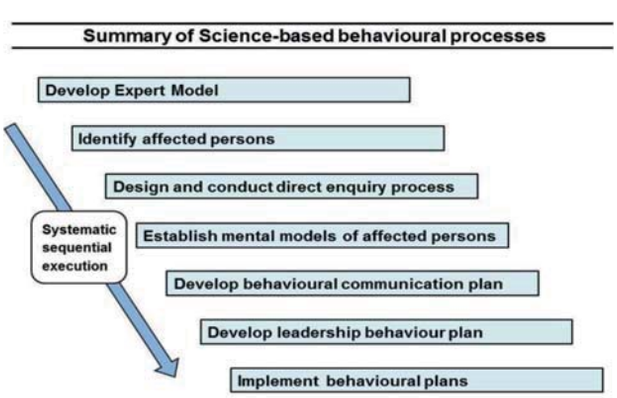

Figure 8—Schematic of essential MOSH behavioural processes

Key challenges in development of the overall system

Although development of the MOSH behavioural processes represented a major step forward, there were a number of other important developments in evolution of the overall system.

Communities of practice for adoption

In developing the guidelines for initiating and operating a successful community of practice for adoption (COPA), it soon became apparent that there was both a strong preference and need for the COPAs to operate in a much more structured manner than originally envisaged. In particular, a MOSH adoption team manager, serving as the COPA coordinator, needed to fulfil a number of key functions, as follows:

- Explaining the various adoption processes to COPA members
- Assisting mine adoption teams with implementation of the adoption processes
- Training or arranging training of mine persons in direct enquiry techniques
- Monitoring and reporting to industry on progress at mines in the adoption of leading practices
- Arranging presentations at COPA meetings to facilitate the exchange of adoption experience at mines
- Arranging and conducting regular COPA meetings to enable and sustain the adoption process.

Guidelines were accordingly developed and provided for the COPAs to be established and operated in this way. The key role of the COPAs in facilitating widespread adoption of leading practice soon emerged, particularly in respect of the COPAs established in the area dealing with falls of ground. In essence, the COPA harnessed, sustained, and directed the collective energy of a group of peers to acquire and apply the skills needed to secure successful adoption of a leading practice at their respective mines. In so doing the COPAs became the key means of effectively energizing and facilitating the widespread adoption of leading practice, and thus progress towards the achievement of zero harm. Fundamental to the establishment of a successful COPA was the identification and involvement of those people at potential adoption mines who would be central to deciding and enabling successful adoption of the practice at those mines. This key aspect of the process was emphasized in the guidelines that were developed, and in progress meetings of the adoption teams.

Process requirements at adoption mines

Notwithstanding the participation of mine representatives in COPA meetings, and the explanation and guidance provided during those meetings, the teams established at mines to manage adoption encountered a number of difficulties. Most of these difficulties were associated with the 'people aspects' of the adoption process, namely customization and implementation of the behavioural communication and leadership behaviour plans. In addition, the systematic requirements of the adoption process were not readily appreciated or implemented by the mine adoption teams. It soon became clear that there was a need for more detailed explanation of the concepts as well as the provision of more detailed guidance on execution of the various adoption processes.

These two needs were addressed by the MOSH adoption team leaders arranging for the various adoption processes to be explained in more detail during COPA meetings, and by the preparation of a more comprehensive guidance document for use by mines in adopting the leading practice. This guidance document, the 'Leading Practice Adoption Guide', sets out in detail each of the 16 steps for successfully adopting a particular leading practice at a mine. In addition to providing guidance on each of the 16 steps, the document provides the generic behavioural communication and leadership behaviour plans, as well as the technical details that have been developed for the leading practice. It is these three elements that are essential for successful and sustainable adoption of a leading practice. Without them the adoption is unlikely to be successful, and even less likely to be sustainable. These three elements are likened to the legs of a three-legged stool in that all three must be in place for a successful outcome. In addition to its intended use at adoption mines, the Leading Practice Adoption Guide also serves as a basic resource for use in COPA meetings. Guidance to assist the MOSH adoption teams in the preparation of these user-friendly documents for each of their leading practices was thus developed and included in the Handbook. The sixteen steps are shown later as part of the overall system that emerged.

Time scale of the process

One of the major problems that became increasingly apparent during the piloting process was the lengthy time delay between identifying the leading practice and making it available to mines for adoption. In essence, there were two reasons for this. The first was the time needed to document the identified leading practice at the source mine, to conduct the direct enquiry process and to then develop the required behavioural communication and leadership behaviour plans. All going well, this took about three to four months. The second was the time taken to demonstrate adoption of the leading practice at a selected 'demonstration mine'. This demonstration process, was partly to test the behavioural plans, but also to finalize the value case for the leading practice and to prepare a document to guide adoption at future adoption mines. Once again, all going well, this took another three to four months. In practice, the total delay period was thus between six and nine months. During this period the management at some mines became impatient and the potential for uninformed and unsuccessful adoption attempts became real. It was recognized that such attempts, in addition to being costly, could unjustly discredit both the leading practice and the adoption process.

Fortunately, based on growing experience and ongoing development of the process, it became apparent that it would be possible to provide a comprehensive generic draft of a 'Leading Practice Adoption Guide' to mines at the time the adoption team was ready to demonstrate adoption of the leading practice. This opened the way to shortening the process. By forming a COPA in parallel with initiating and facilitating adoption of the leading practice at a 'lead adopter mine', the adoption team could then use the COPA to ensure that other mines electing to adopt the practice in parallel were

kept abreast of any changes needed to the draft guide as a result of experience gained at this lead adopter mine. Facilitation of widespread adoption of the leading practice at other mines could thus proceed in parallel with the lead adopter mine. Furthermore, the lead adopter mine could be identified by the adoption team at an early stage, and it could in effect serve very much the same purpose as a demonstration mine. On completion of the adoption process at the lead adopter mine, the draft leading practice adoption guide could then be revised to fully take account of the experience gained. In addition to reducing the time scale by about four months, introduction of these adjustments also increased the importance and vibrancy of the COPA.

Simple leading practice

Another aspect of concern was that the time and effort required to document and secure adoption of a comparatively simple practice seemed unwarranted. Indeed, examination of the nature of some of these simpler leading practices revealed a strong case for developing a much quicker and simpler set of processes for such practices, particularly if their adoption involved few people and relatively little training. In considering such practices, the primary concern was nevertheless that the benefit of using behavioural communication and leadership behaviour techniques to secure successful and sustainable adoption should not be lost.

Fortunately, a review of the behavioural plans developed for different practices showed that a number of the elements in the plans were effectively common. This finding led to the proposal that instead of following the full process, these 'generic elements' could be applied to these simpler practices to achieve many, although not all, of the benefits expected from the development of practice-specific plans. This would considerably shorten and simplify the process. Accordingly, a set of criteria for the identification of practices that could be treated as 'simple leading practices' was developed, along with a set of procedures and guidelines for documenting and presenting the practice to potential adoption mines. Similarly, a set of simple procedures was developed to guide adoption of the practice at mines. The procedures included a formal review process to ensure that the simplified and shortened process was not inappropriately applied to more complex leading practices; or to situations where the full adoption process is considered necessary to achieve sustainable adoption. Following acceptance of the above proposal, detailed guidance on the processes was introduced into the Handbook.

Development of a credible value case

One of the key elements of any innovation process, and thus also of the Adoption System, is user awareness of the benefits expected to accrue from adoption of the innovation in question. Development of a credible statement of these benefits thus became a fundamental consideration in both selecting and presenting a leading practice for adoption. Importantly, it provides key information for communication to mine management to enable and assist them in making a well-founded decision about whether to adopt the leading practice at their mine.

However, it was recognized that some of the important benefits of adopting a leading practice could be qualitative and not readily reduced to a simple financial business case. Accordingly, consideration was given to developing a much broader value case for adoption of a leading practice at a typical adoption mine, as opposed to the more usual business case. The guidance developed for preparing such a value case thus included consideration of qualitative benefits not readily expressed in financial terms. It also included an assessment of the extent to which the benefits might vary between mines, as well as an estimate of the collective benefit to industry should all of the identified potential adoption mines elect to adopt the practice.

Notwithstanding the long experience of adoption team managers in conducting cost-benefit assessments of projects at mines, preparation of the envisaged value cases for the various leading practices proved to be difficult. This was largely due to difficulties in acquiring the required information for a 'typical adoption mine', let alone for mines on either side of such a mine in the benefit spectrum. It was, however, also due to the difficulty and discomfort of taking qualitative assessments into account in developing the value case. It has been shown that such fundamental changes in approach take a lot of cognitive effort (Kahneman, 2011). Unfortunately, development of value case statements of the envisaged detail and quality remains a challenge.

Contrary to expectations, this shortcoming appears not to have hindered the process of achieving widespread adoption of the selected leading practices. Instead, it appears that the compliance requirements of the Mining Charter have had a strong effect in securing adoption uptake. Unfortunately, however, in the long term, adoption motivated in this way is likely to have a counterproductive effect. Indeed, mine management is likely to become increasingly resistant to participating in structures that identify leading practices that carry Mining Charter obligations. The long-term consequences of such tendencies, which are already beginning to appear, would be disastrous. These tendencies clearly need to be reversed. The achievement of sound value case statements is thus an issue that requires further investigation, as such statements provide a sound basis for both the selection and voluntary and eager adoption of a leading practice.

The need for early behavioural communication

Allied to the above is another important point, namely the need for early behavioural communication with managers at identified potential adoption mines. Unfortunately, the need for implementing a special behavioural communication plan to ensure that mine managements are fully informed about the leading practice, as well as the adoption process, before they decide whether to adopt was initially not properly recognized. However, it was eventually realized that such a communication plan was needed to address any possible misperceptions and knowledge gaps that could be material to management making a well-founded decision about the leading practice. Clearly, misperceptions or inadequate understanding and knowledge about a practice or the adoption process may exist at all levels and in all people. Having recognized this key point, it was equally clear that for each leading practice, an appropriate behavioural

communication plan needed to be developed and implemented as soon as possible by the adoption teams. Accordingly, development and application of a behavioural communication plan for a leading practice was adjusted to become a two-pronged process. In particular, the direct enquiry questionnaires were adjusted to include a section addressed primarily to 'deciders' (those responsible for deciding about adoption of the practice) and the analysis of interview responses was structured to yield two mental model reports. The first dealt with the group at the mine responsible for deciding to adopt the leading practice, and the second with all persons at the mine, at all levels, who are key to securing successful operational adoption of the practice. These two reports then formed the basis for developing the required two behavioural communication plans. Guidance in the Handbook was similarly updated to reflect this two-pronged process.

The developed MOSH adoption system

It will be apparent from the above that the MOSH Leading Practice Adoption System, as documented in the Guidance Handbook, is very different from that put forward in the original proposal in 2007. Notwithstanding its incremental development path, and the volume and detail of its documented processes, the logic and essence of the current MOSH Leading Practice Adoption System can nevertheless be presented in a single graphic. This is shown in Figure 9. With regard to Figure 9, it must be noted that it is the MOSH adoption teams, with support from specialists within the Learning Hub in using the guidance provided, that take responsibility for implementing the 15 processes shown. The more complex detail is thus dealt with by trained specialists and not persons at mines.

Regarding the adoption process at mines, which is the responsibility of individual mines, guidance for mines in their adoption of a leading practice is provided in the relatively brief user-friendly documents prepared by the MOSH adoption teams for each leading practice. The MOSH adoption teams are required to ensure that these Leading Practice Adoption Guides are suitably user-friendly and that they properly take account of mine and practice-specific issues. The 16-step adoption process that they outline in detail for use by mines is shown in Figure 10.

The logic and essence of the entire MOSH Leading Practice Adoption System is thus summarized in Figures 9 and 10, with detailed guidance for proper execution of the various processes being outlined in the Handbook (Stewart, 2014). This guidance is extensive, but the challenge of achieving eager voluntary adoption is not simple.

Discussion

The Leading Practice Adoption System has undergone a lengthy development process with much being learned along the way. Many have benefited from this learning process, at mines, in the Learning Hub, and in the mining industry in general. Importantly, in addition to the benefit of greater understanding and more effective processes, there appear to have been significant OHS-related benefits.

OHS impact of the adoption system

Firstly, there is the direct benefit to mines and industry from the adoption of leading practices, particularly in the area of falls of ground. Leading practices presented for adoption by 2013 are listed in Table VIII. In each case, the leading practice was selected because of its potential to achieve progress toward the goal of zero harm.

The adoption of such leading practices has been described in many unpublished internal and conference presentations, but there is unfortunately a lack of published data on the OHS improvements at mines following the adoption of a particular practice.

Secondly, there is the participation by many mining industry persons in the oversight and operational structures of the Adoption System. Their participation contributed towards a well-directed increase in the focus on health and safety issues across industry. A similar comment applies to the participation of mine staff in the various COPAs and in the adoption processes at mines. Importantly, along with other factors discussed below, this increased focus on OHS

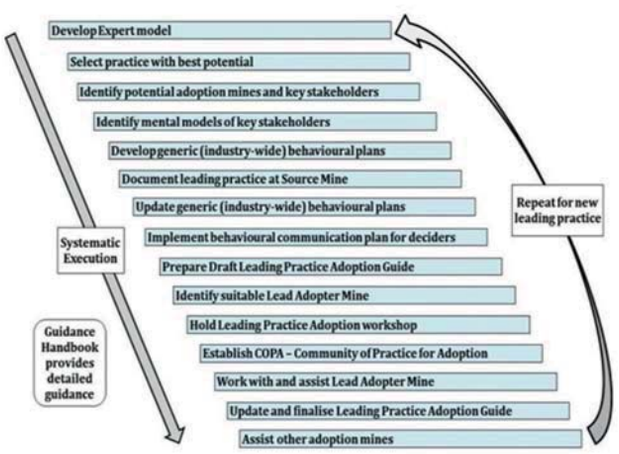

Figure 9—Major process steps of the MOSH Leading Practice Adoption System

Figure 10—16-step process for adoption of a leading practice at a mine

Table VIII

MOSH leading practices presented for adoption by 2013

Falls of ground

- *Entry examination and making safe*—A procedure involving the entire team in making the workplace safe, and in formally agreeing that this has been done, before work starts.
- *Nets with bolting*—Installation of nets attached to roofbolting to prevent falls of ground in areas where men are working.
- *Trigger Action Response Plan* (TARP)—A systematic check of known hazards in the workplace against predetermined risk criteria to trigger a planned response, escalated to the necessary level of authority until safety is restored.

Transport and machinery

- *Proximity detection systems*—Electronic systems installed on trackless and railbound equipment to detect nearby workers and/or beacons and equipment to prevent collisions and injury.

Noise

- *Hearing protection device selection tool and awareness training material*—A software package to enable optimal selection of HPDs for particular exposure situations, and communication and training materials to enable their effective use in practice.

Dust

- *Fogger/mist sprays*—The use of nozzles to create a mist of water droplets below 7 µm in size to enable the capture of airborne respirable dust particles in selected locations.
- *Footwall and sidewall treatment – Simple Leading Practice*—A practical procedure of wetting the foot- and sidewall with water and surfactants to consolidate the dust and prevent it from becoming airborne.
- *Multi-stage filtration system – Simple Leading Practice*—Provides filtration efficiencies of ≥98.5% at 0.5 µm and larger size particles discharged into air routed through an orepass.
- *Scraper winch cover – Simple Leading Practice*—A cover is fitted over the operating drums of a scraper winch to reduce the harmful dust exposure experienced by winch operators.

appears to have contributed significantly to the safety improvements achieved by industry since agreement to the 2013 milestones in 2003. These improvements are illustrated in Figure 11.

Compared with the minimal safety improvements achieved in the previous 15 years, as shown in Figure 1, Figure 11 shows a remarkable change in the nature of the safety performance trends after about 2001–2003. Agreement to the milestones in 2003 and the observed significant shift towards improved safety performance in all mining sectors are thus coincident in time. Although some of this improvement may be attributed to the adoption of new technology at some mines, it is likely that most of the improved performance following agreement to the milestones was due to the increase in focus on OHS issues by mine managements, organized labour, and the inspectorate.

However, it should be noted that the improvement in OHS performance was not always continuous. Figure 11 shows that safety performance in the gold sector deteriorated over the years 2004 to 2007, and in the coal sector from 2007 to 2008. However, the focus of top-level management on OHS was demonstrated in 2005 when CEOs of the major mining companies made a public commitment for their companies to achieve the 2013 milestones, and ultimately, the goal of zero harm. It was this commitment that led to the establishment of the High-Level Task Force in 2005, and development of the initial Adoption System proposal in 2007. The period of deteriorating OHS performance in the gold mining industry from 2005 to 2007 was thus accompanied by a steady increase in focus on OHS issues in mining companies at the highest level. Figure 11 shows that since 2007 there has been a relatively steady improvement in safety performance in all mining sectors.

Notwithstanding the logic of the above arguments, it must be recognized that many other factors have also contributed to the significant safety improvement shown in Figure 11. These include:

- ➤ Increasingly stringent enforcement by the Mine Health and Safety Inspectorate
- ➤ Implementation of various safety initiatives at individual mines
- ➤ Widespread introduction of MOSH leading practices at mines
- ➤ Introduction of leading practice reporting requirements in the Mining Charter
- ➤ Increased focus and cooperative participation by management and employees on achieving improved OHS.

Unfortunately, it is not possible to realistically quantify these separate contributions. However, in respect of the Adoption System's contribution, it is appropriate to note that one of the primary purposes in the design of the Adoption System was to secure the direct involvement and buy-in of key mining industry personnel. In practice this involved not only key high-level persons in all major mining companies, but also all key stakeholders and operational persons involved in more than 250 leading practice adoption processes across more than 55 major mines. Through participation in the oversight and operational structures of the Adoption System, including the various COPAs, and then also the many MOSH adoption processes implemented at mines, the number of persons directly involved in the Adoption System is numbered in thousands. Importantly, the majority of the persons involved in the adoption process at mines would have been exposed to, and affected by the

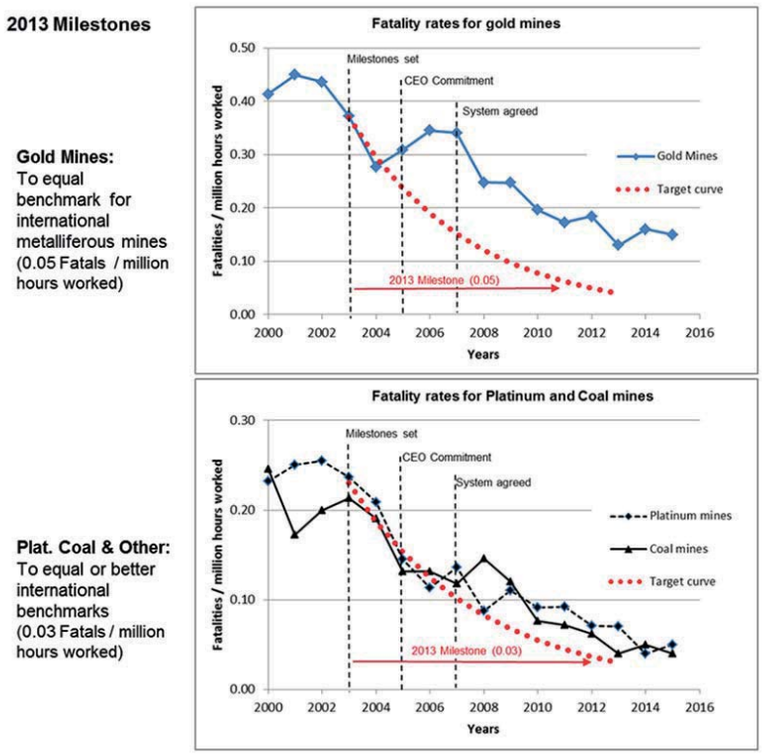

Figure 11—Mining industry safety improvements since setting milestones in 2003

behavioural messages communicated to them as part of the leading practice adoption process. In particular, these messages would have helped individuals improve not only their leadership behaviour but also their operational on-the-job risk assessments and the quality of their consequential behaviour.

User resistance

Notwithstanding the positive effect considered above, it appears that the behavioural processes, which are such an important aspect of the Adoption System, are considered by operational management at some mines to be too detailed and time-consuming, and to require expertise not available at the mine. In particular, many technical persons at the mines did not readily relate to the behavioural processes of the Adoption System. Furthermore, many mines already had their own processes for managing change. This has resulted in resistance at some mines, with some deciding to implement MOSH leading practices without applying the MOSH behavioural processes. This short-cut has become known as *implementation* of a MOSH leading practice, as distinct from *adoption*, which applies when the MOSH behavioural processes are properly used.

In retrospect, this resistance is not surprising, given that the MOSH behavioural processes were introduced in the period 2008-2011 without any systematic attempt being made to identify and address the resistance factors that would inevitably be present. Unfortunately, at that time, a full appreciation of the behavioural processes was simply too new for it to be recognized that the very processes being introduced into the Adoption System should have been used for their own introduction to industry. Ironically, they are the very processes that would have enabled identification of the knowledge gaps, misperceptions, and other barriers that needed to be addressed. They would also have yielded an appropriate behavioural communication programme to address the identified barriers. In regard to this important realization, it is worth noting that over time it had become apparent that many key persons had an inadequate familiarity with and understanding of the adoption system. This was confirmed through a direct enquiry investigation. However, although an informative video was produced in an attempt to address the issue (MOSH, 2014), the full extent of the shortcoming only emerged later.

Noting the different approaches to adoption explained above, the Culture Transformation Framework established for the mining sector (MHSC, 2011) called for a common approach to identifying and facilitating the adoption of leading OHS practices and research outcomes. In response, the Mine Health and Safety Council recently developed, with input from the Learning Hub, a brief generic guideline for identifying and facilitating the adoption of leading OHS practices (MHSC, 2016). Importantly, the guide is in essence consistent with the requirements of the MOSH Adoption System, although it does not provide the same level of process detail. Instead, in the areas covered by the MOSH behavioural processes it simply requires the use of recognized and valid processes. Inescapably, therefore, it appears that the need to address resistance to the use of such processes, be they from MOSH or elsewhere, still needs to be addressed. This matter is currently being considered within the Learning Hub.

Effectiveness of the system

Much like the strength of a chain, the effectiveness of the Adoption System is determined by its weakest element. This is particularly true in respect of behavioural communication, starting with development of the expert model right through to development and delivery of the behavioural communication plan. It is thus important that the specialists within the Learning Hub guard against the possibility that execution of the various processes becomes in practice an ineffective box-ticking exercise.

In this regard there is an aspect of the behavioural communication process that requires particular attention, namely development and testing of the detailed communication material. While the format of the behavioural communication plan shown in Table VII clearly sets out all its key elements, it does not directly contain the detailed communication material. The brief statement in the plan of the message to be communicated generally falls far short of what is needed to effectively convey the identified message. To be fully effective, the behavioural communication material needs to include detail that is credible and readily understood by the intended recipients. Importantly, the prepared material and the manner of its presentation need to be tested to ensure their effectiveness. This, however, can be costly, time-consuming, difficult, and thus inhibiting.

Increasingly, it has been recognized that the behavioural communication material being used at mines generally falls short of what is required for it to be fully effective. Although the importance of this point has been emphasized, and guidance on the preparation of effective communication material strengthened, it appears that this remains an area of weakness. It is thus an issue that warrants further attention. Continued weakness in this area will compromise the effectiveness of not only the behavioural processes, but ultimately, also the credibility and use of the Adoption System.

A leading practice in its own right

Given the sound basis of the Adoption System, and the key behavioural aspects that differentiate the system from other ways of securing technology transfer and innovation, it has been recognized as a leading practice in its own right. This point was made in 2013, in a presentation to industry representatives at the annual Mine Health and Safety Conference held in South Africa (Malatji and Stewart, 2013). It was later also recognized by the US Army Corp of Engineers in their published review of mental models technology (Wood, 2017), when they decided to include a chapter on the Adoption System (Stewart and Butte, 2016). Importantly, as pointed out in the Handbook, the MOSH Leading Practice Adoption System is a system that can be readily adapted for use in other settings.

New goals and priorities

While establishment of the milestones in 2003 marked the start of a remarkable period of occupational safety improvement in the South African mining industry, a similarly strong improvement is not readily evident in the area of occupational health. This is disappointing, given the major need for improvement in the areas of silicosis and noise-induced hearing loss. Unfortunately, the priority given to addressing these issues has not been as intense as it should have been, perhaps because the consequences of unsafe exposure to dust and noise are usually not

Table IX

New OHS milestones agreed in 2014 - the road to zero harm

Area	Agreed milestones
Fatalities and Injuries	• Every mining company must have a target of ZERO fatalities. • Fatalities to be eliminated by 2020. • Up to Dec. 2016, serious injuries to be reduced by 20% per annum. (Not achieved - 15% achieved in 2016) • From Jan. 2017 onwards, lost time injuries to be reduced by 20% per annum.
Occupational lung diseases	• By Dec. 2024, 95% of all exposure measurements of respirable crystalline silica to be below 0.05 mg/m^3. • By Dec. 2024, 95% of all exposure measurements for platinum dust respirable particulate to be below 1.5 mg/m^3, and < 5% crystalline silica. • By Dec. 2024, 95% of all exposure measurements for coal dust respirable particulate to be below 1.5 mg/m^3, and < 5% crystalline silica. • Using present (2014) diagnostic techniques, no new cases of silicosis, pneumoconiosis, coal worker's will occur amongst previously unexposed individuals.
Noise-induced hearing loss	• By Dec. 2024, total operational or process noise emitted by any equipment must not exceed a sound pressure level of 107 dB(A). • By Dec. 2024, no employee's Standard Threshold Shift will exceed 25 dB from baseline when averaged at 2000, 3000, and 4000 Hz in one or both ears. • Establish a multi-stakeholder team to consider different compensation systems.
TB and HIV AIDS	• By Dec. 2024, TB incidence rate to be at or below the National TB incidence rate. • 100% of employees to be offered HIV counselling and testing annually with all eligible employees linked to an anti-retroviral therapy programme as per the National Strategic Plan.
Culture transformation	• By 2020 there will be 100% implementation of the following Pillars of the Culture Transformation Framework: Leadership, Risk Management, Bonus and Performance Incentive, Data Management, Diversity and Leading Practice. • After 2020, the remaining pillars of the framework will be implemented, namely: Integrated Mining Activity, Technology, Inspectorate, and Tripartism and Regulatory Framework.
Centre of Excellence	• Launch Centre of Excellence, undertake quick-win projects, and implement technology and knowledge transfer of quick-win projects. • Centre of Excellence to be operational by 1 April 2016. (Scheduled for November 2017)

immediately apparent, and may take many years to develop. However, the need to effectively address the health challenge has been increasingly recognised across industry. The CEO Zero Harm Task Team established by employers is focused equally on health and safety, and the new OHS milestones that were agreed to by the tripartite partners in 2014 (MHSC, 2014) have a clear focus on key health issues. A summary of these milestones is presented in Table IX.

Conclusion

A key point brought out in this paper is the value of a holistic systems approach when addressing a multifaceted issue such as occupational health and safety. In particular, such an approach provided insightful guidance in developing a climate conducive to innovation; it proved to be fundamental to understanding the behavioural processes of the Adoption System, and it underpinned the design and development of the adoption system. Indeed, in retrospect it is appropriate to recognize that the significant OHS improvements reported in this paper stem from the combined effect of the Leon Commission of Enquiry, the ILO Convention on Safety and Health, the Mine Health and Safety Act and its structures, establishment of the tripartite agreed OHS milestones, the initiatives of individual mines, and development and implementation of the MOSH Leading Practice Adoption System. Finally, in regard to the system, it has become abundantly clear that managing behaviour change is not a simple matter, that this challenge cannot be made simpler than it is, and that short-cuts will be counterproductive in the long-term.

Acknowledgement

The contribution that many persons made willingly, both directly and indirectly, to the development of the MOSH Adoption System described in this paper are gratefully acknowledged. There are too many to name them all, but the input and assistance of G. Butte and S. Thorne of Decision Partners, S. van der Woude of the Chamber of Mines, and all members of the four MOSH Adoption Teams warrant special recognition.

References

Butte, G. 2007. Expert model of innovation. Decision Partners LLC, Pittsburgh, USA. Personal communication.

Decision Partners. 2008. Adoption planning process workbook and resource kit. Decision Partners LLC, Pittsburgh, USA.

Gouws, M.J. 2004. Review of industry health and safety performance. Chamber of Mines of South Africa, Unpublished document. Personal communication.

Harrington, J.S., McGlashan, N.D., and Chelkowska, E.Z. 2004. A century of migrant labour in the gold mines of South Africa. *Journal of the South African Institute of Mining and Metallurgy*, vol. 104, no. 2. pp. 65–71.

Hermanus, M., Coulson, N., and Pillay, N. 2015. Mine Occupational Safety and Health Leading Practice Adoption System (MOSH) examined – the promise and pitfalls of this employer-led initiative to improve health and safety in South African Mines. *Journal of the Southern African Institute of Mining and Metallurgy*, vol.115. pp. 717–727.

Kahneman, D. 2012. Thinking, Fast and Slow. Penguin Books.

MAC, 2003. A field guide for building shared understanding for: Towards Sustainable Mining. Mining Association of Canada.

Malatji, S and Stewart, J.M. 2013. The MOSH Leading Practice Adoption System: A leading practice in its own right. *Proceedings of Minesafe 2013*, Johannesburg, 22–23 October. Southern African Institute of Mining and Metallurgy, Johannesburg.

MHSC. 2003. Milestones of the 2003 Mine Health and Safety Summit. http://www.dmr.gov.za/mine-health-a-safety.html

MHSC. 2011. The culture transformation framework. Mine Health and Safety Council, Johannesburg. http://www.mhsc.org.za/sites/default/files/Final Document - The Culture Transformation Framework 2011.pdf

MHSC. 2014. Mine Occupational Health and Safety Summit – The Road to Zero Harm – New Milestones. Mine Health and Safety Council, Johannesburg.http://www.mhsc.org.za/sites/default/files/Mr%20Msiza%202014%20Milestones_0.pdf

MHSC. 2016. MHSC guideline for the identification and adoption of leading OHS practices. Mine Health and Safety Council, Johannesburg.

Morgan, M.G., Fischoff, B., Bostrom, A., and Atman, C.J. 2002. Risk Communication – A Mental Models Approach. Cambridge University Press, New York, USA.

MOSH. 2014. MOSH leading practice adoption system video. http://www.mosh.co.za/mosh-leading-practice-adoption-process.

NACI. 2003. Utilisation of research findings – Extent, dynamics and strategies. National Advisory Council on Innovation.

National Mining Association. 2016. Handbook about CORESafety and Health Management System. http://nma.org/wp-content/uploads/2016/09/CORESafety-Handbook.pdf.

Scott Geller, E. 2005. Behaviour-based safety and occupational risk management. *Behaviour Modification*, vol. 29, no. 3. pp. 539–561.

Skinner, B.F. 1952. Science and human behaviour. BF Skinner Foundation. http://bfskinner.org/store

Smith, T.A. 1999. What's wrong with behaviour-based safety? *Professional Safety*. September. pp. 37–40

Smith, M.K. 2003. Communities of Practice. *The Encyclopedia of Informal Education*. www.infed.org/biblio/communities_of_practice.htm

Stewart, J.M. 1982. Practical aspects of human heat stress. *Environmental Engineering in South African Mines*. Mine Ventilation Society of South Africa. Johannesburg. pp. 535–567.

Stewart, J.M. 1995. The role of legislation and regulation in health and safety in mines. *Journal of the South African Institute of Mining and Metallurgy*, vol. 95, no. 2. pp. 91–100.

Stewart, J.M. 2004. Historical background to levies and SIMRAC. Report submitted to Mine Health and Safety Council.

Stewart, J.M. 2007a. From sharing to widespread adoption of technology and best practice to improve occupational health and safety in mines. Report submitted to the Chamber of Mines of South Africa [reproduced in full in Stewart, 2014].

Stewart, J.M. 2007b. Key concepts and insights from past work on technology transfer. Report submitted to the Chamber of Mines of South Africa.

Stewart, J.M. 2014. MOSH Leading Practice Adoption System Guidance Handbook. Chamber of Mines of South Africa. http://www.mosh.co.za/hub/handbook

Stewart, J.M. and Butte, G. 2017. The Chamber of Mines of South Africa Leading Practice Adoption System. *Mental Modelling Approach – Risk Management Case Studies*. Wood, M.D., Thorne, S., Kovacs, D., Butte, G., and Linkov, I. (eds). Springer, New York, USA.

The Distance Consulting Company. 2000. Community of practice start up kit. http://www.srpc.ca/ess2016/summit/copstartupkit.pdf

Van der Woude, S., Stewart, J.M., Ally, I., and Leburu, T. 2005. Strategies for sustainable safety improvements in South African mines. *Proceedings of the NOSHCON Conference on Occupational Health and Safety*, Sun City, South Africa, 4–7 April.

Van Zyl, A. 2010. Mining Industry occupational safety and health process for the adoption of leading practices. *Proceedings of the Second Hard Rock Safe - Safety Conference*, Johannesburg, 4–6 August. Southern African Institute of Mining and Metallurgy, Johannesburg.

Wenger, E. 1998. Communities of Practice: Learning, Meaning and Identity. Cambridge University Press.

Wood, M.D., Thorne, S., Kovacs, D., Butte, G., and Linkov. I. 2017. Mental Modelling Approach – Risk Management Case Studies. Springer, New York, USA.

Wyndham, C.H. 1974. Research on the human sciences in the gold mining industry – 1973 Yant Memorial Lecture. *American Industrial Hygiene Association Journal*, vol. 35. pp. 113–136. ◆

SAIMM
THE SOUTHERN AFRICAN INSTITUTE OF MINING AND METALLURGY

Geometallurgy Conference 2018

BACK TO THE FUTURE

Supported by

GSSA Geological Society of South Africa
MINSA Mineralogical Association of South Africa
SAIMM THE SOUTHERN AFRICAN INSTITUTE OF MINING AND METALLURGY
WESTERN CAPE BRANCH

6th August 2018–Technical Workshop • 7-8th August 2018–Conference
Lagoon Beach Conference Venue, Cape Town, South Africa



Background

The theme of this first geometallurgy conference '**Back to the future**' is inspired by looking both into the past and the future: the concept of Geometallurgy goes back to some of the earliest mining activities when mineral recognition, mining, separation and concentration were undertaken simultaneously. Over time, changes in operational structures, product expansion and specialisation ultimately led to the diminishment and breakdown of this holistic approach.

In the last two decades 'Geometallurgy' has become a sophisticated yet entirely logical return to this integrated approach to mine planning. In a world of exponentially increasing ore heterogeneity and economic complexity, Geometallurgy is effectively a highly structured, integrated multi-disciplinary collaboration for optimising the value of an ore deposit. The approach is premised on acquiring multi-dimensional, spatially constrained (blocked) ore body knowledge that quantifies and qualifies all aspects of ore body variability. This data must include each element's response to blasting, excavation, crushing, grinding, separability and the environment and of course, its economic factors. These discrete elemental data sets are modelled to optimise a mine plan which takes into account the respective threshold criteria for each of the dataset components. Geometallurgy provides for truly integrated mine planning, ore flow management and processing from exploration to operations and through to final closure and rehabilitation. (Think of it as 4D Whittle on steroids, but for the entire mine life cycle, not just the optimised pit or stope envelope for the mining operation).

Looking into the future, we need to visualise what our 'ideal' mining operation in Southern Africa should look like, how it will function, and be equipped to articulate what we need to do to achieve this. Geometallurgy is a critical tool in achieving this.

Keynotes

Prof. Alice Clark
Director of Production Centres, SMI-BRC & SMI-JKMRC, University of Queensland, Australia

Sello Kekana
Head of Technical Training and Development, Ivanhoe Mines

Alistair Macfarlane, *Chamber of Mines*

Matt Mullins
Director: Tecoma Strategies

Dr Carlo Philander
Regional Manager South Africa Mineral Resources Development Tronox

Sponsors

Geovariances
SCANTECH www.scantech.com.au

For further information contact: Head of Conferencing, Camielah Jardine, SAIMM, P O Box 61127, Marshalltown 2107
Tel: +27 11 834-1273/7, Fax: +27 11 833-8156 or +27 11 838-5923, E-mail: camielah@saimm.co.za, Website: http://www.saimm.co.za


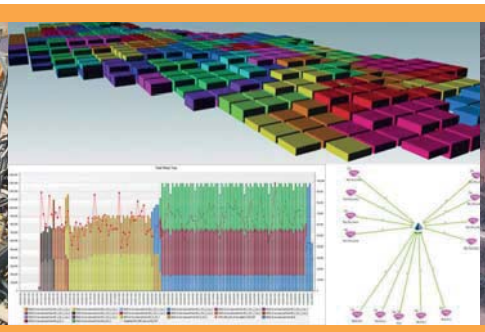


Conference Announcement

http://dx.doi.org/10.17159/2411-9717/2018/v118n3a10

A structured key cost analysis methodology to identify value-contributing activities in mining projects: a case study of the Chuquicamata Underground Project

by E. Córdova*, V. Mobarec*, E. Pizarro†, and A.R. Videla*

Synopsis

Traditional project evaluation methods for estimating operating costs of mining projects mostly produce static and over-conservative evaluations. In this study, a systematic model for managing the economic risk of the operating costs for an ongoing 'supercave' project, the Chuquicamata Underground Project, is presented. Key cost generators are identified, and their inherent variability is characterized based on a similar underground operation and expert judgment. Using Monte Carlo simulations, variability is factored into the evaluation, and the economic risk associated with each variable is quantified, after which the simulated data is used to identify the underlying risk, as well as mitigating actions and opportunities. The methodology can serve to identify how variability may impact the value of the project and how mitigation actions could decrease the present value of the estimated operating cost of the project by more than 10%. As a result of the analysis, the project managers became aware that labour and energy costs are the major contributors from a risk-value perspective, and mitigating actions such as construction of a power plant and implementation of a well-designed labour productivity incentive plan could be justified with a reduction of the overall risk value of the project.

Keywords
risk quantification, risk management, underground mining operating cost, Monte Carlo simulation, quantitative risk analysis.

Introduction

The development of a large-scale underground mining operation, from initial discovery of the orebody to first production, takes several years and moves through different stages. These are generally defined as scoping, prefeasibility, feasibility, engineering design, and site construction and mine development (SME, 2011). Each stage deals with more detail than the preceding one, therefore reducing the levels of uncertainty (Tulcanaza, 2014). Based on this information, the key variables of the project are estimated, which allows for a global economic evaluation to be developed for the future mining operation.

Any economic decision during the development of a mining project must take into account its projected financial impact. Assuming the project has been correctly designed and achieves the expected production levels and recoveries, income may be considered an exogenous variable depending on metal prices. In such a scenario, most of the effort is focused on correct cost projections associated with mining design, which will determine the final cash flow of the project. The overall cost of a mining operation is usually divided into capital and operating costs. Capital costs refer to the investment required for the design and implementation of the operation, and are incurred primarily during the early years of the project. In contrast, operating costs relate to expenses associated with all the unit processes that enable mineral production, from orebody characterization to extraction of the ore and subsequent processing throughout the life of the mine (LoM). These operating costs will depend on both internal and external project variables. The former relate to the particular circumstances and requirements of the operation and the latter to market conditions and commodity prices.

One major problem that any mining project confronts is that economic evaluations, especially in their early stages, do not identify the major risk factors associated with cost drivers. A detailed feasibility study may contain thousands of cost items and activities, making it quite difficult to extract key cost drivers from the data-set. This usually leads to projects underperforming due to higher operating costs and lower performance indicators than expected (Mackenzie, 2007). Indeed, almost 70% of mining megaprojects fail to meet at least one of their estimated key success criteria (Merrow, 2011).

In recent years, operating costs in the mining industry have become a critical issue due to their substantial rise in relation to total spending (Perez-Oportus, 2008). Consequently, uncertainty and possible risks

* *Mining Engineering Department, Pontificia Universidad Católica de Chile, Chile.*
† *Chuquicamata Underground Mining Project, CODELCO.*

 ISSN 2225-6253. Paper received Mar. 2017; revised paper received Jun. 2017.

related to varying operating costs during the LoM should be considered as relevant factors. Risk analysis techniques based on Monte Carlo simulation, such as Quantitative Risk Analysis (QRA), offer a more appropriate path than traditional evaluation methods for understanding the responses and robustness of a project. This is especially the case given the time-frame and the intrinsic uncertainty related to the estimation variables (Merrow, 2014; Heuberger, 1995; Chinbat and Takakuwa, 2009; Brown, 2012). Unlike traditional methods that incorporate uncertainty as a percentage of total expenditure, using factors such as 'contingency' or 'overall expenses', QRA relies on stochastic modelling and simulation of the key project variables to calculate the combined impact of the model's various uncertainties in order to create a probability distribution of the possible model outcomes.

The need to understand the causes and sources of risk in the mining industry drives the combination of expert judgment analysis with quantitative methods. This will allow the company to quantify increasing levels of uncertainty and help it to understand potential project responses to the range of possible variations and future conditions (Summers, 2000).

The method applied in this paper includes a systematic risk management approach, combining quantitative and qualitative analysis, to identify the main sources of risk and propose risk mitigation alternatives. The method has been applied only to the Chuquicamata Underground Mine Project, an ongoing operation in the north of Chile and state-owned through Codelco. To preserve confidentiality of the data, all cost values have been anonymized by multiplying them by a factor.

The results show that the operating economic risk of the project relates to just a few of its cost generators. Risk can be managed by introducing specific risk mitigation alternatives that target these generators, thus reducing uncertainty and even improving the expected economic value of the project.

Objective

The objective of the study was to develop a method to estimate the associated economic risk of operational costs for the Chuquicamata Underground Mine Project (CUMP). To that end, the main cost drivers are identified, their variability is characterized, and the impact on the project in several scenarios is simulated to estimate the value that they provide. The proposed methodology is summarized in Figure 1.

Chuquicamata Underground Mine Project cost description

Chuquicamata has been operating as an open pit since 1915, and is being transitioned to an underground project, starting as a four-panel macro-block caving operation. The project is designed to operate at a production rate of 140 kt/d over a life of 40 years, with a 7-year ramp-up, 28 years of steady-state production, and a 5-year ramp-down, with an initial 10 years of development. This will turn it into a so-called 'supercave' and one of the largest underground operations in the world (Chitombo, 2010). The project is now entering the detailed engineering stage, with production expected to start in 2019. Figure 2 shows a basic schematic diagram of the mine operation.

The data used for the analysis is based on initial cost estimations for the feasibility study, including development and production schedules, and all technical and economic parameters considered for the economic evaluation throughout the LoM (2019–2058). Present values of all operating costs of the project add up to US$2.582 billion

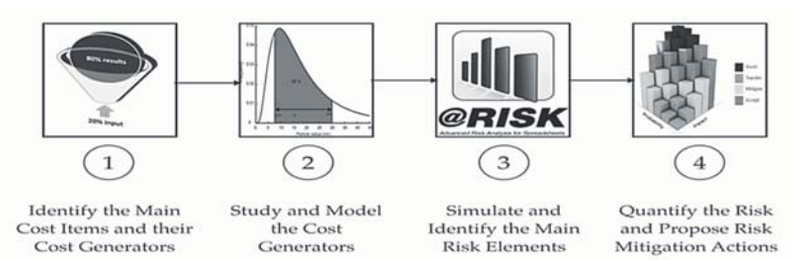

Figure 1—Stages of a structured operative cost risk analysis

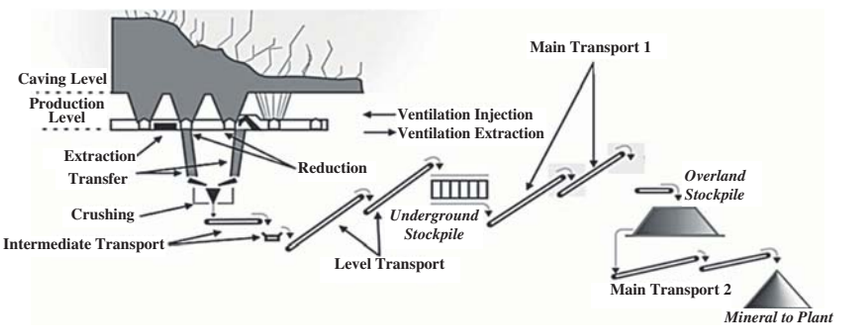

Figure 2—Simplified schematic layout of the Chuquicamata Underground Project operation

(2014 US$, 8% discount rate), and are divided into two main activities: mine development and production costs. Each activity contains multiple sub-activities, which are further divided into elements of expenditure.

Mine development costs include all expenses related to the construction of the mining facility and supporting infrastructure. The current estimate for the present value of the cost of this activity reaches US$844 million, representing 30% of the total operating cost of the project. Development costs consist of 10 sub-activities and seven elements of expenditure, with a total of 67 cost items.

Production costs, on the other hand, include the expenses of all unit operations involved in the actual extraction of the orebody, including additional activities or services required to fulfil the mine production schedule. The current estimate for the present value of the cost of this activity is $1.738 billion, which represents the remaining 70% of total operating costs. Production costs consist of 13 sub-activities and six elements of expenditure, with a total of 84 cost items. Table I summarizes the structure of the CUMP operating costs.

Systematic cost analysis

Identification of main elements of costs

As above, there are 151 cost items (67 from development, 84 from production) categorized as activity–sub-activity–element of expenditure. The evaluation compared the different cost items according to their net present value of costs (NPVC). Considering the horizon of the project (40+ years), this alternative outweighs other available options, for example comparing the items according to their added nominal value. Using a discount rate accounts for the effect of time as part of the expenditure evaluation, resulting in a more realistic comparison. The NPVC of a cost item is calculated by summing all the discounted expenses of that item throughout the LoM:

$$NPVC_i = \sum_{j=0}^{LoM} \frac{Expenses_{i,j}}{(1+\delta)^j} \quad [1]$$

where

$NPVC_i$	Net present value of cost (i)
LoM	Life of mine
$Expenses_{i,j}$	Expense of cost i at time j
δ	Anual discount rate

The study uses 2014 as the initial year for the evaluation and an annual discount rate δ of 8%. The total net present value of the operating costs of the project is calculated by summing the NPVCs of all cost items.

The most relevant cost items were determined with the Pareto principle, ranking and segregating the items that represent 80% of the total operating cost NPV. From the analysis, it followed that 30 out of 151 cost items (*i.e.*, 19.86%) accounted for 80.2% of total expenditure. Out of the 30 cost items identified, eight relate to development activities, with an NPVC of US$678 million, and the remaining 22 to production activities, with an NPVC of US$1.394 billion. Figure 3 illustrates the global proportion represented by each element of expenditure within these 30 cost items, and detailed information about them appears in Appendix A.

Identification and categorization of cost drivers

The relevant cost items identified in the previous section are analysed to isolate their specific cost generators. These cost generators are divided into three categories: input prices (IP), consumptions intensities (CI), and production and development requirements (PDR). The total expense (TE) of each cost item identified in the previous section, during any period of the evaluation, can thus be written as a combination of these variables:

$$TE\left[\frac{\text{US\$}}{\text{period}}\right] = IP\left[\frac{\text{US\$}}{\text{unit}}\right] * CI\left[\frac{\text{unit}}{\text{ton or m}^2}\right] * PDR\left[\frac{\text{ton v m}^2}{\text{period}}\right] \quad [2]$$

Table I

Operational cost structure of CUMP

Activity	Sub-activity	Element of expenditure
Development	Caving level	Labour
	Production level	Operation materials
	Ventilation Injection level	Maintenance and repair materials
	Ventilation suction Level	Supplies (diesel and water)
	Transfer level	Energy
	Crushing level	Contractors
	Intermediate transport level	Depreciation
	General Infrastructure	
	Administration	
	General expenses	
Production	Extraction	Labour
	Reduction	Operation materials
	Transfer	Maintenance and repair materials
	Crushing	Supplies (diesel and water)
	Intermediate transport	Energy
	Level transport	Contractors
	Main transport	
	Ventilation	
	Mine services	
	Damaged areas repair work	
	Administration	
	ICO	
	Production support services	

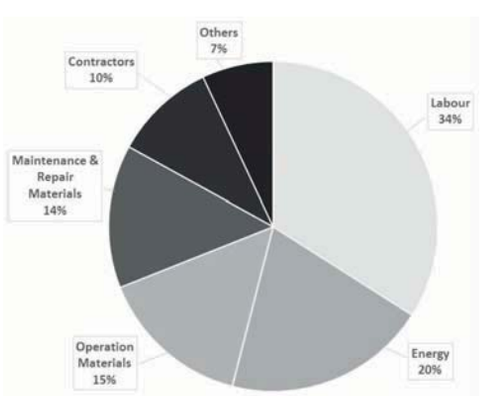

Figure 3—Proportion of elements of expenditure that represent 80% of the total expenditure of the project

Cost variability modelling

Once the main operating cost generators have been identified, their variability needs to be understood and characterized. The methodology applied to estimate such variability for elements of each cost category is explained below for each cost item.

Unit market prices

Market prices represent the price per unit of consumption of the inputs of each cost item. The inputs included as part of the CUMP case study (and which represent the main inputs of almost any underground mining project) are energy, steel, concrete, diesel, explosives, and labour. The unit prices were modelled using a time-spatial variogram correlation to incorporate the increment in value uncertainness as time projection increases. By incorporating initial prices used in the feasibility stage of the project plus market projections and their historical variability, different scenarios can be projected. Appendix B presents the methodology used to model the input prices.

Consumption intensities

This category considers consumption rate of supplies per square metre developed or ton produced, depending on the activity in question. Consumption intensities will be related to the elements of expenditure of each activity, in this case labour, materials, supplies, energy, and contractors. We modelled the intensities by combining the initial estimations used in the feasibility stage of the project with the variability observed in a real operation in a similar block caving underground mine, Codelco's El Teniente, the only underground operation in Chile comparable in size to CUMP. Appendix C shows the methodology used to model the consumption intensities.

Production and development requirements

These requirements represent the number of square metres that will be developed and the tons that will be produced in each period of mine life. Production is considered as fixed input; therefore any value risk assessment ignores variations in production at this stage.

Cost variation along the LoM using Monte Carlo simulations

The total information is combined in an application that allows estimation of the economic performance of the project under different scenarios. Simulations are conducted using the @Risk software by Palisade with N=10 000 iterations. The operational cost structure proposed in the feasibility stage is used as a basis for the analyses, as well as the models and correlation matrices defined in the cost generators modelling section. A detailed simulation input table appears in Appendix D. The main output of the simulation is a distribution function of the present value of the operating costs of the project during the LoM. Figure 4 shows the obtained probability distribution function.

Model results

The simulated NPV of the operational costs ranges from US$2.351 billion to US$2.829 billion, with a mean value of US$2.582 billion and a standard deviation of US$65.9 million. The estimated mean value of US$2.582 billion matches the value estimated for the base case scenario, since the base estimations were used as the mean values for the input variables. Figure 4 shows that the operational cost variability can impact the NPV of the operational costs of the project by up to 10%, or US$250 million.

Risk assessment and quantification

To identify the major cost/risk sources of the project, 'unacceptable' scenarios are defined and economic risk is calculated as the difference between their mean value and the base estimation. Subsequently, the elements of expenditure are ranked according to their contribution to total economic risk. For the CUMP case study, the top 5% of simulated scenarios, *i.e.*, scenarios in which the present value of the operational cost exceeds US$2.692 billion, are dismissed as unacceptable. The mean present value of these scenarios is US$2.72 billion, resulting in a total economic risk of US$138 million. Figure 5 shows the average contribution of each element of expenditure to the calculated economic risk.

As appears in Figure 5, the most relevant risk sources are energy and labour, which together account for 70% of the total risk value. Any risk mitigation efforts should thus focus on these elements of expenditure. Also, contrasting these results with Figure 3 suggests that economic risk is not always proportional to total expenditure. Indeed, energy and labour represent 55% of total expenditure, but make up 70% of the total risk value. Operational materials and maintenance and repair materials represent 29% of total expenditure, but

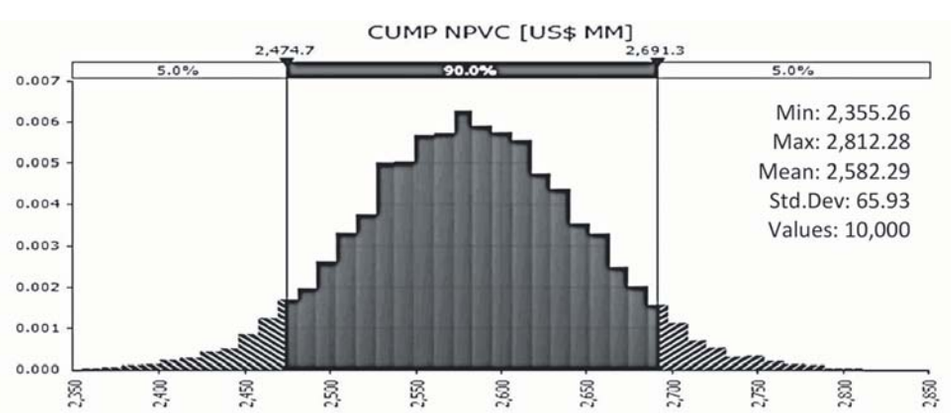

Figure 4—Probability distribution function for operating cost of the Chuquicamata Underground Project

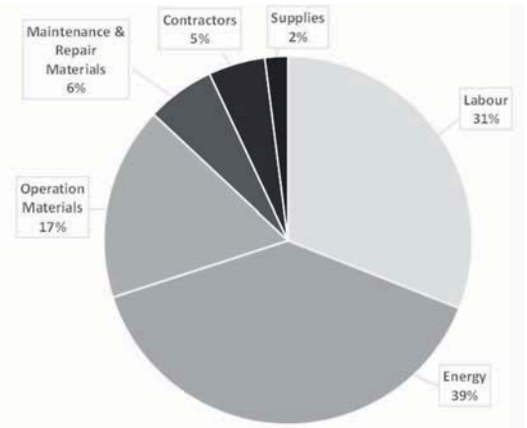

Figure 5—Average contribution (in %) of elements of expenditure associated with the economic risk of the project

their contribution to total risk value is 23%. This illustrates the necessity for each of the elements of expenditure to be analysed independently.

To suggest any mitigation effort in the CUMP, it was necessary to understand how risk is distributed among the labour- and energy-related cost items. Using the same set of 'unacceptable' scenarios, the economic risk of the cost items was quantified as the difference between their mean present value under these scenarios and the base case estimation. The resulting economic risk for the energy and labour cost items appears in Tables II and III, respectively.

In Table II it can be seen that energy-related economic risk is heavily skewed toward two production sub-activities: main transport and ventilation. Together, these two factors account for more than 80% of the total energy-related risk.

In contrast, Table III shows that labour cost risk value is related to 11 sub-activities, and is more evenly distributed among them than is the case with energy.

Risk management analysis

Having identified labour and energy as main risk sources and calculated their economic risk value, we proceed to evaluate risk control alternatives. It is essential to fully understand the cost structure of the items related to these elements of expenditure, so that risk mitigation alternatives that target these specific cost generators can be proposed.

Energy cost items

The total energy expenditure (TEE) per year for the cost items in Table IV emerges from energy price (EP), energy consumption intensity (ECI), and the requirements of the production and development plan for that year as shown in Equation [3].

$$TEE\left[\frac{\text{US\$}}{\text{year}}\right] = EP\left[\frac{\text{US\$}}{\text{MWh}}\right] * ECI\left[\frac{\text{MWh}}{\text{ton or m}^2}\right] * PDR\left[\frac{\text{ton or m}^2}{\text{year}}\right] \quad [3]$$

Energy price

In the CUMP feasibility study evaluation, the energy price (EP) has a fixed value throughout the entire LoM. In reality, the EP is not static since it depends on electricity market conditions (which are external to the project and vary over time). However, there are various alternatives that will allow us to manage the uncertainty related to this cost generator. The first alternative would be to establish electricity supply contracts (so-called 'power purchase agreements', or PPAs) with one or more energy companies. This would fix a price for the power purchased throughout the LoM and allow the mine to eliminate uncertainty relating to energy price variability. However, the real economic impact of this

Table II

The present value of the economic risk calculated for the four energy-related sub-activities

Activity	Sub-activity	Element of expenditure	RPV (US$ million)
Development	Production level	Energy	5.1
Production	Level transport	Energy	3.7
Production	Main transport	Energy	28.2
Production	Ventilation	Energy	16.4
Total			53.4

Table III

Present value of the economic risk of labour-related sub-activities

Activity	Sub-activity	Element of expenditure	RPV (US$ million)
Development	Caving level	Labour	7.3
Development	Production level	Labour	6.2
Production	Extraction	Labour	4.9
Production	Reduction	Labour	4.2
Production	Transfer	Labour	3.3
Production	Crushing	Labour	2.5
Production	Intermediate transport	Labour	2.3
Production	Mine services	Labour	1.7
Production	Damaged areas repair work	Labour	1.5
Production	Administration	Labour	6.4
Production	ICO	Labour	2.6
Total			43.4

Table IV

Main parameters used for the solar photovoltaic plant evaluation. (Parameters consider all expenses related to the construction and operation of the plant, and were estimated using information provided by energy consulting firms)

Solar PV average cost and parameters		
Investment cost	US$/kW	2000
Fixed O&M cost	US$/MWh	13.3
Life	Years	20
Capacity factor	%	35

alternative remains unclear, since it will depend on the difference between the price set by the contract and the future spot prices traded on the electricity market, which is usually addressed by market options valorization and is beyond the objective of the present study. A more suitable approach is to value the incorporation of a power plant, which could supply the project with at least some of its energy requirements. Developing a power plant for a mining operation is not a new concept in the mining industry. Some Chilean operations, like the Pelambres and Escondida mines, are already opting for this alternative. Considering the location of CUMP (the Atacama Desert) and the energy projects currently being developed in that region, the logical choice would be a power plant based on photovoltaic (PV) solar energy. The parameters used for the analysis of this alternative have been estimated using information provided by energy consulting firms for similar solar PV projects, and are outlined in Table IV.

For the purposes of evaluation, it is assumed the processing plant is commissioned in 2017 and begins operating in 2019, together with CUMP. The capacity of the plant will depend on the initial investment, which we assume will match the value of risk determined in the previous section for this element of expenditure (US$67.2 million in 2017). This will result in an installed capacity of 33.66 MW, capable of generating approximately 103 GWh per year. The impact on the project value is assumed as a consequent reduction in energy cost variability. By including this alternative within a new simulation model, we obtain a new probability distribution function for the operating cost NPV, shown in Figure 6.

According to the results, the proposed plant significantly impacts the energy-related economic risk, reducing it by 20.9%. Additionally, the mean present value of the operating cost of the project decreases by US$16 million. Given these positive results, we consider the proposed solar PV plant a good alternative for managing the energy-related economic risk.

Energy consumption intensity

The second factor contributing to the TEE is energy consumption intensity, which represents the energy consumed by each sub-activity per square metre developed or ton processed. This value will depend on variables such as equipment installed, operational conditions, characteristics of the mineral being processed, specific requirements of the processes involved in each sub-activity, and more, meaning its inherent variability is complicated to manage. An alternative for controlling the economic impact of this cost generator is to improve the efficiency of the required equipment, which will result in reduced overall energy consumption and, therefore, less uncertainty. To achieve this, we need to focus on the most relevant energy-related sub-activities for this case study: main transport and ventilation.

The CUMP main transport system consists of several conveyor belts carrying the mined material from extraction points to the processing plant located at surface level. The idea of conveyor energy efficiency has been adopted in the mining industry and successfully applied in practice. Conveyor efficiency can be improved at four levels: performance, operation, equipment, and technology (Zang and Xia, 2011). Since the CUMP transport system has not been constructed yet, any of these levels could potentially be optimized for decreasing its energy consumption. This is particularly noteworthy given that a 10% reduction in the energy consumption of the CUMP conveyors would decrease the present value of the project operating costs by US$25 million, and the energy risk would fall by 6%.

The CUMP ventilation system provides fresh air to underground operations through multiple main and auxiliary fans that run on electricity. Many recent studies have shown that mine ventilation energy efficiency can be improved by optimizing the traditional technical and operational conditions of fan systems (Pritchard, 2009). New technologies such as variable speed drives, composite materials, and 'hermit crab' techniques have proved feasible and cost-effective alternatives for this purpose (Belle, 2008). These technologies will be evaluated in the next stage of the project. A 10% reduction in the ventilation energy consumption would decrease the present value of project operating costs by US$13 million and reduce the energy economic risk by 3.2%.

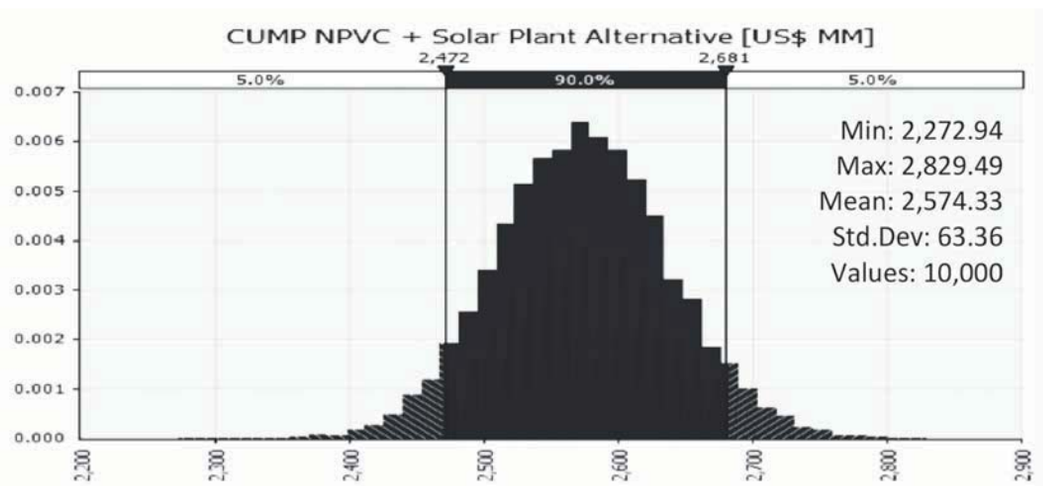

Figure 6—Probability distribution function for the operating cost NPV of the project with the alternative of a solar PV plant

Labour cost items

The total labour expenditure (TLE) per year for each labour activity in Table V is the product of labour price (LP), labour consumption intensity (LCI), and the production and development requirements for that year.

$$TLE\left[\frac{\text{US\$}}{\text{year}}\right] = LP\left[\frac{\text{US\$}}{\text{employee}}\right] * LCI\left[\frac{\text{employee}}{\text{ton or m}^2}\right] * PDR\left[\frac{\text{ton or m}^2}{\text{period}}\right] \quad [4]$$

Labour price

Labour price, or salary, represents the remuneration paid to employees in return for their work. In this case, the LP estimations are closely related to the market rates for people performing similar work in similar industries in the same region, so LP should be considered non-negotiable. Importantly, research into the evolution of LP in the mining industry over the last 20 years suggests that a real annual growth factor exists that is ignored in the CUMP base estimations (Consejo Minero, 2013). Using historical data derived from the Chilean mining labour price, it is possible to model this factor as an independent variable that fits a lognormal distribution with a mean of 2.61% and a standard deviation of 1.41%. The variable is included in the model and new simulations are created, obtaining a new probability distribution function for the operating cost net present value, shown in Figure 7.

With the LP real annual growth factor included in the case study, a mean NPV for the operational costs of the project of US$2.88 billion – US$298 million above the initial estimation – is obtained. The standard deviation of the distribution increases by 27.7% and the labour-related economic risk value doubles. These results suggest that annual growth of labour price represents a critical variable for the project, so it should be considered a major risk source and included in future evaluations.

Labour consumption intensity

Labour consumption intensity represents the number of employees needed to develop a square metre or to produce a ton during the LoM. In the mining industry, this cost generator is known as productivity, and it can potentially be managed. Studies show that the Chilean copper mining productivity index has decreased by more than 30% over the last 10 years (Keller, 2013). As a result, it is becoming a crucial topic of discussion, especially if we consider the relevance of labour costs for the total costs of any mining project. In the CUMP case study, the LCI for a sub-activity i can be expressed as:

$$LC_i\left[\frac{\text{employee}}{\text{ton or m}^2}\right] = SLRF_i\left[\frac{\text{employee} - \text{shift}}{\text{ton or m}^2}\right] * PRP\left[\frac{\text{employee}}{\text{employee} - \text{shift}}\right] \quad [5]$$

The sub-activity labour requirement factor (SLRF) represents the specific number of employees per shift that is needed for each of the sub-activities to operate. The personnel rotation parameter (PRP) is a fixed value representing the total number of employees needed for every employee per shift counted, taking into account the shift system and an estimated level of leave of absence. Attracting more highly skilled workers to the project and introducing new sub-activity-focused technologies can improve the SLRF. Optimizing shift systems and adopting specific measures to reduce absenteeism can improve PRP. Recent studies addressing the matter suggest that the shortage of skilled labour, at both managerial and operational levels, as well as the lack of process analysis, are the key factors affecting mining productivity, suggesting that a perceptible and significant correlation exists between human resources management and labour productivity (Huselid, 1995; Koch and Gunther, 1996; Perez-Oportus, 2008; Thorpe, O'Callaghan, and Guthridge, 2012). They also prove that sophisticated human resources planning and investments in hiring and employee development have an economically and

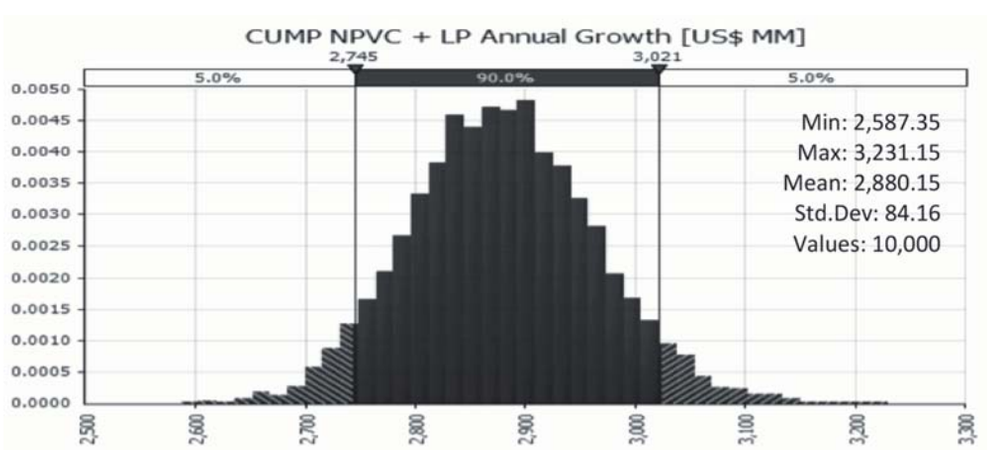

Figure 7—Operating cost NPV probability distribution function using historical data from Chilean mining labour prices

statistically significant impact on labour productivity, especially in capital-intensive organizations like mining companies. Based on these findings, the CUMP is evaluating new investments to improve productivity. Some relevant measures include the introduction of workshops targeting the specific industry skill requirements, the development of results-oriented incentives for workers, the optimization of current processes regarding projects and operations, and boosting human resources planning and hiring budgets. Implementing such measures is critical and will be evaluated in subsequent project stages, especially considering that a 10% improvement in labour productivity at CUMP would decrease the presently valued operating costs by US$70 million and further reduce the project's economic risk value.

Conclusions

A quantitative risk analysis methodology was successfully developed and executed to characterize and manage the risk associated with the variability of the key cost generators in an underground mining project. In the case analysed, the Chuquicamata Underground Project, the methodology identifies the main sources of risk related to cost drivers, helping to focus mitigation plans. Indeed, the results show that variability can potentially increase the present value of the estimated operating cost of the project by more than 10%, with labour and energy being the most relevant risk sources, comprising almost 70% of the total cost-driven economic risk.

After further data analysis, it was possible to discern that energy cost uncertainty arises from only two main activities, ventilation and main transport. In contrast, labour cost risk value is more homogenously distributed, and focusing on a few activities is difficult. Risk mitigation in the case of energy can be addressed by incorporation of a power plant to meet the energy demands of the project, and optimization of the conveyor and ventilation systems to increase energy efficiency. In the case of the labour cost item, mitigation requires a general focus on productivity, organizational structure, and appropriate incentives.

The method enables the most relevant cost items with the highest impact on risk value to be recognized during the early stages of a project. As result, management can focus time and effort on controlling the variables that matter.

The proposed risk analysis approach can be effectively applied to the operating cost structure of any underground mining project in order to identify its risk sources and assist in the decision-making process during the early stages of project evaluation.

References

Belle, B. 2008. Energy savings on mine ventilation fans using "quick-win" Hermit Crab Technology. *Proceedings of the 12th US/North American Mine Ventilation Symposium*, Reno, NV. Wallace, K.G. (ed.). University of Nevada. pp. 427–433.

Botín, J.A., Guzman, R., and Smith, M. 2011. A methodological model to assist the optimization and risk management of mining investment decisions. *Dyna. Journal of the Faculty of Mines. National University of Colombia*, vol. 78, no. 170. pp. 221–226.

Brown, J. 2012. Managing large-scale capital projects. 2012. *Americas School of Mine*, May 15-17, Scottsdale, AZ. PriceWaterhouseCoopers LLP. https://www.pwc.com/gx/en/mining/school-of-mines/2012/pwc-managing-large-scale-capital-projects.pdf

Chinbat, U. and Takakuwa, S. 2009. Using simulation analysis for mining project risk management. *Proceedings of the 2009 Winter Simulation Conference*, Austin, TX. Rossetti, M.D., Hill, R.R., Johansson, B., Dunkin, A., and Ingalls, R.G. (eds.). IEEE, New York. pp. 2612–-2623.

Chitombo, G.P. 2010. Cave mining – 16 years after Laubscher's 1994 paper "Cave mining – state of the art". *Caving 2010. Proceedings of the Second International Seminar on Block and Sublevel Caving*, Perth, Australia, 20–22 April 2010. Australian Centre for Geomechanics. Nedlands, Australia. pp. 45–61.

Consejo Minero. 2013. Gran minería de Chile: Desafíos de productividad. Working paper, Consejo de Competencias Mineras, Santiago, Chile. http://dev.consejominero.cl/wp- content/uploads/2016/03/Consejo-Minero-Competitividad-y-Productividad-JV-Agosto-2013-F.pdf

Heuberger, R. 2005. Risk analysis in the mining industry. *Journal of the South African Institute of Mining and Metallurgy*, vol. 105. pp. 75–80.

Huselid, M. 1995. The impact of human resource management practices on turnover, productivity and corporate financial performance. *Academy of Management Journal*, vol. 38. pp. 635–672.

Isaaks, E. and Srivastava, R. 1989. An Introduction to Applied Geostatistics. Oxford University Press, New York. pp. 55-65.

Keller, T. 2013. Competitividad de la Industria Minera Chilena. *Proceedings of Exposición Internacional de la Industria Minera – EXPONOR 2013*, Antofagasta, Chile, 17-21 June 2013., https://www.codelco.com/prontus_codelco/site/artic/20130117/asocfile/20130117172641/presentacion_pe_exponor_17jun2013.pdf

Koch, M. and Gunther, R. 1996. Improving labor productivity: Human resource management policies do matter. *Strategic Management Journal*, vol. 17. pp. 335–354.

MacKenzie, W. and Cusworth, N. 2007. The use and abuse of feasibility studies. *Proceedings of the 2007 Project Evaluation Conference*, Melbourne, Victoria, 19–20 June 2007. Australasian Institute of Mining and Metallurgy, Melbourne. pp. 1–12.

Marx W.M. *et al.* 2008. Development of energy efficient mine ventilation and cooling systems, *Mine Ventilation of South Africa Society Journal*, vol. 16, April/June. pp. 5–9.

Merrow, E. 2011/ Industrial Megaprojects: Concepts, Strategies, and Practices for Success. Wiley, Hoboken, NJ.

McCarthy, P. 2013. Why feasibility studies fail. *Working paper*, Australasian Institute of Mining and Metallurgy, Melbourne.

Pérez-Oportus, P. 2008. Costos de la minería: ¿*Cuánto impactan los insumos en la industria del cobre? Working paper*, Comisión Chilena del Cobre, Santiago, Chile.

Pritchard, C. 2009. Methods to improve mine ventilation system efficiency. *Working paper*, National Institute for Occupational Safety and Health, Spokane, WA.

Thorpe, J., O'Callaghan, J., and Guthridge, M. 2012. Productivity scorecard. *Working paper*, PriceWaterhouseCoopers, Sydney, Australia.

Tulcanaza, E. 2014. Certificación y valorización de recursos y reservas mineras. Committee for Mineral Reserves International Reporting Standards. http://comisionminera.cl/docs/folleto-curso-octubre.pdf

Society for Mining, Metallurgy, and Exploration, Inc. 2011. Mining Engineering Handbook, 3rd edn. Littleton, CO. pp. 227–231.

Summers, J. 2000. Analysis and management of mining risk. *Proceedings of Massmin 2000*, Brisbane, Queensland, 29 October–2 November 2000. Australasian Institute of Mining and Metallurgy, Melbourne. pp. 63–79.

Xia, X. and Zhang, J. 2010. Energy efficiency and control systems from a POET perspective. *Proceedings of the IFAC Conference on Control Methodologies and Technology for Energy Efficiency*, Vilamoura, Portugal, 29–31 March 2010. Ferrera, P.M. (ed.). Elsevier. pp. 255–260.

Zhang, S. AND Xia, X. 2011. Modeling and energy efficiency optimization of belt conveyors. *Applied Energy*, vol. 88. pp. 3061–3071. ◆

Appendix A—Pareto analysis

Table A1: Cost items and the net present value of their cost for 30 of 151 cost items that represent 80% of the total operational expenditure, from Pareto analysis

N	Activity	Sub-activity	Element of expenditure	NPVC
1	Production	Main transport	Energy	229.0
2	Development	Production level	Operation materials	161.9
3	Production	Ventilation	Energy	130.8
4	Development	Caving level	Operation materials	116.0
5	Production	Crushing	Labour	108.2
6	Development	Production Level	Labour	96.1
7	Production	Administration	Labour	96.0
8	Development	Production level	Contractors	91.4
9	Production	Extraction	Maintenance and repair materials	88.6
10	Production	ICO	Labour	81.3
11	Development	Production level	Depreciation	80.7
12	Production	Main transport	Maintenance and repair materials	76.6
13	Production	Extraction	Labour	66.6
14	Production	Crushing	Maintenance and repair materials	63.8
15	Production	Intermediate transport	Maintenance and repair materials	60.7
16	Production	Mine Services	Labour	54.5
17	Development	Caving Level	Labour	47.6
18	Development	Caving Level	Depreciation	46.1
19	Production	Production support services	Contractors (mineral handling maint.)	43.9
20	Production	Damaged areas repair work	Labour	42.4
21	Production	Transfer	Labour	38.4
22	Development	Production Level	Energy	37.2
23	Production	Damaged areas repair work	Operation materials	35.2
24	Production	Intermediate transport	Labour	31.3
25	Production	Reduction	Labour	26.8
26	Production	Production support services	Contractors (closure plan)	25.7
27	Production	Production support services	Contractors (food service)	25.1
28	Production	Production support services	Contractors (building and road maint.)	24.5
29	Production	Extraction	Supplies	23.4
30	Production	Level transport	Energy	21.0
			Total	2071

Appendix B—Input price modelling

Table B1: Historical data series (1994–2013) for real prices of inputs considered in the case study

Input	Unit	1994	1995	1996	1997	1998
Energy (1)	US$/MWh	63.3	59.3	56.0	53.1	46.7
Steel (2)	US$/dmt	33.6	31.6	30.9	33.3	35.1
Concrete (3)	Index	103.5	103.8	104.3	106.6	112.5
Diesel (4)	US$/litre	0.119	0.118	0.142	0.140	0.100
Explosives (5)	Index	115.9	115.6	114.6	116.8	118.5
Labour (6)	Index	75.4	78.9	82.8	85.2	86.5
Input	**Unit**	**1999**	**2000**	**2001**	**2002**	**2003**
Energy	US$/MWh	39.9	38.3	36.8	42.0	35.9
Steel	US$/dmtu	37.7	34.2	36.2	39.2	38.7
Concrete	Index	114.5	111.4	113.0	116.5	111.2
Diesel	US$/litre	0.141	0.223	0.200	0.207	0.228
Explosives	Index	115.3	103.2	106.4	112.7	113.0
Labour	Index	89.3	90.9	91.6	94.3	95.2
Input	**Unit**	**2004**	**2005**	**2006**	**2007**	**2008**
Energy	US$/MWh	39.9	41.9	53.9	65.5	116.8
Steel	US$/dmt	40.1	44.6	74.1	77.1	128.9
Concrete	Index	109.9	112.6	118.5	117.9	111.1
Diesel	US$/ litre	0.279	0.383	0.450	0.469	0.593
Explosives	Index	115.1	109.6	109.2	106.8	106.1
Labour	Index	97.6	98.2	100.0	102.9	104.2
Input	**Unit**	**2009**	**2010**	**2011**	**2012**	**2013**
Energy	US$/MWh	122.9	102.8	108.1	96.3	90.8
Steel	US$/dmt	151.7	82.9	145.9	154.1	119.5
Concrete	Index	123.8	114.0	104.9	106.3	108.7
Diesel	US$/litre	0.403	0.497	0.600	0.614	0.617
Explosives	Index	114.6	102.2	100.3	102.7	108.7
Labour	Index	105.8	111.7	114.9	117.6	122.6

(1) Chilean National Energy Commission (CNE): Historic Price Data of Chilean Electricity Systems
(2) The World Bank (WB) Commodity Price Data: Iron Ore Spot Real Prices
(3) The Bureau of Labour Statistics (BLS): Producer Price Index Commodities - Concrete Products
(4) The World Bank (WB) Commodity Price Data: Crude Oil Spot Average Real Prices
(5) The Bureau of Labour Statistics (BLS): Producer Price Index Commodities - Chemical and Allied Products - Explosives, Propellants and Blasting Accessories
(6) Chilean National Statistics Institute (INE): Real Wage Index

Appendix B (continued)

Table B2—Reference prices for the inputs considered in the case study and their calculated standard deviations for the 2015–2030 period

Input	Energy	Steel	Concrete	Diesel	Explosives	Labour
2014	118.2	142.1	110	0.60	110	126
2015	7.04	13.60	2.65	0.04	2.64	1.42
2016	11.34	16.20	3.43	0.05	3.51	2.59
2017	14.62	16.10	3.38	0.06	3.63	3.68
2018	17.88	21.20	3.82	0.07	3.39	4.77
2019	20.07	24.60	3.93	0.08	3.06	5.69
2020	21.83	28.20	4.00	0.10	3.52	6.59
2021	23.59	31.60	4.10	0.12	3.45	7.53
2022	25.07	34.70	4.10	0.14	3.90	8.47
2023	25.99	36.60	4.20	0.16	4.16	9.37
2024	26.46	38.70	4.24	0.17	3.46	10.39
2025	26.45	41.40	4.65	0.18	3.67	11.36
2026	26.67	44.23	5.32	0.19	4.66	12.53
2027	26.69	46.86	5.44	0.20	5.69	13.67
2028	26.73	49.88	5.45	0.22	5.84	14.92
2029	26.74	50.75	5.45	0.22	5.85	16.39
2030	26.75	50.80	5.46	0.23	6.28	18.06

Table B3—Correlation matrix between the input prices for the simulation

Input	Energy	Steel	Concrete	Diesel	Explosives	Labour
Energy	1.00	0.90	0.05	0.74	–0.43	0.65
Steel	0.90	1.00	0.16	0.87	–0.55	0.83
Concrete	0.05	0.16	1.00	0.15	–0.02	0.24
Diesel	0.74	0.87	0.15	1.00	–0.74	0.93
Explosives	–0.43	–0.55	–0.02	–0.74	1.00	–0.69
Labour	0.65	0.83	0.24	0.93	–0.69	1.00

http://dx.doi.org/10.17159/2411-9717/2018/v118n3a11

Trials of the Garford hybrid dynamic bolt reinforcement system at a deep-level gold mine in South Africa

by F. Sengani

Synopsis

Efficient dynamic bolt reinforcement is crucial in deep-level gold mines prone to rockbursts. Deep-level gold mining in South Africa is approaching 4000 m, so appropriate support designs need to be implemented to manage ground stability challenges associated with these great depths. In order to extract the orebody, both novel mining methods and massive mining techniques have to be applied. Currently, massive mining techniques are used and destressing is imperative. Destressing is accomplished by cutting a series of overlapping, 5 m high horizontal slots across the reef. Although the minor span of each slot is about 100 m, stresses are extremely high due to presence of abutments. In order to protect workers from the effects of small seismic events, a yielding support system consisting of weld mesh (100 mm apertures and 5 mm strands) and 2.5 m long Garford hybrid bolts has been developed. The support system allows installation to be made at 0.5 m from the advancing face without significant damage by the blast. A tendon pretension of 49.3 kN ensures an active support system at installation, with 29 kJ/m^2 energy absorption capacity during seismic events, and static tensile capacity of 147 kN. The effectiveness of the Garford hybrid bolt is discussed in this paper.

Keywords
ground support, yielding support, dynamic bolt, Garford bolt.

Introduction

As mining progresses from deep to ultra-deep levels, stress levels increase rapidly. This compromises the effectiveness of support systems and the stability of excavations underground (Ortlepp, 1992). Excavations driven into highly stressed ground typically suffer from stress-induced damage (Mühlhaus, 1990; McCreath and Kaiser, 1992; Maxwell, and Young, 1997; Daehnke *et al.*, 1998). Stress-induced damage can result from either the creation of new fractures or the reactivation of existing fractures in the rock mass (Brady and Brown 1993). As a result of these challenges, rock support systems for underground excavations have changed significantly due to improved technologies and experience gained (Ortlepp, 1992; Jager and Ryder, 1999)

Ground support/reinforcement design

Ground support/reinforcement design has evolved into a comparatively complex discipline involving the quantification of various rock mass and support parameters (Villaescusa, and Wright, 1997, 1999). A flow chart indicating the principal design steps that should be followed when designing support systems specific to a given geotechnical environment is shown in Figure 1. The generic procedure consists of several distinct steps. In many instances, there may be nothing technically wrong with the design and the performance can be considered acceptable. However, rock mass conditions usually change with the progress of a mine (*e.g.*, stresses increase as depth of mining increases and when the extraction increases) and accordingly, the performance of the ground support may change and become unacceptable (Brady and Brown 1993; Villaescusa, and Wright, 1997, 1999; Jager and Ryder, 1999).

Destress technique

A deep-level gold mine is currently mining at a depth of about 2600 m below surface, with a horizontal-to-vertical stress ratio of about 0.7. Virgin stresses are high in deep to ultra-deep mines, which makes it difficult to implement massive mining techniques. Hence a series of horizontal destress cuts is used to destress the area. The destress cuts are mined through the

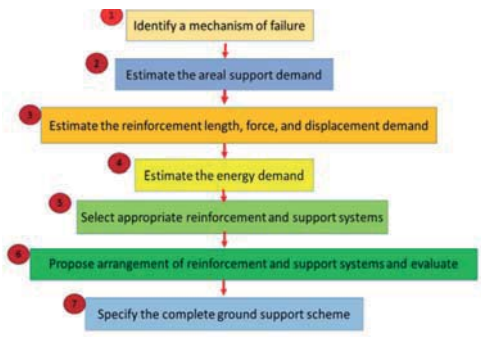

Figure 1—The generic procedure of ground support design

* *South Deep Goldfields Mine, South Africa.*
 ISSN 2225-6253. Paper received Mar. 2017; revised paper received Jan. 2018.

strata with a maximum span of about 180 m and a 20 m overlap between successive cuts (see Figure 2). The mining configuration of destress cuts has the shape of an arrowhead to account for proper leads and lags in the high stress conditions. These destress cuts are mined at a stoping height of 5.5 m, the stoping widths are about 5 m, and the lengths 15 m. Subsequently, 10 m of the 15 m is backfilled, to create a 5 m wide strike access drive (SAD), and then the adjacent excavation is mined in the same direction (see Figure 3). In essence, the destressing reduces the vertical stress so that the major principal stress is in the horizontal direction. These destress cuts are supported with 2.5 m long Garford hybrid bolts with 3 m × 1.5 m rectangular weld mesh on both sidewalls and hangingwall.

The support system in the destress cuts is designed to absorb sufficient energy during a seismic event to protect workers and maintain the integrity of the highly stressed excavations. Hoek and Brown (1980) pointed out that the objective of reinforcing the rock mass is to strengthen it and to prevent loss of strength, thus enabling the rock mass to support itself. The support system within destress cuts also retain the broken rock, which is required for safety reasons. It also becomes essential under high stress conditions as a way of preventing progressive failure leading to unravelling of the rock mass (Zvarivadza *et al.*, 2017).

Methodology

The performance of the Garford hybrid dynamic bolt reinforcement system was evaluated through laboratory tests, which included static pull, dynamic drop, and torque tests), and underground tests (pull test, torque test, and quality of the installation). The performance of the bolts during seismic events was also evaluated. It was found necessary to indicate the required support resistance and energy absorption for areas (ground control districts) where Garford bolts were installed.

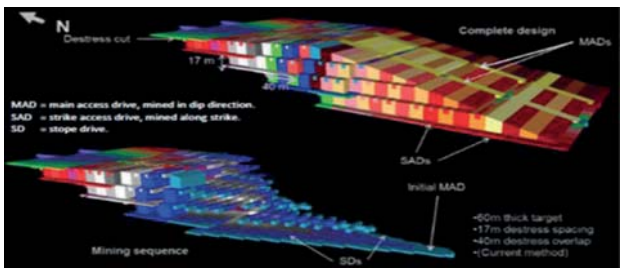

Figure 2—An oblique view of a destress cut

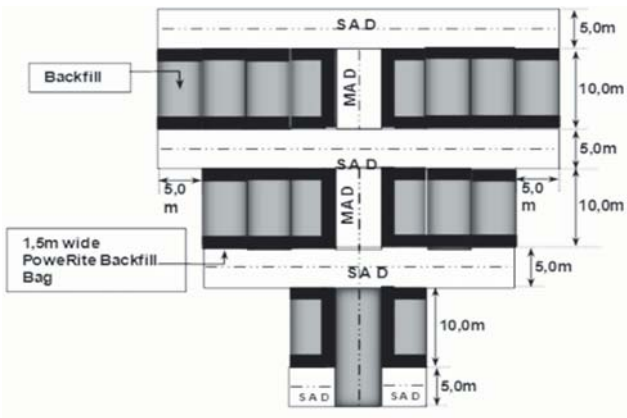

Figure 3—Plan view of horizontal destress layout. MAD – main access drive, SD – strike drive, SAD – strike access drive

Support design

The Garford hybrid dynamic bolt reinforcement system was designed to reinforce development ends, also called destress cuts. The previous fallout thickness within the conventional stope and detress cuts, rock mass classification and kinematics analysis, and other rock engineering principles such as rule of thumb were implemented when designing the support requirements for destress cuts. In this case the required support resistance and energy absorption were calculated to determine the required reinforcement system.

Dynamic performance tests

The objective of the dynamic performance tests was to assess the performance of the overall Garford hybrid dynamic bolt system under dynamic loading conditions. Each test consisted of dropping a mass of 3000 kg from a height of 750 mm onto a plate connected to the bolt specimen inside the steel installation tube. The kinetic energy input into the system was 22.06 kJ for each drop test. The testing rig in its actual configuration had a capacity of 3 t; the maximum velocity of 3.26 m/s was used in all tests. The total extension (mm), peak force load (kN), yield deflection (mm), and test time (seconds) were recorded. Figure 4 shows the detailed views of the test assemblies.

Static pull test procedures

All equipment and procedures were developed to meet or exceed the Deep Level Goldmine Standard Test Method for Laboratory Determination of Rock Anchor Capacities by Pull and Drop Tests. Two hydraulic rams with a capacity of 300 kN and total displacement of 300 mm were used. The hydraulic rams were operated, using an electric pump, from the initial phase of loading until the bolt failed, or the rams reached their stroke capacity (300 mm). Figure 5 displays the configuration of the electric pump with Garford bolt. The pressure of the hydraulic ram was measured at both ends of the test specimen (*i.e.* plate and toe ends) using electronic pressure transducers. All measuring instruments were connected to an automatic data-acquisition system and zeroed at the beginning of each test. A data sampling rate of 1 Hz was used.

Underground pull tests and quality control tests

Underground pull tests were conducted by assembling and attaching the pull gear at the collar of the bolts. The dial indicator was attached with the adjustable rod in line with

Figure 4—Drop test assemblies

Figure 5—Static pull test set-up

the bolt axis to allow the bolt to be pulled directly down on the dial indicator, and the dial indicator was adjusted to zero. Immediately after the above steps, loading of the ram from zero to 3 t began and the recorded load and displacement were noted. Continuous pumping and recording of the load for each subsequent 0.05 mm displacement continued until the bolt yielded before full expansion of the ram, when the test was stopped.

Support requirements

A database of all reportable falls of grounds (FOGs) has been kept since 1995. Most of the FOGs occurred in the old conventional stopes and destress cuts, where areal coverage was not good. These records provided valuable information on the support requirements. The reach and capacity of the support was calculated on the 95th percentile of the conventional database (see Figure 6).

Figure 6 shows that the support should anchor above a height of 1.05 m (assuming the suspension theory). An appropriate mechanical anchor length of 1.8 m was chosen to ensure that the loose rock is properly anchored. The support resistance (SR) was calculated assuming a 1.05 m fallout thickness:

$$SR = \rho g t \quad [1]$$

where

ρ is the density of the immediate hangingwall rock (2.68 t/m^3)

t is the 95th percentile thickness of measured falls of ground (1.5 m)

g is acceleration due to gravity (9.81 m/s^2).

Factor of safety for steel: 1.2

SR = (2.68*9.81*1.5*1.2)/(1 m*1 m) = 47.3 kN/m^2 (required support resistance).

Brady and Brown 1993, stated that where peak ground velocities exceed 1 m/s, significant kinetic energy and momentum are imparted to the rock, resulting in potentially large displacements. Using the fallout thickness determined above as the potential depth of instability, it is possible to calculate the minimum energy absorption (EA) requirement per square metre of rock wall. The EA criterion for the hangingwall support system at the mine is 30 kJ/m^2, based on:

$$EA_{hw} = {}^1/_2 mv^2 + mgh \quad [2]$$

where

m is the mass of ejected rock (4020 kg/m^2)

v is the anticipated peak ground velocity (3 m/s^2)

h is the distance over which the energy is absorbed (0.3 m)

g is acceleration due to gravity (9.81 m/s^2).

EAHW = 0.5*4020*9+(4020*9.81*0.3) = 29.9 kJ (required EA for hangingwall)

EASW = mgh = 4020*9.81*0.3 = 11.8kJ (required for sidewall).

Support configuration

The support consists of weld mesh, with 5 mm thick strands and an aperture of 100 × 100 mm, and 2.4 m long yielding anchors. The anchors are installed with 300 × 280 mm faceplates and pre-tensioned to 30 kN at installation. This tensioning effectively stretches the mesh tight against the hangingwall and provides an active support. The Garford hybrid dynamic bolt spacing is 1 m across and 5 m along the width of the excavation and placed 1.2 m in the direction of the advancing face. The latter spacing fits the 2.4 m face advance. Support configuration in plan view is shown in Figure 7.

Yield support and test results

The Garford hybrid dynamic bolt is a ground reinforcement system that comprises a high-strength steel tube with a slot along its entire length. One end of the friction bolt is tapered to assist insertion into the hole, and the other end has a spherical steel collar to retain a bearing plate and the yielding portion at the end (see Figure 8).

Static pull test results

Five specimens were tested under static conditions to evaluate the installation method. The results obtained are presented as displacements *vs* load curves in Figures 9–13, and summarized in Table I.

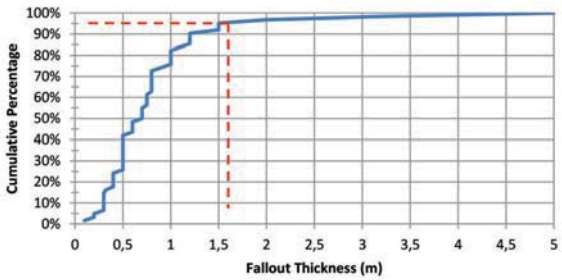

Figure 6—FOG fallout thickness using data from old conventional and destress cuts

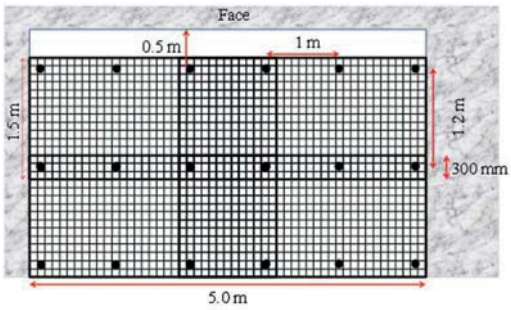

Figure 7—Support configuration in plan view

Figure 8—Schematic view of the Garford hybrid bolt

Table I

Summary of static pull test results

Specimen no.	Peak load (kN)	Sliding load (kN)	Max. extension (mm)
1	220.634	160	257
2	232.77	155	270
3	183.53	165	257
4	211.88	157	252
5	186.34	153	280

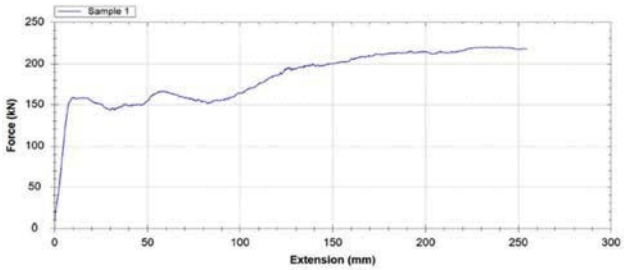

Figure 9—Static pull test for the first specimen

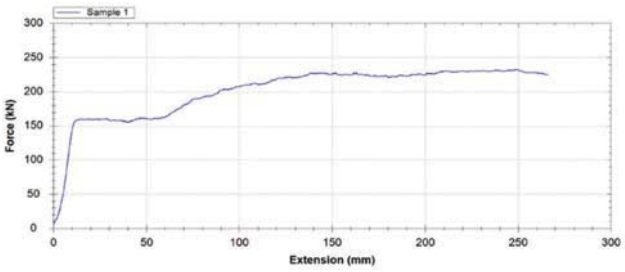

Figure 10—Static pull test for the second specimen

In all tests, after a short sliding distance, the dynamic device anchored into the split set bolt and then the load increased until the solid bolt began to be pulled through the dynamic device. From this test, it can be deduced that the Garford hybrid bolts were capable of withstanding a tensile load ranging from 183.53 kN (18.3 t) to a maximum of 232.77 kN (23.277 t) with a maximum extension of about 280 mm.

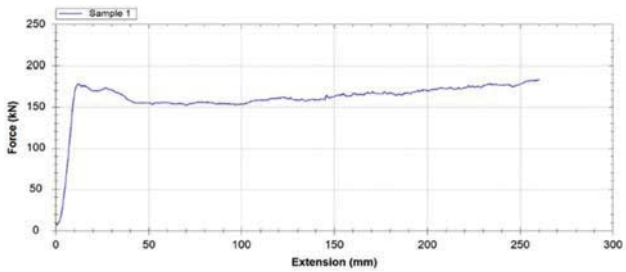

Figure 11—Static pull test for the third specimen

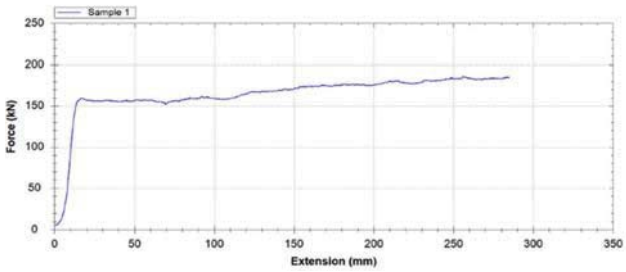

Figure 12—Static pull test for the fourth specimen

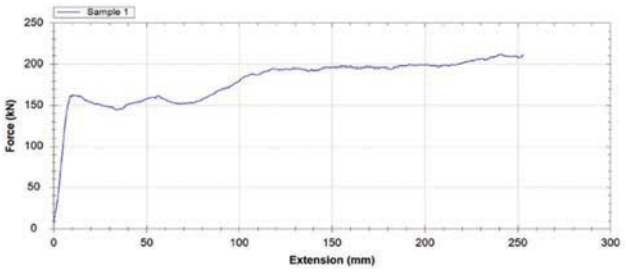

Figure 13—Static pull test for the fifth specimen

Dynamic impact drop test results

The drop test cycle is illustrated schematically in Figure 14. The results from a single drop configuration are summarized in Table II, and the results from tests on five specimens are presented in Figures 15–19. The first specimen withstood the first impact with a peak load of 191.79 kN, and the time

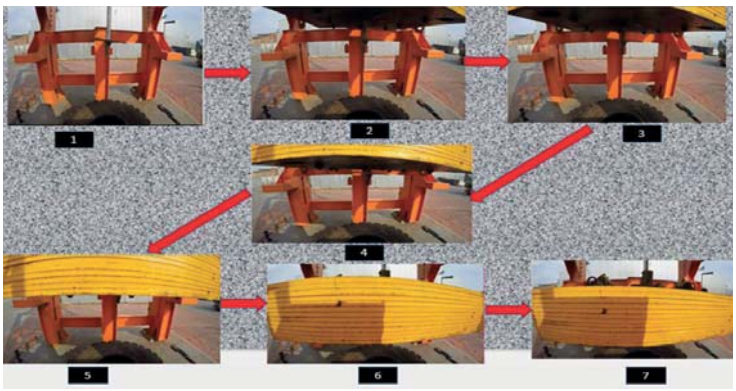

Figure 14—Drop test cycle on a Garford hybrid bolt

Table II

Dynamic impact drop test results with the continuous tube configuration

Sample	Drop height (mm)	Energy (kJ)	Max. velocity (m/s)	Peak force (kN)	Test time (s)	Total extension (mm)	Yield deflection (mm)	Peak force between 120–250 kN	Energy between 21–26 kJ	Yield deflection between 200–300 mm
1	750.0	22.06	3.26	191.79	20.20	971.37	221.00	Pass	Pass	Pass
2	751.0	22.09	2.90	217.95	21.10	941.54	191.00	Pass	Pass	Pass
3	752.00	22.12	3.28	141.45	21.40	980.44	228.00	Pass	Pass	Pass
4	755.00	22.21	3.28	138.18	17.50	986.85	232.00	Pass	Pass	Pass
5	750.00	22.06	3.25	157.98	20.50	956.46	206.00	Pass	Pass	Pass

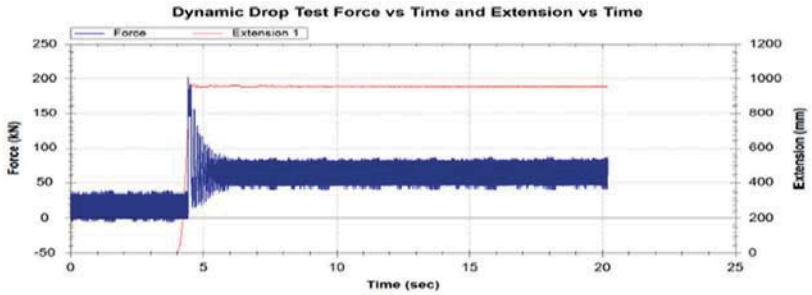

Figure 15—Drop test on the first specimen

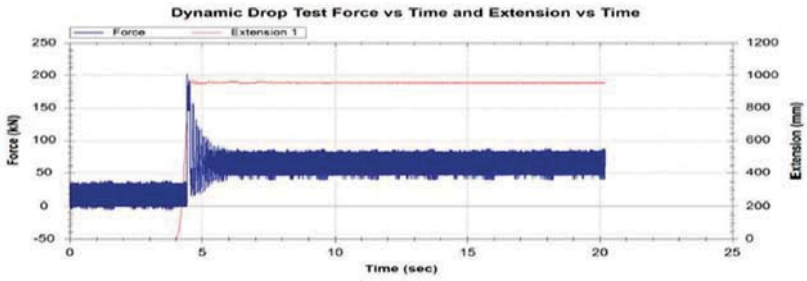

Figure 16—Drop test on the second specimen

taken for a test was 20.20 seconds, with a yield deflection of 221 mm. During this test, a maximum velocity of 3.26 m/s was achieved, with the energy absorbed being 22.06 kJ. After the test, no longitudinal cracks were observed along the bolts, unlike other types of bolt. The second specimen withstood the impact with a peak load of 217.95 kN and the time taken for a test was 21.10 seconds, with a yield deflection of 191mm. A maximum velocity of 2.9 0m/s was achieved with the energy absorbed being 22.09 kJ. Unlike the first and second tests, the third specimen withstood the

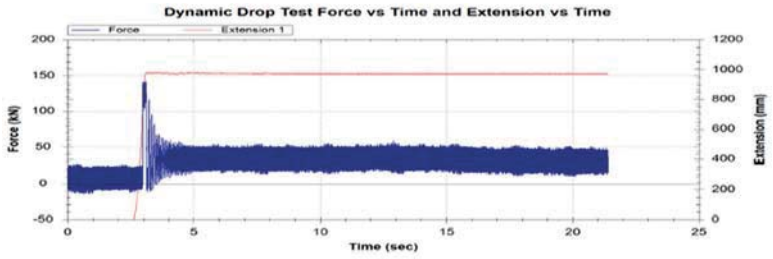

Figure 17—Drop test on the third specimen

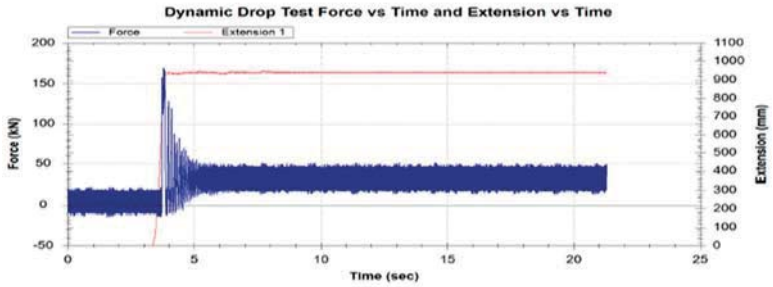

Figure 18—Drop test on the fourth specimen

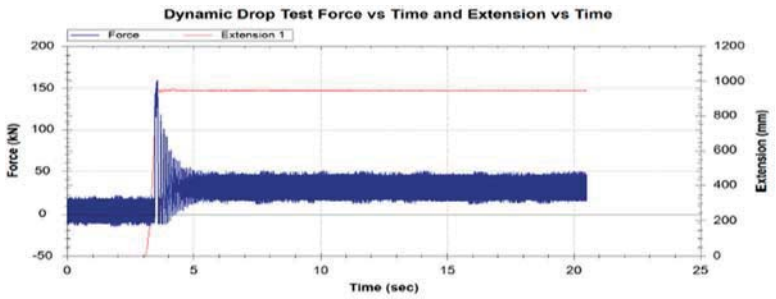

Figure 19—Drop test on the fifth specimen

impact with a peak load of 141.45 kN and the time taken for a test was 21.40 seconds, with a yield deflection of 228 mm. The maximum velocity was 3.28 m/s, with the energy absorbed being 22.12 kJ. The fourth specimen withstood the impact with a peak load of 138.18 kN and the time taken for the test was 17.50 seconds, with a yield deflection of 23 2 mm. During this test, a maximum velocity of 3.2 8m/s was achieved with 22.21 kJ energy absorbed. The last specimen was found to withstand the impact with a peak load of 157.98 kN and the time taken for a test was 20.50 seconds, with a yield deflection of 206 mm. The maximum velocity was 3.25 m/s and the energy absorbed 22.06 kJ. Figure 14 confirms the sliding of the dynamic device into the split set before plastic deformation of the solid bolt.

Torque tests

The laboratory torque test was conducted using nuts in different conditions, including rusted, new, and gritty nuts. The performance of all nuts was found to be effective and suitable for the bolts. Figure 20 shows the torque test performance on surface.

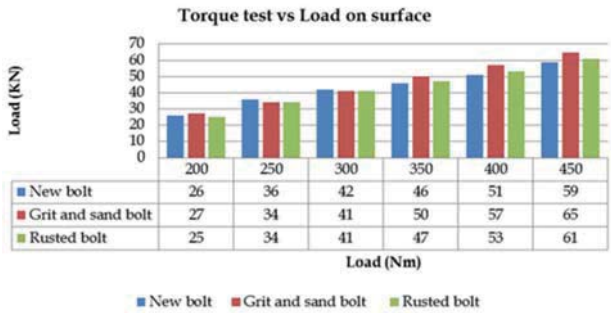

	200	250	300	350	400	450
New bolt	26	36	42	46	51	59
Grit and sand bolt	27	34	41	50	57	65
Rusted bolt	25	34	41	47	53	61

Figure 20—Garford bolt torque tests *vs* load (tests on surface)

Underground pull tests

To investigate the behaviour of Garford bolts in actual mine conditions, underground pull tests were conducted. The results of the study indicated that, as expected from the surface test results, none of the tested bolts could withstand more than 160 kN, most of the bolts failing between 60 kN

and 130 kN (see Figure 21). Only one bolt withstood 160 kN. Further underground investigations included torque tests and assessing the quality of installation.

Performance of Garford hybrid bolts under dynamic conditions

During the trials, several seismic events occurred ahead of the mining faces and in the back areas. Most of the areas affected by these events were found to be stable and the performance of the bolts was found to be effective. Although some of the bolts were noted to pull out from the in-stope pillar, the majority of the bolts managed to withstand several seismic events (see Figures 22–24).

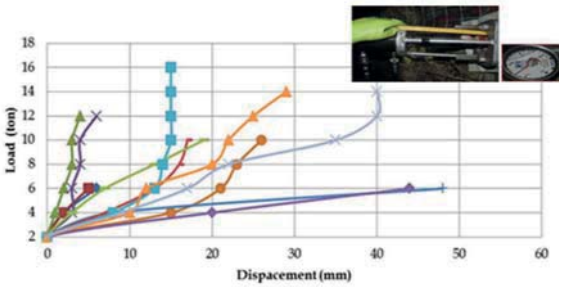

Figure 21—Underground pull test results for Garford hybrid dynamic bolts

Underground torque test results

Underground torque tests were conducted using a torque tester. The tests were assessed based on the number of turns

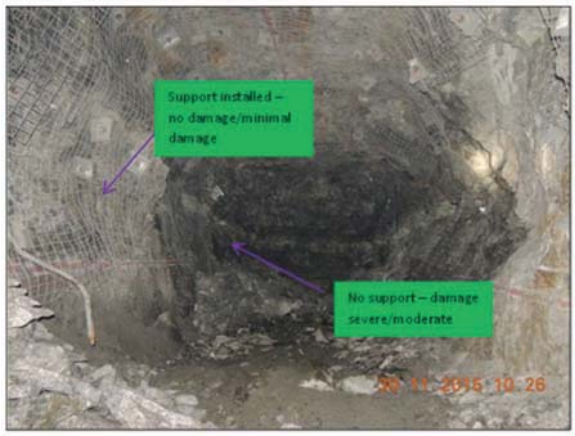

Figure 24—Performance of Garford bolt in a seismic event

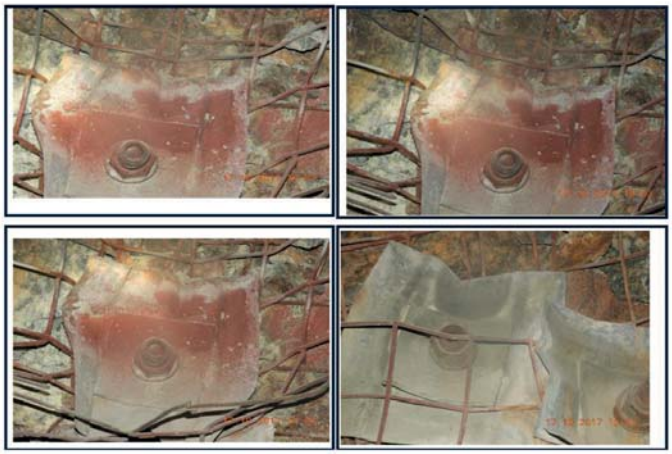

Figure 22—Performance of Garford bolts in a seismic event

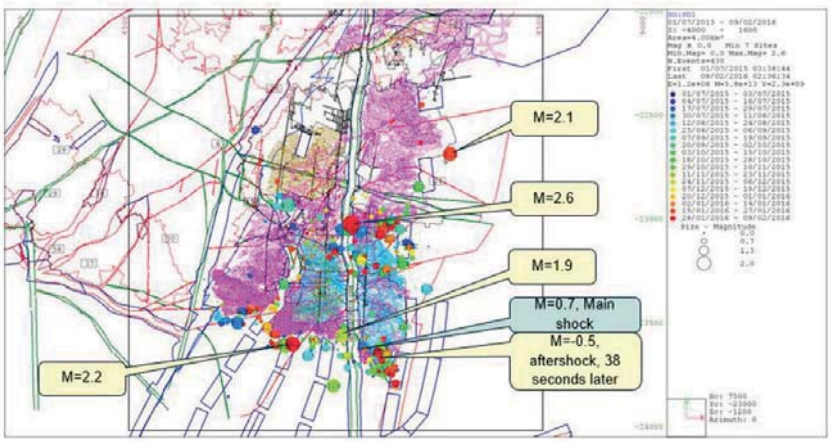

Figure 23—Localities of seismic events

Table III

Torque test results

Garford hybrid dynamic bolt torque tests							
Bolt number	**Before test**	**After test**	**Turns**	**Bolts number**	**Before test**	**After test**	**Turns**
1	Tight	2600 Nm	No turn	10	Tight	2600 Nm	1 1/2 turn
2	Tight	2600 Nm	No turn	11	Tight	2600 Nm	No turn
3	Tight	2600 Nm	1 1/2 turn	12	Tight	2600 Nm	No turn
4	Tight	2600 Nm	No turn	13	Tight	2600 Nm	No turn
5	Tight	2600 Nm	1 1/2 turn	14	Tight	2600 Nm	No turn
6	Tight	2600 Nm	No turn	15	Tight	2600 Nm	1 1/2 turn
7	Tight	2600 Nm	No turn	16	Tight	2600 Nm	No turn
8	Tight	2600 Nm	No turn	17	Tight	2600 Nm	1 1/2 turn
9	Tight	2600 Nm	No turn				

in which the span rotated. The results of the study showed that five of the tested bolts out of seventy were not properly tensioned (the turns were either a half turn, full turn, or quarter turn) (see Table III).

Underground performance

The actual performance of the bolts underground was found to be different from that in surface tests. Several contributing factors to this were identified, including poor angle of installation, poor tensioning, the use of a larger drill bit than required, and highly fractured ground conditions which hampered proper installation. Poor support spacing was also found to contribute to the ineffectiveness of the Garford bolt in some area.

These issues have, to some extent, been addressed by providing sections with dedicated air compressors and hydraulic drilling machines. The bit size has been reduced to 41 mm to make it easily differentiable from the 45 mm blast-hole bit. It is also possible to fit standard drill-rod couplings into the 41 mm diameter support holes.

During the trials, several seismic events occurred ahead of the mining faces and also in the back areas. It was noted that most of the areas affected by events were found to be stable and the performance of the bolts were found to be effective. Although some of the bolts were noted to pull out from the in-stope pillar, majority of the bolts manage to withstand several seismic events (see Figure 23 and 24).

Conclusions

In order to determine the dynamic capability of the Garford hybrid bolt, static and dynamic tests were performed at the Videx Mining test facility in South Africa. The Garford hybrid bolt was found to withstand a maximum peak load of 217.9 5kN, with a minimum peak load of 138.18 kN; this was achieved in a test time of 17.50–21.40 seconds. Energy absorption ranged from 22.06 kJ to 22.21 kJ, with the velocities ranging from 2.90 m/s to 3.28 m/s. The maximum yield deflection of the bolts was found to range from 191 mm to 232 mm, indicating that the bolts were able to stretch adequately. The tensile tests have shown that the Garford hybrid bolts were capable of withstanding a tensile load ranging from 183.53 kN (18.3 t) to a maximum of 232.77 kN (23.277 t), with a maximum extension of about 280 mm. The underground performance of the bolts was different from that in the surface tests, but this was largely due to the quality of installation and ground conditions. Garford hybrid bolts were found to perform well during seismic events that occur at the vicinity of the mining faces and back areas.

Acknowledgements

The author is grateful to Mr Nin Nacker his support, and also the mine for facilitating the research. In addition, the participation of Mr Tawanda Zvarivadza in providing assistance and editing the work is also acknowledged.

References

Brady, B.H.G. and Brown, E.T. 1993. Rock Mechanics for Underground Mining. 2nd edn. *Chapman & Hall, London*. 571 pp.

Daehnke, A., Andersen, L.M., de Beer, D., Esterhuizen, G.S., Glisson, F.J., Grodner, M.W., Hagan, T.O., Jaku, E.P., Kuijpers, J.S., Peake, A.V., Piper, P.S., Quaye, G.B., Reddy, N., Roberts, M.K.C., Schweitzer, J. K., Stewart, R.D., and Wallmach, T. 1998. Stope face support systems. Final report for SIMRAC Project GAP 330. CSIR Division of Mining Technology. 407 pp.

Dyskin, A.V. and Germanovich, L.N. 1993. Model of rockburst caused by cracks growing near free surface. *Rockbursts and Seismicity in Mines. Proceedings of the 3rd International Symposium*, Kingston, Ontario, 16–18 August 1993. Young, R.P. (ed.). Balkema, Rotterdam. pp. 169–174.

Hoek, E. and Brown, E.T. 1980. Underground Excavations in Rock. Institution of Mining and Metallurgy, London. 527 pp.

Jager, A.J. and Ryder, J.A. 1999. A Handbook on Rock Engineering Practice for Tabular Hard Rock Mines. Safety in Mines Research Advisory Committee, Johannesburg.

Maxwell, S.C. and Young, R.P. 1997. Assessing induced fracturing around underground excavations using velocity imaging and induced seismicity. *Rockbursts and Seismicity in Mines. Proceedings of the 4th International Symposium*, Kraków, Poland, 11–14 August 1997. Gibowicz, S.J. and Lasocki, S. (eds.). Balkema, Rotterdam. pp. 179–183.

Mühlhaus, H.-B. 1990. Exfoliation phenomena in pre-stressed rock. *Rockbursts and Seismicity in Mines. Proceedings of the 2nd International Symposium*, Minneapolis, MN, June 1988 Fairhurst, C. (ed.). Balkema, Rotterdam. pp. 101–107.

McCreath, D.R and Kaiser, P.K. 1992. Current support practices in burst–prone ground (Task1). Technical Report to the Mining Research Directorate, Sudbury, Ontario. 2 volumes, 94 pp.

Ortlepp, W.D. 1992. Invited lecture: The design of support for the containment of rockburst damage in tunnels – An engineering approach. *Proceedings of the International Symposium on Rock Support in Mining and Underground Construction*, Laurentian University, Sudbury, June 1992. Kaiser. P.K. and McCreath, D.R. (eds.), Balkema, Rotterdam. pp. 593–609.

Villaescusa, E. and Wright, J. 1997. Permanent excavation reinforcement using cement grouted split set bolts. *Proceedings of the Australasian Institute of Mining and Metallurgy*, vol. 1. pp. 65–69.

Villaescusa, E. and Wright, J. 1999. Reinforcement of underground excavations using the CT bolt. *Rock Support and Reinforcement Practice in Mining. Proceedings of the International Symposium on Ground Support,* Kalgoorlie, Western Australia, Australia, 15–17 March. Villaescusa, E., Windsor, C.R., and Thompson, A.G. (eds.), Balkema, Rotterdam. pp. 109–115.

Zvarivadza, T., Sengani, F., and Adoko, A.C. 2017. In-stope pillar scaling and fracturing in Southern African deep level gold mines. *26th International Symposium on Mine Planning and Equipment Selection (MPES2017)*, 29–31 August 2017, Luleå, Sweden, pp. 379–388. ◆

http://dx.doi.org/10.17159/2411-9717/2018/v118n3a12

A review of lashing methods used in shaft sinking

by T.J. Frangakis

Synopsis

Shaft sinking operations involve repetitive activities, some of which require significant amounts of time to complete. Lashing or mucking of blasted material is one such activity, which currently occupies approximately 40% of the cycle time and is also dangerous for workers at the shaft bottom. In this paper, the main lashing techniques used in modern shaft sinking are reviewed and compared in terms of efficiency and safety. An analysis of lashing duration as a function of shaft diameter and bucket volume is conducted, and the results compare reasonably well with published loading rate data. There are opportunities for developing opposed bucket loaders further, possibly adding an extra degree of freedom, and reviewing the bucket action in shallow muckpiles.

Keywords
shaft sinking, loader, cactus grab, excavator, lashing, mucking.

Background

Shaft sinking and equipping is a critical activity in the establishment of new underground mining operations or accessing deeper orebodies in existing mines. A typical mine shaft allows men and materials to be transported underground and ore to be hoisted to the surface. Shafts may be sunk to depths up to, and even in excess of, 3000 m in a single lift (AngoGold Ashanti, 2017; Murray and Roberts, 2017; Engineering News, 1999), while for other engineering applications such as access tunnels for railway systems these may of the order of tens or hundreds of metres.

Shaft sinking therefore requires material such as sand, rock, and water to be excavated from the ground in order to create the shaft. In shallow shafts the excavated material may initially consist of soil, clays, and weathered and sedimentary rock, which may be possible to remove by means of earthmoving equipment such as excavators and roadheaders (in fairly soft rock). For example, the Herrenknecht shaft boring roadheader can mine to a depth of 1000 m in soft, heterogeneous rock (Herrenknecht, 2016). As the depth of the shaft increases it usually progresses into competent rock, which may have medium to high compressive strength, and which may require other means to excavate it.

The traditional method of shaft sinking involves the cyclic activities of drilling, blasting, lashing (cleaning, also known as 'mucking'), blow-over of fines, hoisting of blasted material, support drilling, shaft lining, and shaft equipping. These functions are usually conducted from a shaft-sinking platform or 'stage'. Among these activities, lashing, which is the loading of blasted material into kibbles, and the associated hoisting of waste material, occupies a substantial portion of the time taken to complete one cycle. This part of the sinking cycle also exposes workers to significant hazards. An allied activity that occurs after lashing is 'blow-over', where compressed air is used to gather the remaining fines into heaps so that they can be loaded into the kibbles. This activity of blow-over is also used to expose the blast-hole sockets that have remained after the blast, in order to determine whether any undetonated explosives are present.

Data relating to sinking activities has been presented by Wakefield (2009) and Morgan (2015). These authors indicate that lashing and hoisting of waste rock occupies between 28% and 32% of the cycle time (excluding blow-over). Morgan analysed the cycle times for 152 cycles of the sinking of an 8.1 m diameter shaft, with an advance of 3 m per cycle and an average cycle taking just over 29 hours. He determined that the average lashing time was approximately 9 hours. In addition, blow-over was, on average, just under 3 hours. Of this time, approximately 80% was associated with lashing of the remaining fines. In the particular sinking operation quoted by Morgan the activities of lashing and blow-over combined to occupy almost 41% of the cycle

* *School of Mechanical, Industrial and Aeronautical Engineering, University of the Witwatersrand, Johannesburg, South Africa.*

 ISSN 2225-6253. Paper received Mar. 2017; revised paper received Feb. 2018.

time. This is a significant improvement over historical results such as those presented in MacGillivray (1979), who quotes data for the sinking of two shafts where lashing and blow-over amounted to 62% and 67% of the cycle times of 5.94 hours and 6.79 hours respectively.

Since lashing and hoisting is a significant time component of the cycle, and since delays are often associated with it, it is therefore an important area to investigate in order to speed up the shaft sinking process. Consequently, it is critically important that the shaft sinking system be designed around the lashing and kibble hoisting systems to maximize their effectiveness. There are two alternatives for the kibble hoisting system. In a two-kibble system, a single drum winder is used with one kibble being loaded at the shaft bottom while the other is in transit. In a three-kibble system, a double drum winder is used. While one detached kibble is being loaded at the shaft bottom; a full kibble is ascending and a third empty kibble, which acts as a counterweight, is simultaneously descending to the shaft bottom Bennet *et al.,* (1959). The choice of the number of kibbles employed depends, to some extent, on the shaft diameter and the amount of space in the shaft sinking stage that is required to allow the kibble(s) to pass through. Kratz and Martens (2015) described the relationship between the lashing and kibble hoisting systems. Using the fact that hoisting is dependent on shaft depth (while lashing is not), they showed that in the early part of a sink the lashing system was the limitation in the two functions of lashing and hoisting (since the kibbles did not have far to travel to reach the surface and return). For a two-kibble system, lashing was shown to be the limiting factor until a depth of 780 m. Below this theoretical depth, the hoisting system became the limitation and the lashing system was idle while waiting for an empty kibble to return. They further showed that for a three-kibble system, the lashing system was the limiting factor until a depth of 2 670 m, after which the hoisting system became the limiting factor. In order to assess these results, it is first necessary to investigate a factor that affects them, namely the bucket fill factor.

Bucket fill factor is defined in the Caterpillar Performance Handbook (Caterpillar, 1998) as the ratio of the average bucket payload volume to the heaped bucket capacity, where the heaping is relevant to bucket excavators and allows for slightly more material to be retained in the bucket than the nominal geometric volume of the bucket. In the Caterpillar Handbook, the following ranges of bucket fill factors are defined:

- 0.6–0.75 for well-blasted rock (presumably a narrow particle size distribution and rock fragments that are reasonably small in relation to the bucket size)
- 0.4–0.6 for poorly blasted rock (presumably a wide particle size distribution with some large rock fragments relative to the bucket size).

Kratz and Martens (2015), and Brunton *et al.,* (2003), indicated that as particle size increases, bucket loading time also increases, due to increased resistance encountered in penetrating the muckpile. The coarser size fractions also result in reduced bucket fill factors. The consequence of a reduced fill factor is that the bucket will hold less material, and consequently the lashing rate will be slower. In the Kratz and Martens (2015) simulation results, the bucket fill factors were not specified. It is, however, still reasonable to assume that for most deep shafts (the majority of which will be between the theoretical depths of 780–2 670 m), lashing performance remains the limiting factor. Any reduction in fill factors will increase the depth at which the hoisting rate becomes the limiting factor. The conclusion is therefore that for most sinking operations, which are typically less than about 2 700 m in depth, if a three-kibble system is used the lashing rate will always be the constraint rather than the hoisting rate, and any improvement in the lashing rate will impact on the cycle time.

Bucket fill factor is therefore an important consideration in lashing, since it determines how many scoops of material (or 'bucket passes') are required to fill a kibble, and is indicative of the degree of fragmentation of the rock together with particle size distribution. The depth of the broken material also affects the fill factor, since a bucket cannot be filled efficiently when the layer of broken material becomes shallow.

It is probably reasonable to assume a fill factor in the region of 0.55–0.65 for lashing, taking fragmentation and efficiency (when the layer of the muck becomes shallow) into account.

Returning now to the choice of lashing unit or mucker, this decision should not be taken lightly as it directly affects a number of aspects of the shaft sinking system design, including:

- Kibble dimensions
- Kibble hoist type and number of kibbles used (including the need to detach and re-attach ropes to the kibble at the shaft bottom)
- Shaft sinking stage layout, mass, and mode of operation (openings to suit the number and size of kibbles, whether the lashing system is integrated into the stage or not, whether the lashing system is to be stored on the stage or lowered from surface and required to pass through the stage openings, whether additional power packs are required on the stage for the lashing system, whether the stage needs to be raised or lowered during lashing to accommodate the requirements of the mucker, *etc.*)
- Desired lashing rate and the critical depth at which hoisting becomes the limiting factor
- Kibble and stage hoist rope selection (based on the masses to be supported)
- Blast pattern and density for the required fragmentation (and in relation to the geology)
- Number of workers required at the shaft bottom
- Complexity and location of the lashing equipment for maintenance purposes.

In the following section a critical review of popular lashing techniques is undertaken in detail, with some general comments about other techniques.

Lashing techniques

Prior to the 1930s loading of material into kibbles was done by hand. Since then, a variety of mechanical loaders have been designed and utilized in shaft sinking. The main techniques used in modern shaft sinking are discussed in more detail in this section.

EIMCO 630 loader

Background

In 1937 a patent was awarded for a mechanical lashing machine which became known as the EIMCO rocker shovel, and which was designed to mimic the manner in which a man scoops material manually using a shovel and then hoists it over his shoulder into a receptacle located behind him (oral history transcript in Internet Archive, 1992). This led to the development of the EIMCO rocker shovel loader model 12B, which was introduced in 1938 (ASME, 2000). This particular model was designed for use on railway tracks in areas such as development ends. Subsequently EIMCO developed a variety of other models, including a crawler or tracked version, the model 630, which can be used for general lashing duties and which is still utilized in modern shaft sinking (Graham and Evans, 2008).

Description and operation

The EIMCO 630 loader is a tracked version of the model 12B loader. It consists of a frame mounted on tracks which may be independently controlled by air motors. It has a bucket at the front and a compressed air-operated mechanism to manipulate the bucket so that the material can be raised and discharged. The loader is driven forward so that its bucket penetrates the loose material ahead of it (also known as 'crowding'). The bucket is then raised and the loader is positioned so that the kibble is located directly behind it. The bucket is hoisted up over the loader and discharged into the kibble in an overthrow motion. Hence it is often referred to as an 'overshot loader' or an 'overthrow loader'. Figure 1 shows a schematic of the rail-mounted EIMCO 12B loader, illustrating the principle of loading and discharging. The operator is located on a running-board on the side of the loader so that he is able to move with the loader during the digging and discharging processes.

Specifications

- Dimensions with the bucket in the load position: 2.85 m length × 1.75 m width × 1.51 m height, with a bucket discharge height of 1.9 m for the 630 loader (Trident SA, 2016)
- Mass: 4.7 t (Trident SA, 2016)
- Bucket capacity: 0.27–0.39 m^3 (ASME, 2000; Trident SA, 2016)
- Air supply: pressure of 520–860 kPa, at a flow rate of 18 m^3/min (Trident SA, 2016).

Operational issues

As opposed to the rail-mounted model 12B, the individually controlled tracks of the model 630 enable the loader to turn sharply and have high degree of manoeuvrability (Berry, 1956). However, due to the 5 m^2 footprint of the loader it is suitable for use in medium to large shafts, typically 5.5 m diameter and larger (Berry, 1956; Obert, 1973). It may, however, operate in smaller diameter shafts in the range 4.6–5.5 m provided it is used with a single kibble at the shaft bottom. In such cases, it is also necessary to use a special arm with a smaller nested bucket of 0.14 m^3 capacity (Dengler, 1982). The consequence is that the loading rate will be reduced significantly.

Reported loading rates of the 630 loader vary. Berry (1956) stated that a 630 loader could load 15 to 18 cubic yards of solid material per hour (translating to about 39 t/h based on an assumed solid density of 2800 kg/m^3). Jamieson and Pearse (1959) quoted a loading rate of 72 t/h for a shaft diameter of 7.6 m, while Dengler (1982) stated that loading rates may be as high as 90 t/h in sedimentary formations. In general, loading rates are dependent on the nature of the fragmentation, the size of the bucket and kibble, the available manoeuvring room, the skill of the operator, the

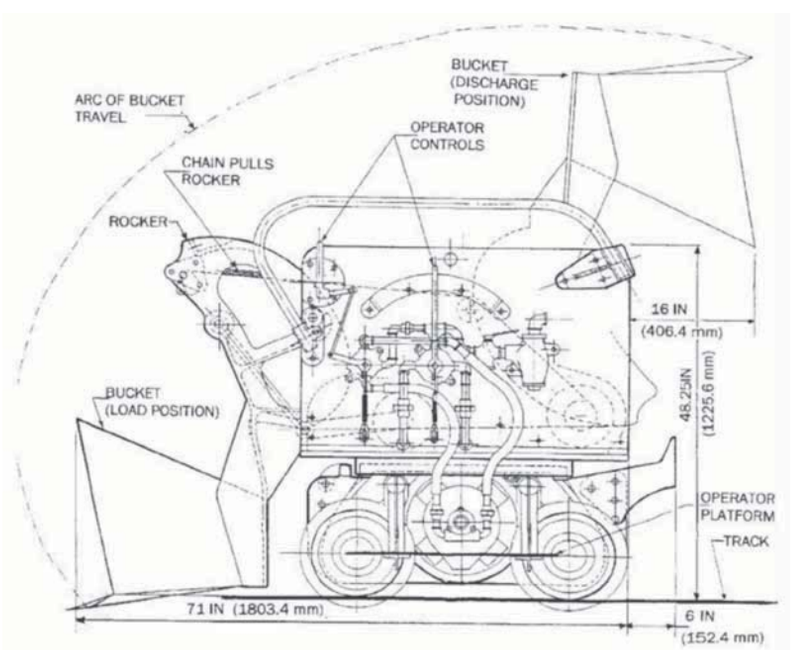

Figure 1—Rail-mounted EIMCO 12B loader showing overthrow action (ASME, 2000)

operational state of the equipment, whether water is present at the shaft bottom, *etc.* An analysis and comparison of the loading rates is given in a subsequent section.

Owing to the size and mass of the unit, the 630 loader is not usually stored on the stage when it is not required (Jamieson and Pearse, 1959). Instead, it is lowered from surface at the start of the lashing part of the sinking cycle. While this facilitates maintenance on surface it does incur time penalties in lowering the loader down the shaft and through the shaft sinking stage. However, once the loader is at the shaft bottom, provided it is connected to an air supply, it can operate largely independently of the position of the shaft sinking stage. Aside from providing clearance for the loader to pass through it, the stage design is not significantly affected as the stage is not required to support the loader. In addition, the installation of shaft steelwork is not affected (Jamieson and Pearse, 1959).

When the loader's bucket is lowered and the unit is driven forward, blasted material is forced into the bucket due to the resistance of the muckpile, which limits the sliding of material fragments over one another. When the muckpile becomes shallow, towards the end of the cleaning cycle, the bucket filling efficiency is reduced substantially due to the shape and angle of the bucket and the lower resistance of the muckpile. This may result in lower fill factors and therefore lower efficiencies.

Dengler (1982) stated that this type of mucker is not suitable in the case of extremely coarse fragmentation or extremely abrasive muck. Britton and Lineberry (1992) stated that for all mechanical lashing, medium-sized fragmentation (approximately 125 mm) is most efficient. In general, fragments in excess of 125 mm will also lead to lower bucket fill factors for the 630 loader, and higher penetration forces will be required to load material into the bucket Singh *et al.,* (2001). If fragmentation is poor and the muck contains large rocks, it will be difficult to scoop these with the bucket and the loader's tracks will also struggle to develop the required traction. Similarly, if large amounts of fines are present the loader may again struggle to develop traction, and small amounts of water could cause the fines to adhere to the bucket and not discharge into the kibble.

Conditions at the shaft bottom affect the ability of the 630 loader to muck efficiently. While small amounts of water are reportedly easily tolerated, if the amount of water becomes substantial then the 630 loader is unsuitable. In extremely wet conditions, mud and water may ingress into the pneumatic motors and controls, which could lead to damage. Also, the water itself poses a risk to the operator who stands on the loader (Obert, 1973). Secondly, the 630 loader requires a reasonably flat working surface. This is also a requirement for the position where the kibble is to be placed, for the purpose of stability and worker safety. If the muckpile is uneven after a blast then it is necessary to shape it before loading can start (requiring 10–15 minutes) (Berry,1956). In addition to an even working surface of the blasted material, the surface of the solid material should be as level as possible. It would be difficult for the loader to traverse an uneven surface to reach all of the remaining muck due to obstacles over which the loader may not be able to move, as well as traction problems, and because of safety concerns for the operator.

The discharge height of the loader limits the rim height of the kibble that can be used (Wakefield, 2009). For the 630 loader the maximum kibble rim height is 1.9 m. Hoisting a specific volume of material necessitates a specific kibble diameter, which, in turn affects the clearance holes in the shaft sinking stage through which the kibbles must pass. Hence, the volume of the kibble becomes constrained when the 630 loader is used. While this may not be a problem for larger diameter shafts, it could present difficulties for smaller diameter shafts where there is limited space to create the clearance holes in the stage, and limited space at the shaft bottom for the kibble.

The number of workers required to operate the loader at the shaft bottom is reported by Berry (1956) to be four: the loader operator, a hose-man to control the pneumatic hose lines, a helper to hook and unhook the kibble cables, and a signalman to the mine hoist. This represents a significant number of workers at the shaft bottom, the location of the highest danger.

Safety is a significant issue when using the 630 loader for additional reasons to those already mentioned. In most cases the loader is pneumatically driven. Pneumatic cylinders and winches have an inherent compliance or 'springiness' due to the compressibility of the air. This results in jerky and imprecise motion of moving parts, which can pose a risk to workers (Moss, 2011). In addition, the process of discharging the material into the kibble is forceful. Since the operator is located immediately adjacent to the bucket and actuating mechanism, he is exposed to increased risks in this regard. If the loader is not correctly positioned, the discharged material may not enter the kibble correctly and some material may impact, and rebound off, the side of the kibble. This may pose a risk to the operator or other workers nearby. This also applies to the loading of oversize rocks, which must be carefully raised and discharged. These risks are exacerbated in smaller diameter shafts. Loading in a 4.3 m diameter shaft was described by Berry (1956) as being 'hazardous' due to the small amount of space available for workers, the kibble, and the loader.

Clamshell-type muckers – Riddell and Cryderman muckers

Clamshell muckers are characterized by two opposed buckets. The key difference between this arrangement and the single bucket arrangement of the EIMCO 630 loader is that the loading of material occurs by enclosing and entraining a volume of material between the two buckets, rather than by the resistance of the material in the muck pile.

Background

The Riddell clamshell-type mucker was introduced in 1943 in Canada and was reportedly immediately successful. The Cryderman mucker was introduced into Canadian mining in the late 1940s and began to gain popularity in the 1950s. It is still reportedly the most popular mucker for Canadian shaft sinkers, and has largely replaced the Riddell muckers in Canada (Graham and Evans, 2008).

Description and operation

Both of these lashing machines have clamshell bucket configurations and are attached to either the underside of the

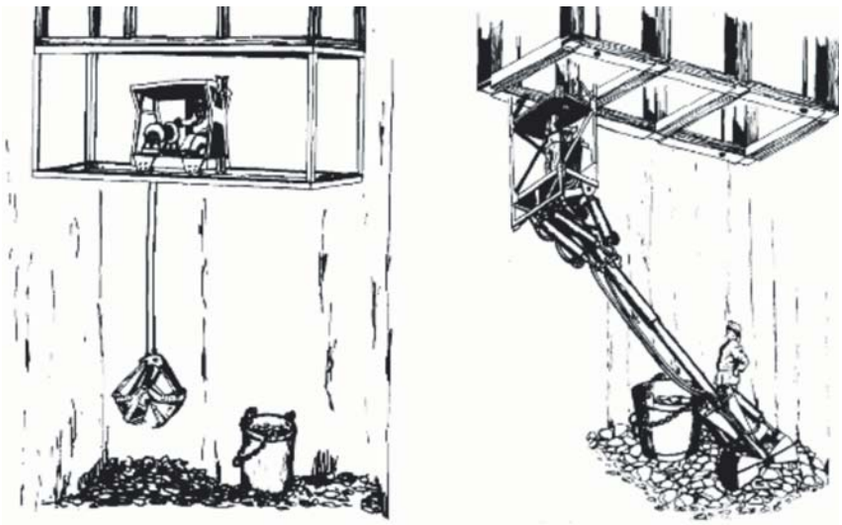

Figure 2—Riddell and Cryderman clamshell muckers (Dengler, 1982)

stage, to a structure that can move independently of the stage, or to the shaft sidewall. In all cases the operator is located in a suspended compartment, rather than at the shaft bottom, for safety reasons (Wilson, 1976). The main difference between the two types of muckers is that the Riddell mucking machine utilizes ropes and winches to suspend and actuate the clamshell buckets, while the Cryderman utilizes cylinders to actuate the buckets and a telescoping arm on which the buckets are mounted (Stout, 1980). The consequence of this difference is very important: the Riddell mucker relies on gravity for the buckets to penetrate the muckpile in order to scoop material, while the Cryderman buckets are able to penetrate the confined material in the muckpile under the action of the cylinder in the telescoping arm. Figure 2 shows the Riddell and Cryderman mucking machines side by side, for a rectangular shaft configuration. The cable suspension of the Riddell mucker and the telescoping arm of the Cryderman mucker are evident.

Riddell muckers rely on a track system to move the buckets within the shaft and were originally successful in rectangular shafts (Bennet, Harrison, and Smith, 1959). In modern circular shafts, the reach of the buckets is not properly catered for by the track system and more than one mucker on parallel track systems is required, as well as workers at the shaft bottom to manipulate the buckets to reach the sidewalls and the kibbles. This poses a risk to the workers since the buckets require some velocity to penetrate the muck pile. It is also potentially problematic in that slack ropes can lead to a dangerous situation, as well as damage to the ropes. The rope system also presents a fouling hazard for the kibbles that are being lowered or hoisted at the shaft bottom (Berry, 1956). Bennet *et al.,* (1959) stated that for square, circular, and inclined shafts the Cryderman mucker was in common use at the time.

Only the Cryderman mucking machine will be dealt with in detail below (but will be contrasted with the Riddell mucking machine, where relevant).

Specifications

All of the following specifications are for the Joy Global VSM 14 model (Joy Global, 2015) which is a modern version of the Cryderman loader.

- Dimensions: length 16.52 m (total length of unit including a base section which is located in a compartment in the stage such that the unit is able to move up and down relative to the stage), width 1.54 m, depth 0.96 m
- Mass: 8.6 t
- Bucket capacity: 0.38 m^3 (standard capacity), 0.57 m^3 (optional larger bucket capacity)
- 4.3 m main cylinder stroke on the telescoping arm (refer also to Moore, 2015)
- Power supply: earlier models utilized compressed air, while modern models utilize a hydraulic power pack located on the stage.

Operational issues

The Cryderman mucker may be attached to the underside of the stage, or it may be nested in the stage (see Figure 3) and lowered by an independent hoist at the commencement of lashing. This allows the unit to be retracted into the stage at the end of lashing so that there is clearance below the stage for drilling and concrete lining. In this retracted position, access for maintenance of the cylinders, hoses *etc.* is facilitated.

Although the 4.3 m stroke of the telescoping arm does accommodate the position of the Cryderman mucker relative to the bucket position and allows lashing of an area of the shaft bottom, it is necessary that the stage position be changed from time to time as the lashing progresses to accommodate the change in the level of the muck. The expansion ratio of blasted to solid rock may be in the range of 1.5–2, so a 3 m round will translate to 4.5–6 m depth of muck, which cannot be reached with an arm stroke of 4.3 m. The telescoping action of the arm allows the Cryderman mucker to scoop material in the muckpile and then retract so that the buckets may be positioned above the kibble and the material discharged. However, depending on the relative positions of the stage, muckpile, and kibble, this motion may be awkward. For example, if the stage is close to the muckpile, the telescoping arm may be near the limit of its

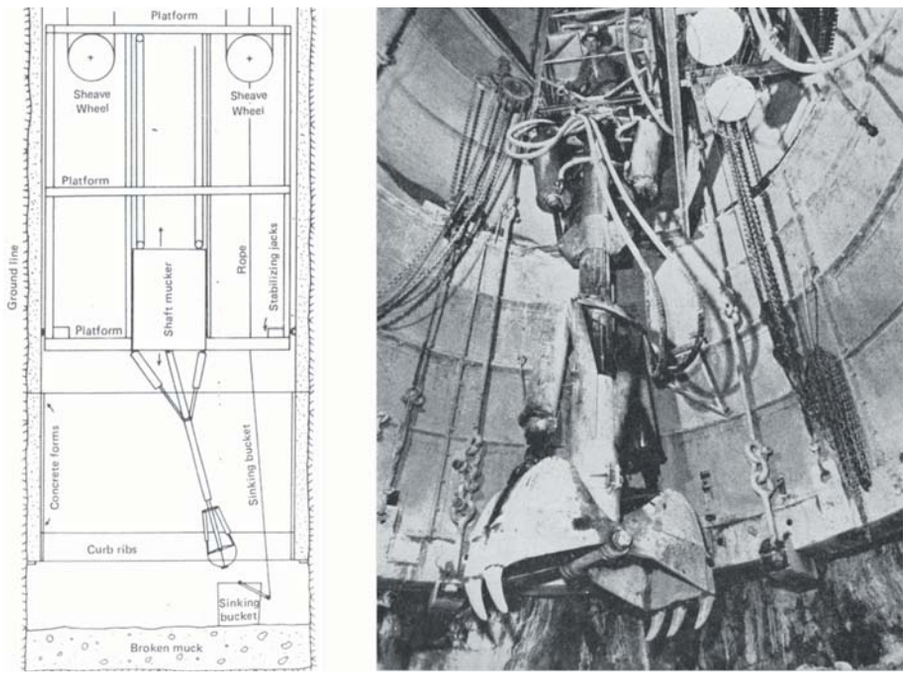

Figure 3—Cryderman clamshell mucker schematic and photograph (Stout, 1980; Bennett, *et al.,* 1959, respectively)

retraction stroke and it may not be able to retract sufficiently to allow the buckets to be raised above the kibble rim, if the kibble is positioned too close to the mucker. This would necessitate that material be discharged into a kibble located further away, where the arm can be angled so that the buckets clear the rim.

Single Cryderman muckers are suitable for use in shaft diameters less than about 5.5 m, but for shafts larger than 5.5 m it is common practice to use two muckers (Dengler, 1982). There are two reasons for this: the muckers are not mounted centrally so the extents of larger diameter shafts cannot be reached from one location only; and the loading rate for a single Cryderman mucker is lower than that of the 630 loader. Data for earlier versions of Cryderman muckers indicated loading rates of up to 50 t/h Dengler *et al.,* (1992), while a more modern hydraulic version was reported by Dengler (1982) to have an expected loading rate of 73 t/h (with the larger bucket volume of 0.57 m^3). Berry (1956) felt that a clamshell loader of the time could probably load up to 15 cubic yards of solid material per hour (or 32 t/h at an assumed solid density of 2800 kg/m^3). There is currently no published data on the loading rate of the newer Joy Global VSM 14 unit, but personal communication between the author and a local contractor indicate that the unit is rated at about 60 t/h.

The Cryderman mucker is powered by either pneumatic or hydraulic cylinders (for lateral positioning of the arm, telescoping of the arm, and closing of the buckets). Pneumatic cylinders will have a significant degree of compliance due to the compressibility of the air which, together with the nature of pneumatic controls, will lead to imprecise movements of the arm and buckets. In contrast, hydraulic cylinders will be stiff and will therefore result in more accurate positional control of the buckets. Since the buckets in the Cryderman mucker are not supported on cables this type of mucker can be used in inclined shafts (Dengler, 1982). Hydraulic versions require an additional power pack to be located on the stage, while pneumatic units use the installed compressed air on the stage.

The ability of the buckets of a Cryderman mucker to penetrate the muckpile under the action of a cylinder is of critical importance in that it leads to potentially higher bucket fill factors than with the 630 loader or any form of muck penetration under the action of gravity alone. Since the buckets are not suspended on ropes, workers at the shaft bottom are not exposed to swaying or uncontrolled motion of the buckets. There are also no ropes that can become slack, or which could become entangled with kibble hoist ropes.

Bucket shape has evolved over time. The original Cryderman clamshell buckets were rounded on the underside. In some versions, such as that shown in Figure 3, the jaw edges are flat (known as the 'Brutus' buckets), while the modern Joy Global unit again has rounded edges. Some benefit may be obtained when using the rounded shape to muck against the sidewall as the angle of the arm to the vertical will result in the bucket being angled to the sidewall, and the bucket may scoop more material if it is rounded. In laboratory experiments conducted by Moss (2011) using a 1:6 scale model of a clamshell digger (based on a Cryderman mucker) it was shown that lashing against a sidewall was easily achieved for the case where the sides of the buckets were parallel to the sidewall) and did not adversely affect the digging forces. The ability to muck against a sidewall is an advantage of this type of mucker. It is unclear from the literature whether the buckets are able to rotate on the telescoping arm so that their sides may be oriented parallel to the shaft sidewall. If this is not the case then lashing against the sidewall will not always be efficient, depending on where the unit is lashing relative to its support location.

In addition to bucket shape, the bucket size should be also chosen in relation to the kibble diameter. Since the arm of the Cryderman mucker will be at an angle relative to the kibble for most of the lashing operations, its clamshell buckets will also be at an angle to the vertical and need to

open sufficiently to be able to discharge the muck into the kibble. If the clamshell buckets are too large there may be insufficient room to open them completely, and they may not discharge the material completely into the kibble. The result could be spillage or carry-back of material remaining in the buckets, which would reduce the effectiveness of the loading.

Berry (1956) stated that the fragmentation of the rock was less of an issue with the Cryderman mucker than with the 630 loader, provided the rocks were not so large that they did not fit into the clamshell buckets. Large rocks would be problematic with Cryderman muckers. One additional consideration is that if the blasted material has a wide particle size distribution a large rock fragment could prevent the buckets from closing properly, leaving gaps between the jaws through which smaller particles may escape. This would lead to lower bucket fill factors and potentially less efficient loading.

Conditions at the shaft bottom also have an effect on the efficiency of the Cryderman mucker. Water in reasonable quantities is not considered a problem for the Cryderman mucker (as compared with the 630 loader) as the controls are not located anywhere near the water. Safety for the operator is improved, as he is located well away from the shaft bottom (Wilson, 1976), although if workers are required to detach and attach kibbles to the hoist ropes, they would be exposed to risk. Visibility for the operator is improved as he is located above the operations so there are fewer blind spots. Cryderman muckers are also not affected significantly by an uneven material surface after the blast, provided the kibbles can be located such that they are stable. They are also able to muck effectively if the surface of the solid material is uneven, provided they have sufficient reach.

Safety is generally improved when Cryderman muckers are employed for the reasons outlined above. However, while visibility of the working area may be improved with the operator located above the shaft bottom, communication with workers below is more difficult. If a second mucker is used the working area does become congested, and there are increased risks for workers in the vicinity.

No mention is made in the literature of how the remnants of the blasted rock are loaded into the kibble when Cryderman muckers are used for lashing, but presumably material is hand-lashed into the closed clamshell buckets and then loaded into the kibble. The location of the actuating cylinders on the outsides of the buckets may be problematic in this regard, as they could be prone to damage. In addition, the shape of the bottom surface of the bucket (flat *versus* round) may affect the cleaning ability when the layer of muck becomes shallow.

Cactus grab

The cactus grab was introduced In the 1950s, and was used successfully in 1952 during the sinking of No. 2 shaft at the Vlakfontein mine in South Africa (Graham and Evans, 2008). The cactus grab has seen continuous use since its introduction and is globally a popular choice for lashing as it has a high loading rate.

Description and operation

The cactus grab consists of a 6- or 8-tine (or claw) grapple that is activated by a large pneumatic cylinder, and which is suspended from a cable hoist system. The cables are attached to an arm which is pivoted centrally on the shaft sinking stage such that the arm can sweep through 360 degrees. The hoist for the grab can move radially along the arm such that the grab can cover all areas of the shaft bottom. Figure 4 shows a schematic of the cactus grab, cable hoisting system, cantilevered arm, kibbles, and operator's compartment.

The loading action is as follows. The grab is lowered into the muckpile with the tines open. Then the pneumatic cylinder actuates the tines so that they close and entrain a volume of muck. The grab is then raised, positioned over a kibble, and the tines opened so that the load of rock is discharged into the kibble.

Specifications

- Dimensions: grab height 3.2–3.7 m, grab diameter (open) 2.2–2.8 m, (closed) 1.7–1.8 m (Deilmann-Haniel, 2014)
- Mass: 10 t (Martin and Harvey, 1989)
- Shaft diameter range: 7–11 m (Deilmann-Haniel, 2014)
- Grab capacity (volume): 0.4–0.85 m^3 (Dengler, 1982); 0.5–1.2 m^3 (Deilmann-Haniel, 2014), with typical grabs either 20 ft^3 (0.56 m^3) or 30 ft^3 (0.85 m^3)
- Power supply: compressed air at 400–600 kPa with a consumption of between 120–140 m^3/min, depending on grab size.

Operational issues

The cactus grab unit is mounted to the underside of the shaft sinking stage. This is seen as a significant disadvantage as heavier stage steelwork is required to support it. This, in turn, necessitates larger stage hoist ropes *etc.*, which all add cost to the project. A further disadvantage is the space that the cactus grab occupies underneath the stage. This limits the distance that the stage can be lowered and so the shaft concrete lining may not come as close to the shaft bottom as

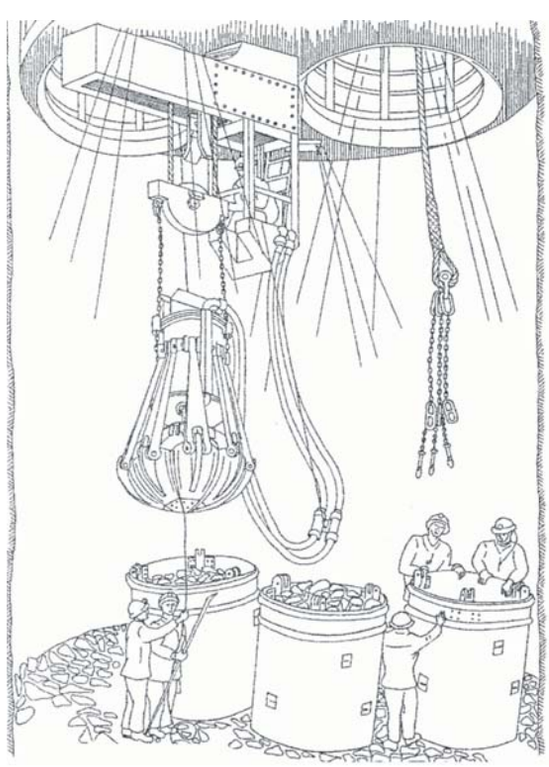

Figure 4—Cactus grab (Douglas and Pfutzenreuter, 1989)

is desirable. According to Martin and Harvey (1989) this, as well as the particular geology, was the reason that the cactus grab was not chosen as the lashing system for the sinking of the Asfordby shafts. An advantage of the cactus grab system, though, is that provided its hoist ropes are long enough it may operate reasonably independently of the stage position.

Cactus grabs are suited to larger diameter shafts. Obert (1973) stated that cactus grabs may operate in shafts less than 6.7 m diameter, but they are economically suited to larger diameter shafts. He further stated that for shafts larger than 9.8 m diameter the cactus grab is the only economically viable option.

The loading rates published in the literature vary. Dengler *et al.,* (1992) stated that typical loading rates may be in excess of 100 t/h, Wakefield (2009) stated that 180 t/h is possible, while according to MacGillivray (1979) peak loading rates up to 250 t/h are possible with a large capacity grab (0.85 m^3). MacGillivray (1979) further noted that 'A lashing unit with a pneumatic cactus grab is unequivocally the fastest shaft mucker in vertical shafts and is universally adopted for rapid sinking in large deep shafts'. Despite the high instantaneous loading rates that are quoted by MacGillivray and Wakefield, the data presented by Morgan (2015) indicates that the average loading rate was about 50 t/h, excluding blow-over, on the basis of an 8.1 m diameter shaft, 3.15 m advance per blast, estimated solid rock density of 2800 kg/m^3, and lashing duration of 9 hours. In reality, instantaneous rates should be significantly higher, but Morgan's figures would be comparable to other types of loaders.

In a similar manner to the Riddell mucker, the cactus grab relies on gravity for the tines to penetrate the muckpile. This has the consequences of uncontrolled motion during the scooping action, potentially shallow penetration, slackening of the grab's hoist rope, and potential fouling of the grab ropes with the kibble ropes. Due to the shape of the grab and tines, it cannot clear material effectively against the shaft sidewalls because of the distance between the tines when they are open, and the shape of the grab when the tines are closed. In addition, the cactus grab is not effective towards the end of the cleaning cycle when the layer of muck becomes shallow and the tines make contact with solid material. MacGillivray (1979) indicated that the amount of material removed in the blow-over phase (when the grab has become ineffective) was as much as 60 t for larger shaft diameters, about 10 t of which had to be hand-lashed as the cactus grab was ineffective in clearing this material. Morgan (2015) indicated that the depth of loose material at which the grab became ineffective was about 200 mm, by which stage the large fragments had already been loaded, and smaller fragments were escaping through the gaps between the tines. Using the same data as quoted by Morgan above, and assuming an expansion ratio of two for the blasted material, this layer of muck amounts to approximately 14 t, which is in reasonable agreement with MacGillivray. Hand lashing is done by placing the material into the closed grab through the gaps between the top of the tines, and then using the grab to deposit the material into the kibble (Douglas and Pfutzenreuter, 1989).

Large rocks are more easily handled with a cactus grab than with other types of loaders (Dengler, 1982); however, fine fragments are more difficult to handle, particularly when the tines are worn. Britton and Lineberry stated that typically 70–80% of the muck produced in a blast has fine fragmentation with the rest being coarse. The combined effects of fines and worn tines will therefore lead to lower loading rates.

Conditions at the shaft bottom do not affect the cactus grab significantly. It is able to operate if the blasted material surface is uneven, provided the kibbles are stable, and is also able to operate if water is present.

Due to the location of the cactus grab on the underside of the stage, maintenance is an issue. MacConachie (1959) stated that typically four units were utilized in a sinking operation: one operating, one spare, one undergoing minor repairs, and one undergoing major overhaul. He also stated that repairs were generally not carried out *in situ* (unless of a minor nature), but that the damaged unit was rather replaced and brought to the surface for repairs. The size, complexity, location, and mass of the components in a cactus grab system make this task difficult. Care must also be taken with regard to the grab hoist ropes. In the analysis that Morgan (2015) conducted for 152 sinking cycles, of the 429.8 hours of engineering-related delays (out of 4440.5 actual hours worked) the cactus grab accounted for almost 122 hours of delays (or 28% of the engineering delays). In particular, 59 hours of delays associated with the cactus grab were associated with ropes.

When using a cactus grab, safety is a serious issue. The size and mass of the grab, the use of a rope support system for the grab, and the need for the grab to penetrate the muckpile under the action of gravity all make it dangerous to operate with workers in the vicinity. While the operator does have good visibility, depending on the location of the stage while lashing is in progress (which is considered an advantage of this system), the operator may be located quite far from the shaft bottom. This makes communication more difficult, and reduces the controllability of the grab even further. There is also the need to ensure that kibble hoist ropes do not become entangled with the grab.

Other types of mucking systems

The main lashing techniques that are currently employed worldwide have been covered above. However, there are other techniques, although these will not be explored in as much detail. These include excavators, roadheaders, and shaft borers.

Roadheaders such as the Herrenknecht shaft boring roadheader (Herrenknecht, 2016) can reportedly be used in shaft sinking applications for 8–12 m diameter shafts, sunk to a depth of 1000 m, where the application is in 'soft to medium-hard rock'. However, no details of rock strength, hardness, abrasivity *etc.* were supplied. The roadheader uses a pneumatic system to hoist the rock fragments from the cutting process.

Shaft borers such as the Herrenknecht shaft boring machine (Herrenknecht, 2016) can reportedly be used in shaft sinking applications for 10–12 m diameter shafts, sunk to a depth of 2000 m. The unit uses vertical conveyors to hoist the muck.

Excavators have also been used in lashing operations in shaft sinking. Dengler (1982) mentions an Alimak mucker which is based on a single bucket mounted on an articulating arm (in the same configuration as a backhoe). The arm may be attached to the underside of the stage or onto a structure

temporarily attached to the sidewall. There are other excavators employing similar action using a single bucket, such as the Terex S20 excavator, which is mounted on the underside of the shaft sinking stage.

Lastly, track-mounted excavators have also been used. Morgan (2015) gave some data on cycle times and experience gained used an excavator, and also made some predictions of lashing cycle times. In the data presented, a Hyundai R60-9S 5.6 t excavator with a 0.31 m³ bucket capacity was used in a sinking application. An average digging cycle time of 13 seconds was recorded (although this was measured for only five complete digging cycles incorporating a swing angle of 90 degrees). It is not clear whether these cycle times were achieved in an actual lashing context. Morgan (2015) also described the use of another track-mounted excavator (a Hyundai R55-7 5 t unit) which was used in the sinking of a 9 m diameter shaft. It had advantages of increased mobility, was able to be operated independent of stage location, and it allowed blow-over material to be blown directly into the bucket. No data for this application was presented. The main issues that were experienced were the need to hoist the excavator from surface before lashing could begin (and to remove the driver's cabin and excavator arm), having openings in the stage that could accommodate the excavator, and failures in the hydraulic and electrical systems. The author would add efficiency of bucket filling, due to the need for resistance in the muckpile, to the disadvantages. Morgan proposed that it would be possible to allow the kibble ropes to remain attached during loading, and indicated that the excavator could be adapted for remote control, which would remove people from the shaft bottom and also do away with the operator's cabin.

Analysis of lashing rates

In order to assess the lashing rates of the various types of lashing machines, the following equation was derived:

$$\dot{m} = V_{bucket} \cdot F_f \cdot \left(\frac{\rho_{solid}}{R_e}\right) \cdot \left(\frac{1}{t_{cycle}}\right) \cdot \left(\frac{3600}{1000}\right)$$

where $\dot{m}$ = mucking rate (t/h)

V_{bucket} = bucket geometric volume (m^3)

F_f = bucket fill factor (dimensionless)

ρ_{solid} = density of solid rock $\left(\frac{kg}{m^3}\right)$

R_e = expansion ratio of blasted rock (dimensionless)

t_{cycle} = mucker digging cycle time (seconds)

$\left(\frac{3600}{1000}\right)$ = conversion constant: kg to tonnes, and seconds to hours

Note that this equation does not take into account the time taken to detach and re-attach kibbles, varying bucket fill factors as the muckpile becomes shallow, operator fatigue and reduced efficiency, or the effect that any other activity not related to lashing will have on the lashing rate. In reality, these factors could reduce the instantaneous lashing rate substantially.

For the purposes of comparison, the following parameters will be used:

- Bucket size from 0.18–0.50 m³ for an excavator, 0.27–0.39 m³ for an EIMCO 630 loader, 0.27–0.57 m³ for a Cryderman loader, and 0.57–1.20 m³ for a cactus grab
- Bucket fill factor approximately 0.65
- Expansion ratio from solid to broken rock approximately 2
- Density of solid rock 2800 kg/m³
- Advance per blast 3 m, with shaft diameters varying from 6–12 m
- Only one mucker operational
- Instantaneous digging cycle times vary linearly as a function of bucket volume, from 15 seconds for a 0.18 m³ bucket to 35 seconds for a 1.2 m³ grab. Efficiencies that may relate to both bucket fill factors as well as increased cycle times have been included in the analysis, ranging from 50% to 100%. The assumed cycle times do not take into account inherent differences in the lashing techniques.

The results are shown in Table I. At the top of the table, various bucket volumes are indicated, as well as the typical bucket sizes associated with various lashing techniques. The cycle times have been scaled linearly between 15 and 35 seconds based solely on bucket volume. Morgan (2015) indicated cycle times for an excavator of 13 seconds while Kratz and Martens (2015) assumed cycle times of 25 seconds for a Cryderman loader. No information on cycle times for a cactus grab were obtained from the literature.

In the lower portion of the table the masses of solid material associated with shaft diameters ranging from 6–12 m have been determined (based on a solid density of 2800 kg/m³), as well as the duration of the lashing cycle based on the bucket volume and cycle times. At the bottom of the table the instantaneous lashing rates are determined, and compared with reduced efficiencies, which may account for time taken to detach and re-attach kibbles, poor fragmentation, lower efficiencies towards end of lashing cycle in shallow material, *etc.* The latter may be considered to be more in line with average lashing rates.

The lashing rates quoted in the literature and those estimated in Table I compare as follows:

- EIMCO 630 loader: quoted rates varied between 39–72 t/h, which compare favourably with the estimates in the table, which range from 40–67 t/h for efficiencies of 75% and higher. The figure of 90 t/h quoted by Dengler (1982) in sedimentary formations may be indicative of better fragmentation, better bucket fill factor, and hence increased performance.
- Cryderman loader: quoted rates varied between 32–73 t/h, which also compare favourably with the estimates in the table, which range from 35–82 t/h, albeit with lower efficiencies at the lower end of the range. Presumably, the rate of 32 t/h quoted by Berry (1956) was at a reduced efficiency for operational reasons.
- Cactus grab: quoted rates varied between 100–180 t/h. MacGillivray (1979) estimated that rates may be as high as 250 t/h, and Wakefield (2009) indicated that loading rates of 180 t/h are possible, while estimated rates vary between 62–112 t/h for efficiencies above 75%. The data in Morgan (2015) showed that average loading rates were considerably lower at about 50 t/h, which is consistent with an efficiency between 50 and 66.7%, using a 0.57 m³ grab.

Table I

Lashing duration as a function of shaft diameter (solid volume), bucket volume, digging cycle time, and lashing efficiency (for a 3 m advance and bucket fill factor of 0.65)

Bucket vol, m^3		0.18	0.27	0.39	0.50	0.57	0.85	1	1.2
Excavator		■	■	■	■				
EIMCO 630 loader			■	■					
Cryderman loader			■	■	■	■			
Cactus grab						■	■	■	■
Cycle time, s		15	17	19	21	23	28	31	35
Diameter, m	Mass, t	Lashing duration, h							
6	238	6.0	4.5	3.6	3.1	2.9	2.4	2.3	2.1
7	323	8.2	6.1	4.8	4.2	3.9	3.3	3.1	2.9
8	422	10.7	8.0	6.3	5.5	5.1	4.3	4.0	3.8
9	534	13.6	10.1	8.0	6.9	6.5	5.4	5.1	4.8
10	660	16.8	12.5	9.9	8.6	8.0	6.7	6.3	5.9
11	798	20.3	15.1	11.9	10.4	9.7	8.1	7.6	7.1
12	950	24.2	18.0	14.2	12.3	11.5	9.6	9.0	8.5
Instantaneous lashing rate, t/h		39	53	67	77	82	99	105	112
Lashing 75% efficiency, t/h		29	40	50	58	62	74	79	84
Lashing 66.7% efficiency, t/h		26	35	45	51	55	66	70	75
Lashing 50% efficiency, t/h		20	26	33	38	41	49	53	56

- Excavators: the only available data is given in Morgan (2015), which indicates cycle times of 13 seconds using a 0.31 m^3 bucket. The estimated loading rates for excavators vary between 29–77 t/h for the range of bucket sizes. Using Morgan's cycle time of 13 seconds and a bucket volume of 0.31 m^3, the mucking rate would be approximately 59 t/h (assuming a 75% efficiency). It is the author's view that the 13-second cycle time is probably slightly optimistic, as the data presented by Morgan was for a 90 degree swing only.

A graph of the lashing durations given in Table I is presented in Figure 5. The data is extrapolated to assess how long it would take to muck the volume of material generated for the different shaft diameters (with the same assumptions of 3 m advance, bucket fill factor of 0.65, solid density of 2800 kg/m^3, expansion ratio of 2, and digging cycle times linearly related to bucket volume). The figure shows, for example, that the theoretical lashing duration for an 8 m diameter shaft would be 8 hours if a bucket volume of 0.27 m^3 was used and the lashing operated at 100% efficiency.

The lashing duration is compared with an 8-hour shift time, and an efficiencies of 100%, 75%, 66.7%, and 50% are applied to assess how operational efficiencies could affect the lashing duration (for example lowering of the mucker from surface, or detaching and re-attaching ropes to kibbles, *etc.*). The figure shows that larger bucket volumes are required for larger shaft diameters if the lashing durations are to be below 8 hours. For example, a bucket volume of at least 0.5 m^3 should be used when an 8 m diameter shaft is being sunk (if the system has an efficiency of approximately 66.7%). Care should be taken, though, in using this information because an average bucket fill factor of 0.65 was used and larger buckets are likely to suffer from significantly reduced fill factors towards the end of the lashing cycle due to the shallow layer of muck remaining.

Summary and recommendations

There are numerous advantages and disadvantages for all of the shaft lashing techniques reviewed in this paper. Since the lashing cycle time is dictated by the rate at which material is lashed (rather than the time taken to hoist and lower kibbles), and since lashing occupies a significant portion of the overall cycle time, it is clear that the loading rate is the primary criterion by which the lashing system is selected. There are, however, additional factors to be considered which relate either to the system as a whole or to the front end of the system where the actual lashing takes place. These include:

- The shaft diameter and number of lashing units required
- The mass of the lashing equipment
- Whether the lashing system is supported on the stage or not
- The cost of the equipment (capital and operational)
- The location where the lashing equipment is stored when not in use and whether this affects other stage functions and sinking operations
- Constraints and risks that the lashing system imposes on the kibble hoisting system and stage design
- Whether the stage is required to be moved to accommodate the changing level of the muck
- Whether the muck surface after a blast and the surface of the solid material below the blasted material are level or not

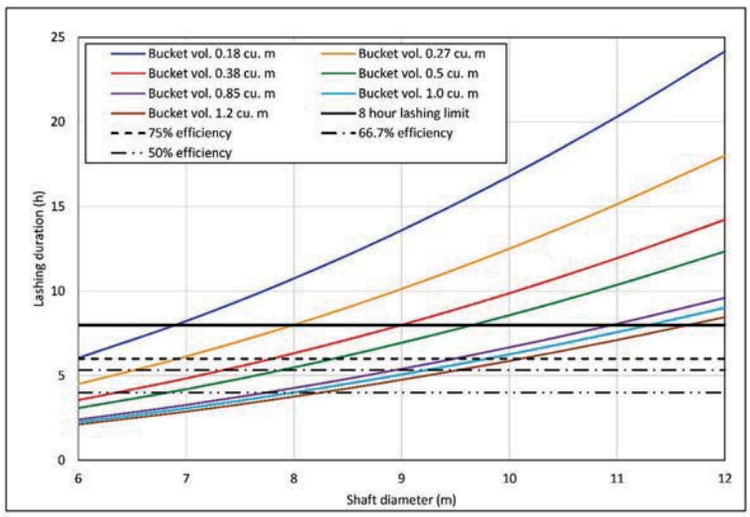

Figure 5—Lashing duration as a function of shaft diameter, bucket volume, and cleaning efficiency

- The ability of the lashing system to load material against the sidewall
- The ability to lash when the layer of muck becomes shallow
- How much material is required to be moved and hand-lashed during blow-over
- Worker safety during shaft bottom operations and the number of workers required to operate a specific system
- Communication between workers and operators
- Whether water is present at the shaft bottom and in what quantity
- Maintenance of lashing equipment
- Energy source
- The drilling pattern and type of explosives used, and the resulting fragmentation.

The EIMCO 630 loader and the Riddell clamshell mucking system were shown to have significant disadvantages, primarily related to safety of operations and suitability to particular shaft configurations, the fragmentation size, and condition of the blasted material. Consequently, they are not commonly used any longer.

The Cryderman mucking system has been shown to address some of the issues of the Riddell mucking system. In particular, the telescoping arm increases the safety of workers at the shaft bottom by providing accurate control of the positioning of the clamshell buckets. It was also shown that it has a better ability to clean material against the sidewall. The main concerns with the Cryderman mucking system are the loading rate and dealing with oversize rock fragments. In certain shaft sinking operations it was shown that two Cryderman loaders could be used simultaneously to increase the loading rate provided the shaft diameter was large enough. While this would increase the cost and complexity of lashing operations, and would reduce safety levels for workers at the shaft bottom somewhat, it does, however, also introduce a measure of redundancy should one of the units fail in service.

It is clear from the literature that the cactus grab has the highest instantaneous loading rate, but it is not clear whether the average loading rates are significantly lower due to the need to hand-lash a large amount of material at the end of the lashing cycle, due to the inefficiency of the grab when the layer of muck is shallow. There are numerous other disadvantages of the cactus grab. In particular, a few aspects that are of concern are the weight of the unit (which affects the stage design), the significant amount of space that it occupies underneath the stage (which inhibits other cycle functions), its reliance on gravity in order for the tines to penetrate the muckpile, its inability to clean effectively against the sidewall or when there is a shallow layer of material or the material contains a large proportion of fines, its uncontrolled and therefore unsafe movements as a result of the rope suspension system, and difficulty in conducting maintenance *in situ*.

Excavators appear to be promising but there is little published data available. Since they have one bucket they rely on the resistance of the muckpile to force material into the bucket, which is a disadvantage. Storage of the excavator on surface is also problematic as the transport time and stage requirements to allow it through are onerous.

An analysis of lashing duration as a function of shaft diameter and digging cycle times was conducted for an assumed advance of 3 m per blast, bucket fill factor of 0.65, solid rock density of 2800 kg/m^3, and expansion ratio of 2. The predicted lashing durations compared favourably with current lashing techniques.

Taking into account the advantages and disadvantages of the various lashing systems described so far, and without consideration of other functions of the shaft sinking cycle, the ideal lashing system should:

- Have opposed buckets to entrain muck without relying on the resistance of the muckpile
- Be able to clean against the sidewall as well as scoop muck effectively in a shallow layer
- Have a bucket volume of at least 0.5 m^3 and be able to scoop reasonably large fragments
- Either be located at the shaft bottom so as to work independently of the stage location (which would require either storage on the underside of the stage, or ability to pass through the stage to be stored on the

surface), or be integrated into the stage but have independent motion so as to be able to muck with minimal movement of the stage
- Be flexible enough to cope with varying height differences between the location of the buckets, the relative location of the top rim of the kibble, and the surface of the muckpile
- Be able to muck shafts with diameters in the range of 6–12 m with reasonable scalability (*i.e.* duplication to two muckers in larger diameter shafts)
- Have lateral and vertical positional control by means of cylinders (including penetration of the muckpile) in order to improve safety and bucket fill factors
- Be tolerant of water and uneven surfaces at the shaft bottom
- Improve safety in the shaft bottom by having a smooth, well-controlled motion, by limiting the number of workers required at the shaft bottom, by not occupying a large amount of space (which could be dangerous in small diameter shafts where space is limited)
- Have a mass as low as possible if it is to be attached to, or slung from, the stage
- Be maintainable on the stage or at the shaft bottom.

Of the lashing methods assessed in this review, the Joy version of the Cryderman mucker is the only one with an opposed bucket configuration and direct cylinder action to penetrate the muckpile. It does have constraints as far as cylinder stroke and positioning relative to the shaft bottom are concerned, particularly when operating in larger diameter shafts. There is the potential to introduce an additional degree of freedom such as a knee joint, which would give it more flexibility, but at the cost of increased complexity and mass. In addition, there is scope to address the bucket action for the case of a shallow layer of muck. Ideally, a deep penetrating bucket action would be better when the layer of muck is deep, while a shallow, gathering action would be beneficial when the layer is shallow.

References

AngloGold Ashanti. 2017. South Africa. http://www.anglogoldashanti.com/southern-africa/ [accessed 16 February 2018]

ASME Engineering History Landmarks. 2000. The EIMCO Rocker Shovel Loader Model 12B. ASME International, Miner's Plaza, Park City, Utah. https://www.asme.org/about-asme/who-we-are/engineering-history/landmarks/212-eimco-rocker-shovel-loader-model-12b [accessed 19 February 2017].

Bennett, W.E., Harrison, P., and Smith, G.E. 1959. Shaft sinking in Canada. *Proceedings of the Symposium on Shaft Sinking and Tunnelling*, July 1959. Institution of Mining Engineers, London. pp. 238–252.

Berry, T.M. 1956. Shaft loading: clamshell vs crawler-mounted loader. *Proceedings of the Loading and Transportation Symposium. Mining Engineering*, vol. 8, no. 12. pp. 1196–1198.

Britton, S.G. and Lineberry, G.T. 1992. SME Mining Engineering Handbook. 2nd edn, vol. 2. Hartman, H.K. (ed.). Society for Mining, Metallurgy, and Exploration, Inc., Littleton, CO, USA. Section 17, pp. 1543–1678.

Brunton, I., Thornton, D., Hodson, R., and Sproutt, D. 2003. Impact of blast fragmentation on hydraulic excavator dig time. *Proceedings of the 5th Large Open Pit Conference*, Kalgoorlie, WA, 3-5 November 2003. Workman-Davis, C. and Chanda, E. (eds). Australasian Institute if Mining and Metallurgy, Melbourne. pp. 39–48.

Caterpillar. 1998. Caterpillar Performance Handbook, Edition 29. Caterpillar Inc., Peoria, IL, USA. pp. 4–120.

Engineering News. 1999. World's deepest single-lift shaft project. http://www.engineeringnews.co.za/article/worldx2019s-deepest-singlelift-shaft-project-1999-11-26 [Accessed 16 February 2018].

Deilmann-Haniel Mining Systems. 2014. Grab systems technical data. http://www.dhms.com/en/products/shaft-hoisting-shaft-sinking-equipm/grab-systems-dh-dg.html [accessed 12 April 2017].

Dengler, W.R. 1982. Shaft machines. *Underground Mining Methods Handbook*. Society of Mining Engineers of the American Institute of Mining Engineering. Chapter 10, pp. 1263–1266.

Dengler, W.R., Shaver, W.M. and Letourneau, R. 1992. New technology in shaft sinking - the Craig Project. *Proceedings of the SME Annual Meeting*, Phoenix, AZ, 24-27 February 1992. Society for Mining, Metallurgy and Exploration, Inc., Littleton, CO.

Douglas, A.A.B. and Pfutzenreuter, F.R.B. 1989. Overview of current South African vertical circular shaft construction practice, *Proceedings of Shaft Engineering*, March 1989, Institution of Mining and Metallurgy, London, UK. pp. 137–154.

Graham, C., and Evans, V. 2008. History of Mining – The evolution of shaft sinking systems (Part 5), Shaft sinking from 1940 – 1970: The golden age. *CIM Magazine*, March/April 2008.

Herrenknecht Technology. 2016. Mining - Safe and fast development of underground mines. Product brochure 2382. https://www.herrenknecht.com/en/applications/mining.html [accessed 4 October 2017].

Internet Archive, 1992. EIMCO, Pioneer in Underground Mining Machinery and Process Equipment, 1926-1963: Oral History Transcript, pp.49-67. https://archive.org/details/pioneerunderground00roserich [accessed 28 February 2017].

Jamieson, D.M., and Pearse, M.P., 1959. Shaft planning for mines in the new Consolidated Gold Fields Group. *Proceedings of the Symposium on Shaft Sinking and Tunnelling*, July 1959. . Institution of Mining Engineers, London. pp. 318–331.

Joy Global. 2015. Shaft sinking equipment product overview. Joy Global, Milwaukee, WI.

Kratz, T., and Martens, P.N. 2015. Optimization of mucking and hoisting operation in conventional shaft sinking. *Mining Report* , vol. 151, no 1. pp. 38–47.

MacConachie, H. 1959. Shaft sinking practice in South Africa. *Proceedings of the Symposium on Shaft Sinking and Tunnelling*, July 1959. Institution of Mining Engineers, London. pp. 3–28.

Murray and Roberts. 2017. Underground mining. http://www.murrob.com/cap-under-mining.asp [accessed 16 February 2018].

MacGillivray, D.M.,1979. High speed shaft sinking techniques in South Africa. *Proceedings of the Rapid Excavation and Tunnelling Conference*, Atlanta, GA, 18-21 June 1979. Vol. 2. Maevis, A.C. and Hustrulid, W.A. (eds). Society of Mining Engineers, New York.

Martin, C.J.H. and Harvey, S. 1989. Sinking of the Asfordby Mine shafts. *Shaft Engineering*. Institution of Mining and Metallurgy, London, UK pp. 289–296.

Moore, E. 2015. Building a better shaft mucker. CIM Magazine, October 2015.

Morgan, G. 2015. Investigation into current shaft sinking processes with a view to proposing improvements in work practices with regard to productivity and safety. MEng investigational project report, University of the Witwatersrand, Johannesburg, South Africa.

Moss, S.T., 2011. Development of a scale model clamshell mucker and validation by discrete element modelling. MSc thesis. University of the Witwatersrand, Johannesburg, South Africa.

Obert, L. 1973. Opening and development. *Mining Engineering Handbook*. Society of Mining Engineers (SME), New York. Volume 1, section 10. pp. 10.2–10.104.

Singh, S., Glogger, M. and Willock, D., 2001. Effect of fragmentation on loader efficiency. In *Proceedings of the Annual Conference on Explosives and Blasting Technique.* Vol. 2. ISEE, New York. pp. 77–88.

Stout, K.S. 1980. Mining Methods and Equipment. McGraw-Hill, New York, USA. pp. 68-69, 98–103.

Trident SA. 2016. 630 Rockershovel. http://www.tridentsa.co.za./630.html [accessed 28 February. 2017].

Wakefield, T. 2009. Approaches to improve safety and recover lost productivities in vertical shaft sinking by making use of industrial engineering and risk driven 3-D modelling techniques. *Proceedings of the Shaft Sinking and Mining Contractors Conference 2009*, Johannesburg, South Africa. Southern African Institute of Mining and Metallurgy, Johannesburg.

Wilson, J.W. 1976. Shaft sinking technology and the future needs of the mining industry. *Proceedings of the 1976 Rapid Excavation and Tunneling Conference*, Las Vegas, NV, 14-17 June 1976. Robbins, R.J. and Conlon, R.J. (eds.) Society of Mining Engineers, New York. pp. 103–125. ◆

http://dx.doi.org/10.17159/2411-9717/2018/v118n3a13

Silicomanganese production at Transalloys in the twenty-tens

by J.D. Steenkamp*, P. Maphutha*, O. Makwarela*, W.K. Banda*, I. Thobadi*, M. Sitefane*, J. Gous†, and J.J. Sutherland†

Synopsis

Transalloys is currently the largest producer of silicomanganese in Africa, with its smelter complex based outside the town of eMalahleni, in the Mpumalanga Province of South Africa. It operates five open submerged arc furnaces and produces an alloy containing > 16% Si, < 2% C, and > 65% Mn. Manganese ore is the main source of manganese units, supplemented by dust and alloy fines recycled into the furnace as briquettes. Transalloys has mature technology and systems in place, which are described in more detail in this paper.

Keywords
silicomanganese, submerged arc furnace, Transalloys.

Introduction

Transalloys is currently the largest producer of silicomanganese (SiMn) in Africa. Its smelter complex is based outside the town of eMalahleni, in the Mpumalanga Province of South Africa (Figure 1). Transalloys was commissioned in the 1960s as an integrated high-carbon/low-carbon ferrochromium plant based on the Perrin process, and converted to SiMn production in 1967 due to constraints in the ferrochrome market (Basson, Curr, and Gericke, 2007; Bezemer, 1995). Currently, the installed production capacity is 180 kt/a saleable SiMn. The majority of this is exported via Durban and Richards Bay harbours.

High-level process flow

The business strategy followed at Transalloys is that of a high-volume, low-margin operation. Plant operations consist of five furnaces, operated 24 hours per day, 365 days per year (including maintenance), by 280 permanent employees, with up to 120 contract employees on site at any given time.

The high-level process flow at Transalloys is summarized in Figure 2. SiMn is produced by carbothermic reduction of manganese-bearing ore sourced from the Kalahari Manganese Field in the Northern Cape Province, and quartz from South African producers. The main source of carbon is bituminous coal from South African coal mines, supplemented with imported coke. The SiMn is produced primarily for the export market, and is exported via Richards Bay harbour. The slag produced is discarded on slag dumps, and process off-gas vented to the atmosphere after cleaning using a specification of 2–30 mg/Nm^3. The remainder of the paper addresses the process flow and major equipment in more detail, as well as metallurgical considerations, where applicable.

Product description

The chemical composition of SiMn produced at Transalloys is typical of ASTM grade B (ASTM Standards A483 / A483M - 10. 2010) (Table I). The product size ranges, in comparison with the ASTM specifications, are summarized in Table II.

Process description

A simple schematic of the operation, on which the description is based, is provided in Figure 3.

Raw material

The feed to the furnaces comprises a blend of raw materials: manganese ores, coal and coke, quartz, SiMn alloy fines, Mn-bearing briquettes, and lumpy spillages. Depending on the composition of these raw materials, the recipe is adjusted to produce SiMn containing between 15 and 16.5% Si, 65 and 67% Mn, and a maximum of 2% C.

The primary source of manganese in the blend is manganese ores, which are sourced from a number of mines near Postmasburg and Kuruman in the Kalahari region of the Northern Cape Province – United Manganese of Kalahari (UMK), Mamatwan, Wessels, and Nchwaning. The ores are delivered by railway, and have a required size range of –75 + 6 mm. Ore chemistry varies, as indicated in Table III. The mineralogy of manganese-bearing ores

* *Mintek, Randburg, South Africa.*
‡ *Transalloys, eMalahleni, South Africa.*
 ISSN 2225-6253. Paper received Nov. 2017; revised paper received Feb. 2018.

Figure 1—The manganese orebody is located near the town Hotazel in the Northern Cape Province of South Africa. Transalloys's operation is located near eMalahleni in the Mpumalanga Province of South Africa. Alloys produced are mainly exported through Durban and Richards Bay harbours in the Kwazulu-Natal Province (Google maps)

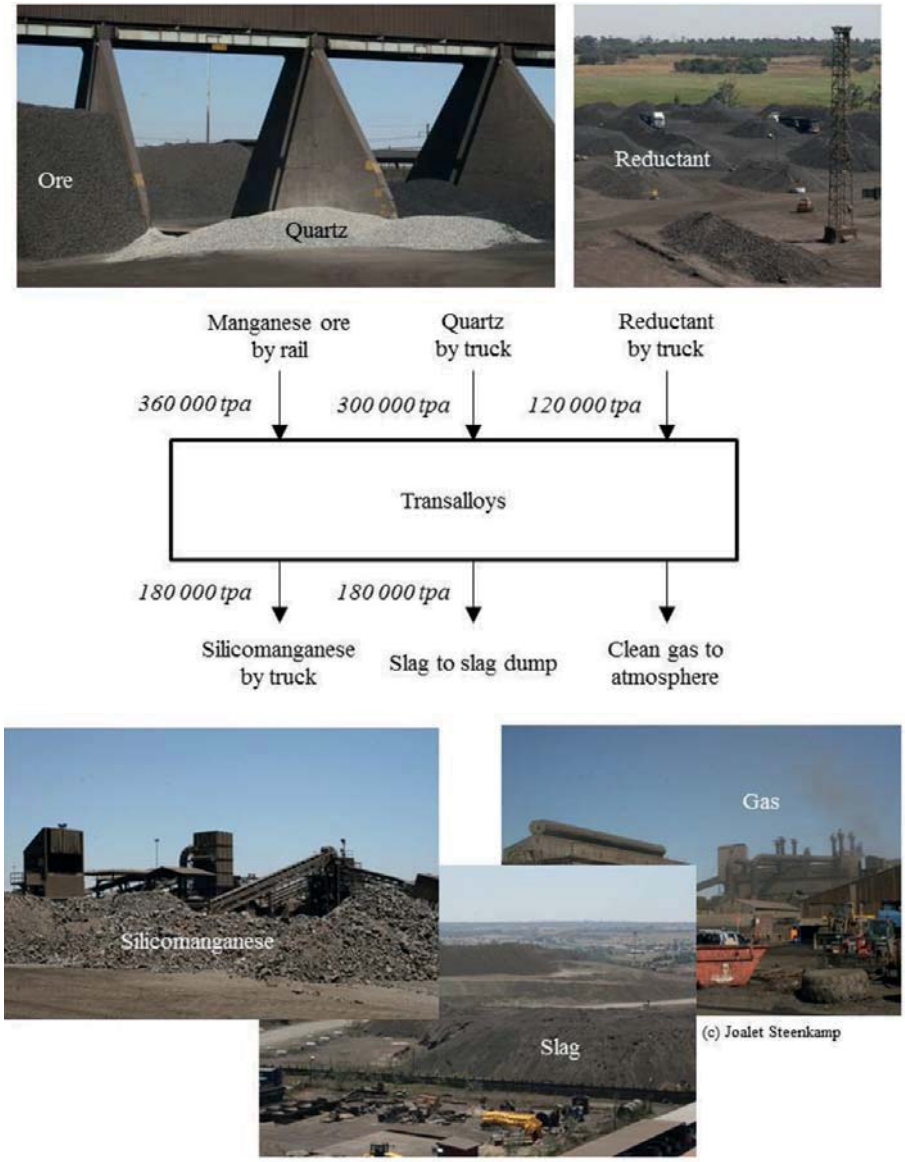

Figure 2—High-level process flow at Transalloys

Table I

ASTM grades for SiMn (mass%) (ASTM Standards A483 / A483M - 10. 2010)

	Mn	Si	C max	P max	S max	As max	Sn max	Pb max	Cr max	Ni max	Mo max
ASTM Grade A	65.0–68.0	18.5–21.0	1.5	0.20	0.04	0.10	0.010	0.030	0.50	0.20	0.10
ASTM Grade B	65.0–68.0	16.0–18.5	2.0	0.20	0.04	0.10	0.010	0.030	0.50	0.20	0.10
ASTM Grade C	65.0–68.0	12.5–16.0	3.0	0.20	0.04	0.10	0.010	0.030	0.50	0.20	0.10

Table II

Sizes of products produced at Transalloys, compared to standard sizes and tolerances in the ASTM specification for SiMn (ASTM Standards A483 / A483M - 10. 2010)

ASTM product size (mm)	Tolerance		Transalloys product size (mm)#
	Top size	Bottom size	
200–100	40 kg lump, max.	10% max. passing 100 mm sieve	-
200–50	40 kg lump, max.	10% max. passing 50 mm sieve	-
100–25	10% max. retained on 100 mm sieve	10% max. passing 25 mm sieve	–75 +20
50–5	10% max. retained on 50 mm sieve	10% max. passing 5 mm sieve	–50 +10 –25 +10*
< 50	10% max. retained on 50 mm sieve	15% max. passing 5 mm sieve	–12+3 –10 +6*

* Recovered from metal recovery plant

Tolerances depended on contract specification, but typically 5%

from the Northern Cape is complex (Chetty, 2008; Chetty and Gutzmer, 2008). Iron can be present in the divalent and trivalent states and manganese in divalent, trivalent, and even tetravalent states. That is the reason why Fe and Mn assays are typically reported as the zero valent state, as is the case for Table III.

The selection the ore blend fed into the furnaces is driven by techno-economic factors: Ore with 37% Mn forms the baseline, with the selection being based on cost of ore per ton alloy produced. Higher grade ore is added to increase the Mn grade of the SiMn product.

Other sources of manganese are manganese ore spillages from the feed system and reclamation area and surplus SiMn alloy fines (3 mm) from the metal crushing plant. The briquettes have a Mn content of 35%. The recycled SiMn alloy fines, material for which no market exists, improve the production capacity of the furnaces. The –6 mm SiMn alloy fines from the metal recovery plant and from the crushing plant are sent to the briquetting plant as discussed in following sections.

The primary source of silicon in the blend is quartz, the typical composition of which is indicated in Table III, although both the manganese-bearing ores and the reductants also contain some SiO_2. Quartz is sourced from two local suppliers around Gauteng and delivered by truck. The quartz is also added to adjust the basicity (B_3, defined in Equation [1]) of the slag. Slag basicity is controlled to manage Si recovery.

$$B_3 = \frac{CaO + MgO}{SiO_2} \quad [1]$$

The sources of carbon – required for the reduction of manganese, SiO_2, and iron oxides – are coal from a number of coal mines around Mpumalanga and Gauteng and pea coke, sourced mainly from China but also reclaimed at the reclamation area as discussed below. All reductants are delivered by truck. As indicated in Table IV, the fixed carbon content of the coal is significantly lower than that of the coke. Yet, coal is the preferred source of carbon due to its significantly lower cost. Also, it is speculated that the methane gas that is generated during devolatilization of coal will improve the prereduction of the ore in the upper part of the furnace, and this is potentially a useful topic to be researched at the laboratory scale.

Raw material receiving and storage area

The flow of raw materials through the raw material receiving and storage area is summarized schematically in Figure 4.

The wagon tippler is the main receiving point for raw materials delivered by railway (manganese ores) and road (quartz and reductants). Railway wagons arriving are

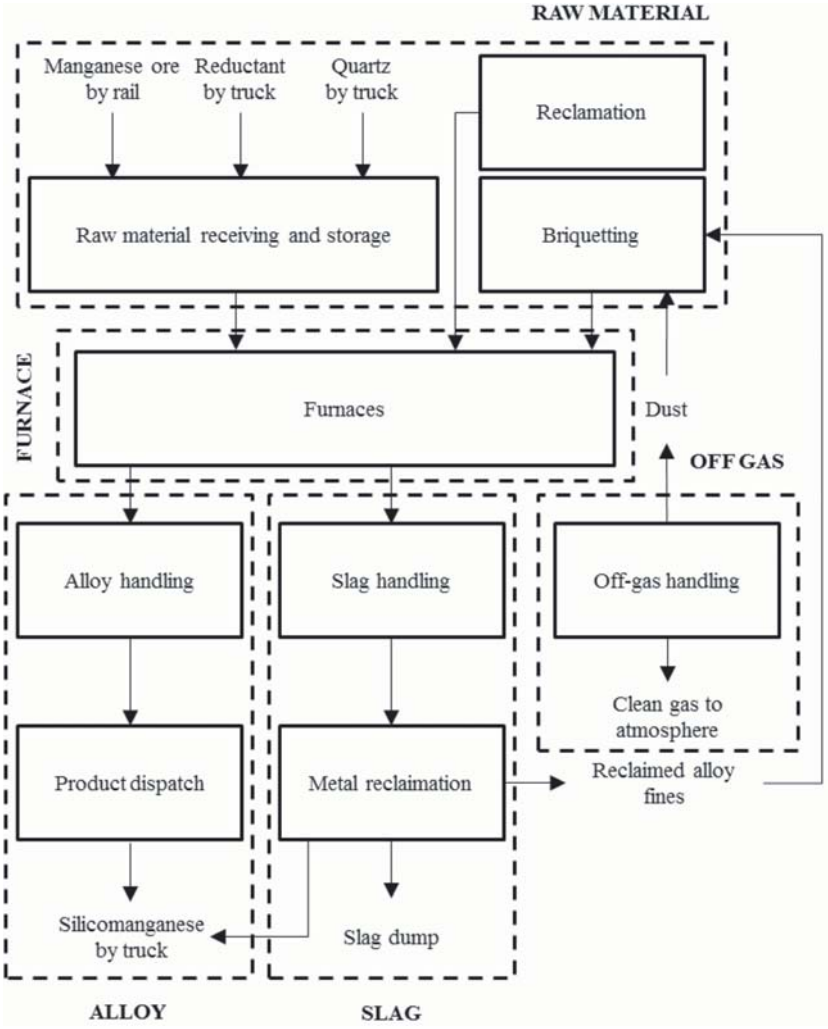

Figure 3—Simple schematic of Transalloys operation, indicating sections discussed in more detail

Table III

Typical chemical compositions of the manganese ores, and quartz (mass%)

Constituents	UMK	Mamatwan	Wessels	Nchwaning	Quartz
Mn	37.0	36.4	39.9	36.3	-
Fe	5.7	4.3	7.7	14.8	-
MgO	2.8	3.5	2.5	0.9	-
Al_2O_3	0.3	0.4	0.6	0.3	1.5
SiO_2	5.9	5.4	7.5	5.0	98.5
CaO	11.9	13.6	9.5	7.2	-
Mn/Fe ratio	6.49	8.47	5.18	2.45	-
Total	63.6	63.6	67.7	64.5	100

positioned over the wagon tippler table and rotated to discharge material into four underground hoppers. Raw materials delivered by side-tipper trucks are also discharged into the hoppers, provided that there are no train wagons lined up at the wagon tippler at the time of delivery; alternatively, the trucks are unloaded at specific storage bunkers. Trucks pass through a weighbridge before and after unloading to determine the quantity of material delivered for contractual purposes.

From the wagon tippler hoppers, raw materials are discharged by vibratory feeders onto a conveyor belt, and transported to specific storage bunkers. The conveyor belt has a mobile tipper car that elevates the belt, and discharges material through a chute into a specific bunker. An operator controls the movement, and position, of the tipper car using an automated control system. An automatic sampler positioned along the conveyor belt takes representative samples of material from the conveyor, and discharges the

Table IV

Typical chemical compositions of reductants (mass per cent)

	Constituents	Coal #1	Coal #2	Coal #3	Pea coke
Proximate analysis	Inherent moisture	3.05	4.75	4.07	1.69
	Volatile matter	30.23	31.69	27.91	1.90
	Ash (dry basis)	18.12	15.18	17.48	15.61
	Fixed carbon (dry basis)	50.69	51.55	53.41	82.46
XRF analysis	SiO_2	7.42	5.36	9.47	9.39
	Al_2O_3	5.05	4.15	5.29	2.67
	MgO	0.16	0.15	0.07	0.04
	CaO	1.40	1.67	0.40	0.27
	Fe_2O_3	0.94	0.94	0.34	0.90
	TiO_2	0.23	0.17	0.18	0.34
	S	0.56	0.56	0.55	0.62
	P_2O_5	0.06	0.07	0.01	0.04

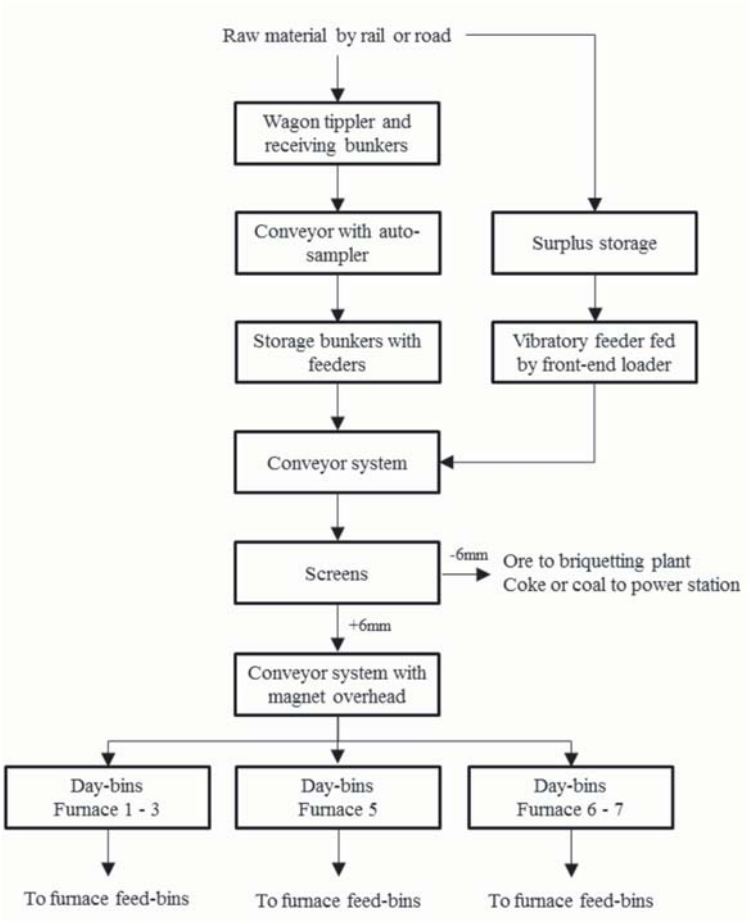

Figure 4—Schematic flow diagram of the raw materials handling section

sample into a chute which feeds it into a sample bag for collection. The sample is taken to the laboratory for chemical characterization by X-ray fluorescence (XRF), reductants by LECO (proximate analysis), and physical characterization (particle size distribution) for contractual purposes.

There are five storage bunkers, two allocated for the storage of manganese ore, two for coal, and one for quartz. Other raw materials are stockpiled alongside the feed system and fed to the conveyor system via a vibratory feeder, using a front-end loader. From the storage bunkers, raw materials are directed onto a conveyor system; the quantity of material to be discharged is dependent on the amount of material required to fill the day-bins. The conveyor system feeds raw materials onto two double-deck screens positioned in parallel, with the specific purpose of removing the –6 mm fraction to ensure gas permeability of the burden in the submerged arc

furnace (SAF). The –6 mm fraction is discharged from the screens through a hopper, collected, and sent to the briquetting plant in the case of manganese ores, and to local power stations in the case of coal or coke fines.

The +6 mm fraction is discharged via a vibratory feeder onto a conveyor system that transfers the raw materials to the day-bins. A magnet that scavenges metallic objects, *i.e.* metal shavings, nails, and wire from the feed material, is suspended above the conveyor belt. There are three sets of day-bins from where raw materials are batch-fed into the furnace feed-bins. The first set of day-bins, consisting of 12 bins in succession, feeds raw materials into the feed-bins of furnaces 1 and 3. The second set of day-bins, with 12 bins in pairs, feeds raw materials into the feed-bins of furnace 5. The last set of day-bins, with 14 bins in pairs, feeds raw materials into the feed-bins of furnaces 6 and 7. Each bin is a vertical cylinder made of steel with a conical outlet at the bottom to discharge material onto the conveyor belt. The bins have capacities ranging from 76 m³ to 190 m³ to accommodate the raw materials required for the 24-hour operation of each furnace at maximum throughput. Belt weighers are installed at various sections under the conveyor belts to monitor raw material feed rates and quantities.

A control room operator, based at the delivery station, monitors the quantities of material delivered by rail or truck, and the filling of the day-bins in terms of material type, refill rates, and quantities. The batching and conveying of raw materials from the day-bins to the furnace feed-bins is controlled by the control room operator of each specific furnace.

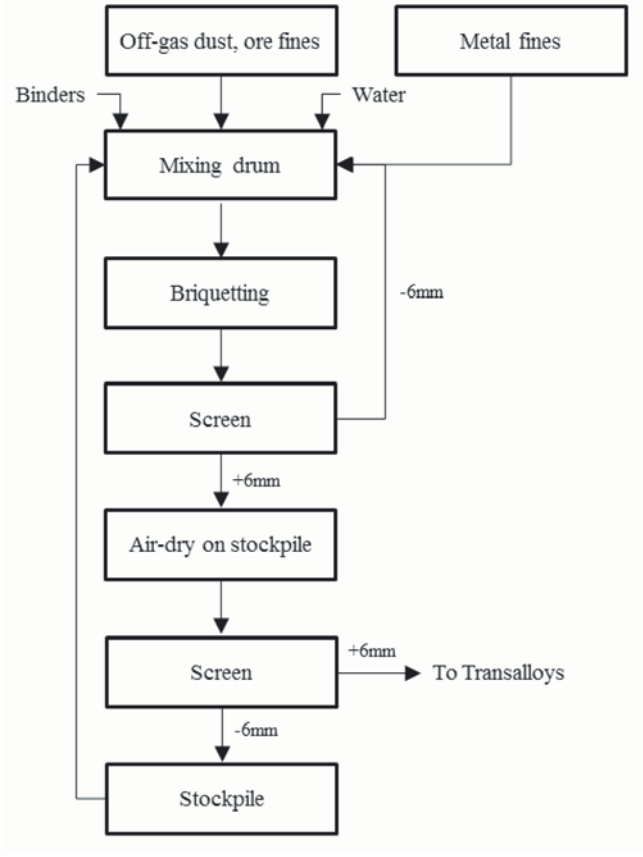

Figure 5—Schematic flow diagram of briquetting plant

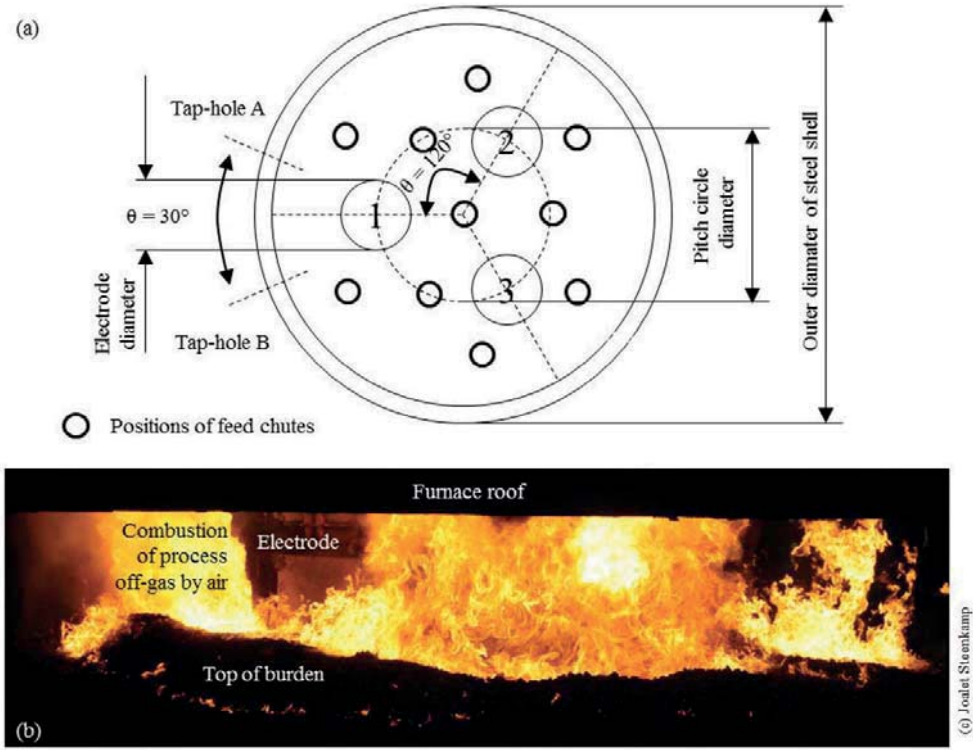

Figure 6—(a) Three Söderberg electrodes, positioned in equilateral arrangement, with electrode diameter (ED), pitch circle diameter (PCD), and outer diameter or steel shell (ODS), indicated. (b) Open SAF (Transalloys Furnace no. 1), where the roof is not sealed, and furnace is off-gas combusted in air on top of the burden

Briquetting plant

The flow of materials through the briquetting plant is summarized in Figure 5. The feed materials for the briquetting process comprise manganese ore fines, briquette fines, off-gas dust, and SiMn fines, generated at the alloy handling area and recovered at the metal recovery plants. The fines are fed into three hoppers, from which feed materials are batched in different quantities and conveyed to a mixing drum, where they are mixed with binders and water to form a homogenous product. The materials are blended in batches of 800 kg. The mixture is then conveyed at a controlled rate to a briquetting machine, where it is compressed in a die to form briquettes with uniform shape and size. The briquettes are pillow-shaped with a typical size of 37 × 54 × 42 mm.

The feed materials are mixed in different ratios to meet the grade, typically 35% Mn, specified by Transalloys. The briquetting machine has a production capacity of 7 t/h. The green briquettes are screened to remove –6 mm fines, which are recycled back to the briquetting machine, and sampled for compression tests. The compression test gives an indication of the strength of the green briquettes. A manual hydraulic pressure test machine is used for this purpose. The rest of the green briquettes are stored, cured for one week (depending on the weather), screened again, and sampled for semi-quantitative XRF analysis. The dry briquettes are then transported to the furnaces, and the fines stockpiled and recycled back to the briquetting plant as feed material.

The briquetting plant produces 4500–5500 t of briquettes per month, which is around 10–15% of the feed to the furnace.

Reclamation

The reclamation area was established to recover saleable products from old spillage dumps arising from past operations at Transalloys. The area has been in operation since 2015 and supplies Transalloys with coal, a coal and coke blend, and UMK and Wessels-type manganese ores. The use of spirals was established by a third party as the best practical technique to separate these material streams from the dumps.

Smelting

At Transalloys, silicomanganese is produced in five open submerged arc furnaces (SAFs) of circular design, with three Söderberg electrodes positioned in equilateral arrangement (Figure 6). Two 7 MVA furnaces (Basson, Curr, and Gericke, 2007) previously utilized in the production of medium-carbon ferromanganese (Barcza and O'Shaughnessy, 1981) have been decommissioned and demolished.

Details of the installed operational furnaces are given in Table V.

Figure 7 depicts a schematic flow diagram of one of the furnaces, showing inputs and outputs. Transalloys uses a blend of manganese ores, briquettes, quartz, coal, coke, and recycled material, the recipe being based on mass and energy balance calculations as well as the material costs. Quartz is used partly as raw material for producing metallic silicon in the SiMn and also as flux. The recycle stream comprises the spillages collected around the plant and the SiMn fines generated in the alloy crushing plant.

Each furnace has about 10 to 16 dedicated primary bins containing raw materials. The mass balance recipe is batched from these bins into the weigh hopper before being transferred to the furnace bins. The final feeders are positioned at different places such that the feed material can be evenly distributed within the furnace. The final feeders in the middle of the furnace (between the electrodes) have a larger capacity than those on the sides because the consumption of the burden is higher in the middle. The transferring of material from one bin to the next is done by means of belt conveyers. There is a sequence followed to

Table V

Furnace design parameters including design power rating (PR), electrode diameter (ED), electrode pitch circle diameter (PCD), and outer diameter of steel shell (ODS)

Furnace no.	Installation date	PR (MVA)	ED (m)	PCD (m)	ODS (m)
1	1969	15	1.143	2.836	8
3	1969	22	1.143	2.881	8
5	1975	48	1.600	4.100	12
6	Early 1980s	22	1.143	3.075	8
7	1987	48	1.600	4.006	12

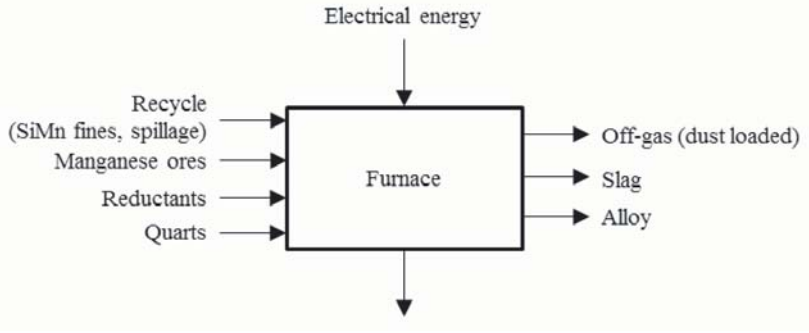

Figure 7—Furnace inputs and outputs at Transalloys

Table VI

Chemical composition (mass %) of tapped alloy, tapped slag (calculated averages and standard deviations, for January–December 2014, and typical dust composition (mass %)

Alloy			Slag			Dust	
	Average	St. dev.		Average	St. dev.		Average
Mn	66.5	1.3	MnO	12.7	1.7	MnO	31.6
C	1.8	0.2	SiO_2	46.2	1.5	SiO_2	38.8
Si	16.4	0.6	MgO	5.7	0.6	MgO	7.3
Fe	15.5	0.9	CaO	25.2	1.6	CaO	8
Total	99.2		FeO	0.3	0.1	Fe_2O_3	1.2
			Al_2O_3	4.8	0.7	Al_2O_3	3.6
			Total	94.9		ZnO	0.4
						Total	90.9

ensure mixing such that the blend of material going into the final feeders is homogeneous. Thereafter, the material in the final feeders is fed into the furnace in a batch system, the frequency of feeding depending on the furnace conditions such as burden level.

The top of the burden in the submerged arc furnaces at Transalloys is open to the atmosphere, and this furnace design is often referred to as 'open'. The furnace roof is completely separated from the furnace shell and the gap between the roof and shell is utilized for rabbling and also for visual inspection of the burden. The burden level must at all times be just above the furnace sill and level throughout. To ensure this, rabbling of the burden is conducted on a regular basis to achieve two main objectives: (1) levelling of the burden, and (2) improving burden permeability. Levelling is needed to minimize heat losses, as well as losses of Mn and Si vapour and fines. Simultaneously, ensuring burden permeability is important to avoid furnace blow-outs, which occur primarily as a result of diffusion of gases through the burden being hindered. Other causes of furnace blow-outs include high slag levels in the furnace, electrode position, and slag basicity resulting in a viscous slag (Muller and Steenkamp, 2013).

An insulating refractory design philosophy is followed in which the intention is to design the hot face refractory material to be chemically compatible with the process material. Water cooling is applied to the shells of the two larger furnaces only to protect the steel shell, and not to form a freeze lining of process material on the hot face of the refractory, as is done in conductive lining designs (Steenkamp, 2014). The hearth refractory in a SiMn furnace typically includes one of two high-wear areas (Steenkamp, Pistorius, and Tangstad, 2015). The effects of carbon undersaturation of the alloy (Steenkamp, Pistorius, and Muller, 2016), distance between the tap-hole and the hearth (Ishitobi, Ichihara, and Homma, 2010), electrode pitch circle diameter power intensity, and hearth power intensity on refractory wear rate will potentially be an interesting investigation (summarized in Table VII).

The electrode pitch circle diameter power intensity (PIT_{PCD}) depends on the operating power (OP) and the electrode pitch circle diameter (PCD), according to Equation [2]. The hearth power intensity (PIT_{hearth}) depends on the operating power (OP) and the internal diameter of hearth refractory (IDH), according to Equation [3].

$$PIT_{PCD} = \frac{OP}{\frac{\pi}{4} \times PCD^2} \quad [2]$$

$$PIT_{hearth} = \frac{OP}{\frac{\pi}{4} \times IDDH^2} \quad [3]$$

The electrical parameters for each furnace are presented in Table VIII. Furnaces 5 and 7 are resistance controlled using Mintek's Minstral™ software, while the other three furnaces are current controlled. There is a substantial difference in the operating currents of furnaces 5 and 7 and those of the other furnaces, which operate at lower power levels. The difference in operating resistance of all furnaces is marginal, implying that the difference in operating power is due to the different operating currents.

Table VII

Operating power (OP), PCD power intensity (PIT_{PCD}), internal diameter of hearth refractory (IDH), and hearth power intensity (PIT_{hearth})

Furnace no.	OP (MW)	PIT_{PCD} (MW/m²)	IDH (m)	PIT_{hearth} (MW/m²)
1	12	1.90	7.388	0.28
3	13	1.99	7.388	0.30
5	28	2.12	11.260	0.28
6	14	1.89	8.158	0.27
7	28	2.22	10.940	0.30

Table VIII

Furnace operating parameters

Furnace	Current (kA)	Resistance (mΩ)
1	60-65	0.95 - 1.10
3	60-65	1.00 - 1.20
5	105-110	0.80 - 0.90
6	63-66	1.00 - 1.20
7	105-110	0.80 - 0.90

As aforementioned, the feeding mechanism is a batch system. Therefore, the feed rates are not captured instantaneously; instead, the feed mass is recorded and consolidated at the end of each production day (24 hours), which can be translated to a daily rate. The control systems of the furnaces focus only on the electrical operation. The smaller furnaces are controlled by current (*I*, kA), and each has a single three-phase transformer. The larger furnaces are controlled based on electrode-to-bath resistance (*R,* mΩ). Both systems regulate the electrode holder position to maintain the respective set-points, although the use of resistance control mitigates the problem of electrode current interaction caused by the common neutral point within the molten bath (Barker *et al.*, 1991). On furnaces 1, 3, and 6 (current control) the transformers are tapped up and down automatically to maintain the desired power input. On furnaces 5 and 7 (resistance control), the transformers are tapped automatically by the Minstral™ control system, which enables the transformers to be tapped differentially so as to optimize the power input within the specified circuit limitations (Brereton-Stiles, Rennie, and Moolman, 1999).

Owing to the high currents needed in SAF production of SiMn, Söderberg self-baking carbon electrodes are used at Transalloys, which are prepared by welding cylindrical casings and inserting the electrode paste cylinders. The pressure rings force the contact shoes (which are responsible for the supply of current to the electrode) against the steel cylinder and hold the electrode in place. The jacks can be either pneumatic or hydraulic and are responsible for controlling the slipping of the electrode. The electrode paste melts in the casing and starts to bake at a temperature of around 450 to 500°C. Above these temperatures the electrodes are transformed into solid graphite and become electrically conductive, and the steel casings melt and become part of the charge mix.

The electrode consumption is monitored by using manual readings. The slip calculator provides the operator with the length (in centimetres) of electrode that needs to be slipped, and this is compared to the actual slipped centimetres. Electrode slipping is done hourly and the control room operator manually monitors electrode consumption every four hours. Note that the operator will not slip if the electrode hasn't been properly baked yet, which may cause a difference between the calculated and actual slipped values. The liquid and solid level measurements are used as guidelines to the number of electrode paste bags and cylinders to be added to maintain the liquid level in the appropriate range. Leakage of paste from the casing due to fast slipping and the electrode not being baked properly is termed a *green break*. Thermocouples allow easy identification of green breaks in furnaces 5 and 7, while visual inspection is done on furnaces 1, 3, and 6.

Tapping occurs every four hours at all furnaces. Although some of the furnaces have bi-level tap-holes installed (one dedicated to metal tapping, the other to slag tapping) all furnaces are operated with single-level tap-holes, *i.e.* metal and slag are tapped simultaneously from the metal tap-hole. Tap-holes are drilled open and closed using mudguns on all furnaces; tap-holes are lanced open only when difficulties with drilling are experienced, *i.e.* metal frozen in the tapping channel. The metal and slag flow along a 4–5 m long launder into a refractory-lined ladle. Due to differences in specific gravity, metal settles at the bottom of the ladle and slag overflows into a slag pot. The slag that remains on top of the metal is skimmed off onto the floor, using a scraper.

Alloy processing

After scraping off any slag remaining in the ladle, the ladle is weighed (to determine the liquid alloy content by difference), and cast into casting pits lined with SiMn fines (see Figure 8a). The SiMn fines are also used as an embankment around the casting pits to contain the liquid alloy. A layer cast from one ladle is 40 mm thick, on average. As a layer of alloy is allowed to solidify before the next layer is cast onto it, the layers remain separate. This ensures that when the material is removed, the alloy breaks easily into pieces 40 mm thick. The cast alloy is allowed to cool and solidify before being lifted and moved by front-end loader to the alloy stockpile (Figure 8b). The alloy is transported from the stockpile by front-end-loader to the alloy handling plant for further processing.

The stockpiled material is fed into the crushing and size classification plant where different product sizes are produced (Figure 9). The alloy first passes over a grizzly screen. The –76 mm material from the screen is fed to a multiple deck screen where three product sizes are produced: –76 +50 mm, –50 +12 mm, and –12 +3 mm. The –3 mm size material is classified as fines, which are not saleable; they are stockpiled for use on casting beds and in the briquetting plant. The +76 mm material from the grizzly screen is fed to a jaw crusher which produces –80 mm material. The jaw crusher product is fed to another multiple deck screen which produces +76 mm oversize material, –3 mm fines, a –12 +3 mm product, and –76 +12 mm material. The –3 mm fines are added to the fines stockpile, the –12 +3 mm product size is added to the similar size product from other screens, and the –76 +12 mm size class is fed via a vibratory feeder onto the third multiple deck screen. The third screen produces the –3 mm fines, which are added to the fines stockpile, and three product sizes: –12 +3 mm,–50 +12 mm, and –76 +50 mm. Each day's production of +76 mm material from screen 3 is weighed and stockpiled. This stockpile (+76 mm) is accumulated for a month and processed at the end of the month separately to produce different product sizes. The daily production of different size products is accumulated, weighed, and the materials stored in the products bunkers. The products are transported daily to the port in Richards Bay.

Figure 8— (a) Alloy cast into a casting bed, and (b) alloy stockpile prior to alloy processing plant

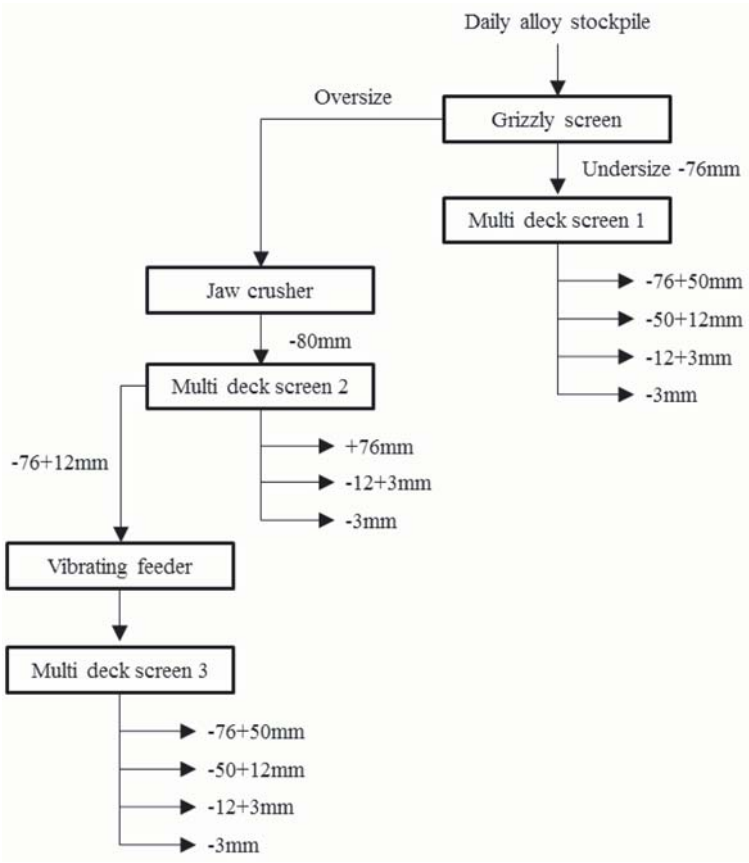

Figure 9—Process flow at alloy handling plant

Slag

Slag that flows out of the ladle into the slag pot is transported to the slag stockpile with Kress carriers. The slag is not further processed because the level of entrained SiMn is very low and cannot be economically recovered. Slag that is scraped off the alloy ladle onto the floor is collected daily and taken to the metal recovery plant. A significant amount of metal is entrained in this slag because the scraping process removes the interface alloy layer along with the slag, and thus the metal must be recovered. Spillages from the tapping hall are also collected from the tapping floor and taken to the metal recovery plant along with the scraped slag.

Metal recovery plant

The metal recovery plant processes 200 t/h of slag-based feed material which has a SiMn alloy content of about 5%. The recovered alloy which is separated into different product sizes (Figure 10). The feed material consists of the scraped-off slag and the spillages from the tapping hall, as well as material from old slag stockpiles. The material is first fed onto a grizzly screen, and the oversize material (+200 mm) is broken using a jackhammer and returned to the grizzly screen. The undersize material first passes an electromagnet which removes magnetic metallic pieces. The nonmagnetic material is weighed on a load cell on the conveyer belt

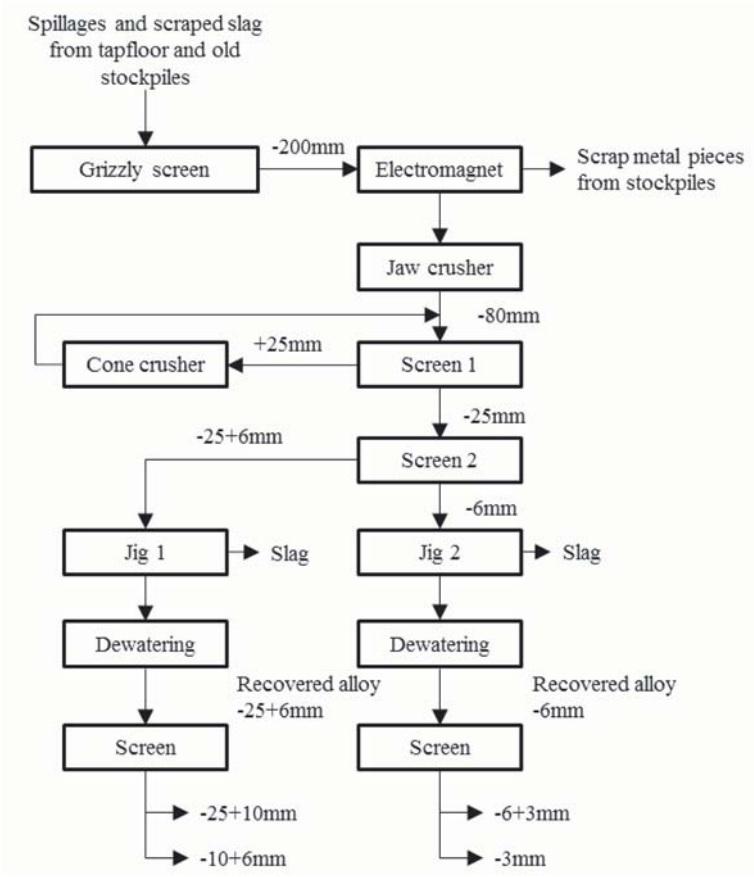

Figure 10—Process flow at metal recovery plant

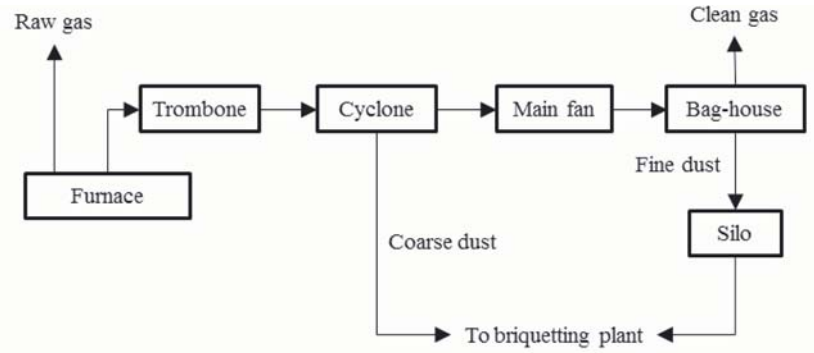

Figure 11—Off gas treatment plant

immediately after the magnetic separation step. The weighed material is fed to a jaw crusher. The jaw crusher produces –80 mm material which is fed onto a double deck screen. The +25 mm oversize from the first screen is fed into a cone crusher where it is crushed further and recycled to the first screen. The –25 mm undersize material from the first screen goes to the second screen, where it is separated into a –25 +6 mm oversize and a –6mm undersize stream. The two final crusher product streams are sent to separate jigs where differences in the densities of the liberated metal particles and the slag are exploited to separate them and recover the metal. The metal recovered from the –25 +6 mm jig feed is dewatered and fed onto a screen where it is separated into two product sizes; –25 +10 mm and –10 +6 mm. The metal recovered from the –6 mm jig feed is also dewatered and fed onto a separate screen where the –6 +3 mm product size is separated from the –3 mm fines. The three products (–25 +10 mm, –10 +6 mm, and –6 +3 mm) are either sold directly or returned to the metal processing section, where they blended with the appropriate cast metal processing plant product, *i.e.* the –25 +10 mm metal recovery product is blended with the –50 +12 mm final product size. The –3 mm fines are returned to the main plant where they are used in the briquetting plant.

Off-gas

The off-gas treatment plant's main equipment comprises stacks, a gas duct, trombones, cyclones, main fan, compartments, pneumatic blower, and the silo. These are fully integrated in a logical sequence to ensure that the dust-laden off-gas from the furnace is cleaned to produce a dust-free off-gas and recover the dust, which contains significant quantities of manganese and silicon and which serves as part of the briquette recipe. The off-gas plant arrangement is shown in Figure 11.

The dust-laden off-gas first passes through the four furnace stacks at an average velocity of 15 m/s. It then is further carried through the stacks to a single, horizontal gas duct, which under normal furnace conditions operates at a temperature between 340–350°C. The main fan draws the dust-laden gas from the furnace. The dust-laden gas is then cooled in the S-shaped trombone, the sensible heat of the gas passing to the shell of the trombone which is cooled by the external ambient air. The main function of the trombone is to reduce the temperature of the dust-laden gas from about 320°C to 220°C, thus minimizing the possibility of burning out the bag filters in the baghouse.

As a temperature control measure, a dilution damper is installed directly after the trombones with a fully automated control system so that if the temperature of the dust-laden off-gas is higher than desired, further cooling is automatically undertaken. The dilution damper immediately opens at a temperature of 260°C, allowing cooler air to flow in. Furthermore, a higher limit of 280°C is setup as a final control measure, and should the temperature exceed this set-point, the main fan immediately turns off and the stacks open to allow for further cooling.

Two cyclones are used for each furnace. The purpose of the cyclones is to remove the coarser dust fraction from the off-gases. This reduces the overall dust load to the baghouse compartments and also minimizes damage to the steel shells due to erosion by coarser dust particles.

The off-gas is further treated in the baghouse to remove fine dust and produce a dust-free off-gas. The baghouses of furnaces 5 and 7 have 12 compartments, that for furnace 6 has 8 compartments, and furnaces 1 and 3 share a baghouse with 8 compartments. Each compartment consists of two dampers at the front (the main and re-inflate damper) and a single reverse damper at the back. The bag filters, which are open at the bottom and closed at the top, lie on the top of the compartment. In the compartment, filtration occurs first when the main and re-inflate dampers open to allow the dust-laden off-gas to enter the compartment. At this stage the reverse damper, which applies negative pressure, is closed. During filtration, dust enters the bottom part of the bag filters and is trapped, allowing clean gas to pass through; some of the dust falls to the bottom-most part of the compartment where the hoppers are stationed. Cleaning of the filter bags, which usually takes 30 seconds, follows filtration; in this stage both front dampers are closed while the reverse damper is opened to promote removal of the remaining adhering fine dust from the bag filters. In a filtration-cleaning sequence, only one compartment is offline for cleaning at a time while the remaining compartments are online for filtration.

The dust-free off-gas escapes to the atmosphere at a temperature of approximately 80°C. The gas is believed to consist largely of CO_2, as back-calculated from the carbon inputs to the furnace. Transalloys holds an atmospheric emission license from the Department of Environmental Affairs in terms of the Air Quality Act of 2004 (Act No. 39 of 2004).

The fine dust is directed by the pneumatic blower to the silo, from which it is collected by a truck two or three times a day, the average mass being 1.8 t per truck. Both the cyclone underflow and compartment dust are taken to the briquetting plant to serve as part of the briquette recipe.

Acknowledgements

This paper is published with the permission of Mintek and Transalloys.

References

ASTM Standards A483 / A483M - 10. 2010. Standard specification for silicomanganese. ASTM International, West Conshohocken, PA. pp. 1–2.

Barcza, N.A. and O'Shaughnessy, D.P. 1981. Optimum slag-alloy relationships for the production of medium- to low-carbon ferromanganese. *Canadian Metallurgical Quarterly*, vol. 20, no. 3. pp. 285–294.

Barker, I.J. de Waal, A., Rennie, M.S., and Klopper, J. 1991. The interaction effect in submerged-arc furnaces. *Proceedings of the 49th Electric Furnace Conference*, Warrendale, PA. The Iron & Steel Society of AIME.pp. 305–310.

Basson, J., Curr, T.R., and Gericke, W.A. 2007. South Africa's ferro alloys industry - present status and future outlook. *Proceedings of the 11th International Ferroalloys Congress (INFACON XI): Innovation in Ferroalloy Industry*, New Delhi, India, 18-21 February 2007. Indian Ferro Alloy Producers' Association. pp. 3–24.

Bezemer, K. 1995. The silicomanganese production process at Transalloys. *Proceedings of INFACON VII*, Trondheim, Norway, June 1995. FFF, Trondheim. pp. 573–580.

Brereton-Stiles, P., Rennie, M., and Moolman, R. 1999. Advanced power control strategy for submerged-arc furnaces. *Proceedings of the 57th Electric Furnace Conference Proceedings*. The Iron & Steel Society of AIME. pp. 167–175.

Chetty, D. 2008. A geometallurgical evaluation of the ores of the northern Kalahari manganese deposit, South Africa. PhD thesis, University of Johannesburg.

Chetty, D. and Gutzmer, J. 2008. Quantitative X-ray diffraction as a tool for smelting optimization of Kalahari manganese ores. *Proceedings of the Ninth International Congress on Applied Mineralogy*, Brisbane, Australia. Australian Insititute of Mining and Mettalurgy, Melbourne. pp. 419–427.

Ishitobi, T., Ichihara, K., and Homma, T. 2010. Operational improvements of a submerged arc furnace in Kashima works (KF-1) relined in 2006. *Proceedings of INFACON XII: Sustainable Future*, Helsinki, Finland. 6–9 June 2010. pp. 509–516. http://www.pyrometallurgy.co.za/InfaconXII/509-Ishitobi.pdf

Muller, J. and Steenkamp, J.D. 2013. An evaluation of thermochemical property models for CaO-MnO-SiO2-Al2O3-MgO slag. *Journal for Manufacturing Science and Production*, vol. 13, no. 4. pp. 251–262.

Steenkamp, J.D. 2014. Chemical wear of carbon-based refractory materials in a silicomanganese furnace tap-hole. PhD thesis, University of Pretoria.

Steenkamp, J.D., Pistorius, P.C., and Muller, J. 2016. Insights into the potential for reduced refractory wear in silicomanganese smelters. *Journal of the Southern African Institute of Mining and Metallurgy*, vol. 116, no. 1. pp. 101–108.

Steenkamp, J.D., Pistorius, P.C., and Tangstad, M. 2015. Chemical wear analysis of a tap-hole on a SiMn production furnace. *Journal of the Southern African Institute of Mining and Metallurgy*, vol. 115, no. 3. pp. 199–208. ◆

http://dx.doi.org/10.17159/2411-9717/2018/v118n3a14

Prediction of cuttability from rock cutting resistance

by V. Raghavan and Ch.S.N. Murthy

Synopsis

The objective of this investigation is to predict rock cuttability from measurements of rock cutting resistance (RCR) during the cutting process and to study the influence of mechanical properties on the depth of cut achieved. Point attack bits with angles of 45°, 50°, 55°, and 65° were used and the experiments were conducted at attack angles of 45°, 55°, and 65°, keeping the rotation speed constant while varying the cutting force and torque during cutting. The depth of each cut was measured and the cut material collected and weighed. The experimental data were compared using an artificial neural network (ANN) and finite element method (FEM) to predict RCR for the measured depth of cut. The results reveal that a 55° attack angle produced the optimum depth of cut.

Keywords

rock cuttability, rock properties, artificial neural network, finite element method, rock cutting resistance.

Introduction

Cutting machines such as shearers, roadheaders, and continuous miners are used extensively throughout the world for the excavation of rock in mining and civil operations. As theory relating to the mechanical excavation of rock has evolved over time, so too has the utilization of these machines, often substituting for traditional drill-and-blast methods, resulting in increased safety and performance and reduced operating costs.

The method by which these rock cutting machines work is influenced by a number of factors (Neil *et al.*, 1994). Machine design, machine power, intact rock properties, and rock mass properties all play a pivotal role in determining the efficiency of the rock cutting process (Karakas *et al.*, 2005). As Roxborough (1987) explained, the engineer has a choice over what size and type of machine to use for a particular excavation, but has no influence over the rock formation that will be encountered without changing the design criteria of the project. Since it is the rock mass, and not machine selection, that governs cuttability, an investigation into the rock mass properties and their effect on cuttability is warranted.

It has been well documented that a number of rock strength characteristics can adversely affect cutting performance (Rostami, 2011). There is an almost linear relationship between rock strength and cutting force required (Hood and Roxborough, 1992). Similarly, it has been found that abrasivity of rock tends to increase with rock strength (Jacobs and Hagan, 2009), and laboratory testing has focused on attempting to find which rock strength properties best describe this relationship. Specific energy is extensively used to evaluate rock cuttability (Tiryaki and Dikmen, 2006). It is a measure of the force required to excavate a unit volume of rock, and hence is a measure of the relative cuttability of a particular rock. McFeat-Smith and Fowell (1977), in their well-known study, correlated rock strength properties with specific energy and found that the cutting performance of cutting machines diminished with specific energy.

Recent studies have focused on an array of properties in an effort to estimate rock cuttability, with strong correlations found between the uniaxial compressive strength and specific energy for a number of different rock types (Speight, 1987). Material hardness, sonic velocity, Young's modulus, and other rock properties that indirectly relate to rock strength have been correlated with specific energy, with varying degrees of statistical significance. To date, however, the most reliable indicator of cuttability has been based on the uniaxial compressive strength of rock.

From a mining perspective, further investigations to confirm the validity and correlation between rock strength parameters and cuttability would be useful in the estimation of machine performance. The ability to predict cutting performance from direct and

* *Department of Mining Engineering, National Institute of Technology Karnataka, Surathkal, India.*

 ISSN 2225-6253. Paper received Jun. 2017; revised paper received Dec. 2017.

indirect rock strength measurements would be of potential benefit to the industry, especially for mining operations interested in assessing the relative cuttability of rock. The purpose of this paper is to develop a method to predict the rock cutting resistance and influence of rock strength of samples tested in the laboratory.

Literature survey

Various procedures, processes, and phenomena treated in science and engineering are often described in terms of differential equations formulated by using their continuum mechanics models. Solving differential equations under various conditions such as boundary or initial conditions leads to the understanding of the phenomena and can predict their future state. However, exact solutions for differential equations are generally difficult to obtain. So, numerical methods are adopted to obtain approximate solutions for differential equations. Among these numerical methods, those that approximate continuation with an infinite degree of freedom by a discrete body with finite degree of freedom are called 'discrete analysis' (Stolarski *et al.*, 2006).

Modelling is a useful tool for engineering design and analysis. The definition of modelling may vary depending on the application, but the basic concept remains the same: the process of solving physical problems by appropriate simplification of reality. In engineering, modelling is divided into two major categories: physical/empirical modelling and theoretical/analytical modelling. Laboratory and *in situ* model tests are examples of physical modelling, from which engineers and scientists obtain useful information to develop empirical or semi-empirical algorithms for tangible application. With the increase in computational speed and power, many numerical models and software programs have been developed for various engineering practices.

The finite element method (FEM) requires the division of the problem domain into a collection of elements of smaller sizes and standard shapes (triangle, quadrilateral, tetrahedral, *etc.*) with a fixed number of nodes at the vertices and/or on the sides. The trial functions, usually polynomial, are used to approximate the behaviour of partial differential equations at the element level and generate the local algebraic equations representing the behaviour of the elements. The local elemental equations are then assembled, according to the topological relations between the nodes and elements, into a global system of algebraic equations whose solution then produces the required information in the solution domain, after imposing the properly defined initial and boundary conditions. The FEM is perhaps the most widely applied numerical method in engineering today because of its flexibility in handling material heterogeneity, nonlinearity, and boundary conditions, with many well-developed and verified commercial codes with large capacities in terms of computing power, material complexity, and user-friendliness. Due to the interior discretization, the finite domain method (FDM) and FEM cannot simulate infinitely large domains (as are sometimes presented in rock engineering problems, such as half-plane or half-space problems) and the efficiency of the FDM and FEM will decrease with too high a number of degrees of freedom, which are in general proportional to the numbers of nodes (Jing, 2003).

The FEM has been used by Wang (1976), Tang (1997), Kou *et al.* (1999) and Liu (2002) to simulate fracture propagation during rock indentation or rock cutting. Generally, these models used a stress-based criterion to form cracks normal to the maximum principal stress (tensile stresses are taken as positive) at the element integration points. Failure occurs if the maximum tensile stress exceeds the specified fracture strength. In compression, the models utilized a Mohr-Coulomb failure criterion to form shear cracks at the element integration points. After the cracks have formed, the strains normal to both the tensile and shear cracks are monitored in subsequent time/load steps to determine if the cracks are open or closed. If a crack is open, the normal and shear stresses on the crack face are set equal to zero for a tensile crack.

Wang (1975) developed a general mathematical rock failure model by applying the available finite element technique to established computer code, which allows simulation of the sequence of penetration mechanisms and provides a better description of the failure phases such as initial cracking, crushing, and chipping. Wang (1975) also used the 'stress transfer' method suggested by Zienkiewicz (1968) to convert excessive stresses that an element cannot bear to nodal loads and reapply these nodal loads to the element nodes, and thereby to the system. If a crack is closed, a compressive normal stress can be carried, but the shear stress is limited to a value described by the Coulomb friction model. The analytical results presented in the studies conducted by Wang (1975) show reasonable agreement with experimental observations.

Numerical analysis of the wedge indentation problem was conducted by Huang *et al.* (1997) using the FLAC software. The numerical analysis indicated that the location of maximum tensile stress (interpreted as the point of crack initiation) moves away from the indentation axis as the lateral confinement increases. They found that a small increase in the confining stress from zero induces a large increase in the inclination of this point on the indentation axis. However, the confinement does not significantly reduce the maximum tensile stress and it hardly influences the indentation pressure.

Carpinteri, Chiaia, and Invernizzi (2004) conducted indentation tests on brittle and quasi-brittle materials and obtained fracture patterns in homogeneous brittle solids by FEM in the framework of linear elastic fracture mechanics. Microstructural heterogeneities were taken into account by the lattice model simulation. Although reality is often much more complex than the theoretical models applied, the study provides interesting indications for improving the performance of cutting tools. The FRANC2D software, developed at Cornell University, was used to simulate fracture in the homogeneous case. This software is able to simulate plane stress, plane strain, as well as axis-symmetric crack propagation in the framework of linear elastic fracture mechanics (LEFM). Carpinteri, Chiaia, and Invernizzi concluded that the cutting performances could be significantly improved by reducing the crushing component and enhancing the chipping ability of the indenters (*e.g.* by increasing their size or depth of penetration).

Liu *et al.* (2002) simulated the rock fragmentation processes induced by single and double truncated indenters

by the rock and tools interaction code, R-T2D, based on the Rock Failure Process Analysis (RFPA) model. The simulated crack patterns were in good agreement with indentation experiments and a better understanding was gained. From the simulated results, a simple description and qualitative model of the rock fragmentation process induced by truncated indenters was developed. The simulated results reproduced the propagation, interaction, and coalescence process of side cracks induced by the two indenters, and the formation of large rock chips. The authors pointed out that the simultaneous loading of the rock surface by multiple indenters seems to provide a possibility of forming larger rock chips, controlling the direction of subsurface cracks, and consuming a minimum total specific energy.

Wang *et al.* (2011) examined the rock fragmentation processes induced by double drill bits subjected to static and dynamic loading by a numerical method. Micro-heterogeneities of the rock are taken into account in this numerical model. For the static case, the simulated results reproduced the progressive process of brittle rock fragmentation during indentation. For the dynamic case, numerical simulations represented radial cracks, incipient chips, pulverized zones, and shell cracks. A comparison of the static and dynamic cases showed that dynamic loading can lead to more efficient rock fragmentation. In addition, the numerical results indicated that the dynamic pressure (P_{max}) plays an important role in the failure of specimens when two indenters are used. Furthermore, the heterogeneity of the rock can also affect the failure modes of the rock when two indenters are used. Finally, the numerical results demonstrated the effect of the spacing between the indenters on the rock. The numerical code RFPA2D (Rock Failure Process Analysis, 2D) (Zhu and Tang, 2006) was used to consider the heterogeneity of rock and simulate the evolution of dynamic fracture initiation and propagation due to impact loading from double indenters.

Saksala *et al.* (2013) simulated dynamic indentation with a numerical method. The method was validated by dynamic indentation experiments with single and triple indenters on Kuru granite. The simulation method included a constitutive model for rock and a model, implemented in FEM, to simulate the dynamic bit-rock interaction. The constitutive model, being a combined visco-plastic damage model, accommodated the strong strain-rate dependency of rock via visco-plastic hardening/softening laws both in tension and compression. The authors carried out indentation experiments with single- and triple-button indenters using a set-up similar to percussive drilling. Despite the continuum approach, the model can capture the salient features of the dynamic bit-rock interaction involved in dynamic indentation and applications alike. The authors concluded that a fairly good agreement existed between the simulated and experimental results, and that the model could be a useful tool in, *e.g.* percussive drill design.

Sulem *et al.* (2002) carried out numerical analysis of the indentation test. They modelled rock as an elasto-plastic medium with Cosserat microstructure and consequently possessing an internal length. The response of the indentation curve to various sizes of indenter as compared to the internal length of the rock was studied in order to assess the scale effect. Using finite element numerical simulations, they concluded that for a material with a Cosserat microstructure, the apparent strength and rigidity increase as the size of the indenter decreases. This scale effect for the strength can reach 15% for a statistical model and 50% for a kinematical Cosserat model when the size of the indenter tool is comparable to the grain size of the rock. The authors concluded that this scale effect is not significantly affected by the condition at the rock-tool interface, and a similar scale effect has been observed experimentally for metals, and ascribed that to the lack of relevant quantitative experimental data for the scale effect in the case of rocks. They suggested that this effect may be important and should be investigated further. The indentation tests constitute an experimental tool for the testing and validation of continuum theories with microstructure and calibration of internal length parameters.

Mechanical properties of rocks tested

The coal and sandstone blocks were collected from Ramagundem Area I, the SCCL, Telangana state. Limestone and dolomite blocks were collected from Chaitanya Industries, JK Cement, Mudhapur, Bagalkot, Karnataka, and also from Andhra Pradesh. Core sample were prepared and tested in the rock mechanics laboratory, Department of Mining Engineering, NITK as per the ISRM standards. The mechanical properties tested were uniaxial compressive strength, Brazilian tensile strength, elasticity modulus, and density. Three readings were taken for each test and averaged – the results are listed in Table I.

Density

Trimmed core samples were used in the determination of natural density. The specimen volume was calculated from an average of several caliper readings and the weight of specimen determined using a sensitive balance. The density was calculated using the following formula: density (g/m^3) = mass of the sample/volume of sample.

Uniaxial compressive strength

Uniaxial compressive strength tests were performed on core samples 54 mm in diameter and with a length-to-diameter ratio of 2.5. The stress rate was applied within the range of 0.5–1.0 MPa/s. Load was applied continuously until failure occurred, and the maximum load (in kN) at failure recorded. The UCS of the specimen was calculated by dividing the maximum load carried by the specimen during the test by the original cross-sectional area.

Brazilian tensile strength

Brazilian tensile strength tests were conducted on core samples with a diameter of 54 mm and a length-to diameter ratio of unity. The tensile load on the specimen was applied continuously at a constant stress rate of 200 N/s, such that failure would occur within 5 mm of displacement, until the sample failed. The maximum load (in kN) at failure was recorded. The BTS of the specimen was calculated by dividing the maximum load applied to the specimen by the original cross-sectional area.

Young's modulus

Young's modulus was measured at a stress level equal to 50% of the ultimate uniaxial compressive strength. Loads

Table I

Mechanical properties of samples

Sample	Density (gm/m^3)	σ_c (MPa)	σ_t (MPa)	*E* (GPa)
Coal 1	1.41	14.2	1.4	2.65
Coal 2	1.48	23.4	2.4	2.68
Sand Stone 1	1.92	14.1	1.4	6.8
Sand Stone 2	1.94	18.3	1.8	7.2
Sand Stone 3	1.95	24.2	2.5	9
Lime Stone 1	1.99	46.8	4.4	9.8
Lime stone 2	2.2	58.6	5.6	12.3
Lime Stone 3	2.69	69.7	6.8	12.4
Lime Stone 4	2.7	70.3	7.1	15.1
Dolomite 1	2.5	44.4	4.2	29
Dolomite 2	2.5	71.2	7.2	30.2

and axial deformations were recorded at evenly spaced load intervals during the test. Ten readings were taken over the load range to define the axial stress-strain curves. Then, the Young's modulus of the specimen was calculated by dividing the ratio of the axial stress change to axial strain produced by the stress change.

Description of rock cutting machine

The rock cutting machine (Figure 1) was constructed to study the influence of cutting parameters like thrust, torque, and rotational speed on the cutting process.

The machine is mounted on a rectangular 1.524 m × 1.066 m frame with four legs that are mounted on wheels for easy manoeuvering capability. The legs are 0.9738 m in height and are made of a hollow pipe rock into which a 0.0508 m pipe is attached to support the frames. A 2 horsepower motor is attached to a shaft pulley by a belt drive. The cutter head is attached to the shaft by a flange. The cutter head consists of a drum 15.24 cm in diameter, 10 cm in length, and with 12 bits mounted at a span of 8 cm and placed in a spiral configuration. The sample holder is connected to a hydraulic cylinder, which can provide sideways movement during cutting operation, and a material collecting bin. The block holder can accommodate a block of 0.3 × 0.3 × 0.45 m in dimension, which is twice the size of the cutting drum.

In laboratory rock cutting, the rotational speed is varied from 225 to 350 r/min, and the thrust from 1.3 to 2.1 kN. During cutting, the cutting force and torque are measured by the cutting tool dynamometer, which is calibrated in the rock mechanics laboratory. The dynamometer is model no. 111285, manufactured by Industrial Engineering Instruments Company (IEICOS), Bangalore, and has specifications force, 5000 N; torque, 50 Nm; speed, 1000 r/min. For each rotational speed and thrust combination, cutting was done for 60 seconds and cutting depth was measured using a vernier caliper. The rocks in the laboratory experiments comprised two types of coal, three types of sandstone, four types of limestone, and two types of dolomite. Despite the sandstone, limestone, and dolomite having different properties from coal, it was found in the experiments that coal offered more resistance to cutting than the rocks, and the rocks were cut, more easily than the coal.

For each combination of rotational speed and thrust, the rock fragments produced were collected and weighed to calculate the specific energy. Attack angles of 45°, 55°, and 65° (the attack angle is the angle between the axis of the tool and the rock) were used. A 60° attack angle was not considered because the performance was found to be same as with a 55° attack angle. For each attack angle, four bit angles – 45°, 50°, 55°, and 65° (the bit angle is the clearance angle given for removal of material in the form of chips) were tested. The influence of wear on cutting rate and specific energy was investigated by conducting experiments with a cutting tool that had been subjected to 5 mm of wear. All the above tests were carried out using all bit-rock combinations, rotational speeds, and thrust settings. The results are shown in Figures 2–9.

Figure 1—Rock cutting machine

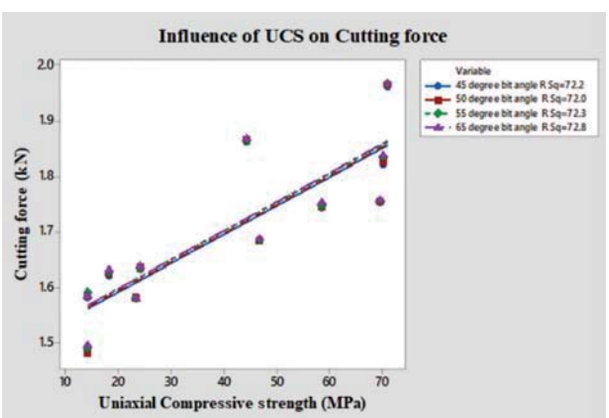

Figure 2—Influence of compressive strength on cutting force for 45° attack angle

Artificial neural network (ANN)

Artificial neural networks have many useful properties and are widely employed in mining and tunnelling applications. The feed-forward back--propagation network was chosen to build a predictive model for cutting force and specific energy in this study. The input layer contained thirteen variables (density, UCS, BTS, Young's modulus, Poisson's ratio, rotational speed, attack angle, bit angle, cutting force, depth of cut, torque, volume broken, and cutting rate) corresponding to the predictors in the model. The single

Prediction of cuttability from rock cutting resistance

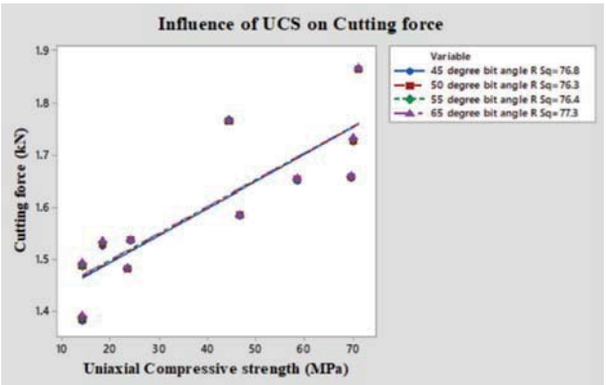

Figure 3—Influence of compressive strength on cutting force for 55° attack angle

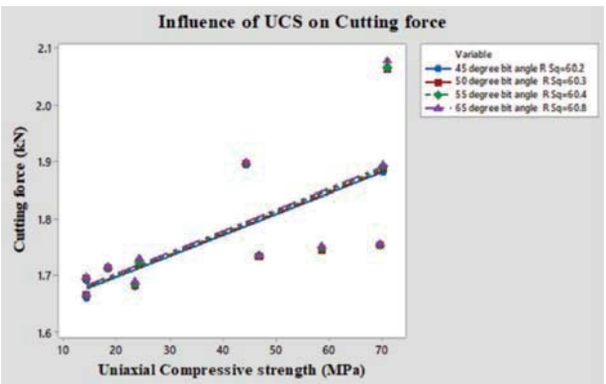

Figure 4—Influence of compressive strength on cutting force for 65° attack angle

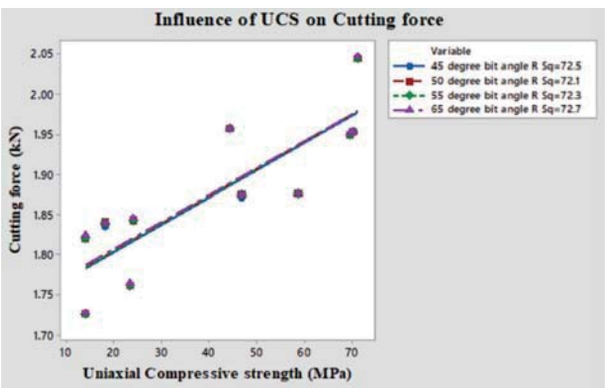

Figure 5—Influence of compressive strength on cutting force for 45° attack angle with 5 mm wear (for all bits)

hidden layer had tangent sigmoid transfer function neurons. The output layer has one pure linear neuron corresponding to cutting force and specific energy. The number of hidden neurons was selected as 16. This architecture is known as a useful neural network structure for function approximation or regression problems.

Before implementing the ANN, the data-set was divided into training (70%), validation (15%), and test (15%) subsets. The sets were picked randomly throughout the data-set. The ANN was built, trained, and implemented with the MATLAB neural network toolbox using the Levenberg-Marquardt (*trainlm*) algorithm for back-propagation.

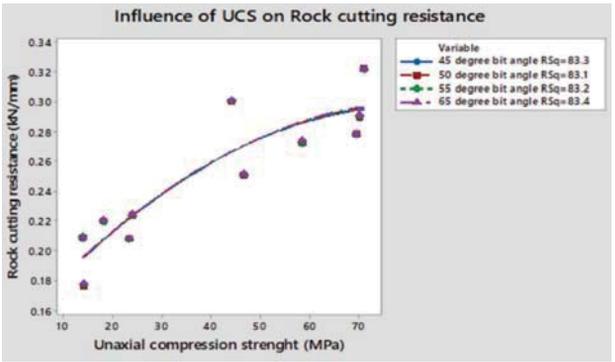

Figure 6—Influence of compressive strength on rock cutting resistance for 45° attack angle

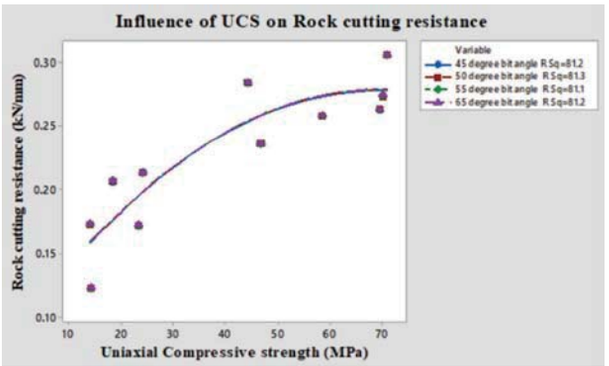

Figure 7—Influence of compressive strength on rock cutting resistance for 55° attack angle

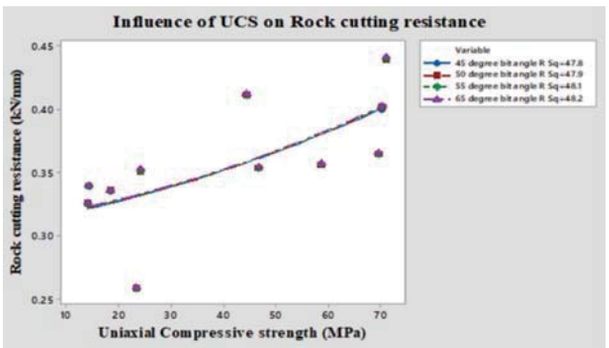

Figure 8—Influence of compressive strength on rock cutting resistance for 65° attack angle

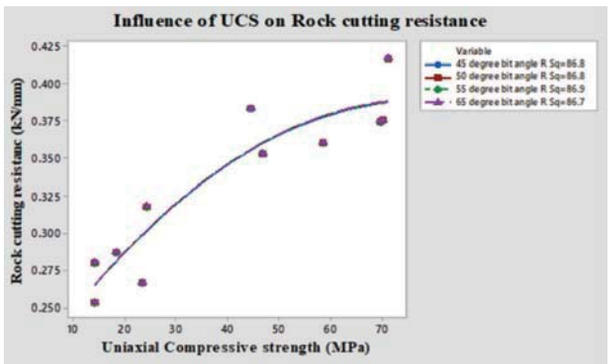

Figure 9—Influence of compressive strength on rock cutting resistance at 45° attack angle with 5 mm wear for all bits

Prediction of cuttability from rock cutting resistance

Network errors for the neural network model of depth of cut were measured to check the progress of training. The results for the model were reasonable, since the test set errors and the validation set errors had similar characteristics, and no significant over-fitting occurred. The network responses were also analysed for the neural network model. After unnormal the network outputs, the entire data-set was put through the network and linear regression performed between the network outputs and the corresponding targets for depth of cut. Figures 10 to 13 show the rock cutting resistance predicted by ANN. The neural network model predicted depths of cut very close to those measured and calculated expressed by an R^2 value of more than 99% for a 55° attack angle.

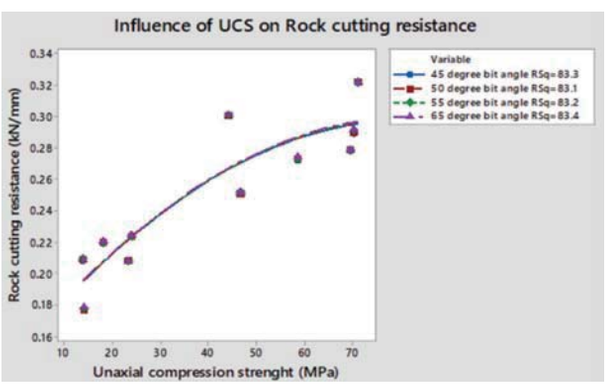

Figure 10—Influence of compressive strength on rock cutting resistance for 45° attack angle

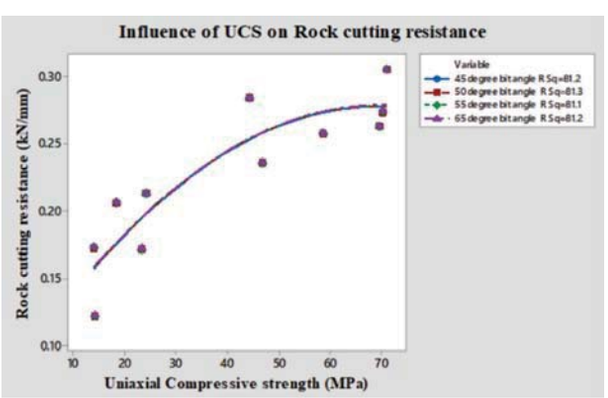

Figure 11—Influence of compressive strength on rock cutting resistance for 55° attack angle

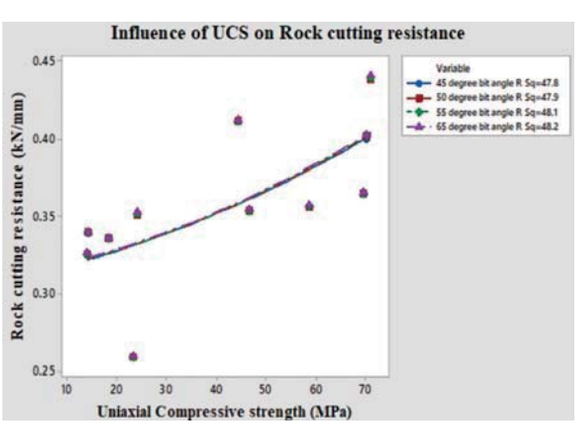

Figure 12—Influence of compressive strength on rock cutting resistance for 65° attack angle

Depth of cut prediction by FEM

Rock was considered as a homogenous, isotropic, and linear elastic medium in order to simplify the analysis. Because of the experimental difficulties in establishing nonlinear behaviour in the three mutually perpendicular directions, even though a nonlinear analysis programme is available in ANSYS, the present work was limited to elastic analysis.

The dimensions of the block were 0.3 × 0.3 × 0.45 m and the material properties included Young's modulus, Poisson's ratio, and rock density. Meshing was done, then the load was applied to determine the depth of cut of the rock, loading at the contact plane between the bit and the rock. The relationship between depth of cut and force applied is shown in Figures 14 to 24. Figures 25 to 28 show the influence of UCS of the rock on the cutting resistance.

Results and discussions

Whatever the combined action of cutting parameters that is transmitted through the cutting bits onto the rock, it will be met with resistance offered by the rock. This has been represented in this alternative concept as rock cutting resistance (RCR), which is defined as the force required to achieve a unit depth of cut, and is expressed in kN/mm. In the present investigation, four rock types (coal, sandstone, limestone, and dolomite).were subjected to point attack with

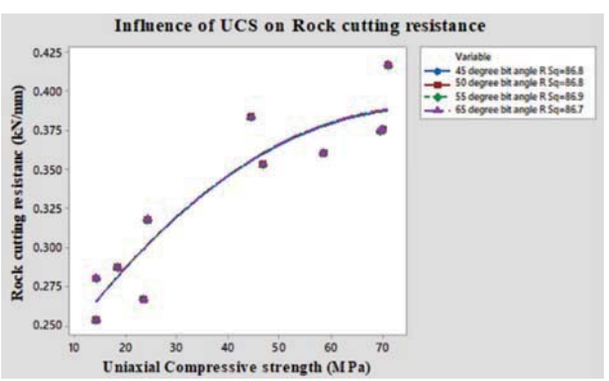

Figure 13—Influence of compressive strength on rock cutting resistance for 45° attack angle with 5 mm wear for all bits

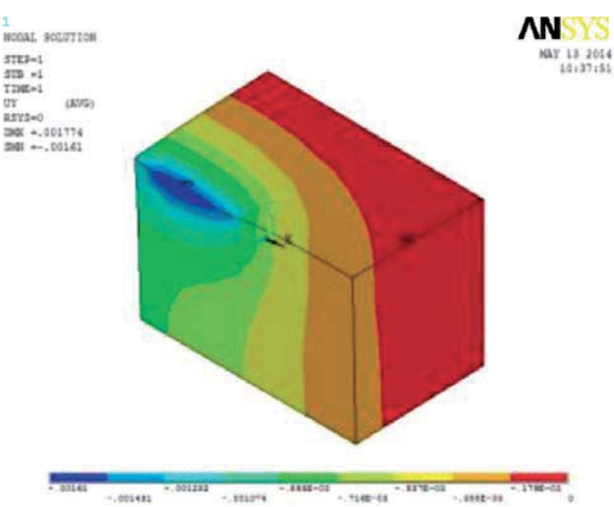

Figure14—Relationship between depth of cut and force applied: coal 1

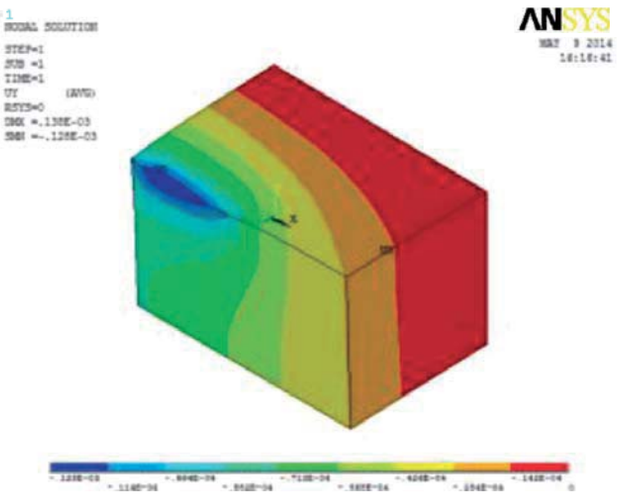

Figure 15—Relationship between depth of cut and force applied: coal 2

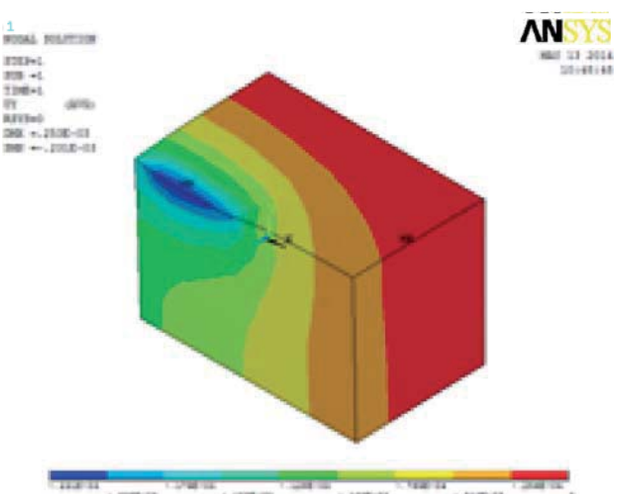

Figure 16—Relationship between depth of cut and force applied: sandstone 1

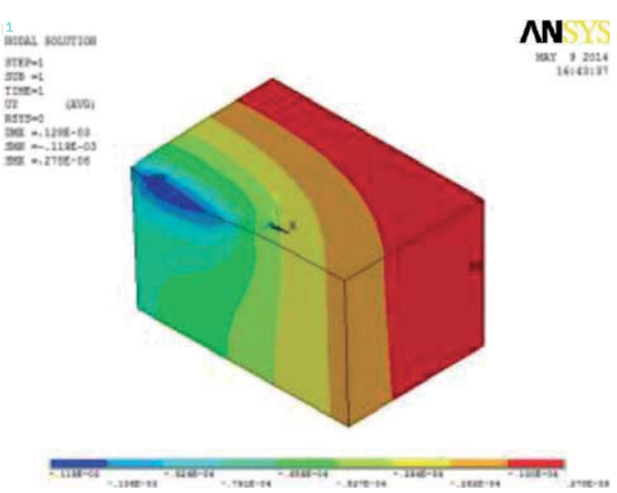

Figure 17—Relationship between depth of cut and force applied: sandstone 2

bits of 45°, 50°, 55°, and 65° bit angles at 45°, 55°, and 65° attack angles, and at 45° attack angle with 5 mm wear on all bits.

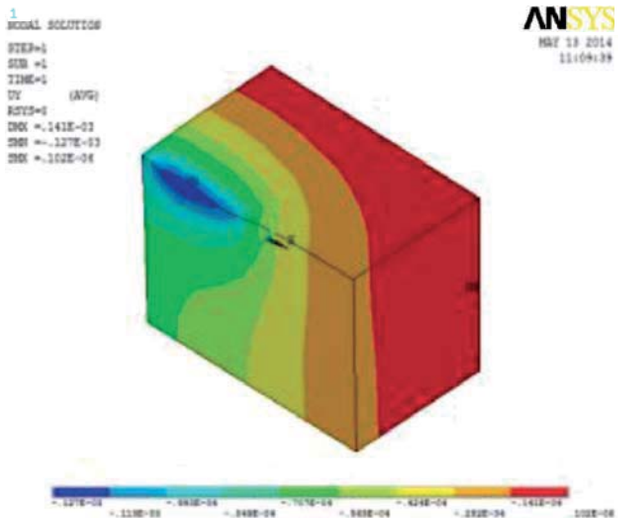

Figure 18—Relationship between depth of cut and force applied: sand stone 3

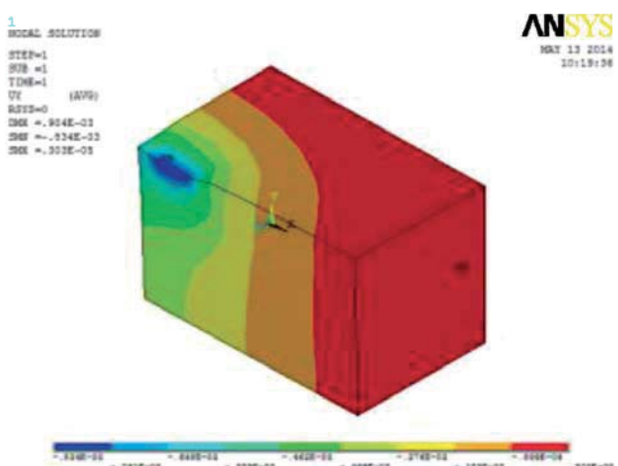

Figure 19—Relationship between depth of cut and force applied: limestone 1

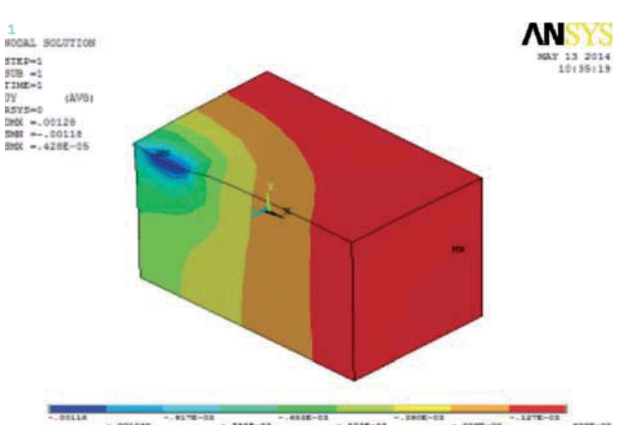

Figure 20—Relationship between depth of cut and force applied: limestone 2

The RCR from the FEM analysis is lower than the values predicted by ANN and those obtained experimentally. In case of FEM analysis, the RCR values are for the ideal rock conditions (isotropic, uniform, homogeneous, linear elastic

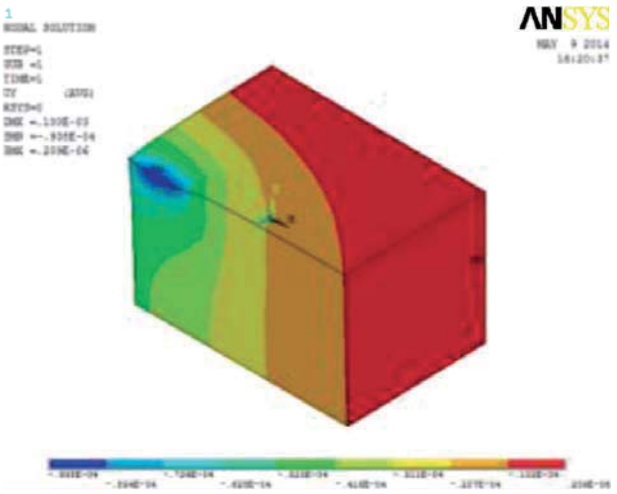

Figure 21—Relationship between depth of cut and force applied: limestone 3

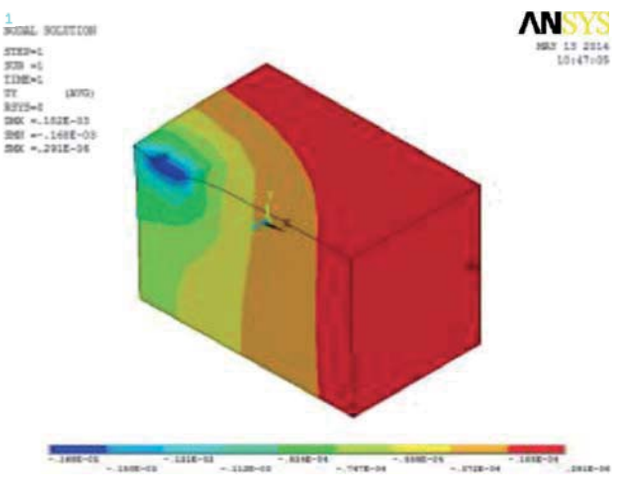

Figure 22—Relationship between depth of cut and force applied: limestone 4

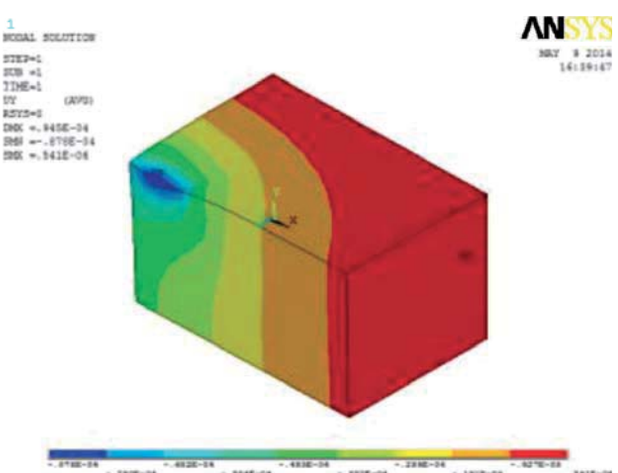

Figure 23—Relationship between depth of cut and force applied: dolomite 1

and devoid of any form of discontinuities), hence the depth of cut achieved was greater than with other two methods, and consequently the RCR values were the lowest.

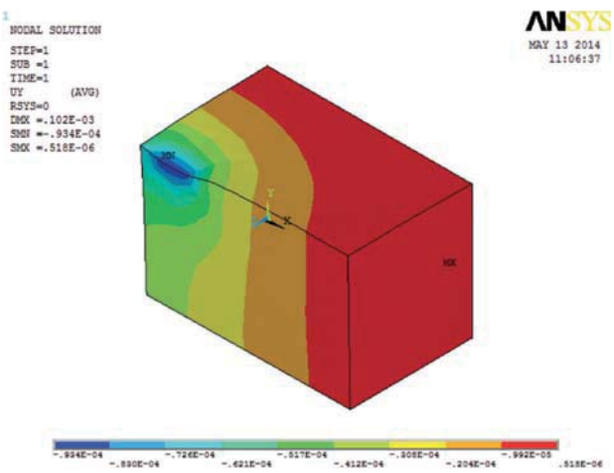

Figure 24—Relationship between depth of cut and force applied: dolomite 2

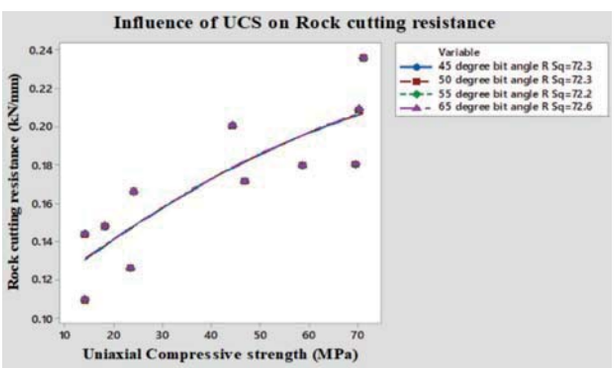

Figure 25—Influence of compressive strength on rock cutting resistance for 45° attack angle

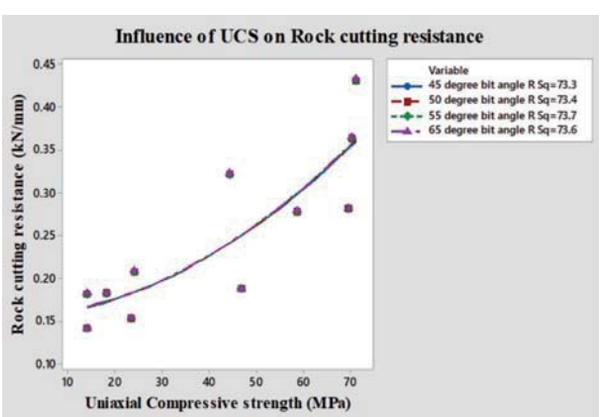

Figure 26—Influence of compressive strength on rock cutting resistance for 55° attack angle

The RCR values were correlated with the depth of cut as obtained from the laboratory rock cutting experiments for different cutting force values. It is observed that the depth of cut decreases linearly with increasing RCR. However, the rate of decrease in the depth of cut is less at higher cutting forces. The trend is similar irrespective of the method (FEM, ANN, or RCM) employed for determining the RCR.

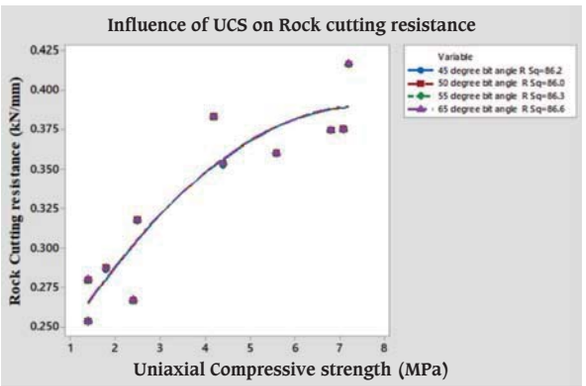

Figure 27—Influence of compressive strength on rock cutting resistance for 65° attack angle

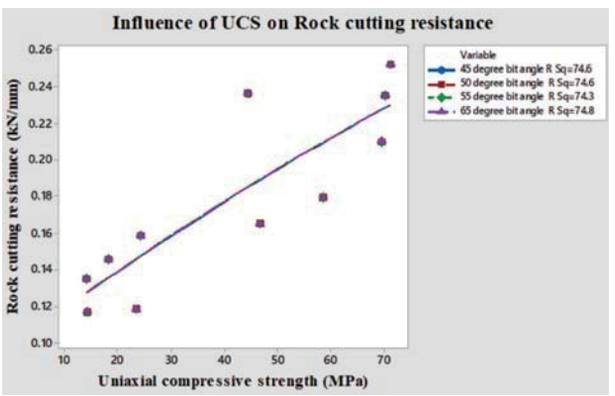

Figure 28—Influence of compressive strength on rock cutting resistance for 45° attack angle with 5 mm wear for all bits

In order to establish the suitability of the concept of RCR, its dependence on the various rock properties has been presented. It is observed that, irrespective of the method used for determining RCR, the RCR increases linearly with an increase in all five rock properties considered in the investigation. It is observed that the 45°, 65°, and 45° bit angles with 5 mm of wear and at 45° attack angle, the RCR, is much greater than at 55° attack angle. Both FEM and RCM experimental investigations indicate that a 55° attack angle offers more resistance to cutting.

Conclusion

1. The best results were obtained with a 65° tip angle and 55° attack angle.
2. The R^2 value predicted by ANN for depth of cut at 55° attack angle is more than 99%, which is less than the experimental value. Both the depth of cut and material cut increase with the specific energy.
3. The R^2 values predicted by ANN for cutting force and depth of cut at 45°attack angle is 95%, and at 65° attack angle is less than 90%.
4. The R^2 value predicted by FEM for depth of cut at 45°attack angle is 95%, and at 65° attack angle is less than 90%.
5. The cutting rate decreases with increasing compressive strength. The maximum cutting rate achieved is at an attack angle of 55°.
6. Even though only a limited variety of rocks were tested in this investigation, the results are encouraging. It is suggested that further investigations be carried in this direction once the mechanical properties of the rocks (like density, UCS, UTS, Young's modulus, and Poisson's ratio) are available, to establish the RCR for different bit-rock interactions. Once this data is available, the depth of cut in rock cutting can be reasonably predicted from the RCR of a particular bit-rock combination, instead of using complicated test procedures to evaluate the cuttability of rocks without actual rock cutting tests.

References

Brown, ET. 1981. Suggested methods for determining the uniaxial compressive strength and deformability of rock materials. *Rock Characterisation Testing and Monitoring – ISRM Suggested Methods*. Pergamon Press.

Carpinteri, A., Chiaia, B., and Invernizzi, S. 2004. Numerical analysis of indentation fracture in quasi-brittle materials. *Engineering Fracture Mechanics*, vol. 71, no. 4. pp.567–577.

Hagan, P. 1990. Some aspects of the application of high pressure water jets to rock cutting. PhD thesis, University of New South Wales.

Hood, M.C. and Roxborough, F. 1992. Rock breakage: mechanical. *SME Mining Engineering Handbook*. Hartman, H.L. (ed.). Society for Mining, Metallurgy and Exploration, Littleton, CO. pp 680-721

Jacobs, N. and Hagan, P. 2009. The effect of stylus hardness and some test parameters on the Cerchar Abrasivity Index. *Proceedings of the 43rd US Rock Mechanics Symposium*, Asheville, NC. American Rock Mechanics Association, Alexandria, VA.

Jing, L.A. 2003. A review of techniques advances and outstanding issues in numerical modelling for rock mechanics and rock engineering. *International Journal of Rock Mechanics and Mining Sciences*, vol. 40. pp. 283–353.

Karakas, A.R, Bilgin, N., Tumac, D., Feridunoglu, C., and Akgul, M. 2005. The performance of a roadheader in high strength rock formations in Küçüksu tunnel. *Proceedings of the International World Tunnel Congress and the 31st ITA General Assembly*, Istanbul. International Tunnelling Association.

Kou, S., Lindqvist, P.A., Tang, C., and Xu, X. 1999. Numerical simulation of the cutting of inhomogeneous rocks. *International Journal of Rock Mechanics and Mining Sciences*, vol. 36, no. 5. pp. 711–717.

McFeat-Smith, I. and Fowell, R. 1977. Correlation of rock properties and the cutting performance of tunnelling machines. *Proceedings of Rock Engineering*, University of Newcastle upon Tyne. British Geotechnical Society. pp. 581–602

Neil, D.M., Rostami, J., Ozdemir, L., and Gertsch, R. 1994. Production Estimating Techniques for New Mexico. *SME*, New York. pp. 1–7.

Rostami, J. 2011. Mechanical rock breaking. *SME Mining Engineering Handbook*. Darling, P. (ed.). Society for Mining, Metallurgy and Exploration, Littleton, CO. pp. 415–434.

Roxborough, F.F. 1987. The role of some basic rock properties in assessing cuttability. *Proceedings of the Seminar on Tunnels: Wholly Engineered Structures*, Sydney, Australia. The Institute of Engineers Australia and AFCC.

Saksala, T., Gomon, D., Hokka, M., and Kuokkala, V.T. 2013. Numerical modeling and experimentation of dynamic indentation with single and triple indenters on Kuru granite. *Rock Dynamics and Applications – State of the Art*. Zhao, J. and Li, J. (eds.). Taylor & Francis. pp. 415–421.

Speight, H.E. 1987. The application of drag pick rock cutting machines. in *Proceedings of the Conference on Equipment in the Minerals Industry: Exploration, Mining and Processing*, Kalgoorlie, Western Australia. *Metalliferous Mining*. Australasian Institute of Mining and Metallurgy, Melbourne. pp. 137–147

Tang, C.A. 1997. Numerical simulation of progressive rock failure and associated seismicity. *International Journal of Rock Mechanics and Mining Sciences*, vol. 34. pp. 249–262.

Tiryaki, B. and Dikmen, A.C. 2006. Effects of rock properties on specific cutting energy in linear cutting of sandstones by picks. *Rock Mechanics and Rock Engineering*, vol. 39, no. 2. pp. 89–120.

Wang, J.K. 1976. Bit penetration into rock - A finite element study. *International Journal of Rock Mechanics and Mining Sciences*, vol. 13. pp. 11–16.

Zienkiewicz, O.C. 1968. Continuum mechanics as an approach to rock mass problems. *Rock Mechanics in Engineering Practice*. Stagg, K.G .and Zienkiewicz, O.C.(eds.). Wiley. Chapter 8, pp. 237–-73.

Zienkiewicz, O.C. 1968. The Finite Element Method. McGraw-Hill, London. ◆

MINESAFE 2018

Striving for Zero Harm

Driving Excellence through Compliance

Gallagher Convention Centre,
Johannesburg

Technical Conference and Industry day

29–30 August 2018—Conference
31 August 2018—Industry Awards Day

WHO SHOULD ATTEND

The conference should be of value to:

- Safety practitioners
- Mine management
- Mine health and safety officials
- Engineering managers
- Underground production supervisors
- Surface production supervisors
- Environmental scientists
- Minimizing of waste
- Operations manager
- Processing manager
- Contractors (mining)
- Including mining consultants, suppliers and manufacturers
- Education and training
- Energy solving projects
- Water solving projects
- Unions
- Academics and students
- DMR.

OBJECTIVES

The conference will focus on improving health, safety and the environmental impact in the mining and metallurgy industry and highlight actions to be taken. It will act as a platform for learning and allow people to share ideas on safety, health and the environment as well as local communities relationship (issues).

This conference aims to bring together management, DMR, Chamber of Mines, Unions and health and safety practitioners at all levels from the industry to share best practice and successful strategies for zero harm and a value-based approach to health and safety. It will address the main challenges in the mining industry such as logistics, energy and safety of employees, contractors and the communities.

SPONSORSHIP

Sponsorship opportunities are available. Companies wishing to sponsor or exhibit should contact the Conference Co-ordinator.

SAIMM
THE SOUTHERN AFRICAN INSTITUTE OF MINING AND METALLURGY

MMMA

SUPPORTED BY:

CHAMBER OF MINES of South Africa

Mine Health & Safety Council
MHSC

mineral resources
Department:
Mineral Resources
REPUBLIC OF SOUTH AFRICA

NUM
National Union of Mine Workers

UASA
THE UNION

SOLIDARITEIT
SOLIDARITY

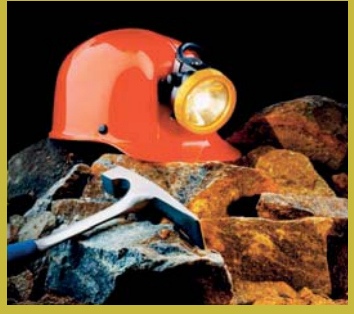

For further information contact:
Head of Conferencing
Camielah Jardine, SAIMM,
Tel: +27 11 834-1273/7
Fax: +27 11 833-8156 or +27 11 838-5923
E-mail: camielah@saimm.co.za
Website: http://www.saimm.co.za

Conference Announcement

NATIONAL & INTERNATIONAL ACTIVITIES

2018

12–14 March 2018 — **Society of Mining Professors 6th Regional Conference 2018**
'*Overcoming challenges in the Mining Industry through sustainable mining practices*'
Birchwood Hotel and Conference Centre, Johannesburg, South Africa
Contact: Camielah Jardine
Tel: +27 11 834-1273/7, Fax: +27 11 838-5923/833-8156
E-mail: camielah@saimm.co.za, Website: http://www.saimm.co.za

23–26 April 2018—**Application of Multiple Point Statistics to Mineral Resource Estimation—School**
School of Mining Engineering at the University of the Witwatersrand
Contact: Yolanda Ndimande
Tel: +27 11 834-1273/7, Fax: +27 11 838-5923/833-8156
E-mail: yolanda@saimm.co.za, Website: http://www.saimm.co.za

15 May 2018 — **Micro TBM Tunnelling coming to the fore in South Africa Seminar 2018**
The Wits Club, University of the Witwatersrand, Johannesburg
Contact: Yolanda Ndimande
Tel: +27 11 834-1273/7, Fax: +27 11 838-5923/833-8156
E-mail: yolanda@saimm.co.za, Website: http://www.saimm.co.za

6–7 June 2018 — **Digitalization in Mining Conference**
'*Mining business make-over –Exploiting the digital resolution*'
Focus Rooms, The Core, Sunninghill, Sandton
Contact: Yolanda Ndimande
Tel: +27 11 834-1273/7, Fax: +27 11 838-5923/833-8156
E-mail: yolanda@saimm.co.za, Website: http://www.saimm.co.za

11–14 June 2018 — **SAIMM: Diamonds — Source to Use 2018 Conference** *'Thriving in Changing Times'*
Birchwood Conference Centre (Jet Park)
Contact: Camielah Jardine
Tel: +27 11 834-1273/7, Fax: +27 11 838-5923/833-8156
E-mail: camielah@saimm.co.za, Website: http://www.saimm.co.za

9–12 July 2018 — **Copper Cobalt Africa in association with The 9th Southern African Base Metals Conference**
Avani Victoria Falls Resort, Livingstone, Zambia
Contact: Camielah Jardine
Tel: +27 11 834-1273/7, Fax: +27 11 838-5923/833-8156
E-mail: camielah@saimm.co.za, Website: http://www.saimm.co.za

30–31 July 2018 — **Introduction to Process Engineering School 2018 Volume 1**
Birchwood Hotel & OR Tambo Conference Centre
Contact: Yolanda Ndimande
Tel: +27 11 834-1273/7, Fax: +27 11 838-5923/833-8156
E-mail: yolanda@saimm.co.za, Website: http://www.saimm.co.za

6–8 August 2018—**Geometallurgy Conference 2018**
Lagoon Beach Conference Venue, Cape Town, South Africa
Contact: Camielah Jardine
Tel: +27 11 834-1273/7, Fax: +27 11 838-5923/833-8156
E-mail: camielah@saimm.co.za, Website: http://www.saimm.co.za

15–16 August 2018 — **The SAMREC and SAMVAL CODES**
'*Advanced Workshop: Can you face your peers?*'
Birchwood Hotel and Conference Centre, Johannesburg, South Africa
Contact: Yolanda Ndimande
Tel: +27 11 834-1273/7, Fax: +27 11 838-5923/833-8156
E-mail: yolanda@saimm.co.za, Website: http://www.saimm.co.za

10–11 September 2018 — **ASM Conference 2018**
'Fostering a regional approach to ASM transformation in sub-Saharan Africa'
Nasrec, Johannesburg (Electra Mining)
Contact: Yolanda Ndimande
Tel: +27 11 834-1273/7, Fax: +27 11 838-5923/833-8156
E-mail: yolanda@saimm.co.za, Website: http://www.saimm.co.za

29–31 August 2018 — **MineSafe 2018 Technical Conference and Industry day**
Gallagher Convention Centre, Johannesburg
Contact: Camielah Jardine
Tel: +27 11 834-1273/7, Fax: +27 11 838-5923/833-8156
E-mail: camielah@saimm.co.za, Website: http://www.saimm.co.za

18–19 September 2018 — **4th Young Professionals Conference**
'Creating a sustainable African minerals industry through applied innovation'
Focus Rooms, The Core, Sunninghill, Sandton
Contact: Camielah Jardine
Tel: +27 11 834-1273/7, Fax: +27 11 838-5923/833-8156
E-mail: camielah@saimm.co.za, Website: http://www.saimm.co.za

14–17 October 2018 — **Furnace Tapping 2018 Conference**
Nombolo Mdhluli Conference Centre, Kruger National Park, South Africa
Contact: Camielah Jardine
Tel: +27 11 834-1273/7, Fax: +27 11 838-5923/833-8156
E-mail: camielah@saimm.co.za, Website: http://www.saimm.co.za

24 October 2018 — **15th Annual Student Colloquium**
Johannesburg
Contact: Yolanda Ndimande
Tel: +27 11 834-1273/7, Fax: +27 11 838-5923/833-8156
E-mail: yolanda@saimm.co.za, Website: http://www.saimm.co.za

25–26 October 2018 — **Higher Education Development in the Extractive Industry 2018 Workshop**
Glenhove
Contact: Yolanda Ndimande
Tel: +27 11 834-1273/7, Fax: +27 11 838-5923/833-8156
E-mail: yolanda@saimm.co.za, Website: http://www.saimm.co.za

2019

13–15 November 2019 — **XIX International Coal Preparation Congress & Expo 2019**
New Delhi, India
Contact: Coal Preparation Society of India
Tel/Fax: +91-11-26136416, 4166 1820
E-mail: cpsidelhi. india@gmail.com, president@cpsi.org. in rksachdevO 1 @gmail.com, hi. sapru@monnetgroup.com

Company Affiliates

The following organizations have been admitted to the Institute as Company Affiliates

3M South Africa (Pty) Limited
AECOM SA (Pty) Ltd
AEL Mining Services Limited
Air Liquide (PTY) Ltd
Alexander Proudfoot Africa (Pty) Ltd
AMEC Foster Wheeler
AMIRA International Africa (Pty) Ltd
ANDRITZ Delkor(pty) Ltd
Anglo Operations Proprietary Limited
Anglogold Ashanti Ltd
Arcus Gibb (Pty) Ltd
Atlas Copco Holdings South Africa (Pty) Limited
Aurecon South Africa (Pty) Ltd
Aveng Engineering
Aveng Mining Shafts and Underground
Axis House Pty Ltd
Bafokeng Rasimone Platinum Mine
Barloworld Equipment -Mining
BASF Holdings SA (Pty) Ltd
BCL Limited (BCL001)
Becker Mining (Pty) Ltd
BedRock Mining Support Pty Ltd
BHP Billiton Energy Coal SA Ltd
Blue Cube Systems (Pty) Ltd
Bluhm Burton Engineering Pty Ltd(BLU003)
Bouygues Travaux Publics
CDM Group
CGG Services SA
Chamber of Mines of South Africa
Coalmin Process Technologies CC
Concor Opencast Mining
Concor Technicrete
Council for Geoscience Library
CRONIMET Mining Processing SA Pty Ltd
CSIR Natural Resources and the Environment (NRE)
Data Mine SA
Department of Water Affairs and Forestry
Digby Wells and Associates
DMS Powders
DRA Mineral Projects (Pty) Ltd
Duraset
Elbroc Mining Products (Pty) Ltd
eThekwini Municipality
Expectra 2004 (Pty) Ltd
Exxaro Coal (Pty) Ltd
Exxaro Resources Limited
Filtaquip (Pty) Ltd
FLSmidth Minerals (Pty) Ltd (FFE001)
Fluor Daniel SA (Pty) Ltd
Franki Africa (Pty) Ltd-JHB
Fraser Alexander (Pty) Ltd
G H H Mining Machines (Pty) Ltd
Geobrugg Southern Africa (Pty) Ltd
Glencore
Hall Core Drilling (Pty) Ltd
Hatch (Pty) Ltd
Herrenknecht AG
HPE Hydro Power Equipment (Pty) Ltd
IMS Engineering (Pty) Ltd
Ivanhoe Mines SA
Joy Global Inc.(Africa)
Kudumane Manganese Resources
Leco Africa (Pty) Limited
Longyear South Africa (Pty) Ltd
Lonmin Plc
Lull Storm Trading (Pty) Ltd
Magnetech (Pty) Ltd
MAGOTTEAUX (PTY) LTD
MBE Minerals SA Pty Ltd
MCC Contracts (Pty) Ltd
MD Mineral Technologies SA (Pty) Ltd
MDM Technical Africa (Pty) Ltd
Metalock Engineering RSA (Pty)Ltd
Metorex Limited
Metso Minerals (South Africa) Pty Ltd
Minerals Operations Executive (Pty) Ltd
MineRP Holding (Pty) Ltd
Mintek
MIP Process Technologies (Pty) Limited
Modular Mining Systems Africa (Pty) Ltd
MSA Group (Pty) Ltd
Multotec (Pty) Ltd
Murray and Roberts Cementation
Nalco Africa (Pty) Ltd
Namakwa Sands(Pty) Ltd
Ncamiso Trading (Pty) Ltd
New Concept Mining (Pty) Limited
Northam Platinum Ltd - Zondereinde
PANalytical (Pty) Ltd
Paterson & Cooke Consulting Engineers (Pty) Ltd
Perkinelmer
Polysius A Division Of Thyssenkrupp Industrial Sol
Precious Metals Refiners
Rand Refinery Limited
Redpath Mining (South Africa) (Pty) Ltd
Rocbolt Technologies
Rosond (Pty) Ltd
Royal Bafokeng Platinum
Roytec Global (Pty) Ltd
RungePincockMinarco Limited
Rustenburg Platinum Mines Limited
Salene Mining (Pty) Ltd
Sandvik Mining and Construction Delmas (Pty) Ltd
Sandvik Mining and Construction RSA(Pty) Ltd
SANIRE
Sebilo Resources (Pty) Ltd
SENET (Pty) Ltd
Senmin International (Pty) Ltd
Smec South Africa
Sound Mining Solution (Pty) Ltd
SRK Consulting SA (Pty) Ltd
Technology Innovation Agency
Time Mining and Processing (Pty) Ltd
Timrite Pty Ltd
Tomra (Pty) Ltd
Ukwazi Mining Solutions (Pty) Ltd
Umgeni Water
Webber Wentzel
Weir Minerals Africa
Worley Parsons RSA (Pty) Ltd

BM
BASE METALS
2018

Copper Cobalt Africa

In Association with

The 9TH Southern African Base Metals Conference

9–12 July 2018

Avani Victoria Falls Resort, Livingstone, Zambia

SAIMM is proud to host the Second Copper Cobalt Africa Conference in the heart of Africa

To be held in Livingstone, Zambia, this anticipated and prestigious event provides a unique forum for discussion, sharing of experience and knowledge, and networking for all those interested in the processing of copper and cobalt in an African context, in one of the world's most spectacular settings - the Victoria Falls.

The African Copper Belt is again experiencing a resurgence of activity following the commodity downturn of recent years. A significant proportion of capital spending, project development, operational expansions, and metal value production in the Southern African mining industry take place in this region. The geology and mineralogy of the ores are significantly different to those in other major copper-producing regions of the world, often having very high grades as well as the presence of cobalt. Both mining and metallurgy present some unique challenges, not only in the technical arena, but also with respect to logistics and supply chain, human capital, community engagement, and legislative issues. This conference provides a platform for discussion of a range of topics, spanning the value chain from exploration, projects, through mining and processing, to recycling and secondary value addition.

For international participants, this conference offers an ideal opportunity to gain in-depth knowledge of and exposure to the African copper and cobalt industries, and to better understand the various facets of mining and processing in this part of the world.

Jointly hosted by the Mining and Metallurgy Technical Programme Committees of the Southern African Institute of Mining and Metallurgy (SAIMM), this conference aims to:

- Promote dialogue between the mining and metallurgical disciplines on common challenges facing the industry
- Enhance understanding of new and existing technologies that can lead to safe and optimal resource utilization
- Encourage participation and build capacity amongst young and emerging professionals from the Copper Belt region.

The organizing committee looks forward to your participation.

Conference Topics

- Mineralogy
- Exploration and new projects
- Open-cast mining
- Underground mining
- Rock engineering
- Mine planning
- Mineral resource management
- Geometallurgy
- Minerals processing
- Pyrometallurgy
- Hydrometallurgy
- Current operational practices and improvements
- Project development and execution
- Novel technologies for this industry
- Socio-economic challenges
- Recycling
- Waste treatment and minimization
- Environmental issues

Sponsors

AARD · AXISHOUSE · BASF We create chemistry · CiDRA Minerals Processing · CM solutions Metallurgical consultancy & Laboratories · DERRICK Authorized Distributor · Elkem Carbon · GE · IMP Innovative Solutions · MASIMO · MASIMO CHEMICALS South Africa · Murray & Roberts · Murray & Roberts Cementation · Outotec · ProProcess · SIBELCO · SOLVAY asking more from chemistry · srk · ZEISS

Media Sponsor MEI

To add your name to the mailing list and to receive further information, please e-mail your contact details to: Camielah Jardine: Head of Conferencing
SAIMM, P O Box 61127, Marshalltown 2107, Tel: +27 (0) 11 834-1273/7
E-mail: camielah@saimm.co.za, Website: http://www.saimm.co.za

SAIMM THE SOUTHERN AFRICAN INSTITUTE OF MINING AND METALLURGY

First choice for the sand and aggregate industry

We supply:
Trio® crushers
Trio® vibrating screens
Enduron® vibrating screens
Trio® feeders
Trio® washers
Trio® conveyors
Sand washing solutions

For more information contact us on +27 11 9292600.
Get more from your quarry with Trio®. Visit www.trio.weir today

WEIR

TRIO®

Minerals
www.minerals.weir